Model development and numerical investigation of soot formation in combustion

Abhijit J. Kalbhor

Model development and numerical investigation of soot formation in combustion

Doctoral dissertation

Abhijit Kalbhor

TU/e EINDHOVEN
UNIVERSITY OF
TECHNOLOGY

ƎSTiMatƎ

Model development and numerical investigation of soot formation in combustion

PROEFSCHRIFT

ter verkrijging van de graad van doctor aan de Technische Universiteit
Eindhoven, op gezag van de rector magnificus prof.dr. S.K. Lenaerts,
voor een commissie aangewezen door het College voor Promoties, in het
openbaar te verdedigen op vrijdag 7 juli 2023 om 11:00 uur

door

Abhijit Kalbhor

geboren te Pune, India

Dit proefschrift is goedgekeurd door de promotoren en de samenstelling van de promotiecommissie is als volgt:

voorzitter:	prof.dr.ir. P.D. Anderson
1^e promotor:	prof.dr.ir. J.A. van Oijen
2^e promotor:	dr.ir. L.M.T. Somers
leden:	Prof.Dr.-Ing. A.M. Kempf (Universität Duisburg-Essen)
	prof.dr. B.P.G. Cuenot (CERFACS)
	prof.dr.ir. H.C. de Lange
adviseur:	dr. D. Mira Martinez (Barcelona Supercomputing Center)

Het onderzoek of ontwerp dat in dit proefschrift wordt beschreven is uitgevoerd in overeenstemming met de TU/e Gedragscode Wetenschapsbeoefening.

To my family . . .

Summary

Model development and numerical investigation of soot formation in combustion

Owing to the adverse environmental and health impact of soot, many stricter norms are introduced by regulatory organizations to curb their emissions from combustion systems. In addition to the overall concentration, the newer norms focus on controlling the size of emitted soot particles. Therefore, in recent years, there is great interest in the development of detailed soot models to effectively capture the size distribution of soot particles emitted from combustion processes. However, the complexities of the physico-chemical processes associated with soot formation make the development of such detailed soot models very challenging. Moreover, the accurate description of soot particle dynamics and the collision phenomenon associated with them make detailed soot modeling computationally intensive. Therefore, to achieve reliable and adequate prediction of soot characteristics, the development of computationally efficient, high-fidelity modeling tools is essential. In this context, the present work is aimed at developing computationally efficient predictive CFD tools based on tabulated chemistry and the discrete sectional method (DSM) to characterize the soot formation in laminar and turbulent flames. Besides addressing this major objective, some fundamental studies on soot formation are conducted on laminar flames. The thesis is, therefore, organized into two major parts.

The first part of the thesis is dedicated to numerical studies of soot formation in canonical laminar counterflow flames with detailed chemical kinetics and a sectional soot model. One of these studies focuses on understanding soot-inhibiting effects and associated chemical pathways of hydrogen addition and water vapour dilution in laminar counterflow flames. Numerical results reveal that the addition of H_2 to the fuel and H_2O to the oxidizer decreases the soot concentration through chemical effects. The chemical effects of H_2 and H_2O addition primarily translate into decreased rates of soot surface growth, which consequently influence the shape of the bimodal particle size distribution (PSD). Moreover, since flame stretch and curvature play important roles in multi-dimensional flames, a comprehensive study is conducted to investigate the influence of flame curvature on soot formation in steady and unsteady counterflow. In this study, a detailed analysis of various soot sub-processes is carried out to acquire insights into the associated mechanism. The results demonstrate that the soot response in curved counterflow flames is strongly correlated to the residence time of soot particles in the soot formation zone and differential diffusion effects due to their high Schmidt numbers.

The second part of the present work concerns the coupling of the DSM-based soot model with Flamelet Generated Manifold (FGM) tabulated chemistry for the efficient prediction of soot formation in laminar and turbulent flames. A comparative assessment of different strategies of coupling DSM with FGM chemistry is performed to

investigate their accuracy and computational performance in canonical 1-D and 2-D laminar flames. Due to the large computational resource requirements of DSM-based soot models, their application in simulations of multi-dimensional configurations is limited. To address this challenge, a novel computationally efficient approach based on the clustering of soot sections is proposed for the numerical prediction of soot formation with the FGM-DSM strategy. Numerical results of 1-D and 2-D flame simulations revealed that the proposed method reproduces the global soot quantities (volume fraction, number density), PSDs, and their dynamic response predicted by detailed kinetics reasonably well. Subsequently, to validate FGM-DSM methods in turbulent flames, which are often relevant to industrial-scale applications, an LES formalism is developed. The LES framework is first applied to a laboratory-scale turbulent sooting jet flame to investigate the effects of filtered soot source term treatment. The LES studies are extended to investigate the effects of differential diffusion and thermal radiation on soot formation and evolution of its PSD in a turbulent environment. LES results show that in turbulent flames, capturing the unsteady evolution of soot from the gas phase, especially near the inception locations is of importance for the accurate quantitative prediction of soot with FGM chemistry. The LES investigation highlights the requirement for future research in flamelet-based approaches for soot modeling in turbulent flames and the development of efficient predictive CFD tools relevant to industrial applications.

Samenvatting

Modelontwikkeling en numeriek onderzoek van roetvorming bij verbranding

Vanwege de nadelige gevolgen van roet voor het milieu en de gezondheid worden door regelgevende organisaties steeds strengere normen ingevoerd om de uitstoot ervan door verbrandingssystemen te beperken. Naast de totale hoeveelheid richten de nieuwere normen zich op het beheersen van de grootte van de uitgestoten roetdeeltjes. Daarom is er de laatste jaren grote belangstelling ontstaan voor de ontwikkeling van gedetailleerde roetmodellen om de grootteverdeling van de door verbrandingsprocessen uitgestoten roetdeeltjes effectief vast te leggen. De complexiteit van de fysisch-chemische processen in verband met roetvorming maakt de ontwikkeling van dergelijke gedetailleerde roetmodellen echter tot een grote uitdaging. Bovendien maken de nauwkeurige beschrijving van de dynamiek van de roetdeeltjes en het daarmee gepaard gaande botsingsverschijnsel, gedetailleerde roetmodellen rekenintensief. Voor een betrouwbare en adequate voorspelling van de eigenschappen van roet is de ontwikkeling van numeriek efficiënte en betrouwbare modelleringsinstrumenten dan ook essentieel. In deze context is het huidige werk gericht op de ontwikkeling van numeriek efficiënte voorspellende CFD-tools op basis van chemie in tabelvorm en de discrete sectional method (DSM) om de roetvorming in laminaire en turbulente vlammen te karakteriseren. Naast deze hoofddoelstelling worden enkele fundamentele studies over roetvorming uitgevoerd op laminaire vlammen. Het proefschrift bestaat daarom uit twee grote delen.

Het eerste deel van het proefschrift is gewijd aan numerieke studies van roetvorming in canonieke laminaire tegenstroomvlammen met gedetailleerde chemische kinetiek en een sectioneel roetmodel. Een van deze studies richt zich op het begrijpen van de remmende effecten op roetvorming en de bijbehorende chemische routes van waterstoftoevoeging en waterdampverdunning in laminaire tegenstroomvlammen. Numerieke resultaten tonen aan dat de toevoeging van H_2 aan de brandstof en H_2O aan de oxidator de roetconcentratie vermindert door chemische effecten. De chemische effecten van de toevoeging van H_2 en H_2O vertalen zich voornamelijk in een verminderde groei op het roetoppervlak, wat de vorm van de bimodale deeltjesgrootteverdeling (PSD) beïnvloedt. Aangezien vlamrek en -kromming een belangrijke rol spelen in multidimensionale vlammen, wordt bovendien een uitgebreide studie verricht naar de invloed van vlamkromming op roetvorming in een stationaire en tijdsafhankelijke tegenstroom. In deze studie wordt een gedetailleerde analyse van verschillende roetvormingsprocessen uitgevoerd om inzicht te krijgen in het onderliggende mechanisme. De resultaten tonen aan dat de roetrespons in gekromde tegenstroomvlammen sterk samenhangt met de verblijftijd van roetdeeltjes in de roetvormingszone en differentiële diffusie-effecten als gevolg van hun hoge Schmidt-getallen.

Samenvatting

Het tweede deel van dit werk betreft de koppeling van het op DSM gebaseerde roetmodel met Flamelet Generated Manifold (FGM) getabelleerde chemie voor de efficiënte voorspelling van roetvorming in laminaire en turbulente vlammen. Een uitgebreide analyse van verschillende strategieën van koppeling van DSM met FGM chemie wordt uitgevoerd om hun nauwkeurigheid en rekenprestaties in canonieke 1-D en 2-D laminaire vlammen te onderzoeken. Omdat DSM-gebaseerde roetmodellen veel rekenkracht vergen, is hun toepassing in simulaties van multidimensionale configuraties beperkt. Om deze uitdaging aan te gaan, wordt een nieuwe rekenkundig efficiënte aanpak voorgesteld, gebaseerd op de clustering van roetsecties, voor de numerieke voorspelling van roetvorming met de FGM-DSM-strategie. Numerieke resultaten van 1-D en 2-D vlamsimulaties toonden aan dat de voorgestelde methode de globale roethoeveelheden (volumefractie, deeltjesdichtheid), deeltjesgrootteverdeling en hun dynamische respons, voorspeld door gedetailleerde kinetiek, redelijk goed reproduceert. Vervolgens wordt een Large Eddy Simulation LES-formalisme ontwikkeld om de FGM-DSM-methode te valideren in turbulente vlammen, die vaak relevant zijn voor toepassingen op industriële schaal. Het LES-model wordt toegepast op een turbulente straalvlam op laboratoriumschaal om de effecten van een gefilterde roetbron te onderzoeken. De LES-studies worden uitgebreid om de effecten van differentiële diffusie en thermische straling op roetvorming en de ontwikkeling van de PSD ervan in een turbulente omgeving te onderzoeken. De LES-resultaten tonen aan dat in turbulente vlammen het vastleggen van de tijdsafhankelijke ontwikkeling van roet uit de gasfase, vooral in de initiële vormingsfase, van belang is voor een nauwkeurige kwantitatieve voorspelling van roet met FGM-chemie. Het LES-onderzoek onderstreept de noodzaak van toekomstig onderzoek naar FGM gebaseerde benaderingen voor roetmodellering in turbulente vlammen en de ontwikkeling van efficiënte voorspellende stromingsmodellen die relevant zijn voor industriële toepassingen.

Contents

Contents

1

Introduction

This chapter presents the global context and motivation behind the current work. The fundamentals of the soot formation process in combustion are provided. The current state-of-the-art and challenges associated with soot modeling are discussed. The research questions and the objectives of this thesis are introduced, followed by the outline.

1.1 Background

For most of history, the combustion of conventional fossil-based fuels has been the primary mean of energy conversion. Although over the last decade, there has been remarkable growth in renewable and non-conventional energy resources (e.g. solar or nuclear power), the transformation to 'fossil-free' energy still has a long way to go. Even in the present day, fossil resources account for about 80% of the worldwide total energy supply (see Fig. 1.1), and the energy dependency on fossil resources is estimated to continue through 2040 [1]. Therefore, for the foreseeable future, the combustion of fossil-based hydrocarbons will remain the prominent energy conversion process for global energy production.
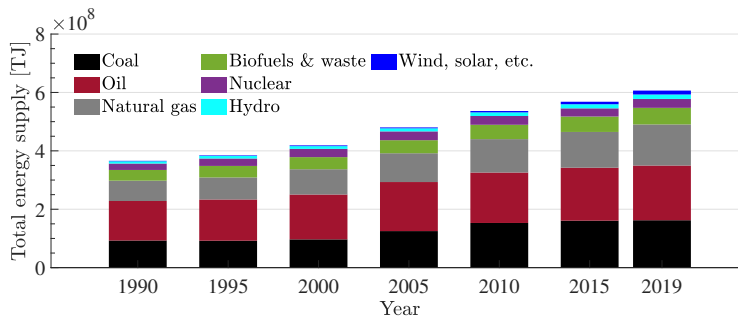
Figure 1.1: World's total primary energy supply by source [1].

Unfortunately, the main concern associated with combustion processes is emissions of harmful byproducts that need to be mitigated. It is common knowledge that greenhouse gases such as carbon dioxide (CO_2) generated through the combustion of fossil fuels have a strong impact on global warming and climate change. In addition, pollutants resulting from incomplete combustion such as carbon monoxide, nitrogen oxides, and particulate matter are responsible for the severe degradation of atmospheric air quality. Particularly, pollutants comprising particulate matter (commonly known as soot) are toxic, carcinogenic, and cause many respiratory and cardiovascular illnesses [2, 3]. Besides harmful health effects, the formation of soot particles can severely compromise the operation of combustion devices through high radiation fluxes and deposition in the form of solid matter [4]. Hence, from the perspective of mitigating health and environmental impacts and controlling the operational efficiency of combustion systems, monitoring soot emissions is critical. Consequently, legislative regulations on limits for industrial and transportation-related soot emissions have become stricter.

For example, in Europe, the Euro standards regulate the emissions from light passenger and commercial vehicles operating on gasoline or diesel engines. According to Euro 6 norm [6] of 2020, a particulate mass (PM) emission limit of 4.5 mg/km shall apply to diesel engine vehicles, which is about factor 5 lower than the Euro 4 standard
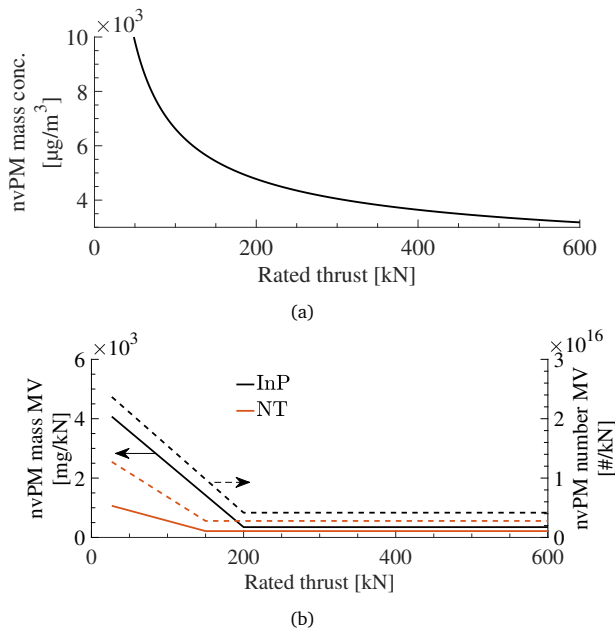
Figure 1.2: Graphical presentation of the CAEP/10 nvPM mass concentration standard (a), the CAEP/11 LTO nvPM mass and number regulatory limits for in-production (InP) and new type (NT) aircraft engines of rated thrust greater than 26.7 kN (b). Adopted from Ref. [5].

of 2005. Moreover, the particle number (PN) emission limit of 6×10^{11} #/km has been introduced in Euro 6 standard. In the aviation industry, the emissions of particulate matter are of great concern considering a drastic increase in commercial air travel over the past decade. The International Civil Aviation Organization (ICAO) has provided regulations for emissions of non-volatile particulate matter (nvPM) (with a diameter smaller than 2.5 microns). Before 2016, the Smoke Number (SN) regulation was the only emission standard related to PM emissions, which required engine emissions to be invisible. However, in 2016, ICAO-CAEP (Committee on Aviation Environmental Protection) introduced CAEP/10 certification standard [5] for maximum nvPM mass concentration (see Fig. 1.2a) along with CAEP/11 LTO (landing and take-off cycle) mass and number emission limit (Fig. 1.2b) to all in-production engine types of rated thrust greater than 26.7 kN. From 1 January 2023 onward, all new aircraft will have to meet both mass and number standards for nvPM emissions to enter operation.

To achieve the goals of such stringent emission norms, seeking novel solutions and technological improvements has become a primary agenda in the design and development of modern-day combustion systems. With advancements in computer architecture, robust numerical schemes, and physically consistent models, computational fluid dynamics (CFD) methods have emerged as efficient, essential, and successful tools for studying combustion processes in practical applications. Hence, CFD techniques are being widely used in the industry for designing combustion devices to meet emission norms. The significant research conducted over the past several decades has remarkably advanced the development of reliable predictive models for soot formation. However, soot formation is a complex multi-physics process, and many of the fundamentals of soot chemistry remain elusive. Therefore, numerical investigation of soot becomes challenging as models for soot prediction suffer from limitations in realistically mirroring the physical phenomena. Prior to addressing the challenges associated with soot modeling, it is imperative to understand the fundamentals of the soot formation process. Despite the gaps in current understanding, some consensus exists on the phenomena associated with soot formation in combustion, which will be discussed in the following section.

1.2 Soot formation fundamentals

In combustion, soot mainly refers to sub-micron-sized carbonaceous aggregated elementary particles produced during the high-temperature pyrolysis or fuel-rich conditions through complex physico-chemical processes [4]. These processes mainly involve precursor formation, nucleation, soot growth, and oxidation.

1.2.1 Precursor formation

Under high-temperature fuel-rich conditions, extensive decomposition and rearrangement of fuel molecules (pyrolysis) occur which leads to the formation of unsaturated

hydrocarbons. These products of pyrolysis (e.g. acetylene) play a key role in the formation of polycyclic aromatic hydrocarbons (PAHs), which are widely recognized as precursors to soot formation [7]. The growth of PAHs starts from the formation of the first aromatic ring (e.g. benzene/phenyl radical or naphthalene). The major pathways of benzene ring formation in aliphatic fuels are reviewed by Wang and Chung [8], which notably concern acetylene addition to butatrienyl radical (n-C_4H_3), propargyl (C_3H_3) recombination, and reaction between cyclopentadienyl (c-C_5H_5) and methyl radical (CH_3), etc. Similarly, the molecular growth beyond the first aromatic ring to larger PAHs proceeds through a wide variety of radical-molecule type reactions [9]. The most well-known pathway for PAH growth relies on the two-step Hydrogen-Abstraction-Carbon/C_2H_2-Addition (HACA) mechanism proposed by Frenklach and Wang [10]. The HACA mechanism involves a repetitive reaction sequence of aromatic activation through the loss of the hydrogen atom from stable molecules, followed by the attachment of acetylene (C_2H_2) to the activated free-radical site, causing aromatic molecules to grow. Although the HACA mechanism is most commonly adopted, the growth of PAHs may also initiate through other pathways. These pathways mainly involve reactions between PAH and propargyl, benzyl, and cyclopentadienyl radicals [8, 11, 12] or the direct aromatic combination. Moreover, aromatic fuels can rapidly proceed to form larger PAH species bypassing fuel decomposition and aromatic ring formation steps [8]. However, the formation of the first aromatic ring and pathways leading to its growth to larger PAHs is still an open question [13] and the relative importance of individual pathways strongly depends on the molecular structures of fuels and flame environments [8].

1.2.2 Nucleation

The subsequent, and perhaps the least understood step in soot formation is the transition of gas-phase precursors to solid-phase nascent soot particles through nucleation [13]. Although a unique soot precursor has not been identified, the formation of soot nuclei through collision and physical coalescence of large PAH molecules following their dimerization advocated by Frenklach and Wang [10, 14], is widely accepted and adopted in soot modeling. Recent experimental observations [15, 16] suggest the presence of dimers as an important intermediate in the formation of the first nascent soot particles. Various other pathways that conceptualize soot nucleation have been suggested in the literature and can be found in the review by Wang [17]. These pathways generally concern the growth of PAHs to fullerene-like curved structures [18], and chemical coalescence between precursors discussed by D'Anna and co-workers [19, 20] to form cross-linked three-dimensional structures. Recently, Johansson et al. [21] proposed a radical-driven hydrocarbon-clustering mechanism to provide a physically viable route to particle formation. While significant efforts have been done on this subject, a definite nucleation mechanism yet needs to be established.

1.2.3 Particle growth

Once formed by nucleation, soot particles continue to grow in mass and size through both chemical and physical processes. The chemical process of particle growth concern mass additions through heterogeneous surface reactions. During surface growth, gaseous species (predominately acetylene) are added to the particle surface forming larger primary particles. Analogous to the formation of gas-phase PAHs, the HACA mechanism proposed by Frenklach and co-workers [10, 14, 22, 23] is the most widely used to describe surface growth. In this mechanism, the soot surface is characterized by aromatic basal planes and edge sites. The particle edge is firstly activated by dehydrogenation forming radical sites followed by acetylene addition to the reactive sites. The molecular orientation and number of active radical sites control the surface reactivity of the soot particle. Several extensions of the HACA mechanism describing dehydrogenation reactions through radical species have been proposed in the literature [24–27]. The physical processes of soot growth include condensation and coagulation. Condensation refers to the deposition of gas-phase soot precursors (mostly PAHs) on the surface of the soot particle [28]. Coagulation is the process wherein soot particles collide with each other and combine into large particles. For relatively small particles, coagulation causes coalescence, forming spherical-shaped primary particles, while as soot particles mature, they tend to aggregate and form chain-like fractal structures. Physical interactions between soot particles through coagulation and agglomeration processes largely influence their number density and morphology leading to poly-dispersed soot ensembles.
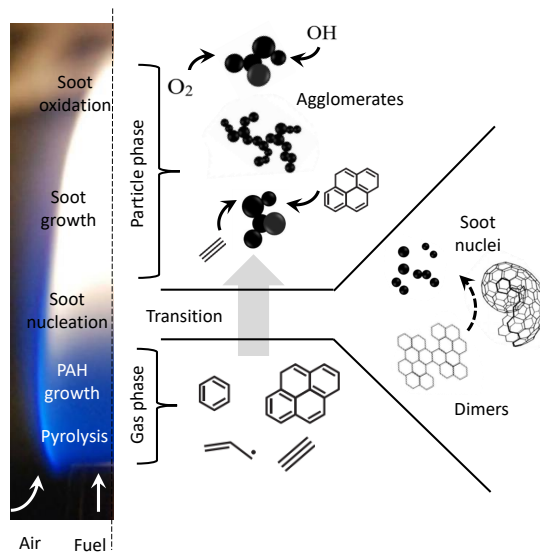
Figure 1.3: Schematic representation of soot formation in a laminar diffusion flame (not to scale).

1.2.4   Soot oxidation

Soot oxidation is a chemical reaction process, in which soot particles are oxidized by the attack of oxidizing species on their surfaces. Oxidation occurs mostly due to the attack of molecules like O_2 and radicals like O and OH resulting in soot mass reduction while converting part of soot back into gases (e.g. CO and CO_2 [29–31]). In a fuel-lean environment, H_2O, CO_2, NO, N_2O, and NO_2 are also important oxidants [32,33]. In contrast to surface growth, which occurs in a specific step, oxidation happens all the time during and after soot formation. Soot oxidation is a key process that influences the overall soot concentration emitted from combustion systems. Besides oxidation, fragmentation or physical division of soot aggregates also leads to the reduction of soot particle size [34]. Furthermore, oxidation-induced fragmentation can also lead to the weakening and division of soot aggregates. A schematic diagram of soot formation in a laminar diffusion flame highlighting different sub-processes is shown in Fig. 1.3.

1.3   Numerical prediction of soot formation

1.3.1   Overview of soot modeling

Successful predictive modeling of soot formation in practical combustion systems requires a fundamental understanding of various soot processes, as well as the development of robust, physically consistent, and computationally efficient techniques to describe these processes. The state-of-the-art soot modeling approaches mainly concern three aspects:

- Modeling of soot formation subprocesses

- Description of soot particle dynamics

- Chemistry modeling

In the following sections, these aspects are briefly discussed.

Modeling of soot formation sub-processes

As emphasized earlier, nucleation remains the most elusive soot formation stage and its modeling is a subject of considerable uncertainty. Supported by several experimental [15, 16] and modeling [10, 14, 27, 35–37] studies, the current consensus among the combustion community relies on the PAH collisions leading to dimerization as the major soot nucleation pathway. Therefore, the choice of specific PAHs becomes critical in the quantitative prediction of soot. Relatively simple yet effective models relying on pyrene as a unique PAH species leading to nucleation find broad applicability in sooting flame simulations [23, 38–40]. However, some studies point out the possibility of nucleation starting in even smaller ones such as naphthalene [41].

Moreover, collisions with variable efficiencies (referred to as sticking coefficients) between PAHs larger than pyrene have also been considered in recent nucleation models [27, 42, 43]. The collision parameters in multiple-PAH-based models are often empirically introduced in conjunction with gas-phase kinetics and require adjustment for different chemical mechanisms. Collisions between PAHs are generally assumed to be irreversible, however, reversible PAH dimerization has also been introduced [44] in nucleation models. Besides PAH dimerization, several other hypotheses exist in the literature for describing the nucleation process. These include nucleation through polymerization by acetylene process [39], clustering of peri-condensed aromatic hydrocarbons, and oligomers of aromatic compounds [45]. Recently, the mechanism called CHRCR (clustering of hydrocarbons by radical chain reactions) is proposed by Johansson et al. [21] recognizing the importance of resonance-stabilized radicals (RSRs) in soot inception and growth. This mechanism is upgraded by incorporating the preferential reactivity of PAHs based on the carbon atoms to form RSR [46]. Moreover, chemical nucleation pathways that describe nucleation through the chemical coalescence of PAHs [19] have been gaining fundamental interest. The advancement of chemical nucleation models inheriting irreversible chemical bond formation after reversible PAH dimerization has been proposed by Kholghy et al. [47].

Besides nucleation, modeling of particle growth processes (primarily surface reactions) is a crucial aspect of the numerical prediction of soot. Although the HACA model has been widely accepted in the combustion community to describe the surface growth of soot particles, different variants of this mechanism exist in the literature. For instance, in flame environments lacking H atoms, dehydrogenation from soot particles via reactions with aliphatic radicals such as methyl (CH_3), ethynyl (C_2H), and propadienyl (C_3H_3) has been proposed [25]. In HACA growth rates, the surface reactivity of soot particles depends on thermal state and particle morphology which may impact the overall accuracy of soot surface kinetics. Although many different empirical models accounting for the variation in soot particle morphology, temperature dependence [23], residence time [48], and soot aging [49] can be found in the numerical works, no universal formulation has been reported yet, and it is still an open topic. The oxidation of soot is another key sub-process, which possesses a wide range of variation in modeling parameters [50–53]. In the classical HACA mechanism [14], OH and O_2 are considered the major species contributing to the surface oxidation of soot particles. However, other oxidizing species such as CO_2, H_2O, and O have also been experimentally examined [32, 33] to be possible contributors to soot oxidation. Moreover, oxidation models incorporating the effects of soot aging, which reduces the surface reactivity of soot particles have also been proposed [54].

Description of soot particle dynamics

Soot models use various approaches to incorporate the dynamics of soot particles, based on their ability to access the number density and particle size distribution (PSD). These approaches are mainly categorized into (semi-)empirical models and

detailed models. In empirical models, 'ad-hoc' or experimentally determined empirical correlations related to temperature [55] or mixture fraction [56] are used to describe the soot formation subprocesses. Although empirical models are simple to implement and computationally efficient, empirical parameters are often insufficient to capture the physico-chemical evolution of soot over varying operating conditions. Semi-empirical models, on the other hand, incorporate additional soot subprocesses beyond simple formation-oxidation and describe the evolution of soot particles in terms of mass and number density (e.g. as proposed in Ref. [57, 58]) by assuming a mono-disperse soot population. Due to easy integration with turbulent models, semi-empirical models have been extensively used to predict soot production in turbulent flames [59, 60]. Although global quantities (volume fraction and number density) can be predicted reasonably well with semi-empirical models at low CPU cost, their validity is limited by the fitted empirical correlations, lack of access to PSD, or morphological description.

In contrast to (semi-)empirical models, the detailed soot models consider aerosol dynamics for predicting soot particle size distribution. To represent the dynamics of a polydisperse particulate system, the population balance equation (PBE) is solved, in either a direct or indirect manner. For the description of the PSD, approaches based on stochastic methods, methods of moments, kinetic models, and discrete sectional methods are commonly used in detailed models. The most accurate evolution of soot particle dynamics can be provided by stochastic models based on Monte Carlo (MC) methods [48, 61]. In MC-based models, soot particles are considered discrete particles, therefore the evolution of their number density can be tracked without any assumption on the PSD shape or soot morphology. However, a large number of particles are required to be transported for converged statistics for PSD, which increase the computational cost of MC methods compared to semi-empirical models. Moreover, coupling of MC to the gas-phase chemistry is not straightforward and often requires specific numerical treatment [62]. Hence, applications of the MC-based models have been mainly limited to simple configurations with 0-D partially-stirred reactors and 1-D laminar flames. Nevertheless, novel methods are being developed that reduce the cost of MC method-based soot models for 3-D applications.

A computationally efficient description of the PBE is offered by Method of Moments (MOM) based models [63, 64]. In MOM models, univariate or multivariate statistical moments of soot particle size distribution or number density function (NDF) are transported. Many of the key soot properties such as number density, volume fraction, and particle diameter can be adequately represented through a finite (three to six) number of moments. Besides, soot morphology can be described with volume-surface description while keeping the computational cost relatively low. As a result, MOM has been widely adopted in laminar [10, 14] and turbulent [65, 66] flame simulations for the computation of soot particle dynamics. However, MOM does not provide direct access to the PSD (or NDF). The reconstruction of PSD with MOM requires approximations and closure models for the unknown moments (non-transported). Several

methods have been developed with varying levels of mathematical complexity to close the source terms for higher moments for PSD reconstruction. These closure models typically rely on the series expansion of the number density [63], presuming the shape of the distribution, interpolative closure for obtaining the fractional moments [64,65], and approximating the moment integrals with numerical quadrature [26, 37, 67].

Another family of detailed models relies on the discretization of the PBE. They are primarily categorized as kinetic sectional models and aerosol discrete sectional models. In kinetic models, soot particles are considered as gas-phase chemical species and their volume is discretized in bins. The evolution of soot particles is described through the transport of mass fractions using a global kinetic scheme and interactions between bins are treated as chemical reactions [13, 52, 68–70]. This strategy facilitates easy coupling between the soot and gas phases and also provides information on PSD. However, the application of these methods is limited to laminar flames as detailed mechanisms and a large number of bins make these methods CPU-demanding and practically impossible for large-scale simulations.

In the discrete sectional method (DSM) [35,71], the continuous soot particle size distribution is divided into a finite number of sections representative of particle size (or mass). The evolution of soot particles is obtained through transport equations of the soot scalar (mass fraction typically), and PSD information can be accessed from the sectional soot scalar. Obviously, for a better representation of PSD, a large number (25-100) of sections is required which increases the CPU cost of simulations. Therefore, the choice of the number of sections depends on the trade-off between numerical accuracy and computational cost. The DSM models have been extended to enable the information on soot morphology [72], which requires an additional transport equation per section for the primary particle number density. Due to relatively higher CPU cost, the application of DSM was mostly limited to RANS [35, 36]. However, in recent years, DSM has been effectively adopted in LES studies of turbulent flames [73], facilitating the investigation of soot PSD evolution.

Besides the aforementioned models, several hybrid approaches [74, 75] combining different categories of models have been proposed. For example, Lagrangian-based approaches, wherein soot is treated as a discrete phase, and trajectories of their evolution are tracked, have been applied in laminar and turbulent flames [76–78]. The Lagrangian soot tracking methodology enables a direct description of the polydispersity of the soot population. Although Lagrangian models have demonstrated promising predictive capabilities, the CPU cost and statistical convergence of Lagrangian models depend on the number of particles tracked, limiting their application in large-scale simulations.

To summarize, the choice of soot model in combustion simulations is often a problem (laminar/turbulent flames) dependent and driven by the level of accuracy from the description of global soot quantities to the prediction of size distribution considering the affordability of computational resources.

Chemistry modeling

Soot formation exhibits strong coupling with the thermochemical state of the reacting flow. Hence, models employed for the description of combustion chemistry have a significant impact on the prediction of soot. In principle, reliable prediction of gaseous phase precursors including large PAHs can lead to more accurate soot prediction. However, the prediction of such large PAHs presents a great challenge as it requires chemical kinetic schemes featuring hundreds of chemical species and thousands of reactions [69]. For canonical 1-D configurations, the use of such large kinetics mechanisms is feasible, however, due to the extremely high CPU cost and numerical stiffness of the system, their application to multi-dimensional flames is practically inconceivable. Moreover, reaction pathways related to the formation of PAHs can significantly differ based on fuel types, which presents an additional challenge for the validation of soot models, as the soot prediction accuracy may be compromised depending on the kinetic mechanism utilized. Several chemistry reduction techniques have been proposed to overcome these limitations. In the context of kinetic reduction techniques, analytically reduced, optimized kinetic schemes along with systematic automation are attractive. Analytically-reduced schemes have been applied recently for sooting flame simulations [79]. Nevertheless, the solution of the soot phase remains an additional computational challenge, that supersedes the reduction achieved in the gas-phase description, especially for detailed soot models. Despite the progress in multicore architectures and CPU accelerators, the application of such reduced-order kinetic schemes becomes unaffordable for conditions of potential interest.

On the other hand, due to remarkably low CPU cost, flamelet-based models are popular and often employed in multi-dimensional sooting flame simulations, to efficiently represent the combustion chemistry. In flamelet-based models, pre-computed flamelet solutions are stored in a look-up database and the thermo-chemical state of the system is parameterized with a reduced set of control variables. Several tabulated-chemistry approaches exist in the literature with slight differences in their formulation. These approaches mainly include Flamelet Generated Manifold (FGM) introduced by van Oijen and de Goey [80], the Flamelet Progress Variable (FPV) model proposed by Pierce and Moin [81], and the Flame Prolongation of ILDM (FPI) from Gicquel et al. [82]. Regarding the simulations of sooting flames, tabulated chemistry coupled with semi-empirical [83], MOM-based [66,75,84] models have been widely applied and have been recently extended to DSM models [73]. However, modeling of soot formation with flamelet-based techniques relies on several assumptions such as fast chemistry which is not entirely valid for slowly evolving soot. Generally, the lookup databases are constructed from steady, planar flamelets often neglecting preferential diffusion effects, which may not capture the history of gas and soot phase evolution and can impact the prediction of soot formation. Furthermore, coupling between the gas-solid phase requires special treatments in flamelet-based methods.

Besides flamelet methods, several other combustion models have been explored in the numerical prediction of soot. For example, the Conditional Momentum Closure (CMC)

based combustion model, which enables a more elaborate description of the unsteady local flame structure in mixture fraction space is another promising framework for capturing soot emissions [85]. Very recently, Sewerin and Rigopoulos [86] used the combustion model based on stochastic field equations for the soot kinetic process to predict the soot particle size distribution in turbulent flames. New techniques based on machine learning models [87] and virtual chemistry [88] have been proposed in recent times for the prediction of soot formation in laminar flames at drastically reduced CPU cost.

1.3.2 Soot modeling in turbulent flows

The current state of the art suggests that detailed soot models coupled with detailed kinetics, transport, and radiation models tend to provide a fairly good prediction of soot formation in laminar flames after careful calibration of models. The progression towards soot prediction in turbulent flames is, however, very challenging [89]. Although different soot modeling techniques in combination with combustion models have been investigated in the context of turbulent flames, there is no consensus on the best approach. Modeling the interaction between turbulence and chemistry is already a key issue in turbulent flames, and the uncertainty associated with soot kinetics makes the prediction of soot formation in turbulent conditions, even more challenging.

Despite their reasonably good capabilities the detailed soot and kinetic mechanisms developed for laminar flows are often too complex and CPU-intensive to be effectively implemented in simulations of turbulent flames. Since PAH formation pathways are very sensitive to fluctuations in flow dynamics, more elaborate turbulent chemistry interaction models are required to accurately capture numerically describing soot evolutions in turbulent flames. Uncertainties in the reliable description of PAHs in turbulent flows can seriously impact the rates of critical processes like nucleation and condensation. Furthermore, the detailed description of soot particle dynamics in turbulent flames is often limited by memory and CPU power.

For large-scale simulations, models that use flamelet-based tabulated chemistry are computationally affordable. However, due to relatively slow timescales, characterizing the physico-chemical system of soot formation and PAH evolution with a few controlling scalars may not yield the expected results. Capturing the interaction of turbulence and soot is another crucial factor in turbulent flames that requires high-fidelity closure models to obtain a reliable description [89]. In general, soot formation is highly intermittent under turbulent conditions making their measurements extremely challenging. The soot model development becomes more restrictive in terms of operating conditions owing to the lack of a comprehensive experimental database. Overall, it can be argued that state-of-the-art modeling strategies still have a long way to go to reliably predict soot formation in situations of industrial interest.

1.4   Objectives and organization of the thesis

1.4.1   Research objectives and scope

Considering the different aspects delineated in the preceding sections, the primary objective of this work is to develop a computationally efficient modeling framework based on FGM chemistry for soot prediction with discrete sectional methods in turbulent flames.

This main objective is further divided into sub-tasks that aim:

- To evaluate the performance of different strategies of coupling discrete sectional method with FGM chemistry on laminar flames for accuracy and CPU cost.

- To develop LES formalism with the discrete sectional method and FGM chemistry for the soot prediction of turbulent sooting flames and burners relevant to industrial-scale applications.

From a practical perspective, the addition of non/low-sooting tendency fuels has been used as an effective strategy for controlling soot emissions. Considering the energy transition towards clean alternative fuels such as hydrogen, the current work is extended to understand the soot-inhibiting effects of hydrogen and water vapor addition on soot formation suppression through detailed simulations and identify chemical pathways.

Moreover, flame stretch and curvature are important in the context of multi-dimensional flames. Hence in this thesis, a comprehensive study is conducted to investigate the influence of flame curvature on soot formation in steady and unsteady counterflow flames and understand the associated mechanism.

1.4.2   Organization of thesis

The present chapter introduces the background of the study along with the current understanding of soot formation in the combustion process. After remarks on the state-of-the-art about soot modeling and associated challenges, key research objectives have been derived. Various investigations performed in addressing these research objectives are organized in the remainder of the thesis as follows:

In Chapter 2, the theoretical and mathematical formalism of reacting flow equations is presented. The discrete sectional method and different models for physical and chemical processes of soot production are described in detail. Subsequently, the comprehensive validation of the sectional soot model is presented for the prediction of soot formation in laminar non-premixed and premixed flames over a wide range of conditions. Remarks on the performance and limitations of the model are provided.

Chapter 3 is focused on understanding the soot-inhibiting effects of hydrogen addition to the fuel and water vapor dilution in the oxidizer on soot formation in non-premixed

counterflow flames. A detailed study of chemical pathways is conducted by isolating dilution and the chemical effects of these additives.

In Chapter 4, the influence of flame curvature on soot formation is investigated under steady and unsteady conditions. The detailed sectional model is applied to study the dynamic response of soot formation to unsteady curvature oscillations introduced to canonical counterflow flames.

In Chapter 5, a comprehensive assessment of different strategies for coupling FGM chemistry with discrete sectional method is carried out. The predictive accuracy and computational performance of these approaches are analyzed for 1-D steady and unsteady flames.

In Chapter 6, a novel computationally efficient method based on the clustering of sections is proposed for the application of FGM in the prediction of soot formation with the discrete sectional method. The capabilities of this method are investigated in laminar steady and unsteady flames.

In Chapter 7, the development of Large Eddy Simulation (LES) formalism with FGM and discrete sectional method is presented for describing soot formation in turbulent flames. The LES formalism is then applied to non-premixed turbulent jet flames to analyze the soot formation mechanism and dynamics of PSD. The effects of soot source term closure, H_2 addition, preferential diffusion, and radiative heat transfer on soot formation are investigated .

Chapter 8 concludes the present thesis with a summary of key results and some recommendations for future work.

2

Modeling of sooting flames

In this chapter, the theoretical and mathematical foundations of modeling soot formation in reactive flows are presented. The equations for chemically reacting flows are introduced, followed by a description of the physical and chemical processes involved in the soot model used. Subsequently, the performance of the soot model in predicting soot formation in a range of conditions is evaluated through simulations of laminar premixed and non-premixed flames.

2.1   Reactive flow equations

The classical governing equations [90] for multi-species reactive flows describing the conservation of total mass, species, momentum, and energy are:

Mass conservation:

$$\frac{\partial \rho}{\partial t} + \nabla \cdot (\rho \boldsymbol{u}) = 0 \tag{2.1a}$$

Species conservation:

$$\frac{\partial (\rho Y_k)}{\partial t} + \nabla \cdot [\rho(\boldsymbol{u} + \boldsymbol{V_k})Y_k] = \dot{\omega}_k \qquad \forall \quad k \in [1, N_s] \tag{2.1b}$$

Momentum conservation:

$$\frac{\partial (\rho \boldsymbol{u})}{\partial t} + \nabla \cdot (\rho \boldsymbol{u}\boldsymbol{u}) = -\nabla p + \nabla \cdot \boldsymbol{\tau} + \rho \sum_{k=1}^{N_s} Y_k \boldsymbol{f_k} \tag{2.1c}$$

Energy conservation:

$$\frac{\partial (\rho h)}{\partial t} + \nabla \cdot (\rho \boldsymbol{u} h) = \frac{\partial p}{\partial t} + \boldsymbol{u} \cdot \nabla p - \nabla \cdot \boldsymbol{q} + \boldsymbol{\tau} : (\nabla \boldsymbol{u}) + \rho \sum_{k=1}^{N_s} Y_k(\boldsymbol{V_k} \cdot \boldsymbol{f_k}) + \dot{\mathcal{Q}} \tag{2.1d}$$

where t is time, ρ is gas density, $\boldsymbol{u}$ is flow velocity vector, p is pressure, $\boldsymbol{\tau}$ is viscous stress tensor; $Y_k, \boldsymbol{V_k}, \boldsymbol{f_k}, \dot{\omega}_k$, respectively, denote mass fraction, diffusion velocity vec-

tor, external force vector, and chemical source term for species k (from total N_s); h is specific enthalpy of the mixture, q is heat flux vector and $\dot{Q}$ is the volumetric external heat source.

The closure for the system of conservation equations 2.1 is achieved through two key auxiliary relations. Using the caloric equation of state the enthalpy is correlated to temperature (T) and species mass fraction through:

$$h = \sum_{k=1}^{N_s} Y_k h_k \quad \text{with} \quad h_k = h_k^0 + \int_{T^0}^{T} c_{p,k} dT \tag{2.2}$$

where h_k^0 is the specific enthalpy of formation at reference temperature T^0, and $c_{p,k}$ is the isobaric specific heat capacity for the kth species. In many of the reactive flow systems gas mixtures are assumed to behave as perfect gases, and their thermodynamic state is given by the ideal gas equation:

$$p = \rho T \frac{R}{W} \quad \text{with} \quad W = \left(\sum_{k=1}^{N_s} \frac{Y_k}{W_k} \right)^{-1} \tag{2.3}$$

where R is the universal gas constant, W is the mean molar mass of the mixture, and W_k is molar mass of the species k.

In order to solve the system of aforementioned conservation equations, additional constitutive relations are required for τ, V_k, $\dot{\omega}_k$, and q. The viscous stress tensor τ for a fluid exhibiting a Newtonian behavior is modeled as:

$$\tau = \mu \left[\nabla u + (\nabla u)^T \right] - \frac{2}{3} \mu (\nabla \cdot u) I \tag{2.4}$$

where I is the identity tensor and μ is the dynamic viscosity. The dynamic viscosity μ depends on temperature and mixture composition and can be calculated through mixture-averaged approximation of Wilke [91] as:

$$\mu = \sum_{k=1}^{N_s} \frac{X_k \mu_k}{\sum_{j=1, k \neq j}^{N_s} X_j \Phi_{kj}} \tag{2.5}$$

In this expression, X_k is the molar fraction, and μ_k is the dynamic viscosity of species k. The dimensionless quantity Φ_{kj} is given by:

$$\Phi_{kj} = \frac{1}{\sqrt{8}} \left[1 + \left(\frac{W_k}{W_j} \right) \right]^{-1/2} \left[1 + \left(\frac{\mu_j}{\mu_k} \right)^{1/2} \left(\frac{W_j}{W_k} \right)^{1/4} \right]^2 \tag{2.6}$$

In multi-component gas mixtures, diffusion of species is caused by concentration gradients, pressure gradients, temperature gradients (Soret effect), and body forces.

Therefore, the diffusion velocity of individual species can be defined based on models with varying complexity levels. To avoid expensive numerical computation of diffusion velocity, the Hirschfelder and Curtiss approximation [92] similar to Fick's Law expression is often used, such that:

$$\boldsymbol{V_k} = -\frac{D_k}{X_k}\nabla X_k \tag{2.7}$$

where, D_k is the mixture-averaged diffusion coefficient of species k. Under the Hirschfelder-Curtiss approximation, D_k is evaluated using:

$$D_k = \frac{(1 - Y_k)}{\sum_{j \neq k}^{N_s} \frac{X_j}{\mathcal{D}_{k,j}}} \tag{2.8}$$

where $\mathcal{D}_{k,j}$ is the ordinary binary diffusion coefficient. A frequently used simplification for modeling diffusive terms is employed through the assumption of a constant Lewis number. Lewis number relates thermal conduction to species diffusion as:

$$D_k = \frac{\lambda}{\rho c_p Le_k} \tag{2.9}$$

where λ is thermal conductivity and c_p is the mixture-averaged isobaric specific heat capacity:

$$c_p = \sum_{k=1}^{N_s} c_{p,k} Y_k \tag{2.10}$$

For the calculation of thermal conductivity λ, the semi-empirical formulation of Mathur et al. [93] is applied as:

$$\lambda = \frac{1}{2}\left[\sum_{k=1}^{N_s} X_k \lambda_k + \left(\sum_{k=1}^{N_s} \frac{X_k}{\lambda_k}\right)^{-1}\right] \tag{2.11}$$

where λ_k is the thermal conductivity of the species k. The sum of diffusion fluxes should be zero as per the definition $\sum_{k=1}^{N_s} \boldsymbol{V_k} Y_k = 0$. Hence, to guarantee mass conservation, species transport equation (Eq. 2.1b) is typically solved for N_s–1 species, and from total mass conservation, $\sum_{k=1}^{N_s} Y_k = 1$, the concentration of the remaining abundant species (e.g. N_2) is obtained.

The chemical source terms $\dot{\omega}_k$ of various species are usually modeled through detailed chemical kinetic mechanisms, which describe the system of gas-phase interactions in reactive flows. The combustion of fuels is governed by many elementary reaction steps and intermediate species. In a general form, an elementary reaction in a detailed

kinetic scheme can be written as:

$$\sum_{k=1}^{N_s} v'_{k,j}\mathcal{M}_k \underset{k_{r,j}}{\overset{k_{f,j}}{\rightleftarrows}} \sum_{k=1}^{N_s} v''_{k,j}\mathcal{M}_k \qquad \forall \quad j \in [1, N_r] \tag{2.12}$$

where, $v_{k,j}$ represents the stoichiometric coefficients (the number of moles) of species $\mathcal{M}_k$ participating in the reaction j (from total N_r). The upper indexes $\prime$ and $\prime\prime$ indicate the reactants side and the products side, respectively. $k_{f,j}$ and $k_{r,j}$ are the rate coefficients for the forward and reverse reactions, respectively. $k_{f,j}$ is modeled in Arrhenius form as:

$$k_{f,j} = A_j T^{\beta_j} \exp\left(\frac{-E_{a_j}}{RT}\right) \tag{2.13}$$

where A_j is the pre-exponential factor, β_j is the temperature exponent, and E_{a_j} is the activation energy for reaction j, which are all empirical coefficients given by kinetic mechanisms.

In general, the reactions are reversible, hence the reverse reaction rate $k_{r,j}$ is also found through equilibrium constant $K_{c,j}$, as:

$$k_{r,j} = k_{f,j}/K_{c,j} \tag{2.14}$$

The equilibrium constant is given by [90]:

$$K_{c,j} = \left(\frac{p_a}{RT}\right)^{\sum_{k=1}^{N_s}\left(v''_{k,j} - v'_{k,j}\right)} \exp\left(\frac{\Delta S_j^0}{R} - \frac{\Delta H_j^0}{RT}\right) \tag{2.15}$$

where $p_a = 1$ bar. The quantities ΔH_j^0 and ΔS_j^0 are respectively enthalpy and entropy changes for reaction j obtained from tabulations. The progress rate of reaction j can be written as:

$$\dot{\Omega}_j = k_{f,j} \prod_{k=1}^{N_s} [\mathcal{M}_k]^{\nu'_{k,j}} - k_{r,j} \prod_{k=1}^{N_s} [\mathcal{M}_k]^{\nu''_{k,j}} \tag{2.16}$$

The reaction source term $\dot{\omega}_k$, of species k, that includes the contribution of all N_r elementary reaction steps becomes:

$$\dot{\omega}_k = W_k \sum_{j=1}^{N_r} \left(\nu''_{k,j} - \nu'_{k,j}\right)\dot{\Omega}_j \tag{2.17}$$

Typically, going from non-reacting flow to reacting flow computation causes a significant increase in the number of conservation equations to solve, as most kinetic schemes involve a large number of species ($N_s > 50$).

The heat flux vector $\boldsymbol{q}$ is composed of the heat conduction flux based on the Fourier law, the heat diffusion due to species mass diffusion, pressure gradients, and the heat flux caused by concentration gradients (Dufour effect). In combustion simulations, the Dufour effect and pressure gradients are commonly neglected. Hence, the heat flux vector can be expressed as:

$$\boldsymbol{q} = -\lambda \nabla T + \sum_{k=1}^{N_s} \rho \boldsymbol{V_k} Y_k h_k \qquad (2.18)$$

In combustion simulations conducted in the present study, soot particles are considered distinct dispersed phases interacting with the carrier gas and each other. For the prediction of soot formation, additional governing equations are required besides the gas phase combustion equations. The modeling of various subprocesses of soot generation and its interaction with the gas phase is described in the following section.

2.2 Sectional soot model

As highlighted in the previous chapter, numerical prediction of soot relies on the accurate modeling of soot formation sub-processes, and the description of particle dynamics. The Discrete Sectional Method (DSM) [71] approach of finite discretization of the PSD, is retained in the present study to model soot particle dynamics.

2.2.1 Particles size discretization

In the DSM formulation, the uni-variate (i.e. only function of the soot particles volume) PSD of soot particles is divided with respect to their volume into classes of finite sizes referred to as 'sections'. The most common approach of discretization assumes
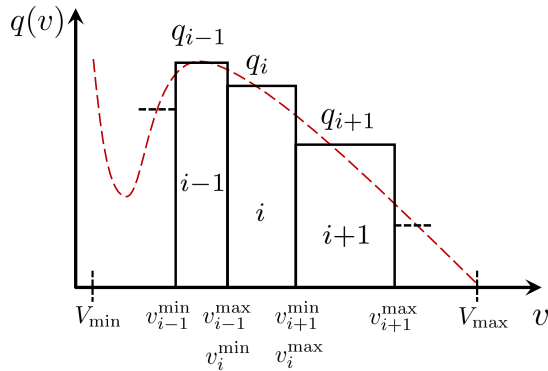

Figure 2.1: Discretization of the soot volume fraction density into a finite number of sections.

19

growth of particle size in sections on the logarithmic scale [35, 40]. Accordingly, the PSD between the smallest volume of the considered particles, V_{min}, and the largest modeled particles with volume V_{max}, is discretized in N_{sec} sections (see Fig. 2.1). Each section i represents the soot particles within the volume range of v_i^{min} and v_i^{max}:

$$v_i^{\mathrm{max}} = V_{\mathrm{min}} \left(\frac{V_{\mathrm{max}}}{V_{\mathrm{min}}} \right)^{i/N_{sec}} \qquad \forall \quad i \in [1, N_{sec}] \tag{2.19}$$

In this discretization, sections are contiguous. Therefore the upper boundary of section i is also the lower boundary for section $i + 1$, such that $v_i^{\mathrm{max}} = v_{i+1}^{\mathrm{min}}$.

For numerical simplification, the soot particles within section i are assumed spherical and are represented by a mean volume $\bar{v}_i$, and mean diameter $\bar{d}_{p,i}$ as:

$$\bar{v}_i = \exp \left[\frac{\ln \left(v_i^{\mathrm{max}} \right) + \ln \left(v_i^{\mathrm{min}} \right)}{2} \right] \tag{2.20}$$

$$\bar{d}_{p,i} = (6\bar{v}_i/\pi)^{1/3} \tag{2.21}$$

The smallest volume of particles, V_{min}, is considered equal to the carbon-equivalent volume (v_{C}) of the number of carbon atoms of two soot precursor (incipient) molecules. The volume of carbon atom is given by:

$$v_{\mathrm{C}} = \frac{W_{\mathrm{C}}}{\mathcal{N}_A \rho_s} \tag{2.22}$$

where W_{C} is the molar mass of carbon, $\mathcal{N}_A$ the Avogadro number, and ρ_s the soot density (equivalent to solid carbon) which is assumed constant at a value of $1860 \, \mathrm{kg/m^3}$ [39, 73]. Considering pyrene ($C_{16}H_{10}$) as the aromatic soot precursor as suggested in [40, 94], V_{min} becomes equal to $32v_{\mathrm{C}}$. The number density of particles decreases with an increase in their size and becomes negligible for the infinitely large size particles. In the sectional method, the last section characterizes the range of the largest modeled particle, hence V_{max} is chosen as an unattainable soot particle volume such that the particles no longer accumulate in the last section.

Inside each section, a scalar q_i characterizing the soot is presumed. The scalar can be written in a generalized form as [40, 71]

$$q_i(v) = av^b n_i(v) \tag{2.23}$$

where a and b are constants (taken to be unity in the present model), and $n_i(v)$ is the presumed size distribution of particles in section i that comprehends the volume v. In the model, q_i denotes the soot volume fraction density.

Based on the presumed scalar q_i, the soot volume fraction $Q_{s,i}$, and soot number density, $N_{s,i}$ within each section, respectively, are:

$$Q_{s,i} = \int_{v_i^{\min}}^{v_i^{\max}} q_i(v) dv \tag{2.24}$$

$$N_{s,i} = \int_{v_i^{\min}}^{v_i^{\max}} \frac{q_i(v)}{v} dv \tag{2.25}$$

In the present model, the soot volume fraction density $q_i(v)$ is presumed to be constant within each section, which gives:

$$Q_{s,i} = q_i \left(v_i^{\max} - v_i^{\min} \right) \tag{2.26}$$

$$N_{s,i} = \left[\frac{Q_{s,i}}{v_i^{\max} - v_i^{\min}} \right] \ln \left(\frac{v_i^{\max}}{v_i^{\min}} \right) \tag{2.27}$$

The global soot quantities, such as the total soot volume fraction (f_v) and total soot number density (N), and the average particle diameter (D_{avg}) are given by:

$$f_v = \sum_{i=1}^{N_{sec}} Q_{s,i} \tag{2.28}$$

$$N = \sum_{i=1}^{N_{sec}} N_{s,i} \tag{2.29}$$

$$D_{\mathrm{avg}} = D_{63} = \left[\frac{\sum\limits_{i=1}^{N_{sec}} N_{s,i} \cdot (\bar{d}_{p,i})^6}{\sum\limits_{i=1}^{N_{sec}} N_{s,i} \cdot (\bar{d}_{p,i})^3} \right]^{1/3} \tag{2.30}$$

The total soot mass M_s over a volume V of the system relates to soot volume fraction through:

$$M_s = \rho_s V f_v \tag{2.31}$$

Finally, the particle size distribution function within each section i can be determined as:

$$[\mathrm{d}N/\mathrm{d}(\log{(d_p)})]_i = 3\ln{(10)} q_i \tag{2.32}$$

Here, the PSD is assumed constant inside each section. For modeling simplicity, the morphology of the soot particle is not considered in the present approach. Thus, larger particles could be assumed to have an equivalent volume of aggregates.

2.2.2   Conservation equations for soot particles

Since the volume of all soot particles is negligible with respect to the total volume of gas, the sectional soot mass fraction $Y_{s,i}$ can be expressed as a function of $Q_{s,i}$ via:

$$Y_{s,i} = \frac{\rho_s}{\rho} Q_{s,i} \tag{2.33}$$

To describe the evolution of soot in a combustion system, the transport equation of soot mass fraction is solved for N_{sec} number of sections. The sectional soot transport equation is formulated as:

$$\frac{\partial(\rho Y_{s,i})}{\partial t} + \nabla \cdot (\rho(\boldsymbol{u} + \boldsymbol{V_T})Y_{s,i}) = \nabla \cdot (\rho D_{s,i} \nabla Y_{s,i}) + \rho_s \dot{Q}_{s,i} \quad \forall \quad i \in [1, N_{sec}] \tag{2.34}$$

where $\boldsymbol{V_T}$ is the thermophoretic velocity, $D_{s,i}$ is the molecular diffusion coefficient of soot, and $\dot{Q}_{s,i}$ is the formation rate of soot volume fraction in section i. The thermophoresis (transport due to temperature gradient) phenomenon is particularly important in soot particles. Therefore, thermophoretic velocity is computed through expression by Friendlander et al. [95], as:

$$\boldsymbol{V_T} = -\frac{3}{4}\left(1 + \frac{\pi \alpha_T}{8}\right)^{-1} \nu \frac{\nabla T}{T} \approx -0.554 \nu \frac{\nabla T}{T} \tag{2.35}$$

where ν is the kinematic viscosity. The thermal accommodation coefficient, α_T, is taken here as 0.9 [26, 96]. The molecular diffusion is generally negligible for soot particles. However, the value of $D_{s,i}$ is set to 1×10^{-6} m^2/s [97] solely for numerical stability. The soot source term $\dot{Q}_{s,i}$ of each sectional transport equation is evaluated from the different physical and chemical growth processes associated with soot formation. These include particle nucleation (superscript $^{\text{nuc}}$), PAH condensation (superscript $^{\text{cond}}$), coagulation (superscript $^{\text{coag}}$), surface growth (superscript $^{\text{sg}}$), and soot oxidation (superscript $^{\text{ox}}$). These subprocesses involved in the soot formation are schematically shown in Fig 2.2. Accordingly, the $\dot{Q}_{s,i}$ term becomes:

$$\dot{Q}_{s,i} = \left(\dot{Q}_{s,i}^{\text{nuc}} + \dot{Q}_{s,i}^{\text{cond}} + \dot{Q}_{s,i}^{\text{sg}} + \dot{Q}_{s,i}^{\text{coag}} + \dot{Q}_{s,i}^{\text{ox}} \right) \tag{2.36}$$

Modeling approaches used for particle growth rates associated with these processes are discussed in detail below.
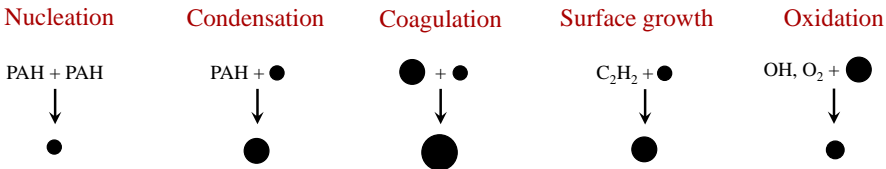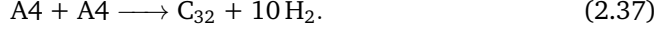

Figure 2.2: Illustration of the physical and chemical phenomena representing soot formation.

Nucleation

Soot nucleation is assumed to occur through the coalescence of two PAH molecules in the first section. In the present nucleation model, pyrene ($C_{16}H_{10}$ or A4) molecules are considered as sole PAH species forming incipient soot particles:

$$A4 + A4 \longrightarrow C_{32} + 10\,H_2. \tag{2.37}$$

The source term for nucleation is given by:

$$\dot{Q}_{s,1}^{\mathrm{nuc}} = 2v_{A4}\beta_{A4,A4}N_{A4}^2 \tag{2.38}$$

where v_{A4} is the volume (carbon equivalent), N_{A4} is the number density ($N_{A4} = [A_4]\mathcal{N}_A$), and $\beta_{A4,A4}$ is the collision frequency factor of A4 molecules. Considering the small size of incipient soot particles, $\beta_{A4,A4}$ in the free molecular regime is:

$$\beta_{A4,A4} = \epsilon_{\mathrm{nuc}}4\sqrt{2}\left(\frac{3}{4\pi}\right)^{1/6}\left(\frac{6k_BT}{\rho_s}\right)^{1/2}(v_{A4})^{1/6} \tag{2.39}$$

where $\epsilon_{\mathrm{nuc}} = 2.2$ is the amplification factor due to Van der Waals interactions [40, 72, 98]. Subsequently, solid-phase and gas-phase are coupled by accounting for the production of H_2 and consumption of A4. Accordingly, the rates (in g/cm^{3}s) of A4 consumption and H_2 production, respectively become [98]:

$$\dot{\omega}_{A4}^{\mathrm{nuc}} = -2W_{A4}\,\beta_{A4,A4}\mathcal{N}_A[A4]^2 \tag{2.40}$$

$$\dot{\omega}_{H_2}^{\mathrm{nuc}} = -5\frac{W_{H_2}}{W_{A4}}\dot{\omega}_{A4}^{\mathrm{nuc}} \tag{2.41}$$

Condensation

The condensation process is modeled as the collision of a PAH molecule and a soot particle (in all the sections) leading to coalescence. The soot particles of section i grow in size due to PAH addition and possibly migrate to the next higher section $i+1$. The volume growth rate through condensation of PAH on particles of section i is [35, 40]:

$$\Delta\dot{Q}_{s,i}^{\mathrm{cond}} = \eta_{\mathrm{cond}}v_{A4}N_{A4}\int_{v_i^{\mathrm{min}}}^{v_i^{\mathrm{max}}}\beta_{i,A4}n_i(v)dv \tag{2.42}$$

where η_{cond} is the condensation probability and is assumed as unity in the present formulation [40]. For numerical simplicity, the collisional frequency between a PAH and a soot particle $\beta_{i,A4}$ is estimated within free molecular regime [99] based on the mean particle volume for each section, such that:

$$\beta_{i,A4} = \epsilon_{\mathrm{cond}}\left(\frac{3}{4\pi}\right)^{1/6}\left(\frac{6k_BT}{\rho_s}\right)^{1/2}\left((\bar{v}_i)^{1/3} + v_{A4}^{1/3}\right)^2\left(\frac{1}{\bar{v}_i} + \frac{1}{v_{A4}}\right)^{1/2} \tag{2.43}$$

23

with $\epsilon_{\text{cond}} = 2.2$ is the Van der Waals amplification factor [98]. Combining with Eq. 2.27, the sectional soot volume growth rate due to PAH condensation becomes:

$$\Delta \dot{Q}_{s,i}^{\text{cond}} = v_{\text{A4}} \beta_{i,\text{A4}} N_{\text{A4}} \left[\frac{Q_{s,i}}{v_i^{\text{max}} - v_i^{\text{min}}} \right] \ln \left(\frac{v_i^{\text{max}}}{v_i^{\text{min}}} \right). \tag{2.44}$$

The growth of particle size in a particular section due to condensation may lead to the movement of particles into the neighboring sections. These inter-sectional movements (or dynamics) of particles play an important role in determining the exact source terms for a particular section. A special formulation is required to account for the distribution of soot particles. The rate of change of volume fraction due to condensation of particles in section i, is given as:

$$\Delta \dot{Q}_{s,i}^{\text{cond}} = \Delta \dot{Q}_{s,i}^{\text{cond}_{in}} + \Delta \dot{Q}_{s,i}^{\text{cond}_{out}} \tag{2.45}$$

where $\Delta \dot{Q}_{s,i}^{\text{cond}_{in}}$ is the source term due to particles that stay in the same section and $\Delta \dot{Q}_{s,i}^{\text{cond}_{out}}$ is the source term due to particles that move out to the next higher section.

The interrelation between these terms is determined based on the conservation of soot number density such that a decrease in the number density for section i through condensation is equal to an increase in the number density for section $i + 1$. This assumption yields:

$$\Delta \dot{Q}_{s,i}^{\text{cond}_{in}} = \Delta \dot{Q}_{s,i}^{\text{cond}} \left/ \left[1 - \left(\frac{v_{i+1}^{\text{max}} - v_{i+1}^{\text{min}}}{v_i^{\text{max}} - v_i^{\text{min}}} \right) \left(\frac{\ln \left(v_i^{\text{max}} / v_i^{\text{min}} \right)}{\ln \left(v_{i+1}^{\text{max}} / v_{i+1}^{\text{min}} \right)} \right) \right] \right. \tag{2.46a}$$

$$\Delta \dot{Q}_{s,i}^{\text{cond}_{out}} = \Delta \dot{Q}_{s,i}^{\text{cond}} \left/ \left[1 - \left(\frac{v_i^{\text{max}} - v_i^{\text{min}}}{v_{i+1}^{\text{max}} - v_{i+1}^{\text{min}}} \right) \left(\frac{\ln \left(v_{i+1}^{\text{max}} / v_{i+1}^{\text{min}} \right)}{\ln \left(v_i^{\text{max}} / v_i^{\text{min}} \right)} \right) \right] \right. \tag{2.46b}$$
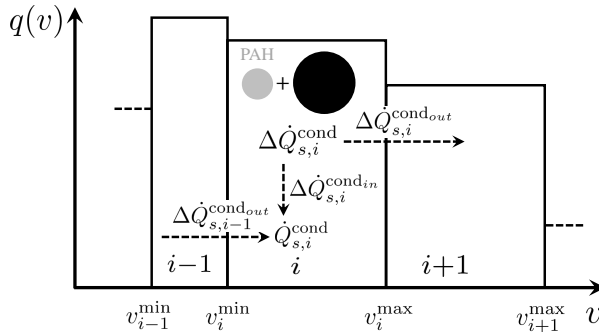

Figure 2.3: Illustration of the inter-sectional dynamics associated with PAH condensation process.

The net sectional condensation rate source term $\dot{Q}_{s,i}^{\text{cond}}$ is evaluated after sectional balance treatment, such that:

$$\dot{Q}_{s,i}^{\text{cond}} = \begin{cases} \Delta\dot{Q}_{s,1}^{\text{cond}} & \text{for } i=1 \qquad\qquad\qquad (2.47a) \\ \Delta\dot{Q}_{s,i-1}^{\text{cond}_{out}} + \Delta\dot{Q}_{s,i}^{\text{cond}_{in}} & \text{for } 1<i<N_{sec} \qquad\quad (2.47b) \\ \Delta\dot{Q}_{s,N_{sec}-1}^{\text{cond}_{out}} + \Delta\dot{Q}_{s,N_{sec}}^{\text{cond}} & \text{for } i=N_{sec} \qquad\qquad (2.47c) \end{cases}$$

The schematic illustration of the inter-sectional dynamics associated with the PAH condensation process is depicted in Fig. 2.3. Finally, the rate of soot condensation in section i is coupled to the gas phase by consumption of PAH (A4) and production of H_2 as:

$$\dot{\omega}_{\text{A4}}^{\text{cond}} = -\frac{W_{\text{A4}}}{v_{\text{A4}}\mathcal{N}_A}\left(\sum_{i=1}^{N_{sec}} \Delta\dot{Q}_{\text{cond},i}\right) \qquad (2.48)$$

$$\dot{\omega}_{\text{H}_2}^{\text{cond}} = -5\frac{W_{\text{H}_2}}{W_{\text{A4}}}\dot{\omega}_{\text{A4}}^{\text{cond}} \qquad (2.49)$$

Coagulation

The coagulation process corresponds to collisions between two particles leading to larger particles in the limit of pure coalescence. In the present work, coagulation is described following the model proposed by Kumar and Ramkrishna [100]. The modeling strategy for the coagulation process is briefly explained as follows:

Consider particles of section i. During the coagulation event, the section i will receive the particles grown from the collision amongst particles in lower sections, simultaneously, it will lose the particles during collisions with particles from other sections. When coagulation of particles of section j and section k occur ($j,k<i$), the resultant particle posses volume that is comprised within ($v_j^{\min}+v_k^{\min}$; $v_j^{\max}+v_k^{\max}$). If the size of this newly generated particle lies within ($v_i^{\min};v_i^{\max}$), the particles are naturally assigned to the section i. However, when such a situation does not exist, the fractions of particle population are assigned to adjacent representative sections $i-1$ and $i+1$ by ensuring the conservation of both mass and number density.

Here, particle population in each section i is represented by number density $N_{s,i}$ and representative mean $\bar{v}_i$. Hence, the number rate of particle coagulation for section i becomes:

$$\frac{dN_{s,i}}{dt} = \sum_{\substack{k\leqslant j\leqslant i \\ \bar{v}_{i-1}\leqslant(\bar{v}_j+\bar{v}_k)\leqslant\bar{v}_{i+1}}} \left(1-\frac{\delta_{j,k}}{2}\right)\Theta\beta_{j,k}\xi_{j,k}N_{s,j}N_{s,k} - N_{s,i}\sum_{k=1}^{N_{sec}}\beta_{i,k}\xi_{i,k}N_{s,k}$$

$$(2.50)$$

where $\beta_{j,k}, \xi_{j,k}$ are the collision frequency factor and collision efficiency (which is assumed to be unity) between particles with a representative size of section j and k, respectively. δ is the Kronecker delta function, and Θ is the splitting factor of the new particles in adjacent sections given by the expression:

$$\Theta = \begin{cases} \dfrac{\bar{v}_{i+1} - (\bar{v}_j + \bar{v}_k)}{\bar{v}_{i+1} - \bar{v}_i}, & \bar{v}_i \leqslant (\bar{v}_j + \bar{v}_k) \leqslant \bar{v}_{i+1} \qquad (2.51\text{a}) \\[4mm] \dfrac{\bar{v}_{i-1} - (\bar{v}_j + \bar{v}_k)}{\bar{v}_{i-1} - \bar{v}_i}, & \bar{v}_{i-1} \leqslant (\bar{v}_j + \bar{v}_k) \leqslant \bar{v}_i \qquad (2.51\text{b}) \end{cases}$$

The first term on the right-hand side of Eq. 2.50 represents the particle number rate of particles received by section i from the collision of particles from lower sections j and k, and the second term represents the number rate of particles from section i colliding with particles of another section k. By using Eq. 2.27 the global coagulation source term can be written as:

$$\dot{Q}_{s,i}^{\text{coag}} = \frac{dN_{s,i}}{dt} \left[\frac{(v_i^{\max} - v_i^{\min})}{\ln \left(v_i^{\max}/v_i^{\min} \right)} \right] \tag{2.52}$$

In order to compute coagulation rates in 2.50, a more general description of collision frequency factor β is obtained based on the limits determined by the Knudsen number, Kn, which is:

$$\text{Kn} = 2\lambda_g/d_c \tag{2.53}$$

where λ_g gas molecular mean free path and d_c is the collisional diameter of particles (approximated as the mean). From kinetic theory λ_g can be defined as:

$$\lambda_g = \frac{RT}{\pi \sqrt{2 d_g^2 p \mathcal{N}_A}} \tag{2.54}$$

where d_g is the diameter of a gas particle considered constant and equal to 0.2 nm [73]. The collisions between particles with size class i and particles with size class j, can be classified into three categories as follows [99]:

- Free molecular regime: $\text{Kn} \gg 10$

$$\beta_{i,j}^{fm} = \epsilon_{i,j} \left(\frac{3}{4\pi} \right)^{1/6} \left(\frac{6 k_B T}{\rho_s} \right)^{1/2} \left(\bar{v}_i^{1/3} + \bar{v}_j^{1/3} \right)^2 \left(\frac{1}{\bar{v}_i} + \frac{1}{\bar{v}_j} \right)^{1/2} \tag{2.55}$$

- Continuum regime: $\text{Kn} \leqslant 0.1$

$$\beta_{i,j}^{c} = \frac{2 k_B T}{3\mu} \left(\bar{v}_i^{1/3} + \bar{v}_j^{1/3} \right) \left(\frac{\text{Cu}_i}{\bar{v}_i^{1/3}} + \frac{\text{Cu}_j}{\bar{v}_j^{1/3}} \right) \tag{2.56}$$

- Transition regime: $0.1 < \text{Kn} < 10$

$$\beta_{i,j}^t = \frac{\beta_{i,j}^{fm} \beta_{i,j}^c}{\beta_{i,j}^{fm} + \beta_{i,j}^c} \tag{2.57}$$

with $\epsilon_{i,j}$ a sticking coefficient taking into account the Van der Waals interactions between particles (taken as 2.2 here); Cu_i is the Cunningham slip factor is calculated as $\text{Cu}_i = 1 + 1.257(2\lambda_g/\bar{d}_{p,i})$ following Ref. [101].

Surface growth and oxidation

The surface growth of soot particles is described through Hydrogen-abstraction-Carbon-addition (HACA) kinetic mechanism developed by Frenklach and co-workers [10,23]. The soot surface reaction scheme including surface growth (HACA) and surface oxidation is presented in Table 2.1. In this mechanism, reactions with O_2 and OH account for soot oxidation. The kinetic rates of surface reactions depend on particle surface area and the available number of surface sites, which are carbon atoms either saturated ($C_{s,n}$-H) or dehydrogenated ($C_{s,n}^*$). The concentration of saturated sites $[C_{s,n}\text{-H}]_i$ on section i, in (mol/cm^3), is calculated by:

$$[C_{s,n}\text{-H}]_i = \frac{\chi_s A_{s,i}}{\mathcal{N}_A} \tag{2.58}$$

where χ_s is the number of sites per unit soot surface area and is set to a constant value of 2.3×10^{15} sites/cm^2 [14,23]; $A_{s,i}$ is the surface density of soot particles in (cm^2/cm^3) which for section i is given by the surface area of soot particles times the

Table 2.1: HACA-based soot surface growth and oxidation reactions. Here $*$ denotes an active site on the soot surface, and $C_{s,n}$-H is a soot particle with n carbon atoms, $k = AT^b \exp\left(-E_a/RT\right)$.

No.	Reaction	A (cm^3/(mol s))	b	E_a (kcal/mol)
SR1$_f$	$C_{s,n}$-H + H $\rightleftharpoons$ $C_{s,n}^*$ + H$_2$	4.2×10^{13}	0.0	13.0
SR1$_r$		3.9×10^{12}	0.0	11.0
SR2$_f$	$C_{s,n}$-H + OH $\rightleftharpoons$ $C_{s,n}^*$ + H$_2$O	1.0×10^{10}	0.734	1.43
SR2$_r$		3.68×10^8	1.139	17.1
SR3	$C_{s,n}^*$ + H $\longrightarrow$ $C_{s,n}$-H	2.0×10^{13}	0.0	0.0
SR4a	$C_{s,n}^*$ + C$_2$H$_2$ $\longrightarrow$ $C_{s,n+2}$-H + H	8.0×10^7	1.56	3.8
SR4b	$C_{s,n}^*$ + C$_2$H$_2$ $\longrightarrow$ $C_{s,n+2}^*$ + H$_2$	8.0×10^7	1.56	3.8
SR5	$C_{s,n}^*$ + O$_2$ $\longrightarrow$ $C_{s,n-2}^*$ + 2 CO	2.2×10^{12}	0.0	7.5
SR6	$C_{s,n}$-H + OH $\longrightarrow$ $C_{s,n-1}^*$ + CO	Collision efficiency $\gamma_{\text{OH}} = 0.13$		

number density. In terms of volume of particles size class i, $A_{s,i}$ can be written as:

$$A_{s,i} = \frac{3\pi}{2} \left(\frac{6}{\pi}\right)^{2/3} \left[\frac{Q_{s,i}}{v_i^{\mathrm{max}} - v_i^{\mathrm{min}}}\right] \left((v_i^{\mathrm{max}})^{2/3} - (v_i^{\mathrm{min}})^{2/3}\right) \qquad (2.59)$$

The concentration of dehydrogenated (active) sites $[\mathrm{C}_{s,n}^*]_i$ is calculated assuming an empirical (steric) parameter α to account for the fraction of surface sites available per unit surface area of soot:

$$[\mathrm{C}_{s,n}^*]_i = \frac{\alpha \chi_s^* A_{s,i}}{\mathcal{N}_A} \qquad (2.60)$$

where χ_s^* is the number of surface radical sites per unit surface area. It can be found using a steady-state approximation for $\mathrm{C}_{s,n}^*$ in the soot-gas surface reactions of the HACA mechanism:

$$\chi_s^* = k_{ss}\chi_s \qquad (2.61)$$

with k_{ss} being the steady-state constant.

During the acetylene addition step of HACA, the surface radicals remain in between the two extremes of complete depletion (SR4a) and complete conservation (SR4b). However, it is still an open subject to be fully understood. To incorporate this phenomenon, Hoerlle and Pereira [94] introduced the adjustable constant parameter ξ_{dc} for the treatment of surface radicals, with ξ_{dc} ranging from 0 to 1 for complete depletion and complete conservation of the surface radicals, respectively. In the current soot model, the steady state relation for k_{ss} is calculated as:

$$k_{ss} = \xi_{dc} k_{ss}^{\mathrm{con}} + (1 - \xi_{dc}) k_{ss}^{\mathrm{dep}} \qquad (2.62)$$

with

$$k_{ss}^{\mathrm{dep}} = \frac{k_{1,f}[\mathrm{H}] + k_{2,f}[\mathrm{OH}]}{k_{1,r}[\mathrm{H_2}] + k_{2,r}[\mathrm{H_2O}] + k_{3,f}[\mathrm{H}] + k_{4,f}[\mathrm{C_2H_2}] + k_{5,f}[\mathrm{O_2}]} \qquad (2.63)$$

$$k_{ss}^{\mathrm{con}} = \frac{k_{1,f}[\mathrm{H}] + k_{2,f}[\mathrm{OH}]}{k_{1,r}[\mathrm{H_2}] + k_{2,r}[\mathrm{H_2O}] + k_{3,f}[\mathrm{H}] + k_{5,f}[\mathrm{O_2}]} \qquad (2.64)$$

where $k_{j,f}$ and $k_{j,r}$ are, respectively, forward and reverse rate coefficients for surface reaction j.

In the present sectional model, the steric parameter, α, is considered to be dependent on particle size and local temperature [23] and is given by:

$$\alpha = \tanh\left(\frac{a}{\log(n_{\mathrm{C}_i}) + b}\right) \qquad (2.65)$$

where a and b are the fitted linear functions of the local temperature given by:

$$a = 12.65 - 0.00563\,T \tag{2.66a}$$
$$b = -1.38 + 0.00068\,T \tag{2.66b}$$

and the average number of carbon atoms of size i, is indicated by n_{C_i} which is the ratio of the average soot particle volume $V_{s,i}$ to the volume of one carbon atom v_C:

$$n_{C_i} = \frac{V_{s,i}}{v_C} = \frac{\left(v_i^{max} - v_i^{min}\right)}{\ln\left(v_i^{max}/v_i^{min}\right)v_C} \tag{2.67a}$$

The rate of volume added due to surface growth is given by reaction SR4 as [40,98]

$$\Delta\dot{Q}_{s,i}^{sg} = 2v_C k_4 [C_2H_2][C_{s,n}^*]_i \mathcal{N}_A \tag{2.68}$$

On the other hand, the total change in soot volume due to oxidation includes the oxidation by O_2 and OH

$$\Delta\dot{Q}_{s,i}^{ox} = \Delta\dot{Q}_{s,i}^{ox,O_2} + \Delta\dot{Q}_{s,i}^{ox,OH} \tag{2.69}$$

where, the change in soot volume due to O_2 oxidation, from reaction SR5, is [98]:

$$\Delta\dot{Q}_{s,i}^{ox,O_2} = -2v_C k_5 [O_2][C_{s,n}^*]_i \mathcal{N}_A \tag{2.70}$$

and the change in soot volume due to OH oxidation is given by reaction SR6 as [98]:

$$\Delta\dot{Q}_{s,i}^{ox,OH} = -\gamma_{OH} v_C [OH]\mathcal{N}_A \beta_{i,OH}\left[\frac{Q_{s,i}}{v_i^{max} - v_i^{min}}\right]\ln\left(\frac{v_i^{max}}{v_i^{min}}\right) \tag{2.71}$$

The global source terms due to surface growth ($\dot{Q}_{s,i}^{sg}$) and oxidation ($\dot{Q}_{s,i}^{ox}$) in each section are calculated through inter-sectional treatment. Similar to condensation, the net sectional surface growth rate source term $\dot{Q}_{s,i}^{sg}$ is evaluated after sectional balance treatment, such that:

$$\dot{Q}_{s,i}^{sg} = \begin{cases} \Delta\dot{Q}_{s,1}^{sg} & \text{for } i=1 \tag{2.72a}\\ \Delta\dot{Q}_{s,i-1}^{sg_{out}} + \Delta\dot{Q}_{s,i}^{sg_{in}} & \text{for } 1<i<N_{sec} \tag{2.72b}\\ \Delta\dot{Q}_{s,N_{sec}-1}^{sg_{out}} + \Delta\dot{Q}_{s,N_{sec}}^{sg} & \text{for } i=N_{sec} \tag{2.72c} \end{cases}$$

with

$$\Delta\dot{Q}_{s,i}^{sg_{in}} = \Delta\dot{Q}_{s,i}^{sg}\bigg/\left[1 - \left(\frac{v_{i+1}^{max} - v_{i+1}^{min}}{v_i^{max} - v_i^{min}}\right)\left(\frac{\ln\left(v_i^{max}/v_i^{min}\right)}{\ln\left(v_{i+1}^{max}/v_{i+1}^{min}\right)}\right)\right] \tag{2.73a}$$

$$\Delta\dot{Q}_{s,i}^{sg_{out}} = \Delta\dot{Q}_{s,i}^{sg}\bigg/\left[1 - \left(\frac{v_i^{max} - v_i^{min}}{v_{i+1}^{max} - v_{i+1}^{min}}\right)\left(\frac{\ln\left(v_{i+1}^{max}/v_{i+1}^{min}\right)}{\ln\left(v_i^{max}/v_i^{min}\right)}\right)\right] \tag{2.73b}$$

Similarly, the net sectional oxidation rate source term $\dot{Q}^{\text{ox}}_{s,i}$ is evaluated using:

$$\dot{Q}^{\text{ox}}_{s,i} = \begin{cases} \Delta\dot{Q}^{\text{ox}_{out}}_{s,2} + \Delta\dot{Q}^{\text{ox}}_{s,1} & \text{for } i=1 & \text{(2.74a)} \\ \Delta\dot{Q}^{\text{ox}_{out}}_{s,i+1} + \Delta\dot{Q}^{\text{ox}_{in}}_{s,i} & \text{for } 1<i<N_{sec} & \text{(2.74b)} \\ \Delta\dot{Q}^{\text{ox}}_{s,N_{sec}} & \text{for } i=N_{sec} & \text{(2.74c)} \end{cases}$$

with

$$\Delta\dot{Q}^{\text{ox}_{in}}_{s,i} = \Delta\dot{Q}^{\text{ox}}_{s,i} \left/ \left[1 - \left(\frac{v^{\max}_{i-1} - v^{\min}_{i-1}}{v^{\max}_i - v^{\min}_i} \right) \left(\frac{\ln\left(v^{\max}_i / v^{\min}_i\right)}{\ln\left(v^{\max}_{i-1} / v^{\min}_{i-1}\right)} \right) \right] \right. \tag{2.75a}$$

$$\Delta\dot{Q}^{\text{ox}_{out}}_{s,i} = \Delta\dot{Q}^{\text{ox}}_{s,i} \left/ \left[1 - \left(\frac{v^{\max}_i - v^{\min}_i}{v^{\max}_{i-1} - v^{\min}_{i-1}} \right) \left(\frac{\ln\left(v^{\max}_{i-1} / v^{\min}_{i-1}\right)}{\ln\left(v^{\max}_i / v^{\min}_i\right)} \right) \right] \right. \tag{2.75b}$$

In order to couple the gas-solid phase chemistry, the production/consumption $\dot{\omega}_l$ rates (in g/cm^{3}s) of gas-phase species l through N_{sr} surface reactions (from Table 2.1) are calculated as:

$$\dot{\omega}_l = W_l \sum_{i=1}^{N_{sec}} \sum_{j=1}^{N_{sr}} \pm n_{l,j} \dot{\Omega}^i_j \tag{2.76}$$

where $\pm n_{l,j}$ is the number of moles produced $(+)$/consumed $(-)$ for gaseous species l through surface reaction j, and $\dot{\Omega}^i_j$ is the rate of progress of surface reaction j for particles in section i, given by:

$$\dot{\Omega}^i_j = \begin{cases} k_{f,j} \prod_{k=1}^{N_{ssr}} [\mathcal{M}_k]_j^{\nu'_{k,j}} - k_{r,j} \prod_{k=1}^{N_{ssr}} [\mathcal{M}_k]_j^{\nu''_{k,j}} & \text{for } j \neq 6 & \text{(2.77a)} \\ \gamma_{\text{OH}}[\text{OH}]\beta_{i,\text{OH}} \left[\dfrac{Q_{s,i}}{v^{\max}_i - v^{\min}_i} \right] \ln\left(\dfrac{v^{\max}_i}{v^{\min}_i} \right) & \text{for } j = 6 & \text{(2.77b)} \end{cases}$$

where $k_{f,j}$, $k_{r,j}$ are the forward and reverse rate for surface reaction j respectively; $\mathcal{M}_k$ is symbol for species k (gas-phase or soot), and N_{ssr} indicates the number species involved in surface reaction scheme. Note that soot particles are assumed to be formed only by carbon atoms in the current model. Therefore, following the approach described in Ref. [98], the conservation of hydrogen during heterogeneous surface reactions is treated through the transfer of H atoms between particles and H$_2$. Since the concentration of H$_2$ is substantially higher than the concentration of H atoms involved in the soot formation processes, this assumption does not introduce any serious error in the formulation.

Mass and energy coupling between soot and gas-phase

In addition to species source terms, the interaction between the soot chemistry and the gas-phase chemistry is accounted for in conservation equations for the total mass and energy following the work of Zimmer et al. [102]. The soot terms are included in the mixture enthalpy and heat capacity as:

$$h = \sum_{k=1}^{N_s} Y_k h_k + \sum_{i=1}^{N_{sec}} Y_{s,i} h_s \tag{2.78}$$

$$c_p = \sum_{k=1}^{N_s} c_{p,k} Y_k + \sum_{i=1}^{N_{sec}} c_{p_s} Y_{s,i} \tag{2.79}$$

where thermodynamic properties of solid carbon (graphite) are specified for soot (h_s and c_{p_s}) following the NIST-JANAF database [103].

In the presence of soot, the mixture density, ρ, is calculated as the density for multi-phase flows according to the expression of Crowe [104]:

$$\rho = \sum_{i=1}^{N_{sec}} \rho Y_{s,i} + \left(1 - \sum_{i=1}^{N_{sec}} \frac{\rho Y_{s,i}}{\rho_s}\right) \rho_g \tag{2.80}$$

with the density of the gas phase ρ_g is calculated by the ideal-gas equation of state:

$$\rho_g = \frac{p}{RT} \bigg/ \left(\sum_{k=1}^{N_s} \frac{Y_k}{\left(1 - \sum_{i=1}^{N_{sec}} Y_{s,i}\right) W_k}\right) \tag{2.81}$$

For simplicity, the mixture viscosity and thermal conductivity are assumed to be unaffected by the soot.

2.3 Model validation on laminar flames

The sectional soot model introduced in the previous section has been successfully validated by Hoerlle [98] in laminar flames. Here, the model validation study is extended to evaluate the capabilities of the retained numerical strategy in predicting soot formation in laminar non-premixed and premixed flames for a wide range of conditions. The soot predictions are analyzed first in Section 2.3.1 for non-premixed counterflow flames. To validate the retained soot modeling approach in non-premixed conditions, several C_2H_4-O_2-N_2 counterflow flames from literature are considered. The selected flames essentially facilitate the investigation of strain rate, dilution, pressure, and unsteady effects on soot production. Subsequently, the soot model validation study is extended to premixed flames in Section 2.3.2 for stagnation and burner-stabilized flame configurations.

The detailed kinetic scheme KAUST 2.0 (KM2) proposed by Wang et al. [105] consisting of 202 species and 1351 elementary reactions, is used to describe gas-phase chemistry. The KM2 mechanism has been extensively validated in literature [27, 98, 99, 105, 106] for the prediction of soot formation in ethylene flames, hence retained in the present study. The additional validation of the KM2 mechanism is provided in Appendix A. The diffusion transport of species is modeled through mixture-averaged approximation [107]. The numerical simulations are conducted with the CHEM1D [108, 109] code. In the simulations, the soot particle volume range ($V_{\min} = 3.43 \times 10^{-22}$ cm^3; $V_{\max} = 5.23 \times 10^{-10}$ cm^3) is discretized into 60 sections considering the compromise between CPU cost and model accuracy. The sensitivity of the soot model to the number of sections is analyzed in Appendix B.

2.3.1 Non-premixed counterflow flames

The burner setup features counter-flowing fuel and oxidizer nozzles separated by a distance of L. In a counterflow burner, fuel and oxidizer jets impinge on each other forming a stagnation plane with a diffusion flame near the stoichiometric mixture fraction position. A schematic illustration of the archetypal counterflow flame is depicted in Fig. 2.4. The counterflow configuration can be planar or axisymmetric. As a consequence, non-premixed counterflow flames can be suitably modeled with a quasi-one-dimensional framework of conservation equations, typically referred to as flamelet equations. A system of governing equations for conservation of total mass, species mass, soot mass, and enthalpy can be derived along the coordinate (x) normal to flame surface as [110–112]:

$$\frac{\partial \rho}{\partial t} + \frac{\partial}{\partial x}(\rho u) = -\rho K \tag{2.82}$$

$$\frac{\partial(\rho Y_k)}{\partial t} + \frac{\partial}{\partial x}(\rho u Y_k) = -\frac{\partial}{\partial x}(\rho Y_k V_k) - \rho K Y_k + \dot{\omega}_k, \qquad \forall\, k \in [1, N_s\text{-}1] \tag{2.83}$$

$$\frac{\partial(\rho h)}{\partial t} + \frac{\partial}{\partial x}(\rho u h) = -\frac{\partial}{\partial x}\left(-\frac{\lambda}{c_p}\frac{\partial h}{\partial x} + \sum_{k=1}^{N_s} \rho h_k Y_k V_k\right) - \rho K h \tag{2.84}$$
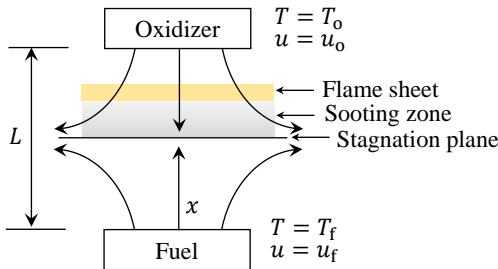

Figure 2.4: Schematic representation of the laminar non-premixed counterflow flame.

$$\frac{\partial(\rho K)}{\partial t} + \frac{\partial}{\partial x}(\rho u K) = \frac{\partial}{\partial x}\left(\mu\frac{\partial K}{\partial x}\right) - \rho K^2 + J \tag{2.85}$$

$$\frac{\partial(\rho Y_{s,i})}{\partial t} + \frac{\partial}{\partial x}(\rho[u + V_T]Y_{s,i}) = \frac{\partial}{\partial x}\left(\rho D_{s,i}\frac{\partial Y_{s,i}}{\partial x}\right) - \rho K Y_{s,i} + \rho_s \dot{Q}_{s,i} \tag{2.86}$$

$$\forall\, i \in [1, N_{sec}]$$

In the 1-D formulation, K denotes the velocity strain rate field in the direction tangential to flame surface y, such that:

$$K(x,t) = \frac{\partial v}{\partial y}. \tag{2.87}$$

To account for the multidimensional effects, a transport equation (Eq. 2.85) is solved for the strain rate K. This differential equation is essentially derived from the momentum equation in the direction tangential to the flame surface. In the Eq. 2.85 reported above, J is the uniform pressure curvature, given by [111]:

$$J = -\frac{1}{y}\frac{\partial p}{\partial y} = \rho_\circ\left(a^2 + \frac{\partial a}{\partial t}\right), \tag{2.88}$$

which is an eigenvalue of the problem. In Eq. 2.88, $\rho_\circ$ is the oxidizer density, and a denotes the applied strain rate at the oxidizer side, which can be a function of time.

The two configurations are possible for modeling counterflow flames based on the boundary conditions of K field. First, is the potential flow approximation. According to this for the oxidizer stream ($x \to L$) a velocity gradient can be prescribed, such that:

$$-\frac{\partial u}{\partial x} = \frac{\partial v}{\partial y} = K = a \quad ; \qquad (x \to L) \tag{2.89a}$$

$$\frac{\partial K}{\partial x} = 0 \quad ; \qquad (x \to 0) \tag{2.89b}$$

In the second configuration, plug flow type boundary conditions are employed ($v = 0$ at both nozzles). In other words, $K = 0$ at the fuel and oxidizer boundaries. Moreover, total mass flux (accounting for diffusion and convection) is specified as boundary conditions for each chemical species instead of their mass fractions. The second configuration is considered mainly for the validation study owing to a more accurate description of experimental conditions.

Soot formation in steady non-premixed counterflow flame

The counterflow diffusion flame studied by Wang et al. [27] is considered as a baseline case to analyze the sooting characteristics captured by DSM. The baseline flame consists of a pure C_2H_4 fuel reacting with an oxidizer composed of 25% of O_2 and
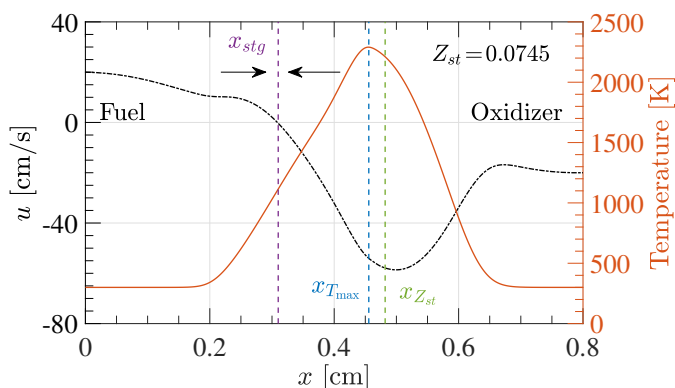
Figure 2.5: The computed flame structure of a counterflow diffusion flame fuel.

75% of N_2 (on a molar basis). The reactant nozzles are separated with a distance of 8 mm. The flow velocities for both the fuel and oxidizer streams are set at 20 cm/s and 300 K inlet temperature. Before presenting soot quantities, a basic flame structure of computed counterflow flame is shown in Fig. 2.5. The flame stagnation plane position x_{stg}, where $u = 0$ is found to be at $x \simeq 0.31$ cm. The maximum temperature appears at $x \simeq 0.46$ cm. The location of stoichiometric mixture fraction ($x_{Z_{st}}$), an indicative of flame position, is found at $x \simeq 0.48$ cm. The position of peak temperature is shifted from the stoichiometric mixture fraction location as a consequence of the diffusion of chemical species.

Computed profiles of global soot characteristics are compared with the experimentally measured data in Fig. 2.6. A good qualitative agreement is found for soot volume fraction f_v between the numerical simulation and the experimental measurements with radical treatment parameter $\xi_{dc} = 0.95$. The sensitivity of f_v prediction to ξ_{dc} is illustrated in the Appendix C. The f_v profiles are skewed towards the stagnation plane suggesting that particles nucleate on the fuel-rich side of the flame and they continue to grow while flowing towards the stagnation plane. The present flame exhibits typical SF (soot formation) flame characteristics [25], where produced soot particles are transported away from the flame toward the stagnation plane. Due to the thermophoretic effect that transports soot particles in the direction of lower temperature, particle stagnation occurs slightly beyond the flow stagnation plane at $x \simeq 0.29$ cm where $u + V_T = 0$. At the particle stagnation position, the diffusion transport and source term for soot balance, leading to a sharp decrement in f_v, which is consistent with the experimentally observed leakage of soot through the stagnation plane. Besides f_v, the experimental and computed profiles of particle number density (N) and average particle diameter (D_{avg}) show reasonably good agreement with experimentally observed behaviors. As the particles are transported toward the stagnation plane, soot particle size increases while their number density decreases. This behavior is mainly a consequence of surface growth and particle coagulation.
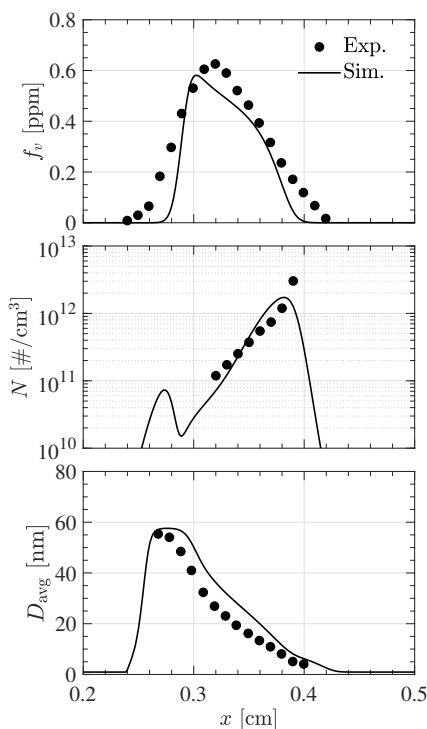
Figure 2.6: Comparison of simulated (solid line) and experimental [27] (symbols) profiles for soot volume fraction, number density, and average particle diameter against the distance from the fuel nozzle x.

The numerical profiles of temperature, and soot-relevant gaseous species (C_2H_4, A4, OH) are shown in Fig. 2.7a to characterize the flame structure. As can be observed the soot precursor species C_2H_2 and A4 are formed in the fuel-rich regions of the flame. Hence, soot nucleation occurs on the oxidizer side of the stagnation plane, where concentrations of PAHs are higher. Soot particles tend to grow through surface reactions, primarily with C_2H_2. While approaching the stagnation plane, the temperature tends to decrease, resulting in reduced surface reactions. For SF-type flames, oxidizing species (such as OH) exist in abundance near the flame front and have a negligible concentration within the soot growth region.

Figure 2.7b presents the profiles of nucleation, condensation, surface growth, and oxidation source terms. The coagulation rate is not shown in Fig. 2.7b as it does not contribute to the mass growth, but only affects the number density of soot particles. It is evident that surface growth is the predominant soot mass production term, followed by condensation and nucleation. Since A4 is the only gas-phase PAH in the present model, the peak nucleation rates are found at peak A4 concentrations. The HACA surface growth rate peak near $x \simeq 0.38$ cm, slightly different to the peak C_2H_2 position, due to the temperature effect on HACA rates. The mass growth from PAH condensa-
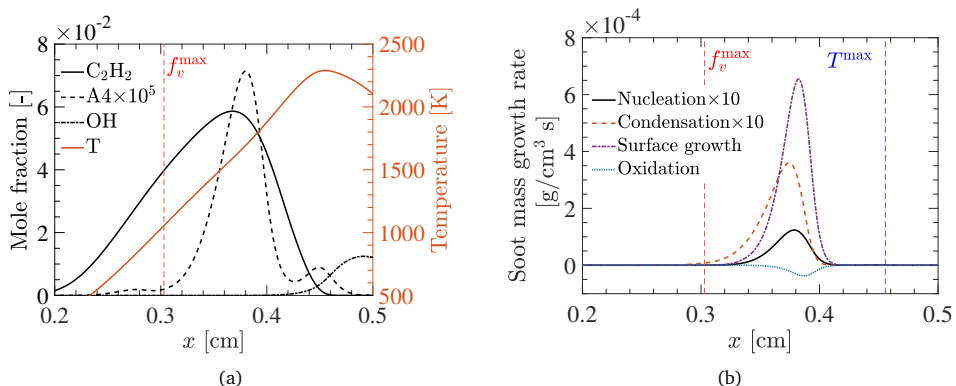
Figure 2.7: Numerical prediction of temperature and key species (a), computed rate profiles of nucleation, condensation, surface growth and oxidation processes (b).

tion persists over a broader region between the soot and gas stagnation planes. The oxidation rate is relatively small compared to HACA growth. As soot particles are transported towards the stagnation plane, because of the high residence time, coagulation is strongly active which influences the size distribution of soot particles.

The evolution of the soot PSD at different positions is presented in Fig. 2.8. At $x \simeq 0.4$ cm, a one-peak PSD shape is observed since particle nucleation is prevalent in this region. As particles grow through surface growth, the particle diameter increases, and a large collision probability between particles makes the PSD shift toward larger diameters. While approaching the stagnation plane, due to the high residence time, the coagulation process is more pronounced, which leads to a characteristic two-peak bimodal PSD shape.
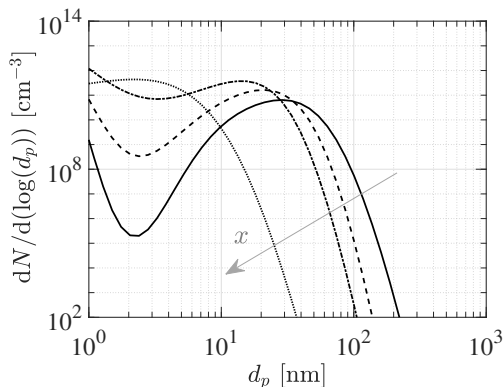
Figure 2.8: Evolution of the particle size distribution (PSD) at different positions $x \simeq 0.3$, 0.325, 0.35, 0.4 cm (indicated by arrow).

Effect of strain rate on soot formation

Soot formation is strongly affected by the flow strain rate. It is well-known that an increase in strain rate tends to reduce soot volume fraction [8]. Since soot formation is characterized by relatively long time scales, the residence time experienced by soot particles (which is related to strain rate) impacts different subprocesses. Besides, the formation of PAH is also sensitive to the scalar dissipation rate (impacted by strain rate). In this context, to generalize the applicability of the soot model, the sensitivity of soot formation in diffusion flames to strain rate is examined for a range of strain rates. The counterflow ethylene flames investigated by Wang and Chung [113] under different strain rates are retained for this analysis. The fuel is pure ethylene and the oxidizer is composed of 25% of O_2 and 75% of N_2 (on a molar basis). The reactant nozzles are separated with a distance of 8 mm. The flow velocities for both the fuel and oxidizer streams are varied from 15 cm/s to 30 cm/s corresponding to four global strain rates K_g ($75\,s^{-1}$, $100\,s^{-1}$, $125\,s^{-1}$, and $150\,s^{-1}$). The global strain rate is defined using the inlet velocity of the oxidizer stream u_o, and nozzle separation distance L as:

$$K_g = \frac{4u_o}{L} \tag{2.90}$$

In Fig. 2.9a, numerically predicted profiles of soot volume fraction are compared against the experimental data for different strain rates. The soot modeling strategy well captures the spatial distribution and the lowered peak f_v values with increasing strain rate. Consistent with the experimental observations, numerical profiles show that the sooting zone thickness decreases with increasing strain rates. Quantitative prediction of soot is, however, underestimated in simulations, and the disparity be-
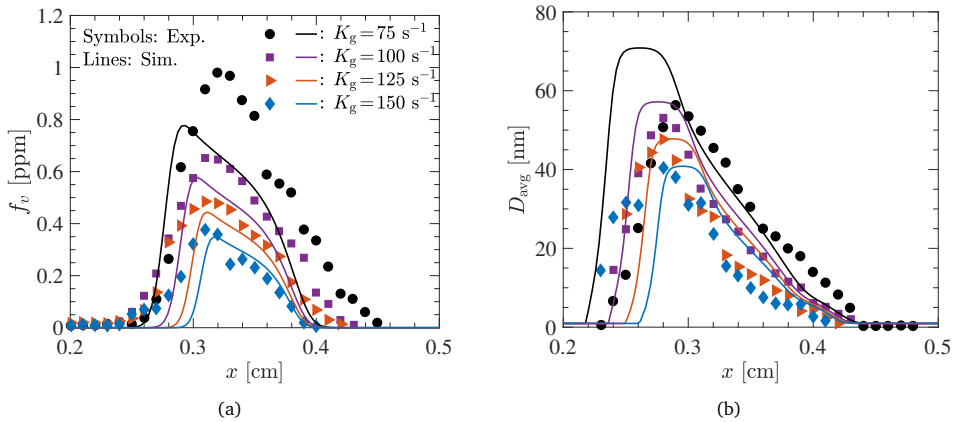
Figure 2.9: Comparison between the numerical (lines) and experimental [113] (symbols) profiles for soot volume fraction (a), and average particle diameter (b) at different strain rates.
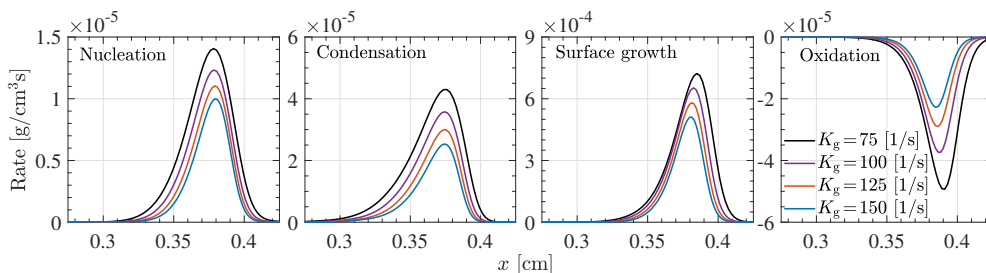
Figure 2.10: Computed rate profiles of nucleation, condensation, surface growth and oxidation.

tween numerical and experimental values decreases with the strain rate. Moreover, the comparison of the measured and the computed profiles of soot particle size with varying strain rates are shown in Fig. 2.9b. The overall profiles of particle diameters can be seen to be well predicted. Due to an increase in strain rate, the residence time of soot particles in the soot growth zone is reduced, which influences the soot volume fraction. As the size of particles primarily depends on volume fraction, an increment in strain rates leads to a reduction in particle diameters.

In order to illustrate the effect of the strain rate on soot production, the source terms for different subprocesses are shown in Fig. 2.10. It is evident that with an increase in strain rates, the source terms for all the subprocesses are decreased. An increase in strain rate is expected to decrease PAH concentrations, hence, nucleation rates. The lowered rates of soot nucleation lead to reduced soot number densities of incipient particles. Since less active surface sites are available for surface growth, the surface growth rates are decreased at higher strain rates. In addition, the lowered residence time of soot particles restricts the collision between particles affecting the coagulation rates, as a consequence the overall soot volume fraction is decreased.

The sensitivity of PAHs to strain rate is an important aspect that affects the soot formation sensitivity. Hence the normalized peak f_v (by the maximum at the strain rate of $75\,\mathrm{s}^{-1}$) and mole fractions of key aromatic species for both experiments and simulation are compared in Fig. 2.11. The numerical results satisfactory capture the strain rate sensitivity of peak f_v, confirming the validity of the modeling technique. Besides, numerical prediction agrees qualitatively with the experiments for different aromatic species. Note that, although the aromatic species A1, A2, and A3 are not considered a precursor in the soot nucleation, the formation pathways of A4 are impacted by these aromatics. The computed profiles of A4 however, show a lower sensitivity compared to other aromatics and f_v. For comparison, the strain rate sensitivity of A4 in computations without the soot model is presented in Fig. 2.11. This difference in the sensitivity of A4 can be attributed to its consumption during soot formation. A decrease in strain rate leads to higher soot amount, which implies higher A4 consumption to form soot. As a result, the sensitivity of computed A4 profiles is found to be reduced [113].
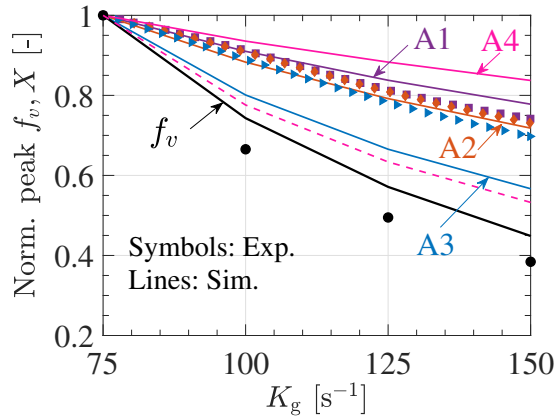
Figure 2.11: Strain rate sensitivity of peak f_v and aromatics. Experimental data from Wang and Chung [113]. The dashed magenta line indicates A4 results without a soot model.

Effect of dilution on soot formation

From a practical aspect, understanding the soot-inhibiting effects of non-fuel additives is a key research area. To assess the capabilities of the soot model in capturing the dilution effects, counterflow ethylene flames subjected to fuel stream dilution by nitrogen and oxygen enrichment of oxidizer stream are considered. The flames experimentally investigated by Wang and Chung [114] and Xu et al. [115] are considered for the nitrogen dilution (N_2 dilution) and oxygen enrichment (O_2 addition) cases, respectively. The counterflow burner employed in both experiments facilitates nozzle separation distance of $8\,mm$, and identical reactant stream velocities of $20\,cm/s$. For the N_2 dilution flame, the fuel stream is composed of 80% of C_2H_4 and 20% of N_2 (on a molar basis), while the oxidizer consists of 25% of O_2 and 75% of N_2 (on a molar basis). In the flame with O_2 addition, the fuel stream features pure C_2H_4, while the oxidizer is composed of 30% of O_2 and 70% of N_2 (on a molar basis). For the analysis of dilution effects, the baseline counterflow flame of Wang et al. [27] is considered as the reference case.

In Fig. 2.12 computed profiles of soot volume fraction are compared against the experimental measurements for N_2 dilution and O_2 addition flames. The f_v profile of the reference flame is also presented for comparison. The numerical simulation captures well the experimentally observed effect of N_2 dilution and O_2 enrichment on soot volume fraction. In the case of N_2 dilution, the reduction in soot concentration is mainly related to thermal and dilution effects. On the other hand, in the O_2 enriched flame the temperature increases leading to an increase in PAH and C_2H_2 concentration due to a thermal effect. Consequently, soot growth by condensation and surface growth also increases causing an increment in f_v.
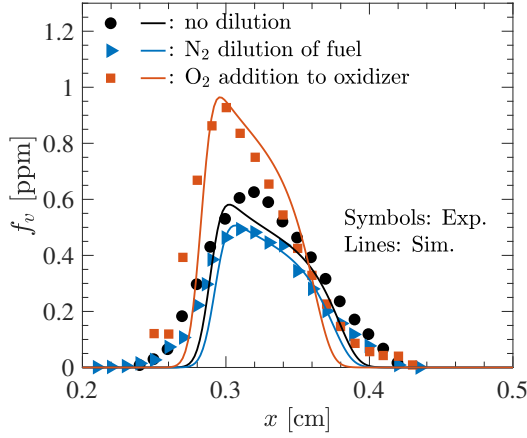
Figure 2.12: Comparison between the numerical (solid lines) and experimental (symbols) soot volume fraction for N_2 dilution to fuel and O_2 addition to the oxidizer.

Effect of pressure on soot formation

Many practical energy conversion systems rely on high-pressure operating conditions for improving thermal efficiency and power density. Soot formation kinetics is strongly influenced by pressure, hence it is important to investigate the performance of the soot modeling strategy under high-pressure conditions. The counterflow ethylene flames experimentally investigated in Amin et al. [116] are considered for their assessment. The fuel stream consists of 30% C_2H_4 diluted with 70% N_2 (on a molar basis), while the oxidizer is air. The fuel and oxidizer nozzle are separated by 8.2 mm and reactant stream flow rates are adjusted to maintain momentum balance. A constant strain rate $K_g = 60\,s^{-1}$ is maintained for all the pressures.

Note that the reaction rates for the HACA growth mechanism are proposed for atmospheric pressures and they may not adequately characterize the surface growth at higher pressures. Recent studies indicated that overall HACA surface growth rates depend on pressure [117, 118]. Therefore, an empirical scaling factor analogous to the expression by Mansouri et al. [118] is introduced to model the pressure dependence of the HACA surface growth reaction rate. Accordingly the sectional surface growth rate ($\dot{Q}_{s,i}^{sg}$) in the HACA mechanism is updated as:

$$\dot{Q}_{s,i}^{sg}(p) = [1 + \alpha_p \ln(p)] \cdot \dot{Q}_{s,i}^{sg} \qquad (2.91)$$

where p is the operating pressure (in atm) and α_p is a model parameter.

The computed profiles of soot volume fraction are compared against the laser extinction measurements in Fig. 2.13 at pressures of 2, 3, 4, and 5 atm. Computed f_v profiles without pressure-dependent scaling are also presented for comparison. It is evident that f_v increases drastically with the pressure, while its peak shifts towards
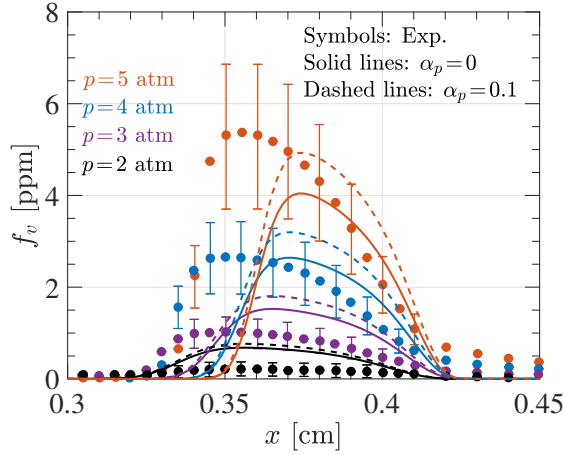
Figure 2.13: Computed (lines) and measured [116] (symbols) profiles of soot volume fraction in a counterflow diffusion flame at elevated pressures.

the flame reaction layer. The numerical results favorably capture the qualitative trends observed in the f_v evolution at different pressure, although the numerical soot stagnation plane is shifted from the experimental one. Compared to the standard HACA model ($\alpha_p = 0$) the proposed model leads to a better quantitative prediction of the f_v at a higher pressure for $\alpha_p = 0.1$ scaling. Note that the selected α_p value does not have general validity and requires calibration with measurements. Besides, with an increase in pressure, the effectiveness of the proposed model in predicting the f_v improves. However, the proposed model for pressure-dependent HACA surface growth requires further improvement and a dedicated validation study.

Non-premixed soot formation oxidation (SFO) counterflow flames

The Soot Formation (SF) type counterflow flames are investigated in previous sections, in which flame is located on the oxidizer side of the stagnation plane while formed soot particles are convected toward the stagnation plane in the direction opposite to the oxidizer stream. On the other hand, in Soot Formation Oxidation (SFO) type flame, the flame is located on the fuel side of the stagnation plane, and soot particles are convected toward the oxidizer stream encountering high-temperature zones leading to a significant level of soot oxidation. The performance of the present model for soot prediction in SFO flames is evaluated. The counterflow ethylene flames experimentally studied by Quadarella et al. [119] are considered. The fuel stream consists of 26% C_2H_4 diluted with 74% N_2 (on a mass basis), while the oxidizer is pure oxygen. The fuel and oxidizer nozzle are separated by 8.0 mm, and reactant stream flow rates are adjusted to maintain momentum balance. The flow velocities for both the fuel and oxidizer streams are varied corresponding to four global strain rates K_g (75 s^{-1}, 100 s^{-1}, 125 s^{-1}, and 150 s^{-1}).

41
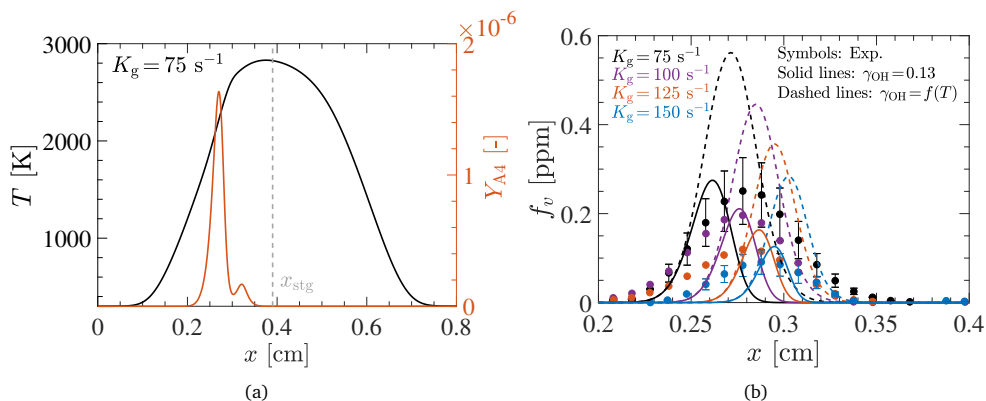
Figure 2.14: Temperature and A4 mass fraction profiles for the SFO flame at $K_g = 75\,\mathrm{s}^{-1}$ (a), and computed (lines) and measured [119] (symbols) profiles of f_v in SFO flames at different strain rates.

In Fig. 2.14a, temperature and A4 profiles are shown for $K_g = 75\,\mathrm{s}^{-1}$ indicating the structure of SFO flame. As can be observed, the PAH exists on the fuel side of the stagnation plane, therefore, soot is formed on the fuel side, which is typical of SFO flames. Besides, the temperature near the stagnation plane is relatively high, with a peak value reaching approximately 2830 K. The computed profiles of soot volume fraction are compared against the experimental data for different strain rates in Fig. 2.14b. The collision efficiency γ_{OH} of OH is found to be a strongly decreasing function of temperature [51, 119]. Therefore, the numerical results are also presented for the temperature-dependent γ_{OH} function given by Quadarella et al. [119]. The $\gamma_{\mathrm{OH}}(T)$ function reads:

$$\gamma_{\mathrm{OH}} = 0.66686 \exp\left(-1.3014 \times 10^{-3} T\right) \tag{2.92}$$

Because of the strong oxidation, the typical Gaussian shape of f_v profiles is observed in the measured and computed profiles. The decrease in the peak f_v with strain rate is captured by the simulations. The reduction of the f_v due to oxidation is more pronounced as particles convect toward the oxidizer side. Hence, compared to experimental data, the shift in the f_v profiles towards the oxidizer side is noticed in the computed profiles. For temperature-dependent γ_{OH}, the soot oxidation is reduced, which tends to yield higher peak f_v values compared to their constant γ_{OH} counterparts. The width of the f_v distribution is, however, well predicted by the inclusion of temperature-dependent γ_{OH}. In general, retained soot model provide good quantitative and qualitative agreement with experimental data in predicting soot formation in SFO-type counterflow flames.

Non-premixed unsteady counterflow flames

Many practical combustion systems employ turbulent conditions, which are inherently unsteady and often manifest spatio-temporal variations of local strain rates affecting the formation of soot. In this regard, it is appropriate to investigate the sooting behavior of laminar flames subject to strain rate fluctuations, to address the unsteady effects of hydrodynamics on soot formation kinetics. The counterflow diffusion flame presents a canonical configuration to study unsteady strain rate effects numerically, as well as, experimentally by subjecting flames to a harmonic oscillation of the nozzle exit velocity. Therefore, the laminar counterflow flames experimentally investigated by Li et al. [120] are considered to investigate the predictive capabilities of soot modeling strategy in capturing the dynamic evolution of soot.

In the investigated atmospheric flames, the fuel stream is pure C_2H_4 and the oxidizer is composed of 25%-75% O_2-N_2 on a molar basis. Fuel and oxidizer streams are separated by 8 mm. Under steady conditions, the velocities of fuel and oxidizer are 22.5 cm/s and 28.8 cm/s, respectively. The global strain rate at steady state conditions is thus $K_g = 144\,s^{-1}$. The strain rate unsteadiness is introduced by imposing sinusoidal fluctuations to the inlet velocities at a frequency f with an amplitude A_u. The velocity fluctuations of the oxidizer stream have the following form:

$$u_o(t) = u_o^{st}[1 + A_u \sin(2\pi f t)] \qquad (2.93)$$

where u_o^{st} is the steady-state value of the inlet velocity for the oxidizer stream. The profile for fuel stream fluctuations is obtained by fitting their measured values [120]. Initially, the flame is in steady state at $K_g = 144\,s^{-1}$, and the corresponding solution presents the initial condition for the application of the sinusoidal oscillations. The imposed variations ($f = 60\,Hz$, $A_u = 50\%$) of nozzle exit velocities with time for the fuel and oxidizer are shown in Fig. 2.15 along with measurements from Li et al. [120].
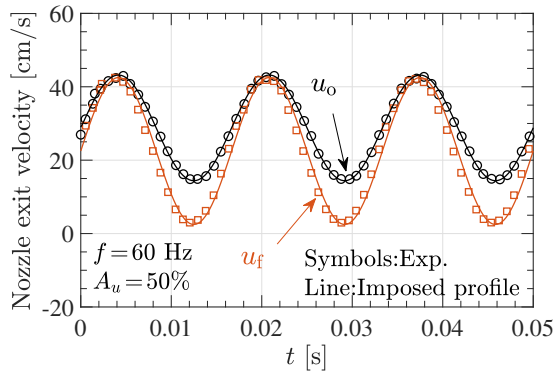
Figure 2.15: Temporal evolution of measured [120] (symbols) and numerical (lines) oxidizer and fuel velocity, u_o and u_f respectively.
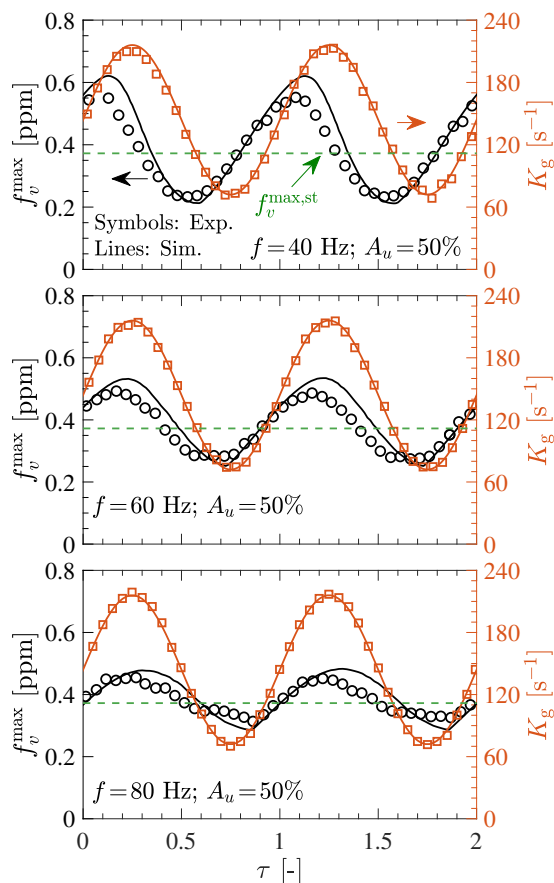
Figure 2.16: Peak values of f_v and global strain rate at several oscillation frequencies. Measurements (symbols) and simulations (lines). The dashed line denotes the steady-state peak f_v value.

In Fig. 6.8, the dynamic response of soot volume fraction peak values (f_v^{max}) is presented against the dimensionless time ($\tau = ft$) for different frequencies. In addition, measured values of unsteady f_v^{max} and K_{g} are plotted for comparison. The f_v profiles show very good agreement with measurements for the transient soot response, including the amplitudes of the induced soot oscillations. The amplitude reduction of the f_v response occurs asymmetrically, about the steady state value indicating enhanced soot formation under unsteady conditions. Consistent with previous studies [121], for an increase in the imposed frequency, the amplitude of induced oscillations of soot volume fraction tends to decrease, while the phase lag between imposed oscillations and soot response becomes larger.

For a more quantitative representation of the unsteady response of soot, the peak and trough values of f_v along with the phase lag (Φ) of the f_v oscillations with respect to the strain rate oscillations are compared in Fig. 2.17. Owing to the asymmetric nature
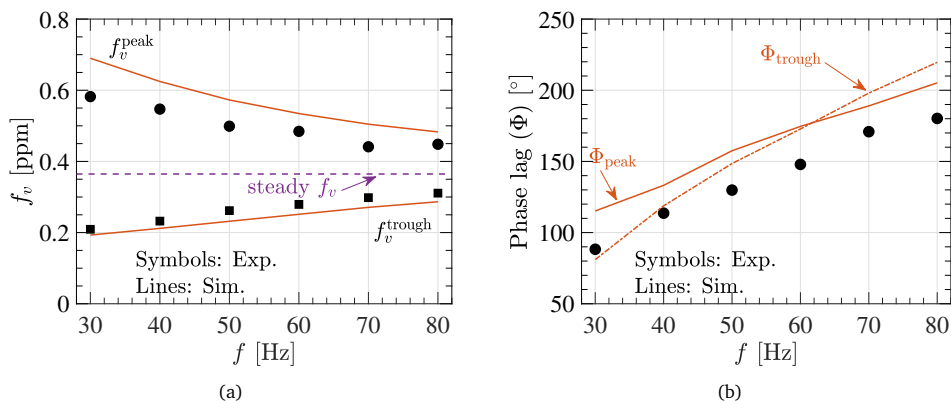
Figure 2.17: Comparisons between frequency responses of peak, trough f_v (a), and the phase shift Φ between f_v and K_g oscillations (b) in unsteady flames. Measurements (symbols) and simulations (lines).

of the induced f_v oscillations, the phase lag observed in the simulated f_v response is presented for the peak as well as trough positions. The departure from the steady-state conditions is evident with an increase in frequency f, the f_v^{peak} tends to decrease while f_v^{trough} increases, reducing the amplitude of induced f_v oscillations. Although the frequency variation is not substantial, it can be expected that a further increase of f would finally lead to decoupling between soot and strain rate oscillations, and the flame reaction zones cease responding to the imposed oscillations. This monotonic variation of f_v with frequency is well captured by the simulations. Besides the maximum soot volume fraction, with an increase in f, the phase shift between the imposed and induced oscillations becomes larger. This is because soot chemistry is characterized by larger chemical time scales, which become larger than the oscillation period at higher frequencies, leading to an increased phase lag. The computed results show good agreement with experimentally measured values for the phase shift, although the numerical response of f_v is somewhat phase-lagged compared to measurements. Overall, numerical results demonstrate the capabilities of retained soot model in favorably capturing the dynamic response of soot under unsteady conditions.

2.3.2 Premixed flames

Burner-stabilized stagnation flames

For validation of the soot model in premixed configurations, laminar premixed burner-stabilized stagnation (BSS) flames of Abid et al. [123] are numerically investigated. The schematic illustration of the BSS flame configuration is shown in Fig. 2.18. The premixed $C_2H_4/O_2/Ar$ mixture with an equivalence ratio of $\phi = 2.07$ is injected from the burner at a cold velocity of 8.0 cm/s (298 K and 1 atm). Soot particles are sampled for PSD analysis at various distances from the burner surface (H_p) by moving the sampling probe (stagnation plate). The modeled flame presents comprehensive mea-
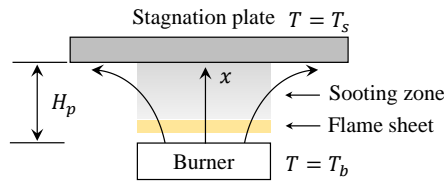
Figure 2.18: Illustration of the BSS flame configuration. T_b and T_s are the burner and stagnation plate temperatures, respectively; H_p is the burner-to-stagnation plate separation distance.

surement data sets for the particle size distribution and is among the flames selected by the International Sooting Flame workshop [124]. The details of the experimental setup and measurement techniques can be found in Ref. [122]. The experimental configuration of the BSS flame is modeled using the one-dimensional formulation described in Section 2.3.1. At the burner boundary, the uniform plug flow with a
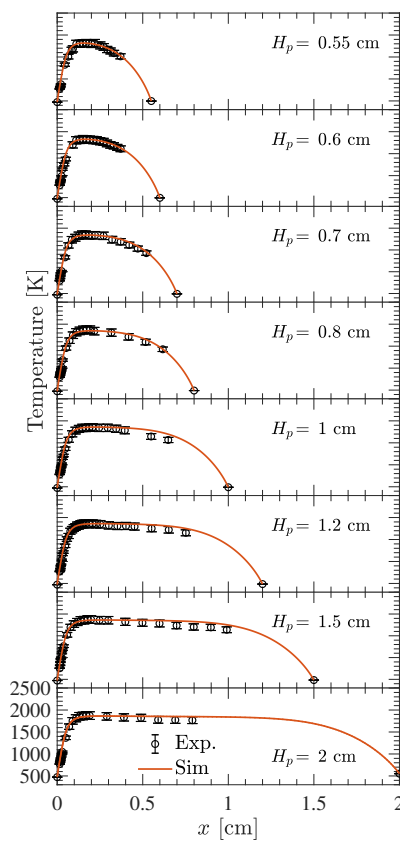
Figure 2.19: Comparison between numerical and experimental [122] temperature profiles for the different positions of the plate above the burner.
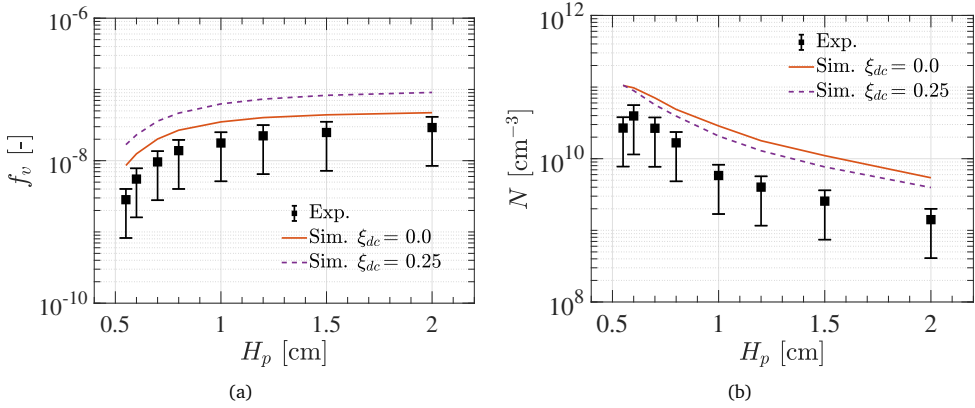
Figure 2.20: Comparisons between computed soot volume fraction (a), and particles number density (b) evolution (for $\xi_{dc} = 0$ and 0.25) with the experimental measurements [122].

fixed mass flux is applied, and the temperature $T_b = 473\,\text{K}$ is specified. A no-slip wall boundary condition is applied at the stagnation plate, with the measured plate temperature T_s (from Ref. [122]).

To compare the gas-phase kinetics, temperature profiles obtained for several heights of the stagnation plate (H_p) are compared with the experimental values from Camacho et al. [122] in Fig. 2.19. A good agreement between numerical results and experimental measurements demonstrates the validity of the employed model in capturing the flame structure. To partially account for the flow aspiration effect [122], the computed soot volume fraction f_v and number density N quantities at 0.2 cm upstream of the stagnation plate are compared against the experimental measurements in Fig. 2.20. Note that the simulation results are presented for two values of ξ_{dc}, which is a model parameter accounting for the conservation/depletion of surface radical sites in the HACA mechanism. As evident in Fig. 2.20a, the soot volume fraction increases up to the stagnation plane, while number density decreases. Since the nucleation process is prominent at the beginning of the sooting zone, the number density is higher, and as soot particles approach the stagnation plate, they coagulate leading to lower N with higher f_v. It can be noticed that simulated f_v and N profiles show a good qualitative agreement with their experimental counterparts. However, compared to experiments, f_v and N tend to be over-predicted by simulations.

In Fig. 2.21 the numerical profiles for the PSDs for different H_p are compared against the experimental measurements. The evolution of the PSD in the BSS configuration is strongly correlated with soot formation subprocesses. Near the flame front, the soot nucleation process is predominant, leading to a power-law type PSD. After the formation of nascent soot particles, the surface growth process tends to shift the PSD towards larger particle sizes. As soot particles approach the stagnation plate, the higher residence time promotes the coagulation process which results in a sharp
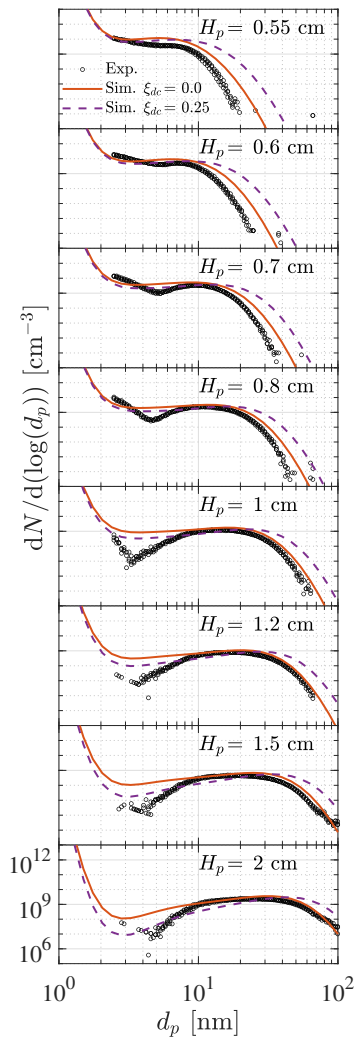
Figure 2.21: Comparison between numerical predicted soot particles size distributions (for $\xi_{dc} = 0$ and 0.25) with the experimental measurements [122].

bimodal shape of PSD. As evident from Fig. 2.21, the bimodal PSD shape is well reproduced by the soot model. For $\xi_{dc} = 0$, the PSD results within the log-normal mode ($d_p > 10$ nm) agree well with the experimental measurements. However, the assumption of depleted surface radicals overpredicts the number density of soot particles near the trough in the PSD profiles (around $d_p \approx 3$ nm). The growth of smaller-sized particles can be fairly well captured with $\xi_{dc} = 0.25$, which, on the other hand, tends to shift the log-normal mode of the PSD towards larger particle diameters.
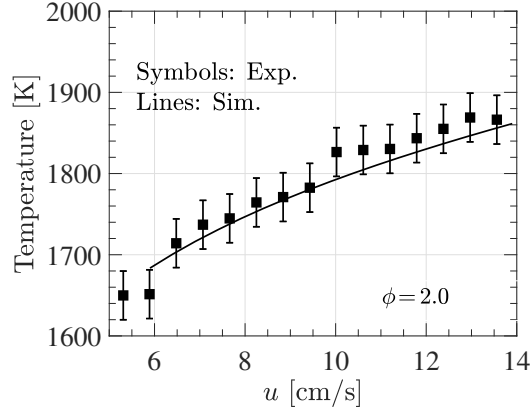
Figure 2.22: Comparison of calculated (lines) and measured [125] (symbols) flame temperatures at (HAB = 5 mm) as a function of exit velocity u for $\phi = 2.0$.

Burner-stabilized premixed flames

The validation of the soot modeling strategy is performed for burner-stabilized premixed C_2H_4-air flames investigated by Langenkamp et al. [125]. In the experiments, the growth of soot volume fraction for varied flame temperatures was studied by changing the velocity of unburned premixed gas at a fixed equivalence ratio. The premixed burner-stabilized flames are simulated by prescribing a mass flux and an inlet temperature (300 K) for the unstretched ($K = 0$) flamelet equations described in Section 2.3.1.

In Fig. 2.22, a comparison between measured and calculated temperatures at 5 mm height above burner (HAB) with exit velocity are presented for $\phi = 2.0$. Since chemical heat release is complete at this distance, the measured temperature is essentially representative of the early stages of soot growth [125]. Despite the exclusion of heat losses (radiative), computations tend to predict temperature variation reasonably well, validating the employed gas-phase kinetics.

Axial profiles of computed and measured soot volume fractions at $\phi = 2.0$ and 2.1 are compared in Fig. 2.23 for exit velocities $u = 5.9$, 8.8, and 11 cm/s. Given the lack of soot oxidation paths in such highly fuel-rich flames, f_v steadily increases with the distance above the burner. It can be observed that, at a fixed distance, the f_v increases with increasing equivalence ratio and decreases with exit velocities. Overall, good agreement with experimental measurements is obtained for $\xi_{dc} = 0$, except for the flame with $\phi = 2.0$, in which f_v is over-predicted by a factor of three. The favorable agreement demonstrates the consistency of the modeling strategy employed here.
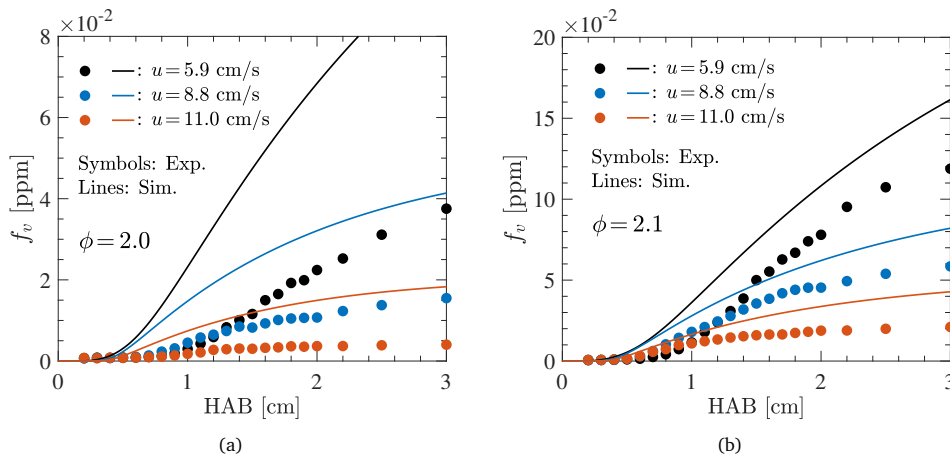
Figure 2.23: Comparison of measured [125] (symbols) f_v for three different exit velocities and calculations (lines) at equivalence ratios $\phi = 2.0$ (a), and $\phi = 2.1$ (b).

Effect of radiative heat loss on soot prediction in burner-stabilized premixed flames

Additional validation of the soot model is performed by including the radiative heat loss effect in simulations of premixed burner-stabilized flames. The ethylene-air flames with $\phi = 2.34$ (C/O = 0.78), and 2.64 (C/O = 0.88) investigated by Xu et al. [126] are considered for this study. The cold gas velocity of 6.73 cm/s and 298 K temperature is maintained at the burner inlet. The radiation from soot particles, and gas-phase species are taken into account in the enthalpy equation (Eq. 4.3). The radiative heat transfer is modeled using an optically-thin approximation. Accordingly, the radiation source term, given by:

$$\dot{\mathcal{Q}}_{\mathrm{rad}} = -4\sigma \left[\sum_i p_i \alpha_{p,i} \right] \left(T^4 - T_a^4 \right) - C_s f_v T^5, \qquad (2.94)$$

where σ is the Stefan-Boltzmann constant (5.669×10^{-8} Wm^{-2}K^{-4}), p_i is the partial pressure (atm) and $\alpha_{p,i}$ is the extinction coefficient for species i; T_a is the ambient temperature (298 K) and $C_s = 4.243 \times 10^{-4}$ Wm^{-3}K^{-5} is the extinction coefficient of soot taken from Smooke et al. [127]. In the above expression, the first term on the right-hand side accounts for the radiative heat loss due to the gas phase, while the second term is related to soot radiation. The extinction coefficients $\alpha_{p,i}$ for species CO_2, H_2O, CO and CH_4 are derived from Refs. [128, 129].
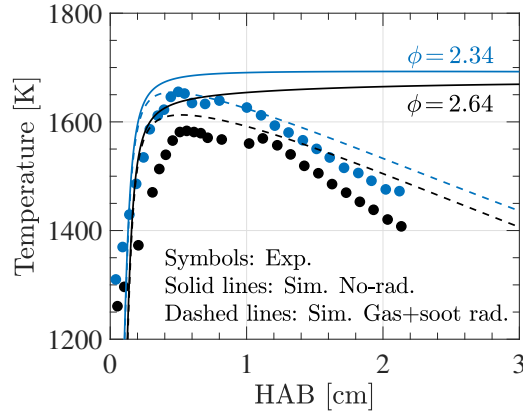
Figure 2.24: Comparison of measured and computed flame temperatures for $\phi = 2.34$ and 2.64 with (dashed lines) and without (solid lines) radiative heat transfer.

In Fig. 2.24, measured temperatures for $\phi = 2.34$ and 2.64 are compared to computed profiles including and excluding radiative heat losses. As can be observed, the inclusion of radiative heat loss shows improved agreement with experimental counterparts compared to adiabatic solutions. The impact of radiative losses on the temperature illustrated by computations is significant at higher distances above the burner. To further illustrate the impact of radiative heat loss on flame structure, the experimental and calculated profiles of the major combustion products are compared in Fig. 2.25. Except for H_2, with significant differences, the agreement is considerably good for other species. The inclusion of radiative heat transfer tends to increase the quantita-
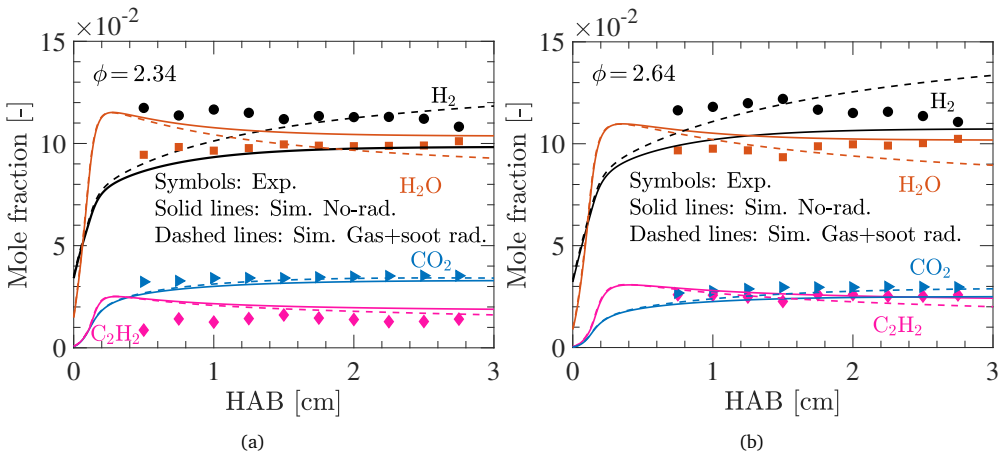
Figure 2.25: Comparison of measured and computed key species concentration for $\phi = 2.34$ (a), and 2.64 (b) with (dashed lines) and without (solid lines) radiative heat transfer.
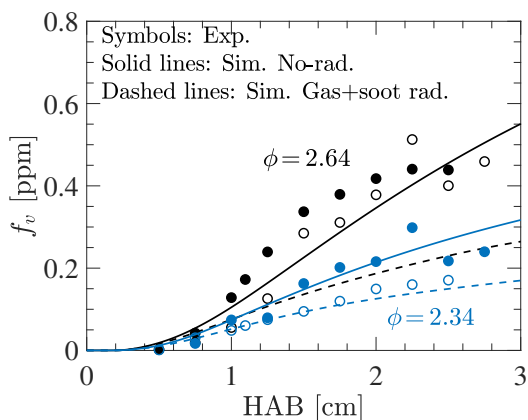
Figure 2.26: Comparison of measured and computed soot volume fraction for ϕ = 2.34 and 2.64. Filled and hollow symbols respectively designate experimental data measured with laser and sampling techniques.

tive prediction of H_2 at the highest concentration level, while for CO_2 the computed profiles agree well with experiments at higher axial distances. Compared to measured and adiabatic counterparts the concentration of C_2H_2 is found to be slightly lowered with the inclusion of radiation effects.

A comparison between measured and calculated soot volume fraction profiles for ϕ = 2.34 and 2.64 is presented in Fig. 2.26. The agreement between numerical and experimental f_v profiles is generally consistent (with $\xi_{dc} = 0$). The numerical calculations with radiative heat transfer, however, show notable underprediction of f_v compared to adiabatic calculations. The differences in numerical prediction correlate to the lowered temperature and C_2H_2 concentration as a result of radiative heat loss, impacting the surface growth of soot particles.

2.4   Summary

In this chapter, the numerical strategy for soot modeling with a sectional method including soot sub-models has been described. The predictive capability and accuracy of the sectional soot model have been evaluated in laminar sooting premixed and non-premixed ethylene-fueled flames over a broad range of conditions. Despite several assumptions (e.g., uni-variate description, no agglomeration, single PAH species, etc.), the precision level of the present soot model is encouraging. Overall, good qualitative, as well as quantitative agreement, is obtained between experimental and computed soot quantities for laminar flames. The strain rate sensitivity of soot formation and dilution effects are well predicted in non-premixed flames. The experimentally observed dynamic response of soot to strain rate unsteadiness is well reproduced by simulations. Moreover, in premixed flames, the experimentally measured evolution of soot particle size distribution is effectively captured by the developed soot model.

In general, soot prediction is found to be sensitive to the variations in surface growth processes related to the treatment of surface radicals, parameterized by ξ_{dc}. Without definite physical validity, the model assessment suggests that, for the employed kinetic scheme, conservation of surface radicals ($\xi_{dc} \to 1$) tends to reproduce experimental values for soot volume fractions in non-premixed counterflow flames, while in premixed flames, the approximation of radical depletion ($\xi_{dc} \to 0$) yields good agreement between computations and measurements. However, the assumption of full depletion or full conservation of surface radicals based on the combustion environment is still an open subject to be fully understood. It would be therefore fruitful to develop a consistent model for radical treatment between complete depletion and full conservation limits. Nevertheless, based on the trends observed in the results, it is proposed to calibrate ξ_{dc} in conjunction with the kinetic scheme on simpler configurations since soot prediction is sensitive to the concentration of key precursor species and PAHs.

Given the complexity of the soot formation process, it is difficult to expect the exact agreement between experimental measurements and calculations for different configurations. In this context, the predictive ability of the retained soot modeling strategy is very promising. However, there is a scope for improvement in the model concerning the description of soot subprocesses and extensions accounting for additional physical phenomena to improve the quality and reliability of modeling predictions. These include detailed nucleation/condensation models based on multiple PAH species, advanced models describing surface growth and soot oxidation (including soot aging effects), alternative particle dynamics models facilitating information on soot morphology etc.. Besides, a detailed assessment of the used soot model on practical fuels is also of interest. These extensions are not explored here but could be the subjects of future research.

3

Soot inhibiting effects of hydrogen and water vapour addition

The modeling approach outlined in Chapter 2 is used in this chapter to investigate soot inhibiting effects of simultaneous, as well as separate addition of hydrogen to the fuel and water vapour to the oxidizer in laminar, counterflow ethylene diffusion flames. The chemical pathways of soot formation under the influence of hydrogen and water vapour addition are studied. Part of the discussion presented in this chapter refers to an article published as: 'Effects of hydrogen enrichment and water vapour dilution on soot formation in laminar ethylene counterflow flames' in International Journal of Hydrogen Energy [130].

3.1 Introduction

Considering the severe environmental and health impacts of soot, the legislative regulations on their emissions from combustion systems have become stringent. In the quest of achieving the goals of these regulations, extensive research is ongoing on the development of advanced technologies for reducing soot emissions while improving combustion efficiency. Concerning this, blending of reactants with various nonfuel diluents, such as N_2, CO_2, H_2O, He, Ar, and reactive additives, such as H_2, CO, dimethyl ether (DME) remains one of the most effective approaches to suppress the soot formation in combustion devices [8]. In principle, such diluents influence the soot formation via four important mechanisms [131]: (a) The dilution effect, which alters the overall oxidizer-to-fuel mass ratio. (b) The thermal effect, as a consequence of the change in the thermal properties of reactants. (c) The chemical effect of reactive diluents, as they participate in chemical reactions. (d) The radiative exchange, through which diluents modify flame temperatures, and affect the overall soot production. Inherently, these effects are strongly coupled, which makes it almost impossible to quantify and investigate the isolated effects through experiments. Owing to this, multiple research activities have been conducted over the past two decades on investigating the effectiveness of various additives and diluents on soot inhibition in

premixed as well as diffusion flames [4,8,94,115,132–144]. However, given the intricacies of physicochemical interactions associated with soot formation, understanding the inherent mechanisms through which various additives influence the flame properties, PAH formation, soot inception, and surface growth stages, is very challenging, and continues to be an active area of research.

Moreover, recent trends in combustion research show a prominent interest in hydrogen as a future combustion fuel. Notably, even small amounts of hydrogen blending in traditional hydrocarbon fuels have shown to improve combustion efficiency, along with a significant reduction in overall soot emissions [145–151]. Hydrogen also plays a key role in the formation of PAHs and the surface growth of soot particles. Therefore, there is a continued research interest in investigating the fundamental pathways leading to the suppression of soot formation as an effect of hydrogen addition. Many researchers have addressed the effects of hydrogen addition to hydrocarbon fuels on soot, PAH formation under different flame conditions through experiments and computations [134–136, 139, 142, 152–162]. The potential role of its chemical effect in soot suppression was first highlighted through the experiments by Du et al. [134] based on the soot particle inception limits in strained diffusion flames. Later, Gülder et al. [135] also demonstrated the additional role of chemical effects in the suppression of soot formation for the laminar co-flow ethylene-air flames. Guo et al. [136] modeled the ethylene flames studied by Gülder et al. [135]. The authors argued that the reduced concentration of H radicals in the surface growth region, and the higher concentration of H_2 in the lower flame region, decrease the H-abstraction rate in the PAH and soot surface growth processes, and eventually reduce the soot formation. Using a detailed soot model, Gu et al. [139] concluded that through chemical effects, the added hydrogen decreases the PAH concentration, which in turn, lowers the soot inception rate. The influence of hydrogen addition on the kinetic pathways leading to PAH formation was, however, not examined.

The potential kinetic pathways concerning the suppression of soot formation by H_2 in laminar co-flow $C_2H_4/(O_2\text{-}CO_2)$ diffusion flames were discussed by Wang et al. [142]. In their study, the reduced nucleation rate through the chemical effect of H_2 was identified as the primary factor in the soot inhibition. Most recently, Xu et al. [161] studied the chemical effects of hydrogen addition on soot formation in methane and ethylene counterflow diffusion flames experimentally and numerically. Through detailed kinetic analysis, the authors reported that the role of hydrogen in the chemical suppression of soot formation is sensitive to oxidizer composition and fuel type. Qiu et al. [162], through a detailed de-coupling approach, numerically investigated the effects of hydrogen blending on flame structure and soot formation in laminar ethylene co-flow flames. Their study suggested a relatively opposing view, that the soot yield, primary number density, and average primary number increase as a result of enhanced HACA rates, PAH condensation rates, and delayed oxidation rates. A literature review reveals that the underlying mechanisms of soot suppression from the addition of H_2 are still not fully understood, and therefore motivates the current study.

Similar to the hydrogen addition, multiple studies investigating the chemical effects of water vapour dilution on soot formation have been reported in the literature [106, 131, 159, 163–167]. In a numerical study by Liu et al. [131], the chemical effects of water vapour dilution of the air stream were found to lower the PAH concentrations, and consequently, the soot nucleation rates. Their analysis also revealed that the added H_2O enhances the formation of OH radicals and reduces the concentration of H radicals primarily through the reverse reaction of $OH + H_2 \rightleftharpoons H + H_2O$. The reduced concentration of H radicals subsequently slows down the soot surface growth through the H-abstraction reaction. Most recently, Mahmoud et al. [106] observed that the addition of H_2O chemically promotes the formation of molecular hydrogen, through the reverse reaction of $OH + H_2 \rightleftharpoons H + H_2O$. The increased H_2 lowers PAH growth rates through the reverse H-abstraction reaction in the HACA PAH formation sequence and tends to decrease the soot nucleation rate. Evidently, while explaining the role of chemical effects in soot suppression, Liu et al. [131] also highlighted the reduced soot surface growth rate. On the other hand, Mahmoud et al. [106] identified the decreased soot nucleation rates as a prime element in the overall soot reduction. Therefore, it is noticed that there are inconsistent conclusions regarding the main kinetic pathways through which the H_2O addition chemically influences PAH growth, soot nucleation, and soot surface growth. Hence, it requires further attention.

In general, previous studies have focused on investigating the effects of either blending fuel with H_2, or adding H_2O to fuel/oxidizer on soot formation in diffusion flames. However, soot inhibiting effects of adding H_2 to the fuel and H_2O to the oxidizer simultaneously, have not been discussed in the open literature. Further, with the addition of H_2 as well as H_2O, the radical pool that influences the overall soot formation process, is expected to be kinetically affected via the reaction $OH + H_2 \rightleftharpoons H + H_2O$. Hence, in view of identifying plausible coupled effects, it is of interest to understand how the chemical pathways of soot formation will be affected by the simultaneous addition of H_2 and H_2O. Moreover, the simultaneous addition of H_2 and H_2O aims to incorporate the concepts of hydrogen-enriched combustion together with flue gas recirculation. Hence, such a study is important from a practical perspective. Besides, many of the previous studies on hydrogen enrichment or water vapour dilution were carried out in co-flow jet diffusion flames. Because of the two-dimensional flow field, the trends in the radial distribution of the soot source terms were found to be varying along the direction of flame height, making the investigation of kinetic pathways more challenging. Therefore, to understand the chemical effects on a fundamental level, it is of interest to carry out a detailed kinetic analysis in a canonical configuration of the counterflow diffusion flame, which is particularly suited for soot mechanism studies.

Against this background, the main objective of this study is to elucidate the detailed kinetic pathways associated with the soot suppression due to H_2/H_2O addition in counterflow ethylene flames, primarily focusing on the role of chemical effects. It also highlights the role of the reaction mechanism in identifying the pathways of soot formation that may lead to a disparity of conclusions. The present study intends to

ascertain if there exists a synergistic interaction between the chemical effects of fuel-side H_2 addition and those of oxidizer-side H_2O dilution in soot formation suppression when added simultaneously. Finally, the effect of H_2/H_2O addition on the particle size distribution (PSD) is discussed to provide insights into the underlying mechanisms of the sooting process.

3.2 Numerical methodology

Numerical simulations of steady sooting counterflow flames are performed using the sectional soot model introduced in Chapter 2. A mixture-averaged approximation is employed for the species diffusion transport while neglecting the radiative heat transfer. Considering the relevance to the present study, brief evidence of model verification for H_2O and H_2 diluted ethylene flames is presented in the next section.

3.2.1 Model verification

To validate the predictive capabilities of the soot model concerning H_2O dilution effects on soot production ethylene flames experimentally investigated by Mahmoud et al. [106] are considered. In these flames, the oxidizer stream is composed of 25% of O_2 and 75% of N_2 (by volume). The temperature of the fuel stream is maintained at 393 K while the oxidizer is kept at 300 K under atmospheric pressure conditions. Simulations are performed for the cases with 10% and 20% (by volume) levels of H_2O dilution to ethylene. Both fuel and oxidizer streams are maintained at 13.5 cm/s exit velocity. The computed profiles of soot volume fraction are compared with experimental measurements in Fig. 3.1. A good agreement is observed between the numerical results and experimental data, indicating that the retained soot model can qualitatively capture the effects of H_2O dilution on sooting characteristics in ethylene flames.
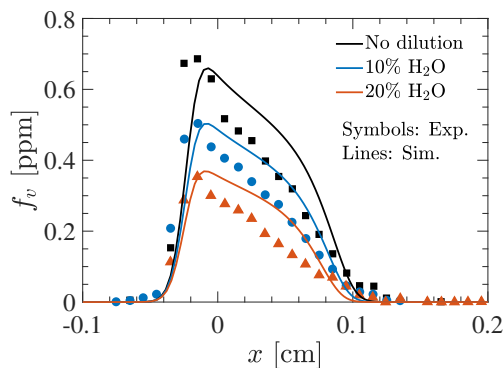
Figure 3.1: Comparison of computed soot volume fraction profiles with experimental results of Mahmoud et al. [106] for H_2O addition to ethylene up to 20%.
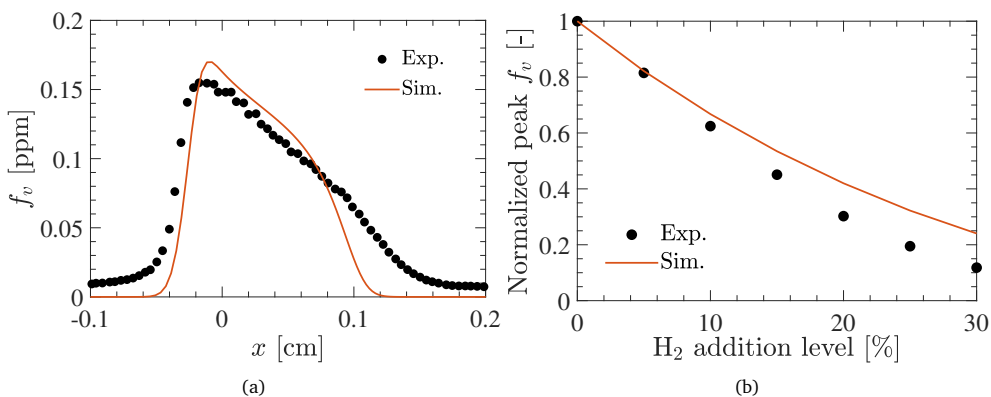
Figure 3.2: Comparison of measured (symbols) and simulated (lines) profiles of soot volume fraction f_v for 20% H_2 addition to ethylene (a), and normalized (to pure ethylene flame) peak f_v with the level of H_2 addition (b) for the counterflow diffusion flames studied by Xu et al. [161].

The model verification is also extended for the prediction of H_2 addition effects on soot formation. Ethylene counterflow flames studied experimentally by Xu et al. [161] are selected for this assessment. In the flames, the oxidizer stream is composed of 24% of O_2 and 76% of N_2 (by volume), and the fuel stream of ethylene is diluted with 20% of H_2 (by volume). Nozzle exit velocities for both fuel and oxidizer streams are maintained at 13.5 cm/s. Both fuel and oxidizer are kept at ambient temperature (300 K) and atmospheric pressure. In Fig. 3.2a the measured and computed profiles for soot volume fraction are compared. A reasonably good match is observed for the computed results against the reported experimental data. Besides, the experimental and simulated profiles of normalized peak soot volume fraction with varied levels of H_2 addition are compared in Fig. 3.2b. The experimentally observed sensitivity of soot formation suppression to the H_2 addition is qualitatively well captured by the present soot model, although quantitative discrepancies still exist. The reasonable agreement between measured and computed values suggests that the current model is capable of predicting the qualitative features of soot evolution in ethylene flames under the addition of H_2.

3.2.2 Investigated flames

The counterflow diffusion flame studied by Wang et al. [27] is considered a baseline case to investigate the effect of H_2/H_2O dilution on soot formation. The baseline flame consisted of a pure C_2H_4 fuel reacting with an oxidizer composed of 25% of O_2 and 75% of N_2 (by volume). The fuel and oxidizer streams are kept at 300 K inlet temperature. The soot model has been validated for this flame in Chapter 2 with the experimental results for global soot quantities. Numerical simulations are carried out for the baseline flame with different combinations of hydrogen addition to ethylene and water vapour dilution of the oxidizer by up to 20% (by volume). To isolate

and quantify the chemical effects from thermal and dilution effects, fictitious inert species i-H_2 and i-H_2O are added to the chemical mechanism. These fictitious species are assumed to have identical thermal and transport properties as real H_2 and H_2O. However, they are treated as chemically inert and are not allowed to participate in chemical reactions, except through the third-body collision processes. Three different conditions are considered to investigate the separate and simultaneous effects of H_2 or H_2O addition. For brevity, these cases are described as follows:

- **SepH2** refer to the flames in which either H_2 or i-H_2 is added to the fuel.

- **SepH2O** refer to the flames in which either H_2O or i-H_2O is added to the oxidizer.

- **SimH2H2O** refer to the flames in which H_2 or i-H_2 is added to the fuel and H_2O or i-H_2O is added to the oxidizer.

The detailed gas-phase chemical mechanism KAUST Mech 2.0 (KM2) [105] is used to describe the reaction kinetics of ethylene. In many of the previous studies investigating H_2/H_2O addition effects, the reaction kinetics of ethylene was modeled using the well-known ABF mechanism given by Appel et al. [23]. Therefore, to identify the differences in the chemical pathways of soot formation, all the cases are also simulated with the ABF mechanism [23], consisting of 101 species and 544 reactions. For the current study, the potential flow approximation is used for the boundary conditions in the quasi-1-D formulation of the counterflow configuration discussed in Section 2.3.1.

3.3   Results and discussion

The important kinetic pathways associated with the chemical effects of adding either hydrogen to ethylene (SepH2 cases) or water vapour to oxidizer (SepH2O cases) are discussed first. Subsequently, the effects of the simultaneous addition of H_2 and H_2O (SimH2H2O cases) on the soot formation suppression are investigated.

3.3.1   Effects of hydrogen addition to the fuel

Temperature is one of the key parameters that influence the sooting characteristics of a flame. Thus, the computed temperature profiles for 20% H_2 and i-H_2 addition are compared with the baseline case in Fig. 3.3a. The difference between the temperature profiles for H_2 and i-H_2 enriched flames essentially demonstrates the chemical effect. Therefore, in the rest of this chapter, the difference between real and inert addition is referred to as the 'chemical effect', while the difference between the baseline and inert addition is specified as the 'dilution effect'. Fig. 3.3a shows a small increment in the peak flame temperature for H_2 addition. Since H_2 participates in fuel oxidation chemistry, it is expected that the released heat results in an increased peak flame temperature. In contrast to H_2, the addition of i-H_2 tends to lower the temperature, through the dilution effect, as pointed out in several studies [136,139]. The effects of
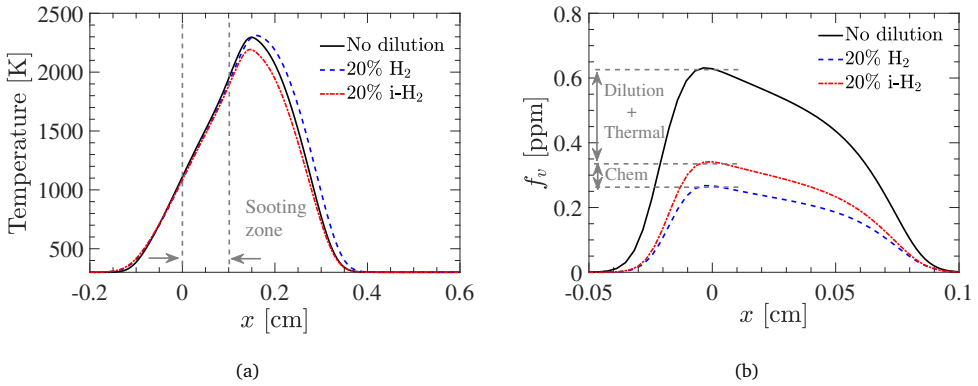
Figure 3.3: Comparison of computed profiles for flame temperature (a), and soot volume fraction (b) in the baseline (no dilution), 20% H$_2$, and 20% i-H$_2$ enriched SepH2 flames.

H$_2$ and i-H$_2$ addition on soot formation can be evaluated from the soot volume fraction distributions as shown in Fig. 3.3b. It is evident that both H$_2$ and i-H$_2$ suppress the soot formation, with H$_2$ being more effective in soot reduction compared to i-H$_2$. The dilution effect of i-H$_2$ plays a key role in soot reduction. However, a further reduction in soot volume fraction is observed due to the chemical effect of H$_2$. These results are qualitatively consistent with previous findings on the relative effectiveness of H$_2$ on soot inhibition compared to i-H$_2$ in various diffusion flame configurations [139, 142, 161].

Figure 3.4: Computed mole fraction profiles of important species for the baseline (no dilution), 20% H$_2$, and 20% i-H$_2$ enriched SepH2 flames. Note the difference in the x range for the top and bottom rows.

To acquire more insights into the underlying mechanism by which H_2 addition affects the soot formation, and to elucidate the important pathways leading to the PAH formation, the computed mole fraction profiles of important species are analyzed in Fig. 3.4. It is to be noted that except for PAH (A4), no significant changes were observed in the species profiles when the soot formation processes were not included (not shown here). From Fig. 3.4, it is clear that when soot processes are included, the addition of H_2 chemically increases the radical pool for species such as H, OH and O. Moreover, the chemical effects of H_2 addition enhance the concentration of acetylene (C_2H_2) and propargyl (C_3H_3), which have an important role in the formation of benzene (A1), and consequentially, pyrene (A4).

PAH formation pathways

To identify the important reactions and species contributing to PAH formation, a rate of production (ROP) analysis was conducted based on the spatially integrated production rates for subsequent species. The ROP analysis indicated that the formation of acetylene (C_2H_2) occurs primarily through the channel $C_2H_4 \rightarrow C_2H_3 \rightarrow C_2H_2$ following the reactions

$$C_2H_4 + H \rightleftharpoons C_2H_3 + H_2 \tag{R1}$$

$$C_2H_3 \, (+ M) \rightleftharpoons C_2H_2 + H \, (+ M). \tag{R2}$$
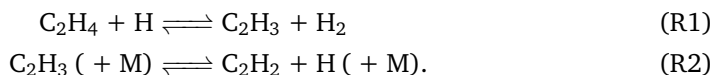
Because of chemical effects, the H radical concentration is increased prominently via reaction

$$OH + H_2 \rightleftharpoons H + H_2O. \tag{R3}$$

The increased H concentration in turn promotes the C_2H_2 production through reaction sequence (R1-R2). The rise in C_2H_2 due to chemical effects can however also be partially attributed to another pathway that reduces the consumption rate of C_2H_2 through reaction

$$C_2H_2 + O \rightleftharpoons H + HCCO, \tag{R4}$$
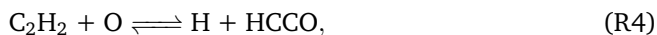
as a result of depleted O radicals within the soot zone [136]. The enhanced concentration of C_2H_2 promotes the formation of propargyl (C_3H_3) radicals by increasing the rates of the dominant C_3H_3 production reactions [106]

$$C_2H_2 + CH_2 \, (or\, CH_2{}^*) \rightleftharpoons C_3H_3 + H, \tag{R5}$$
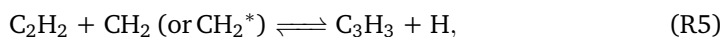
in which methylene (CH_2 and $CH_2{}^*$) species serve as important precursors for propargyl formation. Moreover, the addition of H_2 chemically reduces the consumption rates of CH_2 through

$$CH_2 + H \rightleftharpoons CH + H_2, \tag{R6}$$

and as a result, the propargyl C_3H_3 production is further enhanced. As mentioned before, C_3H_3 plays crucial roles in the formation of the first aromatic ring, benzene (A1), since it is formed primarily through the self-combination of propargyl radicals (C_3H_3) [168] as per the reaction

$$2\,C_3H_3 \rightleftharpoons A1. \tag{R7}$$

Besides R7, an another important pathway

$$2\,C_3H_3 \rightleftharpoons A1^- + H, \tag{R8}$$
$$A1^- + H \rightleftharpoons A1, \tag{R9}$$

exists in the KM2 mechanism which partly contributes to the A1 formation from C_3H_3. Through ROP analysis, it is observed that the latter route (R8-R9) to benzene formation via $A1^-$ becomes predominant compared to the direct route (R7), on the addition of H_2. Consequently, the increased propargyl (C_3H_3) concentration through chemical effects promotes the formation of A1 in SepH2 flames. Such an increment in benzene (A1) concentration due to chemical effects in hydrogen-enriched ethylene is consistent with some of the previous studies [136, 161].

However, it is important to point out that the analysis of chemical pathways is highly influenced by the adequacy of the gas-phase kinetics. For instance, in recent numerical studies by Wang et al. [142] in which the ABF mechanism was employed, the chemical effect of H_2 addition was shown to suppress the A1 production for the laminar

(a) KM2 mechanism
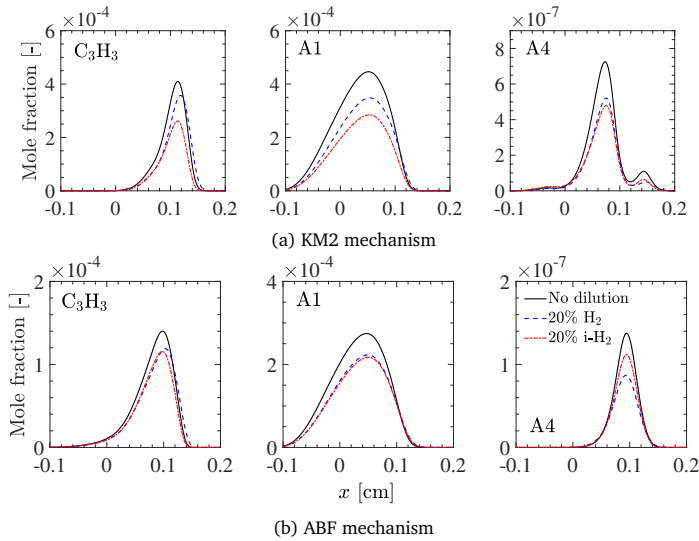
(b) ABF mechanism

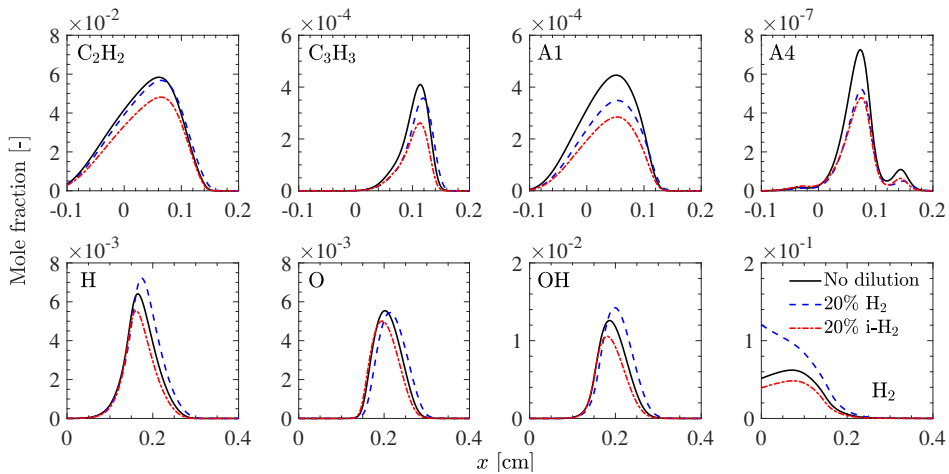Figure 3.5: Computed mole fraction profiles of important species for the baseline (no dilution), 20% H_2, and 20% i-H_2 enriched SepH2 flames with the KM2 (a), and ABF (b) mechanism.

co-flow $C_2H_4/(O_2\text{-}CO_2)$ flames. Therefore, it is imperative to investigate the influence of gas-phase chemistry on the chemical pathways leading to the formation of PAH. Concerning this, in Fig. 3.5, the mole fraction profiles of C_3H_3, A1, and A4 computed through the ABF mechanism are compared against the results obtained from the KM2 mechanism. As observed for the KM2 mechanism, the results obtained by the ABF mechanism also show a marginal increment in C_3H_3 and A1 concentrations under chemical effects, indicating that the kinetic pathways leading to the formation of A1 in SepH2 flames are similar. However, the comparison of A4 profiles reveals that the chemical effect tends to reduce the concentration of A4 in the ABF mechanism, whereas it is found to be increased for the KM2 mechanism. Besides, a significant difference can be observed in the magnitudes of A4 concentrations for the KM2 and ABF mechanisms. This is because other than the HACA sequence, the additional pathways of PAH formation involving odd-carbon number species such as C_9H_7, C_5H_5 are also included in the KM2 mechanism to overcome the issue of substantial under-prediction of A4 by the ABF mechanism [105].

The formation of large PAH such as A4 is mainly controlled by the temperature and the concentrations of species such as C_2H_2, H_2, H, and A1 through the HACA [14] reaction sequence for PAH growth. The chemical effect of H_2 is found to increase the A4 concentration (Fig. 3.4) in SepH2 flames. Hence, to understand the underlying kinetic pathways associated with PAH growth, an additional ROP analysis is carried out. The rate distributions of important elementary reactions responsible for the A4 formation process are presented in Fig. 3.6. The kinetic analysis suggests that the peak in the A4 concentration is mainly caused by the formation reaction:

$$A3^- + C_2H_2 \longrightarrow A4 + H, \tag{R10}$$

$$A3C_2H_2 \rightleftharpoons A4 + H. \tag{R11}$$
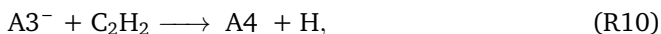
Because of the chemical effect of H_2, the concentration of acetylene (C_2H_2) is found to be increased in the H_2-enriched flame compared to the i-H_2-enriched flame (Fig. 3.4). The enhanced concentration of acetylene, thus, promotes PAH growth through reaction R10. Besides, increased rates of R11 further contribute to higher A4 concentration. On the other hand, the consumption of A4 is largely controlled by reactions of the type

$$A4 + H \rightleftharpoons A4^- + H_2. \tag{R12}$$

Figure 3.6 shows that the chemical effect of H_2 tends to increase A4 consumption by R12, in the second peak (near $x \simeq 0.15$ cm). However, within the region of maximum PAH growth (i.e. sooting zone), the contribution of the chemical effect in A4 consumption is found to be very small. As a result, the overall pyrene concentration is found to be increased by the chemical effects of H_2 addition.
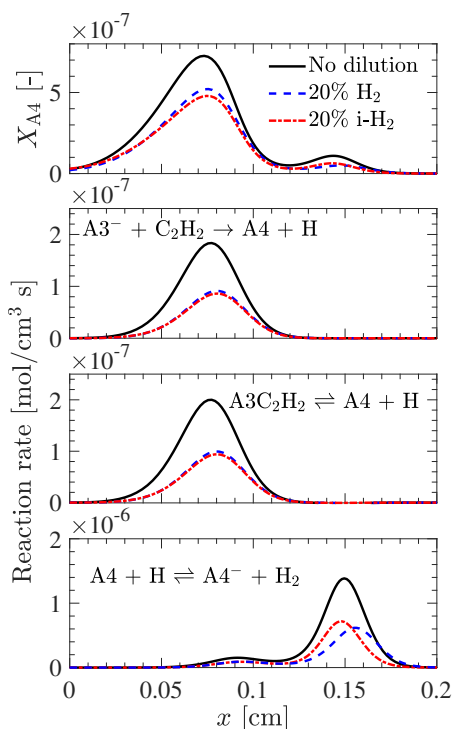
Figure 3.6: Computed distributions of A4 mole fraction, and key reactions associated with its production and consumption for the baseline (no dilution), 20% H_2, and 20% i-H_2 enriched SepH2 flames.

Soot formation rates

Next, the effects of H_2 addition on the rates of the key soot formation processes are investigated. Since soot nucleation is the bottleneck process in the overall soot formation, it is important to examine the chemical effect of H_2 on the soot nucleation rates. Based on the nucleation model used in the present study, PAH concentration and temperature are the main factors affecting the nucleation process. The nucleation rate is proportional to the square of the PAH concentration and the square root of the temperature. Figure 3.7a shows the distribution of nucleation rates in H_2 and i-H_2 enriched SepH2 flames. The increment in the nucleation rates due to chemical effects can be attributed to an enhanced concentration of A4 and a marginal increment in the temperature in the soot nucleating region ($x \simeq 0.05$–0.1 cm). The increased nucleation rates, also result in an increased soot number density as can be observed in Fig. 3.7b.

Although soot nucleation plays an important role in the overall soot formation process, it, however, contributes only marginally to the overall soot yield. For the given flame condition, the majority of soot mass is accumulated due to carbon addition through
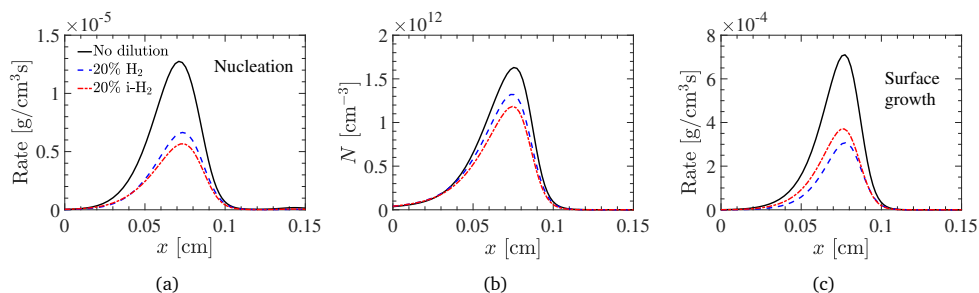
Figure 3.7: Computed profiles of soot nucleation rate (a), soot number density (b), and soot surface growth rate (c) for the baseline (no dilution), 20% H_2, and 20% i-H_2 enriched SepH2 flames.

the HACA sequence. In the HACA mechanism, key reactions in the soot surface growth process are:

$$C_{s,n}\text{-}H + H \rightleftharpoons C^*_{s,n} + H_2 \tag{R13.1}$$

$$C^*_{s,n} + C_2H_2 \longrightarrow C_{s,n+2}\text{-}H + H \tag{R13.2}$$
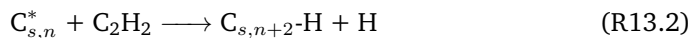
The former is the H-abstraction reaction to form the active site for acetylene addition, and the latter is the acetylene addition reaction. From Fig. 3.7c it can be observed that the surface growth rates are decreased by the chemical effect of H_2, which, consequently is reflected in the reduced soot volume fraction. However, it is also important to understand the major factors contributing to the observed decrement in the soot surface growth rates. Earlier studies [142] highlighted that the key parameters affecting the surface growth rate are temperature, the molar concentrations of H, H_2, and C_2H_2 along with the number density of soot particles generated primarily through the soot nucleation. Given a marginal impact on the temperature, and a significant increment in C_2H_2 concentration within the soot surface growth region, it can be argued that the temperature and C_2H_2 are not the major factors responsible for the reduction in soot surface growth under the chemical effects of H_2 addition.

As stated before, another factor that can affect the soot surface growth rate is the soot number density, originating primarily from soot nucleation. From Fig. 3.7 it can be seen that the enhanced nucleation rates by the chemical effect of H_2 translates into higher soot number density, which ideally tends to increase the soot surface area, and thus, the growth rates. This implies that the adverse contribution of soot number density in the overall reduced soot surface growth rate through the chemical effects remains insignificant. Therefore, it is reasonable to conclude that the reduction in soot surface growth rates by the chemical effects of H_2 addition, is predominantly because of the changes in the HACA reaction sequence. In particular, under hydrogen-rich conditions, the role of H-abstraction reaction becomes critical. This is because the increased H_2 concentration tends to promote the reverse reaction of the hydrogen abstraction step within the soot growth region, and contributes to the inhibition of
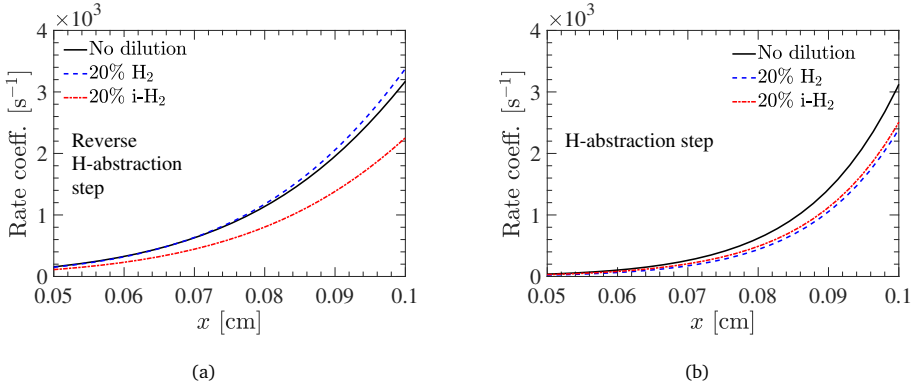
Figure 3.8: Computed profiles of the backward rate of H-abstraction reaction (R13.1) (a), and total rate of H-abstraction reaction (b) within the surface growth region for the baseline (no dilution), 20% H_2, and 20% i-H_2 enriched SepH2 flames.

surface growth. The increased rate of reverse reaction of the H-abstraction step under the chemical effects of H_2 addition is evident in Fig. 3.8a, which consequentially leads to the net reduction of the H-abstraction reaction rate as observed in Fig. 3.8b.

The lowered surface growth rates through chemical effects are consistent with the findings in previous studies [136, 142, 161], although the soot nucleation rates were found to be decreased by the chemical effects in them. It is to note that the lowered surface growth rate due to the chemical effect of H_2 was attributed to the lower concentration of H within the surface growth region, causing reduced forward rates of R13.1 in [136]. However, in the present study, the chemical effect of H_2 showed almost no influence on H concentration. This essentially indicates that the overall suppression of soot growth is primarily governed by an increased concentration of H_2, which leads to the inhibition of the H-abstraction reaction.

As pointed out by Guo et al. [136], the reduced soot surface growth is also a consequence of the production of less active radical sites. This is because, based on the HACA surface growth model [14], the soot surface growth rate depends on the number density of surface sites χ_s^*. The number of active sites for C_2H_2 addition is related to the concentrations of OH, H_2O, H in a complex way through a steady-state relation, k_{ss}, that represents the portion of saturated sites that have been dehydrogenated [94]. In Fig. 3.9a, the distribution of the surface-site number density for acetylene addition (χ_s^*) within the surface growth region is shown. It can be observed that the number density of surface sites in the H_2-the enriched flame is significantly lower than that in the i-H_2-enriched flame. Another key parameter related to the surface growth process is the surface density of soot particles (A_s), which depends on the surface area of soot particles and the number density. The effect of number density on surface growth rates basically occurs through A_s. Therefore, in Fig. 3.9b the distribution of the number of surface-site per unit volume is presented. It can be observed that the number of
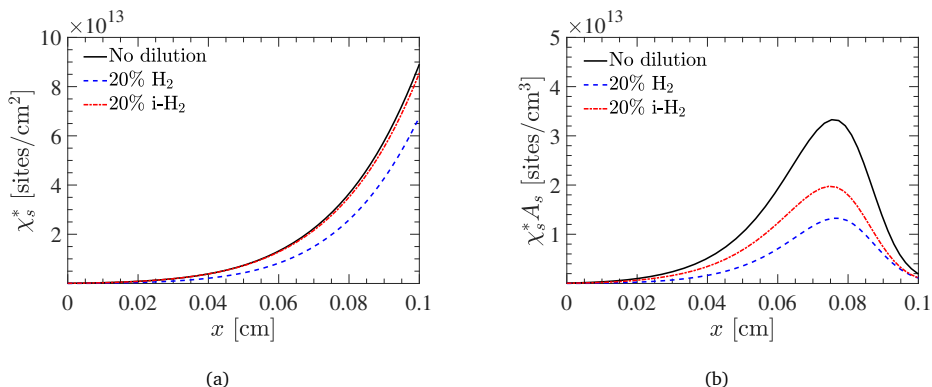
Figure 3.9: Computed profiles of surface-site density (χ_s^*) (a), and surface-sites per unit volume ($\chi_s^* A_s$) (b) within the surface growth region for the baseline (no dilution), 20% H_2, and 20% i-H_2 enriched SepH2 flames.

active sites available for surface reaction per unit volume is lower in the H_2-enriched flame, compared to the i-H_2 flame. Therefore, the lower surface-site number density as a consequence of the chemical effect of H_2 further contributes to the reduction in soot surface growth.

In contrast to earlier reported studies [136, 142, 161], the soot nucleation rate and PAH concentration are found to be enhanced by the chemical effect of H_2. Thus, the present observations indicate that the chemically inhibiting effect of hydrogen addition on soot formation suppression is mainly through the reduced soot surface growth rate as a result of the higher concentration of molecular hydrogen and a decreased number of active surface sites in the soot growth region.

3.3.2 Effects of water vapour addition to the oxidizer

In this section, we investigate the chemical effects of adding H_2O to the oxidizer stream on soot formation (SepH2O flames). The computed profiles of flame temperature and soot volume fraction for H_2O and i-H_2O diluted flames are compared in Fig. 3.10. The marginal increment in the temperature by chemical effects can be attributed to the enhanced conversion of CO to CO_2 due to H_2O addition [131]. It can also be observed that soot formation is significantly suppressed by the addition of H_2O to the oxidizer. However, although the chemical effect of H_2O tends to suppress the soot formation further, its contribution is very small compared to the dilution effect. The results, thus, indicate that water vapour influences the flame temperature and soot formation predominantly through dilution effects.

To elucidate the mechanism behind the chemical suppression of soot by H_2O addition, the mole fraction profiles of important species involved in the soot formation process are plotted in Fig. 3.11. It can be observed that the chemical effect of H_2O tends to

(a)

(b)

Figure 3.10: Comparison of computed profiles for flame temperature (a), and soot volume fraction (b) in the baseline (no dilution), 20% H_2O, and 20% i-H_2O diluted SepH2O flames.

increase OH concentration. This enhancement occurs mainly through reactions

$$O_2 + H \rightleftharpoons OH + O, \tag{R14}$$

$$H_2O + O \rightleftharpoons 2\,OH. \tag{R15}$$

In the process, the O and H radicals get consumed and their concentrations decrease. The chemical effect of H_2O appears to marginally enhance the concentrations of acetylene (C_2H_2), due to a decreased consumption rate of C_2H_2 through reaction R4, as a consequence of the depletion of O radicals. The increased C_2H_2 concentration tends
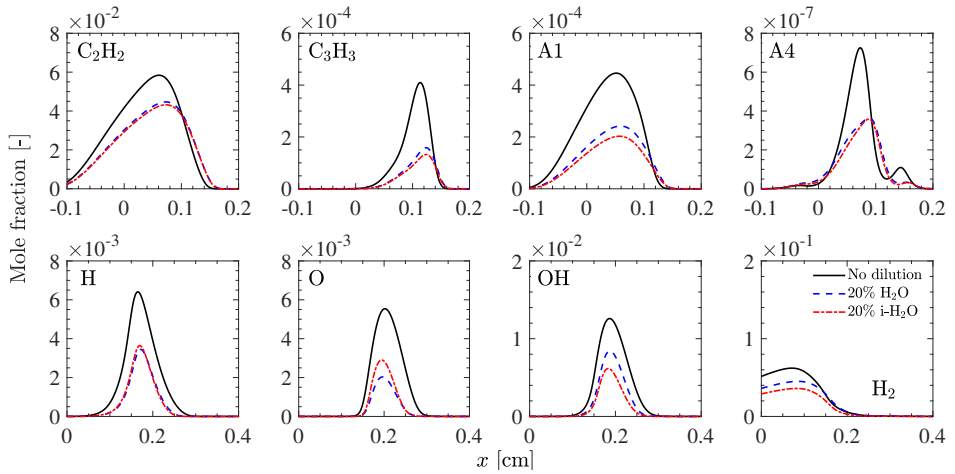
Figure 3.11: Computed mole fraction profiles of important species for the baseline (no dilution), 20% H_2O, and 20% i-H_2O diluted SepH2O flames. Note the difference in the x range for the top and bottom rows.

to promote propargyl formation through reaction R5. The self-combination of propargyl (C_3H_3) via R7 is thus enhanced by the chemical effects, which results in the increased concentration of benzene (A1). The higher amount of A1, in turn, influences the overall PAH growth pathways and causes an increment in the A4 concentration. It is interesting to note that the A4 concentration is only marginally increased, although the chemical effects of H_2O considerably enhance A1 production. Therefore, the increased concentration of A4 needs to be addressed further to understand the underlying chemical pathways. The ROP analysis shows that through chemical effects, the production rate of A4 via reactions R10-R11 is marginally decreased. However, because of the higher H_2O concentration, another pathway contributes to the production of A4 within the PAH growth region through

$$A4^- + H_2O \rightleftharpoons A4 + OH. \qquad \text{(R16)}$$
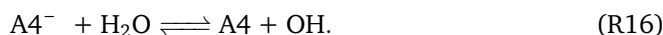
The relative changes in these two reaction pathways tend to cancel each other causing only a marginal variation in the peak mole fraction of pyrene.

To investigate the role of chemical effects on important source terms associated with soot formation, the distributions of soot nucleation rates, surface growth rates, and soot number density are presented in Fig. 3.12. The results indicate that the chemical role of H_2O only minimally affects the peak soot nucleation rate. The small increment (observed in the soot nucleation rates) can be attributed to the negligible change in temperature within the soot nucleating region and the marginal enhancement in pyrene concentration through the chemical effect of H_2O. Since the nucleation process governs the number density distribution, a similar trend is reflected in the number density profiles. However, although the chemical effects weakly increase the soot nucleation rates, the surface growth rates are noticeably reduced, as evident from Fig. 3.12c. The reduced soot surface growth rate is essentially responsible for the lower soot volume fraction under the chemical effect of H_2O in SepH$_2$O flames.

The mechanism behind the inhibition of soot surface growth is found to be similar to that observed for H_2 addition cases. The chemical effect of H_2O increases the H_2

Figure 3.12: Computed profiles of soot nucleation rates (a), soot number density (b), and soot surface growth rates (c) for the baseline (no dilution), 20% H$_2$O, and 20% i-H$_2$O diluted SepH2O flames.

concentration, which enhances the reverse H-abstraction reaction in the HACA pathways and tends to mitigate surface growth. Besides the increased H_2 concentration, a reduction in H concentration due to chemical effects suppresses the forward rate of the H-abstraction reaction and also contributes to the overall reduction in soot surface growth. However, the impact of the chemical effect of H_2O on temperature and concentrations of species like H_2, H, and C_2H_2 is relatively small. Therefore the overall role of chemical effects in soot reduction remains secondary compared to the soot inhibition through dilution effects.

3.3.3 Effects of simultaneous addition of H_2 to the fuel and H_2O to the oxidizer

Chemical effects of simultaneous addition

The chemical effects of the simultaneous addition of H_2 to the fuel and H_2O to the oxidizer (SimH2H2O flames) are discussed in this section. The temperature and soot volume fraction profiles for the baseline flame and SimH2H2O flames with an addition level of 20% are shown in Fig. 3.13. Similar to the earlier observations for the SepH2 and SepH2O cases, the SimH2H2O flames also show an increment in temperature and a reduction in soot volume fraction distribution by chemical effects, as expected.

The mole fraction profiles of several important species are plotted in Fig. 3.14 to evaluate the chemical effects of simultaneous H_2 and H_2O addition on their formation pathways. In the case of simultaneous addition, the characteristics of the radical pool are found to be influenced by the combined aspects of individual chemical effects. For example, the O concentration is reduced in the SimH2H2O case by the chemical effects through reaction R15 as observed in SepH2O flames. On the other hand, the
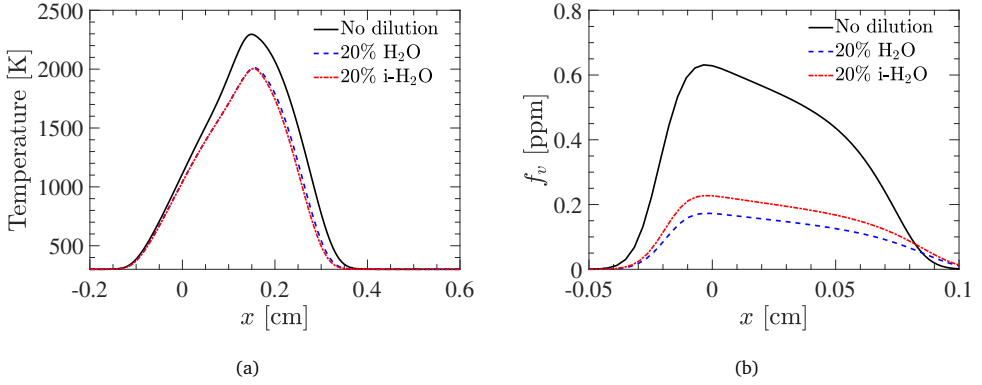

(a) (b)
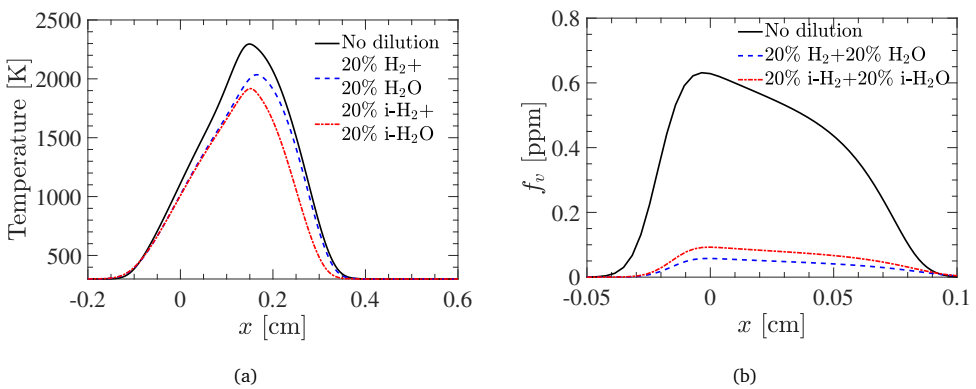
Figure 3.13: Comparison of computed profiles for flame temperature (a), and soot volume fraction (b) in the baseline (no dilution), 20% H_2 + 20% H_2O, and 20% i-H_2 + 20% i-H_2O diluted SimH2H2O flames.
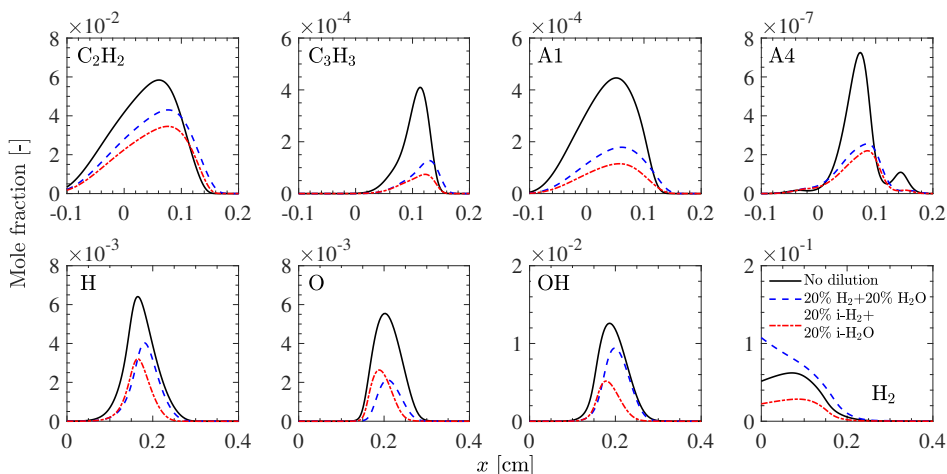
Figure 3.14: Computed mole fraction profiles of key species for the baseline (no dilution), 20% H_2 + 20% H_2O, and 20% i-H_2 + 20% i-H_2O diluted SimH2H2O flames. Note the difference in the x range for the top and bottom rows.

H concentration is found to be increased following the dominant formation reaction R3 through a combined effect of OH and H_2 increments, same as noticed in SepH2 case. Therefore, the chemical effects of simultaneous addition tend to increase C_2H_2 concentration through reaction channel R1-R2 as a consequence of an increased H concentration; and via reaction R4, because of the reduction in O concentration. The rise in C_2H_2 concentration through chemical effects promotes the production of C_3H_3 through reaction R5. The increased C_3H_3 concentration subsequently causes an increment in benzene (A1) and A1$^-$ species through formation channels R7, R8-R9. Following similar pathways of PAH formation as discussed for SepH2 and SepH2O flames, the higher concentration of A1 leads to an increment of the A4 mole fractions through the chemical effects.
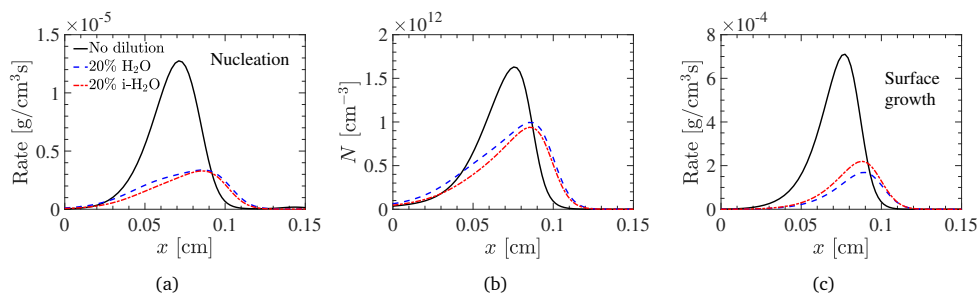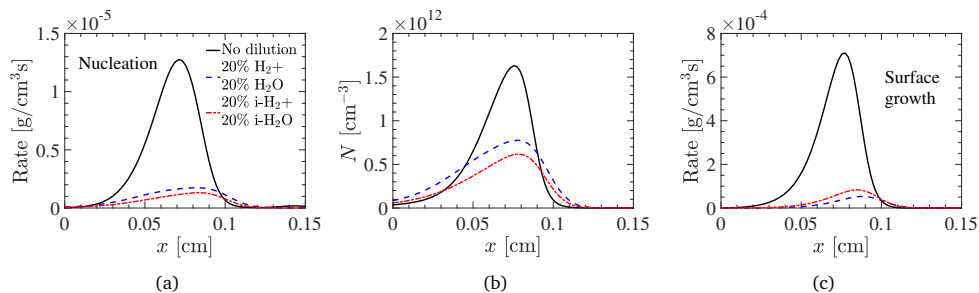

Figure 3.15: Computed profiles of soot nucleation rates (a), soot number density (b), and soot surface growth rates (c) for the baseline (no dilution), 20% H_2 + 20% H_2O, and 20% i-H_2 + 20% i-H_2O diluted SimH2H2O flames.

The rate distributions of the nucleation and surface growth processes accounting for the soot formation are presented in Fig. 3.15. It can be observed that the increment in A4 through chemical effects translates into the increased soot nucleation rate, which leads to a higher number density. However, chemical effects tend to decrease the soot surface growth rate. Therefore, analogous to the SepH2 and SepH2O cases, the soot formation in the SimH2H2O case is also found to be suppressed by the chemical effects as a consequence of the reduced surface growth rates.

Synergistic effect on soot suppression

One of the main purposes of this study is to investigate the potential synergistic interactions of H_2 and H_2O in soot formation suppression. In this regard, the effects of separate and simultaneous H_2, H_2O addition on the normalized peak soot volume fraction are compared in Fig. 3.16. Table 3.1 summarizes the quantitative reduction in the peak soot volume fraction (f_v) for the studied flames with different dilution levels. The effect of the H_2O dilution on inhibiting soot formation is found to be more pronounced than that of H_2 addition. However, the simultaneous addition of H_2 and H_2O leads to significant suppression of soot formation, compared to their separate addition. For instance, compared to the baseline (non-diluted) flame, SimH2H2O flames show about 62.8% and 90.9% decrement in peak soot volume fraction for 10% and 20% dilution levels, respectively.

Considering the contributions of reduction percentages for SepH2 and SepH2O flames with 20% addition level, the simultaneous addition of H_2 and H_2O is expected to reduce the maximum f_v by approximately 88.4%. This quantity is based on the first 57.6% reduction in peak f_v value due to the separate H_2 addition, and an additional 72.6% reduction of the resulting peak f_v because of the separate H_2O addition. However, the actual reduction in the maximum f_v observed in SimH2H2O flames is 90.9%,
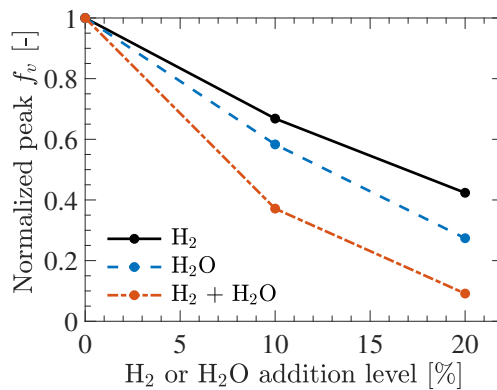
Figure 3.16: Comparison of normalized peak soot volume fraction for separate and simultaneous addition of H_2 to the fuel, and H_2O to the oxidizer. Peak f_v is normalized with the baseline (no dilution) case.

Table 3.1: Percentage of reduction in the maximum f_v for simulated flames.

Addition	Reduction in peak f_v (%)		
(% vol.)	SepH2	SepH2O	SimH2H2O
10	33.2	41.7	62.8
20	57.6	72.6	90.9

which signifies that there exist weak synergistic effects between H_2 and H_2O addition in the soot suppression. Similarly, for the 10% addition level, the actual reduction in peak f_v observed for SimH2H2O flames is found to be equal to 62.8% compared to an expected 61.1%, showing approximately 1.7% additional reduction. This indicates that the synergistic effects of simultaneous H_2 and H_2O addition on soot suppression, tend to be stronger with an increase in the dilution level. However, the analysis remains of speculative nature at this point considering the very low amount of synergistic decrement observed in the computed results.

3.3.4 Evolution of soot particle size distribution

The effect of H_2 and H_2O addition on the dynamics of soot particle size can be illustrated through the evolution of particle size distribution functions (PSDFs). The qualitative features of PSDF are strongly influenced by local flame conditions (such as temperature, PAH concentration) [42,169]. The PSDFs in sooting flames show a characteristic bimodal behavior. The first mode consists of a power-law type distribution reflecting the small-sized, recently nucleated particles. Whereas, the second mode is of log-normal type, representing the larger particles that are grown by coagulation and surface growth [170,171]. The region between the two modes is referred to as a trough, whose shape is influenced by the nucleation and surface growth processes. The transition of PSDF from unimodal to bimodal distribution is primarily governed by the competition between particle nucleation and coagulation [169].

Figure 3.17 presents the PSDF for the baseline and H_2/H_2O diluted flames taken at the different spatial positions. The profiles of soot volume fraction and average particle size are also presented in Fig. 3.18 as a reference to the PSDF locations. Moving from oxidizer to fuel side ($x = 0.1$ cm to $x \simeq 0$ cm), the transition of PSDF from unimodal to bimodal distribution can be observed, as nucleated particles grow while flowing towards the flame stagnation location. The unimodality of distribution for the baseline case, at $x = 0.1$ cm, occurs at a temperature of approximately 1900 K (> 1850 K), in accordance with the findings from Zhao et al. [169]. In general, the evolution of PSDF into a bimodal shape occurs, since small particles collide and coalesce forming larger particles during the coagulation process. As a result, the size of particles increases (see Fig. 3.18) while their number density decreases, causing a trough in the PSDF, which shifts towards the lower particle sizes during this transition.

From the PSD at peak f_v position, it is observed that with the addition of H_2/H_2O, the trough of the bimodal PSDF shifts towards the higher number density and becomes shallower. It indicates the increased number of smaller-sized particles in the system. The reduction in the depth of the trough is more intense for H_2O dilution when compared to H_2. This behavior of PSDF can be attributed to the reduced surface growth rates, coagulation rates, and partially to the reduced nucleation rates as a consequence of H_2/H_2O addition. The decreased nucleation rates resulting from the suppressed PAH formation, lead to a lower number density of nascent particles. Looking at the PSDF at $x = 0.05$ cm, where the nucleation process is more prominent, the number density of the power-law mode is marginally lower for H_2/H_2O diluted flames. However, the distinct change in the shape of the PSDF during its evolution towards the f_v^{max} location can be explained through the abated surface growth rates for H_2/H_2O diluted flames. This is because, in the present model, the surface growth through C_2H_2 addition is the major process responsible for soot mass increment. Singh et al. [171] also observed that an increase in the surface reaction rates tends to increase the trough depth and shift the PSDF towards larger particles, while
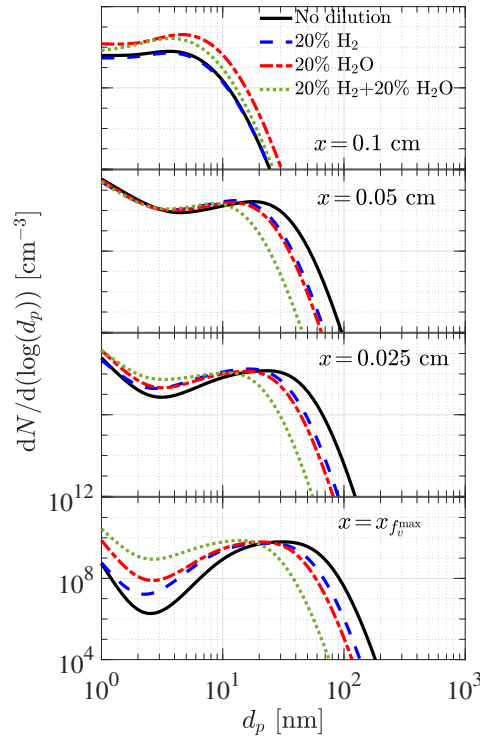
Figure 3.17: Comparison of computed profiles for the particle size distribution function (PSDF) taken at $x = 0.1$ cm, 0.05 cm, 0.025 cm and location of maximum soot volume fraction ($x_{f_v^{max}}$) for separate and simultaneous addition of 20% H_2 and 20% H_2O.
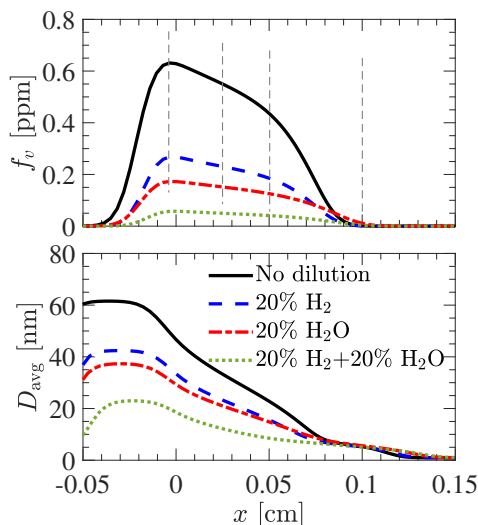
Figure 3.18: Comparison of computed profiles for soot volume fraction (top panel) and average particle size (bottom panel) or separate and simultaneous addition of 20% H_2 and 20% H_2O. Dashed vertical lines indicate the positions of PSDF.

a decline in surface reaction rates does the opposite. Apparently, the reduction in the surface reaction rates decreases the number of bigger-sized particles in the system. This essentially brings down the collision rates of particles and influences the particle dynamics processes such as coagulation. The decreased coagulation rates cause the number density within the trough region to rise and shift the trough upwards while broadening it. The trends of the shift in PSDF shape are analogous to the tendency observed in other soot quantities for H_2/H_2O dilution cases (e.g. soot volume fraction, average particle size), such that the levels of systematic deviation from baseline case become stronger following: SepH2 < SepH2O < SimH2H2O.

The PSDF profiles at $f_v^{\max}$ position also show that the size of the 'largest' detected particles (at the right-end of the log-normal mode) decrease significantly on the addition of H_2 and/or H_2O. Such a change in the PSDF can be connected to the reduction in soot surface growth rates caused by the H_2/H_2O dilution. The reduced surface growth decreases the overall size of soot particles and tends to shift the PSDF toward lower particle size. Besides surface growth, the diminished PAH concentration may also contribute to the shift of the 'largest' detected particles towards lower diameters as reported by Yapp et al. [42]. The modeling results in the present study showed a synergistic reduction (although very weak) in soot formation for SimH2H2O flames compared to SepH2 or SepH2O flames. Therefore, for simultaneous addition, the degree of shift in the PSDF towards the lower particle size is found to be distinctively greater compared to the shift observed for the separate H_2 or H_2O addition. It is also interesting to note that H_2O addition, also leads to the widening of the sooting

zone towards the main reaction layer (see Fig. 3.18), which is reflected in the relatively higher number density and size of the 'largest' particle in the PSDF taken at $x = 0.1$ cm for SepH$_2$O and SimH$_2$H$_2$O cases.

Furthermore, the evolution of the PSDF for H$_2$ and H$_2$O addition cases reveals that the peak in the log-normal mode (also referred to as the 'coagulation peak' [42]), indicative of the average soot particle size, shifts towards the lower particle sizes. During this evolution, the 'coagulation peak' also moves towards higher number densities. This systematic shift can be associated with decreased coagulation rates as a consequence of H$_2$/H$_2$O addition. A close analysis of the sectional source terms revealed a drop in coagulation rates (not shown here). The decreased number of collision events reduces coagulation rates, which leads to a decrease in the average particle diameter. Moving from the oxidizer side towards the peak f_v location, this shift appears more distinct, which eventually reflects into a drastic reduction in average particle size on H$_2$/H$_2$O addition as observed in Fig. 3.18.

Another notable observation concerning the PSDF is that the number density of small-sized particles in the power-law regime rises with H$_2$ and H$_2$O addition. This indicates that on the addition of H$_2$ and H$_2$O, the growth of nucleated particles through coagulation and surface growth processes is suppressed, and many small-sized particles get accumulated in the flame. Such an observation is consistent with the recent experiments by Choi et al. [140], wherein the addition of hydrogen to the fuel stream was found to decrease the size of soot microstructures in ethylene-air diffusion flames. Besides, the upward shift in the 'inception peak' (left end of PSDF) is found to be more intense for H$_2$O addition and almost negligible for H$_2$ addition. Therefore, it may well be argued that the addition of H$_2$ and H$_2$O mainly affects the PSDF, by increasing the number density of smaller-sized particles while limiting the growth of larger-sized particles. Moreover, the simultaneous addition shows a stronger influence on the overall PSDF compared to their separate addition. The qualitative effects of H$_2$/H$_2$O addition on the evolution of PSDF are summarized in Fig. 3.19.

However, the analysis of PSDF remains conditional to the model limitations. This is because, the process of soot aggregation is not considered in the present model, which can influence the number density, and size of soot particles, especially at higher pressures. In general, the size of the primary particles in soot agglomerates typically varies in the range of 25–40 nm [172], which approximately equals the diameter of the 'coagulation peak' in the simulated flames. Thus, in the present model, larger particles can be interpreted as having an equivalent volume of aggregates [94]. Besides, to accurately model the agglomeration process, additional transport equations for the number density of agglomerates are required to be solved, which can significantly increase the overall computational cost. Therefore, considering the scope of the current study on atmospheric flames, the neglecting agglomeration process is expected to be a suitable assumption.
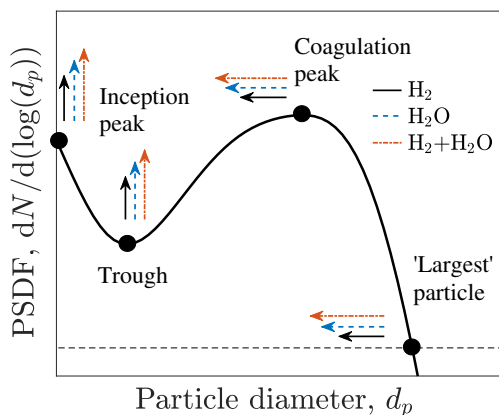
Figure 3.19: Summary of the key effects of H_2/H_2O addition on a bimodal PSDF. Nomenclature of the characteristics points is taken from Yapp et al. [42].

3.4   Summary

This chapter addresses the role of chemical effects in separate, and simultaneous addition of H_2 to ethylene and H_2O to oxidizer on the soot formation in counterflow diffusion flames through numerical simulations with a sectional soot model. The major conclusions of this study are summarized as follows:

Numerical results reveal that the addition of hydrogen to ethylene decreases the soot concentration through chemical effects along with the dilution effect. The mole fractions of pyrene are marginally increased through chemical effects, which leads to an increased soot nucleation rate, and therefore, soot number density. On the other hand, the chemical effects of H_2 tend to suppress the H-abstraction reaction in the HACA mechanism as a consequence of increased molecular hydrogen concentration. Also, the active surface-site number density decreases by chemical effects, causing a reduction in the soot surface growth rate. The lowered soot surface growth rate, eventually, decreases the soot concentration.

Similar to hydrogen enrichment, the addition of H_2O in the oxidizer chemically suppresses soot formation. For the addition of H_2O, the role of chemical effects in the reduction of soot formation is very small compared to the dilution effect. Although the soot nucleation rates show a minimal increment due to chemical effects, it is observed that the overall chemical suppression of soot volume fraction is caused predominantly by a reduction of soot surface growth rates. Simultaneous addition of H_2 and H_2O decreases the soot volume fractions significantly compared to their separate addition for an identical dilution level, and quantitatively, there exist weak synergistic effects between H_2 and H_2O addition. Changes in rates of surface growth and coagulation processes as a consequence of H_2 and H_2O addition, influence the shape of bimodal PSDF, with the effect of the latter being stronger. This primarily leads to the shifting of

a trough to higher number densities and coagulation peak towards lower diameters. Therefore, with the addition of H_2 and H_2O, the number density of small-sized particles increases, while the growth of larger-sized particles decreases, which eventually causes a reduction in the average soot particle size.

The chemical pathways leading to the formation of PAH are considerably influenced by the chemical mechanism, which is mainly reflected in the soot nucleation source term. For the KM2 mechanism employed in the present study, PAH concentration and nucleation rates are observed to be increased contrary to the ABF mechanism used in previous studies. However, in both mechanisms, the soot surface growth is always suppressed through chemical effects and consequently results in a lowered soot volume fraction. Hence, we conclude that the chemically inhibiting effect of fuel-side hydrogen addition and oxidizer-side water vapour dilution is primarily through the reduced soot surface growth, while the contribution of soot nucleation to the overall soot suppression is secondary.

4

Effects of flame curvature on soot formation

In this chapter, a detailed study is conducted to understand the effects of flame curvature on soot formation in laminar non-premixed flames. The analysis of curvature effects on soot formation is carried out for steady soot formation (SF) type counterflow flames. The dynamic response of soot formation to the unsteady curvature is investigated by imposing harmonic oscillations to the curvature. The variability of soot formation response under fluctuating strain rate and curvature is examined. This chapter is partly based on the article 'Effects of curvature on soot formation in steady and unsteady counterflow diffusion flames' published in Combustion and Flame [173].

4.1   Introduction

Many practical combustion systems employ non-premixed flames, which generally exhibit a higher sooting tendency compared to premixed flames [174]. Most of these combustion systems operate under conditions characterized by complex unsteady hydro-thermo-chemical interactions. Therefore, understanding the soot formation process in non-premixed flame fronts under a varied range of conditions encountered in such devices is pivotal, especially, for the development of reliable soot modeling approaches.

In turbulent environments, the soot formation is highly influenced by the unsteady hydrodynamics that introduces spatio-temporally fluctuating stretch and curvature to the flames. On the other hand, in laminar non-premixed flames, where the flame dynamics is not turbulence-induced, curvature effects are also identified [175]. Since flame curvature primarily affects the local flame surface area, it strongly impacts the diffusion transport of different chemical species, and therefore, modifies the overall flame structure. Accordingly, in curved non-premixed flames, the flux of species mass is enhanced towards or away from the fuel-rich or lean zones based on the type of curvature (convex/concave) and diffusivity of the chemical species. Since the soot

formation process is particularly sensitive to local mixture composition and differential diffusion effects, the non-uniformities of the thermochemical variables introduced by flame curvature strongly influence the distribution of soot [175, 176].

There have been notable studies [41,98,176,177] recognizing the effects of flame curvature on soot formation in non-premixed flames. In the context of turbulent flames, previous numerical works [41, 176] established that the curvature induces a relative movement of the main oxidation zone and the soot formation region, which impacts the convection of the soot particles. It was noticed by Lignell et al. [176] that negative flame curvature (for which the center of curvature lies on the fuel side) tends to shift the flame toward the fuel side, which leads to increased temperatures in the fuel-rich soot growth regions and promotes soot formation. Positively curved flames, on the other hand, show the opposite behavior leading to a diminished soot concentration. Franzelli et al. [177] investigated the correlation between soot formation rates and the response of soot precursors to curvature in laminar unsteady diffusion flames. Their numerical study demonstrated that a negatively curved flame front manifests an increased convective motion of gas and soot toward the fuel-rich zone. This enhances the transport of heat from the flame towards the preheat region and leads to increased concentrations of PAHs, and consequently, the overall soot production, while the opposite holds for positive curvature. However, specific soot sub-processes were not analyzed concerning curvature effects. Recently, Hoerlle [98] compared the effect of flame curvature on soot formation in steady laminar counterflow diffusion flames to characterize its influence on flamelet-based models. Although the physical mechanism for the observed steady-state soot response was not explicitly addressed, the increased soot concentration by negative curvature was evident in oxyfuel flames.

In summary, the previous studies show a consensus about the enhancement of soot formation under negative curvature for laminar and turbulent non-premixed flames. However, although various mechanisms have been postulated, the origin of soot response to flame curvature is not well understood. In this context, a comprehensive examination of soot sub-processes with state-of-the-art detailed kinetics and a sectional method-based soot model is useful to encapsulate the mechanism of soot formation and evolution of their size distributions in curved non-premixed flames. Moreover, the impact of curvature unsteadiness on soot production has not been sufficiently addressed. In particular, it would be interesting to characterize the dynamic response of sooting flames subjected to unsteady curvature fluctuations and identify the underlying physical phenomena which control it.

Nevertheless, from a numerical perspective, analyzing unsteady curvature effects on soot formation directly in multi-dimensional flames is very challenging owing to the co-existence of different physical processes impacting chemistry and local flow properties. Therefore, alternatively, the academic configuration of a counterflow diffusion flame is attractive to acquire fundamental insight into the physics and kinetics occurring in non-premixed flame fronts under the influence of curvature [98]. Furthermore, by employing a counterflow configuration, the dynamic response of soot to the

unsteady curvature could be exemplified by systematically exposing laminar flames to harmonically varying curvature over a range of frequencies and amplitudes. Although the fundamental studies on canonical configurations do not reproduce the complexities encountered in fully turbulent simulations, they do provide crucial information to recognize the effects of unsteady curvature fluctuations on the soot formation process and guide the modeling efforts. For instance, the importance of including curvature effects in flamelet-based modeling has been recognized in the literature [98,175,178]. In this context, the analysis of curvature unsteadiness on soot formation would provide important insights into the development of flamelet-based models for application to multi-dimensional non-premixed sooting flame simulations.

Furthermore, in practical burners, flames are subjected to both varying curvatures and strain rates. As a result, the soot formation process is strongly influenced by the changes in the strain rate. The effects of strain rate on the soot and PAH formation in non-premixed flames have been addressed in several experimental [179–181] and numerical works [113,121,182,183]. In general, previous studies showed that an increase in strain rate leads to a reduction in soot formation. Such an effect is attributed mainly to the lowered concentration of soot precursors leading to reduced soot inception rates, and reduced residence time for soot surface reactions and particle-particle interactions. Moreover, strain rate fluctuations significantly affect the local flow time scales [43, 183]. Therefore, to envisage a more complex scenario of flow-flame-soot interaction, it would be interesting to investigate the combined effects of strain and curvature on soot characteristics and the sensitivity of soot formation in curved flames exposed to varying strain rates.

In view of the above considerations, the main objectives of the present study are:

- To conduct a detailed analysis of different soot sub-processes and provide enhanced insight into the mechanism governing soot response in a laminar counterflow diffusion flame under the influence of flame curvature.

- To examine the sensitivity of soot formation in curved flames to strain rate and evaluate the existence of synergistic effects.

- To systematically characterize the unsteady dynamics of soot formation in a counterflow diffusion flame subjected to curvature oscillations and identify the underlying mechanism.

- To investigate the competing effects of simultaneously imposed curvature and strain rate fluctuations on the dynamic response of soot.

To the authors' knowledge, this is the first study that investigates the dynamic response of soot in counterflow diffusion flames under unsteady curvatures. Hence, the findings of the current study provide a fundamental understanding of the curvature effects on soot formation which would be relevant to soot modeling in multi-dimensional flame simulations.

4.2 Numerical methodology

4.2.1 Governing equations

Following the quasi-1-D formulation of the counterflow configuration described in Section 2.3.1, a system of governing equations for curved flamelets can be deduced along flame normal coordinate x:

$$\frac{\partial \rho}{\partial t} + \frac{1}{\varsigma}\frac{\partial}{\partial x}(\varsigma \rho u) = -\rho K \tag{4.1}$$

$$\frac{\partial (\rho Y_k)}{\partial t} + \frac{1}{\varsigma}\frac{\partial}{\partial x}(\varsigma \rho u Y_k) = -\frac{1}{\varsigma}\frac{\partial}{\partial x}(\varsigma \rho Y_k V_k) - \rho K Y_k + \dot{\omega}_k, \quad \forall\, k \in [1, N_s{-}1] \tag{4.2}$$

$$\frac{\partial (\rho h)}{\partial t} + \frac{1}{\varsigma}\frac{\partial}{\partial x}(\varsigma \rho u h) = -\frac{1}{\varsigma}\frac{\partial}{\partial x}\varsigma\left(-\frac{\lambda}{c_p}\frac{\partial h}{\partial x} + \sum_{k=1}^{N_s}\rho h_k Y_k V_k\right) - \rho K h \tag{4.3}$$

$$\frac{\partial (\rho K)}{\partial t} + \frac{1}{\varsigma}\frac{\partial}{\partial x}(\varsigma \rho u K) = \frac{1}{\varsigma}\frac{\partial}{\partial x}\varsigma\left(\mu\frac{\partial K}{\partial x}\right) - \rho K^2 + J \tag{4.4}$$

$$\frac{\partial (\rho Y_{s,i})}{\partial t} + \frac{1}{\varsigma}\frac{\partial}{\partial x}(\varsigma \rho [u + V_T] Y_{s,i}) = \frac{1}{\varsigma}\frac{\partial}{\partial x}\varsigma\left(\rho D_{s,i}\frac{\partial Y_{s,i}}{\partial x}\right) - \rho K Y_{s,i} + \dot{\omega}_{s,i}, \tag{4.5}$$

$$\forall\, i \in [1, N_{sec}]$$

where $\dot{\omega}_{s,i} = \rho_s \dot{Q}_{s,i}$ is the rate of the total soot mass growth in section i, and ς indicates the measure for the flame surface through which the mass transport takes place. The surface area function ς is related to the curvature of flame κ as:

$$\kappa = -\frac{1}{\varsigma}\frac{\partial \varsigma}{\partial x} \implies \varsigma = \exp\left(-\kappa x\right) \qquad \text{for } \kappa \text{ independent of } x \tag{4.6}$$

To obtain the pressure term J in Eq. 4.4, a potential flow approximation is considered in the far-field, which yields $J = \rho_o a^2$ with ρ_o the density of the oxidizer, and a the applied strain rate. The details regarding the derivation and assumptions of the above governing equations can also be found in Refs. [184–186].
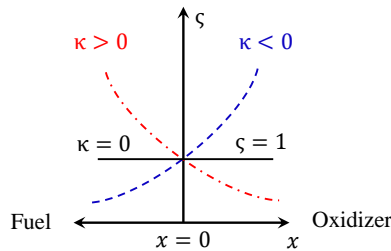
Figure 4.1: Schematic representation of sign convention followed for the flame curvature.

To remove the translational degree of freedom, the stagnation plane (where $u=0$) is specified at $x=0$. In the present formulation, negative curvature ($\kappa<0$) indicates that the center of curvature lies on the fuel side ($x \to -\infty$ here), and the converse is true for positive curvature ($\kappa>0$). It implies, ς increases moving from fuel to oxidizer side along the flame coordinate x for negatively curved flames, while the opposite occurs for positively curved flames. A schematic diagram of the sign convention for the flame curvature followed in the present study is presented in Fig. 4.1.

4.2.2 Target flames

To demonstrate the effects of curvature on the sooting characteristics, the counterflow diffusion flame studied by Wang et al. [27] is considered as the flat baseline case. In this flame, the fuel is pure ethylene (C_2H_4), and the oxidizer composition consist of 25%/75% of O_2/N_2 (on volume basis). Both fuel and oxidizer streams are maintained at atmospheric pressure and 300 K temperature. This flame is an example of an SF (soot-formation) type [25], in which the flame front (characterized by the stoichiometric mixture fraction Z_{st}) resides on the oxidizer side of the stagnation plane. The detailed kinetic scheme KM2 of Wang et al. [105] is used for the gas-phase chemistry calculations. The diffusion transport of species is modeled using a mixture-averaged approximation.

4.3 Simulations of steady flames

Prior to investigating unsteady curvature effects, the soot response to flame curvature in steady-state conditions is analyzed.

4.3.1 Effects of curvature on soot formation in a steady flame

The effects of flame curvature on the soot formation characteristics for the steady target flame are first considered here. The applied strain rate is kept constant ($a = 120\,\text{s}^{-1}$), and a curvature of $\kappa = \pm 5\,\text{cm}^{-1}$ is applied. The value of selected κ is relatively moderate and relates to the diffusion flame thickness $\delta_{f,Z}$ such that:

$$\kappa \delta_{f,Z} = \mathcal{O}(1) \tag{4.7}$$

in which, the diffusion flame thickness $\delta_{f,Z}$ is approximated as [187]:

$$\delta_{f,Z} \approx \frac{2Z_{st}}{|\nabla Z|_{st}}. \tag{4.8}$$

The mixture fraction definition here follows from the work of Bilger [188]. For the baseline counterflow flame considered, Eq. 4.8 yields, $1/\delta_{f,Z} \approx 4.6\,\text{cm}^{-1}$. The radius of curvature is, therefore, comparable to flame thickness.
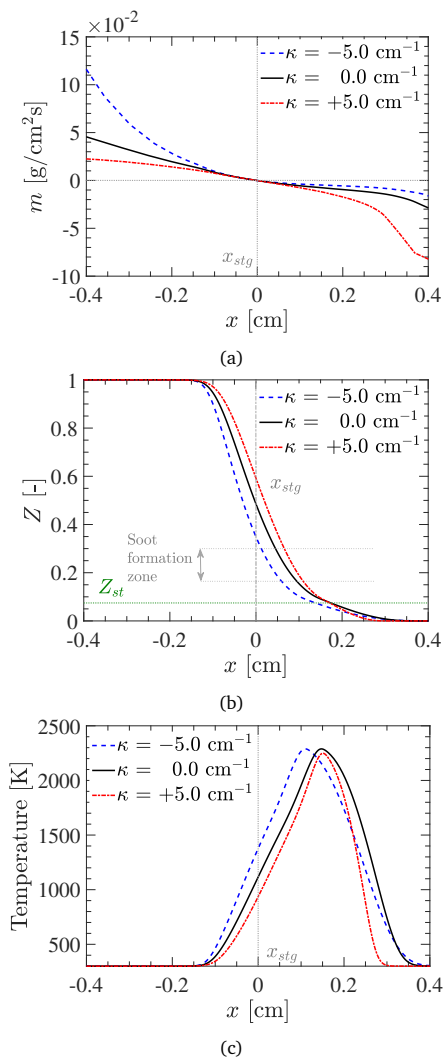
Figure 4.2: Spatial distributions of mass flux m (a), mixture fraction (b), and temperature (c) for curved and flat flames. Notations x_{stg} and Z_{st} denote stagnation and stoichiometric positions, respectively.

Prior to discussing the soot characteristics, it is important to illustrate key features of the flame structure under the influence of curvature. In particular, since the flame curvature causes a relative change in the local area of the flame surface, it alters the mass flux ($m = \rho u$) of the reactants. Figure 4.2a demonstrates that a negative curvature enhances the mass flux of fuel towards the stagnation plane as a consequence of the reduction in the local flame surface area, while positive curvature causes the opposite effect, and increases the mass flux of oxidizer towards the stagnation plane. The change in mass flux strongly impacts the local mixing characteristic of the flame

through the differential transport between the gas-phase species and mixture fraction [175]. The movement of mixture fraction iso-surfaces owing to curvature effects is evident from Fig. 4.2b. A negative curvature tends to shift the reaction zone towards the fuel side. As a result, the mixture fraction at the flame stagnation position is found to be decreased compared to its flat flame counterpart. Positive curvature, on the other hand, shows the opposite effect. As will be shown later, for the target flame under study, the soot formation zone (characterized by the rate profiles of different soot sub-processes) encompasses the composition space from about $Z \sim 0.15$ to 0.3. From Fig. 4.2b, it can be noticed that the soot formation zone shift towards the fuel side of the stagnation plane for negative curvature. On the contrary, the soot formation zone is found to shift towards the oxidizer side for positive curvature. Moreover, flame curvature also impacts the distribution of temperature in physical space (see Fig. 4.2c). For negative curvature, the reaction zone tends to shift towards the fuel side, enhancing the transport of heat from the flame towards the fuel diffusive layer [177]. On the contrary, for the applied value of positive curvature, the temperature profile shifts towards the oxidizer side. The response of temperature to curvature is mainly attributed to preferential diffusion effects [189].

Given the curvature-induced displacement of mixture fraction, the analysis of the soot formation process in physical space is relatively intricate. Therefore to elucidate the curvature effects on soot, in Fig. 4.3, profiles of global soot quantities are presented in Z-space. From the numerical results, it is evident that negative curvature increases the peak value of the soot volume fraction (f_v), whereas it is found to be decreased when positive curvature is applied. Furthermore, it can be observed that negative curvature tends to shift the peak of f_v towards the lower mixture fraction while making its profile narrower in Z-space compared to the flat flame. On the contrary, positive curvature leads to a wider f_v profile with a peak shifting towards higher Z. The observed qualitative response of f_v under curvature is in agreement with the previous works [94, 177]. The density change also contributes to the increasing f_v towards the stagnation plane. To isolate the influence of density change from f_v, the profiles of soot mass fraction Y_s are also compared in Fig. 4.3b. As can be seen, the qualitative trends of Y_s with curvature follow the trend in f_v, and thus the role of density expansion is secondary in soot profiles for curved flames. Moreover, Fig. 4.3c shows that, compared to a flat flame, negative curvature causes a stronger decay in the soot number density (N) as soot particles grow and convect towards the stagnation plane, while the opposite tendency occurs for positive curvature. The lowered number density accompanied by a larger average soot particle diameter D_{avg} (in Fig. 4.3d) mainly reflects the enhanced growth rate of soot particles due to negative curvature. In contrast, the soot particle size tends to decrease under positive curvature, implying a relatively high number density of smaller-sized particles. It is worth highlighting that a small second peak (note the log scale) in number density is found at higher Z. This is caused by the small amount of A4 predicted by the employed KM2 mechanism, which leads to nucleation. However, growth rates of subsequent soot sub-processes are negligible there, and therefore, the soot mass fraction remains small.
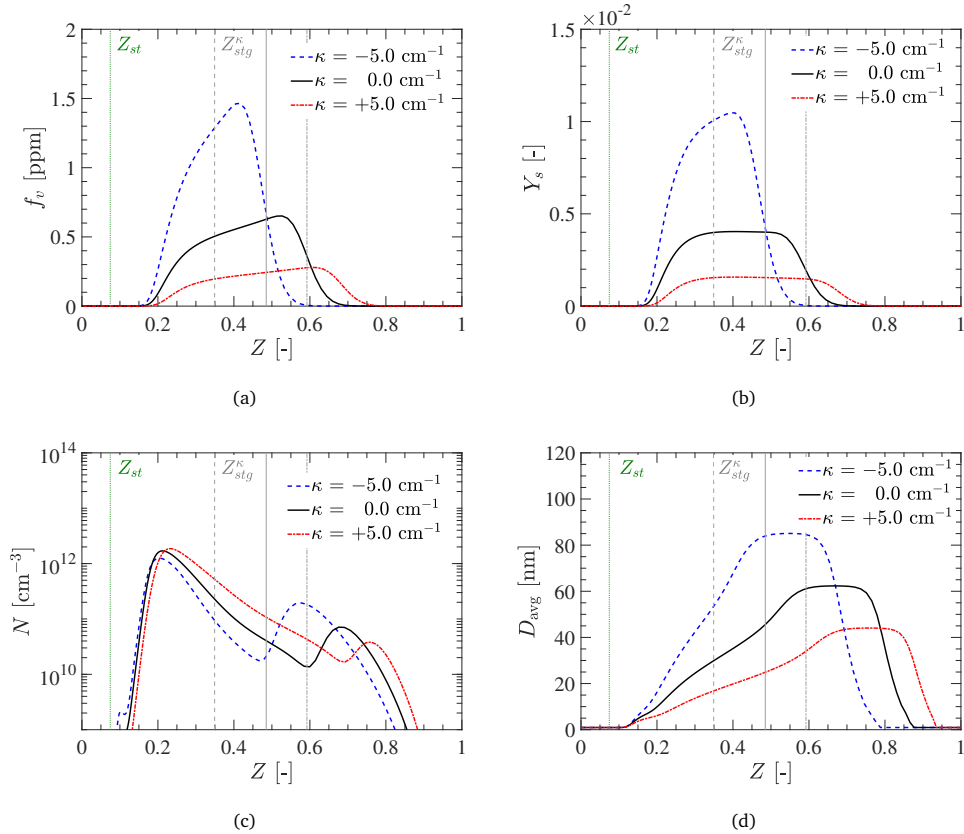
Figure 4.3: Distributions of soot volume fraction (a), soot mass fraction (b), number density (c), and average particle diameter (d) in Z-space for curved and flat flames. Vertical gray lines indicate the mixture fraction at the stagnation plane for corresponding curved flame.

In general, the process of soot formation is strongly influenced by the complex flow-flame interactions, which affect the residence time of soot particles, thermophoresis, and soot chemistry. Therefore, to understand the physical mechanism associated with observed soot response in curved flames, a detailed analysis of the aforementioned phenomena is essential. As mentioned earlier, due to the change in flame surface area, the flame curvature significantly alters the flow characteristics. Since soot formation is a relatively slow process, it is interesting to investigate the impact of curvature on its residence time. To that end, the profiles of soot particle velocity (flow velocity u combined with the thermophoretic component V_T) are plotted against mixture fraction in Fig. 4.4. It can be seen that negative curvature substantially reduces the soot particle velocity compared to that in a flat flame. The lowered velocity implies an enhanced residence time of soot particles as they grow and convect towards the stagnation plane. Therefore, the observed increment in f_v by negative curvature can
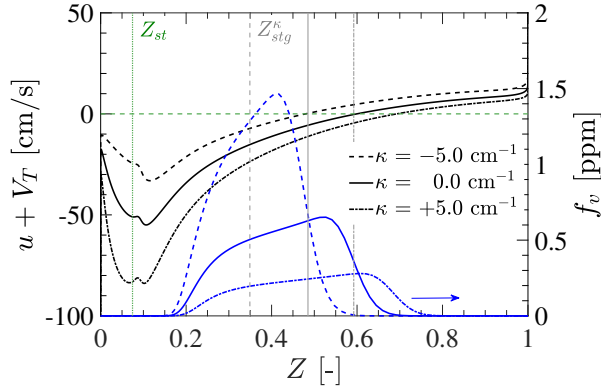
Figure 4.4: Distribution of the soot particle velocity $(u + V_T)$ for curved and flat flames.

be partially attributed to the higher soot residence time, which contributes to the increased soot mass growth. On the other hand, for positive curvature, the soot particle velocity is higher compared to a flat flame, which tends to lower the residence time of soot, consequently lowering its overall growth.

It is well-known that thermophoresis strongly affects the transport of soot particles. Therefore, it is useful to examine the impact of curvature on its contribution to the overall soot response. To address this, the profiles of soot volume fraction in curved flames without thermometric diffusion ($V_T = 0$) are compared in Fig. 4.5. In SF type flames, thermophoresis shifts f_v profiles towards higher Z values while reducing their peaks. Naturally, it can be observed that the peak values of f_v are significantly altered by neglecting thermophoresis. However, it does not impact the qualitative trends in f_v profiles with curvature. Hence the role of thermophoretic diffusion on soot response in curved flames appears to be secondary.
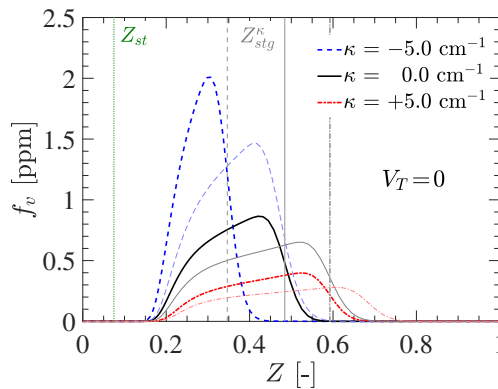
Figure 4.5: Distributions of f_v for curved and flat flames when thermophoretic diffusion is neglected ($V_T = 0$). For comparison, f_v profiles for $V_T \neq 0$ are shown with lighter curves.
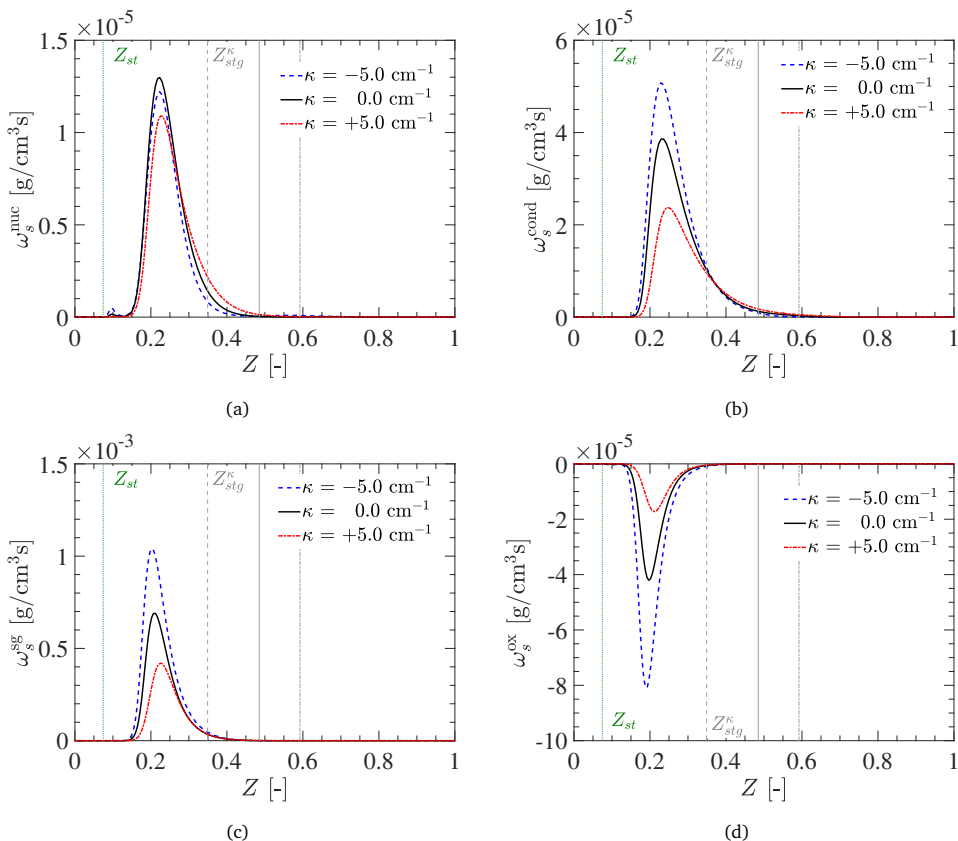
Figure 4.6: Rate profiles of soot nucleation (a), PAH condensation (b), HACA surface growth (c), and soot oxidation (d) for curved and flat flames.

Next, to assess the influence of curvature on soot chemistry, the rate profiles of different sub-processes are presented in Fig. 4.6. As can be observed, rates of PAH condensation, surface growth, and oxidation are enhanced by negative curvature and diminished by positive curvature. On the other hand, the impact of curvature on soot nucleation is somewhat complex. The nucleation rates show lowered peak values for both negative and positive curvatures compared to the flat flame. Since, in the present model, the soot is assumed to nucleate through the dimerization of A4 molecules, the profiles of A4 mass fraction are compared in Fig. 4.7a. The decreased rates of soot nucleation in curved flames are recognized to be a direct consequence of the A4 concentrations. Note that the profiles of A4 presented in Fig. 4.7a include the consumption through soot sub-processes. Therefore, pure gas-phase results (without soot model) are also analyzed (see Fig. 4.7b) to verify the trends in A4 profiles under curvature effects. The gas-phase results for curved flames (irrespective of the sign of the curvature) also do not show enhanced A4 mass fraction peaks compared

(a)

(b)

(c)
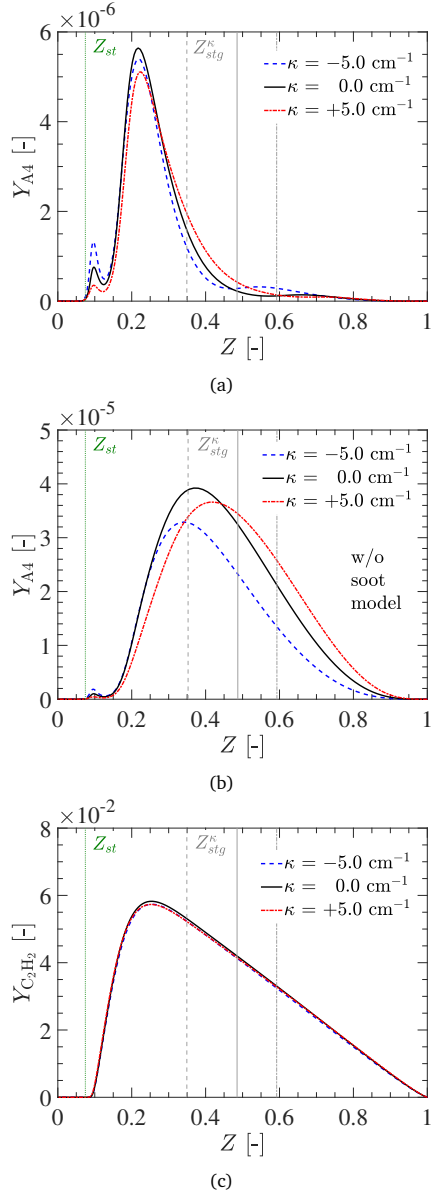
Figure 4.7: Profiles of A4 mass fraction with (a), and without soot kinetics (b), and C_2H_2 mass fraction (c) for curved and flat flames.

to the flat flame. Nevertheless, in the soot formation zone ($Z \sim 0.15$ to 0.3), the A4 mass fraction predicted by the gas-phase simulation for the negatively curved is higher compared to the positively curved flame. On the contrary, in sooting flame

simulations (see Fig. 4.7a) A4 mass fraction are found to be only slightly different. This behavior could be related to increased consumption of A4 through enhanced PAH-condensation rates under negative curvature. Therefore, from the analysis of A4 profiles, the direct causal relationship between PAH and the observed soot response under curvature is not observed. On the other hand, since the rates of surface growth (see Fig. 4.6) are approximately an order of magnitude greater than nucleation and condensation rates, it is clear that the surface reactions predominantly account for the overall soot mass growth rate in SF type flames. Therefore, the increased soot volume fraction for negative curvature can be mainly attributed to the enhanced rate of soot surface growth.

To explicate the enhanced rates of surface growth in negative curvature, it is important to highlight the crucial role of differential diffusion of soot relative to the gas-phase (mixture fraction). The key role of differential transport of soot particles in curved non-premixed flames has also been recognized in literature [41, 176]. Due to their high Schmidt numbers (owing to lower diffusivities), the transport of soot particles in mixture fraction space is strongly affected by the curvature effects. Analogous to gas-phase species, the contribution of curvature in the convection velocity (u^*) of soot mass fraction in Z-space is primarily related to [175, 190]:

$$u^* = \left(1 - \frac{Le_Z}{Le_s}\right)\left[\kappa\sqrt{\frac{\chi D_Z}{2}}\right] \qquad (4.9)$$

where Le_Z, Le_s are the Lewis numbers for mixture fraction and soot particles, respectively, while χ and D_Z denote scalar dissipation rate and thermal diffusivity, respectively. A detailed description of the flamelet equations in Z-space can be found elsewhere [175, 190]. Negative curvature, therefore, induces the convection of soot particles ($Le_s \gg Le_Z$) towards a lower mixture fraction. As a result, soot particles are differentially transported (relative to mixture fraction) towards lower Z values.

A more visual illustration of the differential transport of soot particles is presented through the sectional distribution of particle number density in Fig. 4.8. It depicts the number density of the different particle sizes as a function of Z. It is evident from Fig. 4.8a that under negative curvature, a large number of soot particles are found within the soot formation zone (region of higher rate profiles of sub-processes). As a result, the particles grow and the number density of larger-sized soot particles within the soot formation zone is increased. In contrast, positive curvature tends to transport soot particles towards higher Z, causing them to move away from the soot formation zone, reducing their growth rate. Under the HACA mechanism, employed in the present work, the rate of surface growth primarily depends on the concentrations of C_2H_2 and active surface radical sites. The concentration of active surface radicals is directly related to the size and number density of soot particles. From the mass fraction profiles of C_2H_2 (Fig. 4.7c), it is apparent that the peak C_2H_2 concentration is hardly affected by flame curvature. Therefore, the increment in the surface growth

rate by negative curvature is essentially a consequence of the increased concentration of surface sites facilitated by the curvature-induced transport of soot particles in the sooting zone.

(a)

(b)

(c)
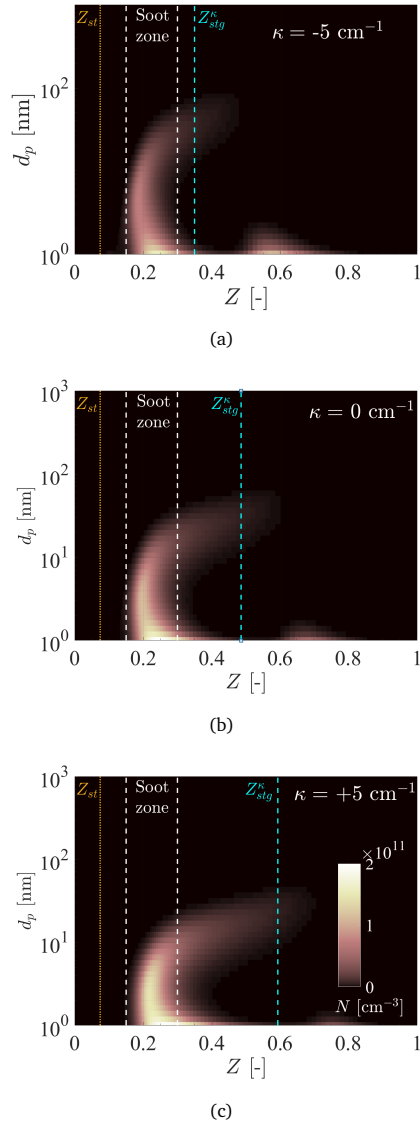
Figure 4.8: Distributions of soot number density N in Z-space for different particle sizes d_p. Vertical white lines indicate the soot formation zone. Vertical lines indicate the stagnation plane (cyan), soot zone (white), and stoichiometric Z (yellow).
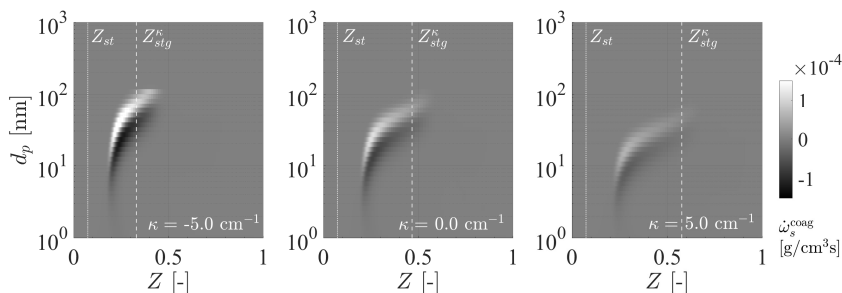
Figure 4.9: Distribution of soot coagulation rate for curved and flat flames.

Moreover, the soot particles grown through surface reaction and condensation, coagulate as they approach the stagnation plane. Naturally, the increased concentration of larger-sized soot particles by negative curvature also impacts the process of soot coagulation. To illustrate this, the distributions of coagulation rates of different-sized particles in mixture fraction space under curvature are compared in Fig. 4.9. The enhanced coagulation rates towards larger-sized particles can be noticed for negative curvature. The increased coagulation rates of larger-sized particles subsequently lead to larger particle diameters, which further promote surface reactions through the increased surface area density of soot particles. Since negative curvature tends to increase the soot surface area density, the soot oxidation rates are also enhanced (see Fig. 4.6d). However, the contribution of the soot oxidation process in the overall soot production is insignificant compared to surface growth. On the contrary, the lowered flux of soot particles in positively curved flames adversely impacts the coagulation rates, contributing to lower soot volume fraction.

In summary, the overall response of soot to curvature effects appears to be governed by two key physical mechanisms that complement each other. For a negatively curved flame, lowered particle velocities tend to enhance the residence time of soot. In addition, the differential transport of soot particles towards the soot formation zone leads to increased surface growth rates. In positively curved flames, the exact opposite behavior is noticed, which results in lowered soot volume fractions.

The use of the sectional method-based model enables the analysis of soot particle size distribution. In this context, the influence of flame curvature on the particle size distribution function at the peak f_v position is shown in Fig. 4.10. PSDF profiles show a bimodal behavior in the flat as well as curved flames. For a negative curvature, the response of PSDF in log-normal mode is driven by the increased rate of surface growth and enhanced rate of coagulation between larger-sized particles, which leads to a shift of the peak in the log-normal mode of the PSDF towards larger particle diameters. The opposite behavior can be noticed in the positively curved flames as a consequence of diminished rates of surface growth and coagulation. On the other hand, negative curvature shows a higher number of incipient particles respective to the flat flame in a
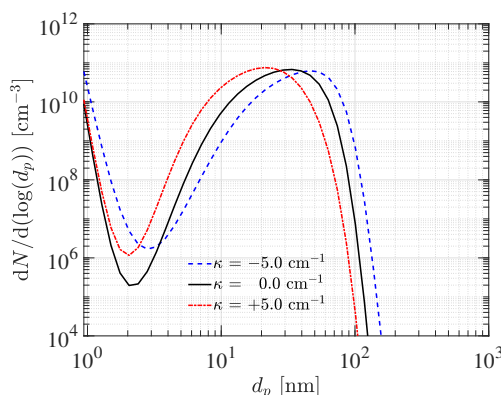
Figure 4.10: Comparison of PSDF at the maximum f_v position under flame curvature for target flame.

power-law mode. This is essentially a reflection of somewhat higher local rates of nucleation compared to its flat and positive curvature counterparts (see Fig. 4.6a). Note that the peak f_v positions for curved flames are shifted in Z-space. While the maximum rate of nucleation was observed to reduce for negative curvature (Fig. 4.6a), the nucleation rates at the location of peak f_v show a slight increase. Moreover, compared to a flat flame, negative curvature shifts the trough in the PSDF towards the larger particle diameters (d_p) while making it shallower with an increment in number density. Note that this discussion of the PSDF only represents qualitative tendencies as soot agglomeration and fragmentation processes are not explicitly considered in the present model.

Moreover, to examine the sensitivity of soot formation processes to flame curvature, additional simulations are carried out for curvature values ranging from $-10\,\mathrm{cm}^{-1}$ to $10\,\mathrm{cm}^{-1}$. The variations of normalized peak soot volume fraction and peak soot formation rates are depicted against curvature in Fig. 4.11. The peak quantities are normalized by their corresponding values for a flat flame. Figure 4.11 reveals that the peak soot volume fraction increases monotonically from positive to negative curvatures. In other words, soot formation tends to enhance for a negative curvature, and mitigate for a positive curvature. However, the relative increment in peak soot volume fraction for negative curvatures is almost similar to its decrement at positive curvatures. Furthermore, the rates of soot surface growth and oxidation show a monotonic increment as curvature decreases from positive to negative values. On the other hand, peak soot nucleation rates and condensation rates do not show a monotonic response to curvature variation. Such a non-monotonic behavior of soot nucleation rates essentially stems from the response of A4 to the curvature. For instance, it is noticed that the peak value of A4 initially increases for negatively curved flames, attains a maximum, and then again tends to decrease at higher values of negative curvatures. In contrast, for positive curvatures, the peak concentration of A4 shows a monotonic decrement with curvature leading to a reduction in soot nucleation rates.
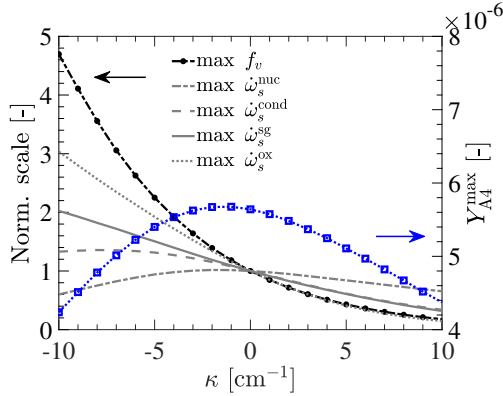
Figure 4.11: Variation of the normalized peak values of soot volume fraction and rate of different sub-processes against the flame curvature.

4.3.2 Strain rate sensitivity of soot formation in steady curved flames

It is known from previous works [113, 182, 191] that at higher strain rates, soot formation is reduced primarily as a consequence of the decreased concentration of gas-phase precursors, and lowered residence time for the growth of soot particles through the coagulation process. To present a more detailed picture of flow-flame-soot interactions, the effects of curvature on soot formation characteristics are investigated for different strain rates. In Fig. 4.12a, the peak f_v are plotted as a function of applied strain rate a for several κ values. An exponential decrease of soot volume fraction with increasing strain rate is apparent at every κ value. The enhancement in f_v^{max} by negative curvature, and reduction by positive curvature are clearly noticed in Fig. 4.12a at different strain rates as well. Moreover, the dependence of f_v^{max} reduction on the strain rate remains almost similar for the covered range of κ.

Since variations in strain rate and curvature can either enhance or diminish the overall soot formation, it would be interesting to evaluate if there exist synergistic effects in terms of soot formation when the flame is curved and strained simultaneously. To quantify such synergistic effects of combined strain and curvature variation on soot formation, we define a synergy parameter (Φ) as:

$$\Phi = \hat{f}(\kappa, a) - \hat{f}_\kappa(\kappa) \cdot \hat{f}_a(a) \tag{4.10}$$

with

$$\hat{f}(\kappa, a) = f_v^{\mathrm{max}}(\kappa, a)/f_v^{\mathrm{max}}(0, a_0) \tag{4.11a}$$

$$\hat{f}_\kappa(\kappa) = f_v^{\mathrm{max}}(\kappa, a_0)/f_v^{\mathrm{max}}(0, a_0) \tag{4.11b}$$

$$\hat{f}_a(a) = f_v^{\mathrm{max}}(0, a)/f_v^{\mathrm{max}}(0, a_0) \tag{4.11c}$$
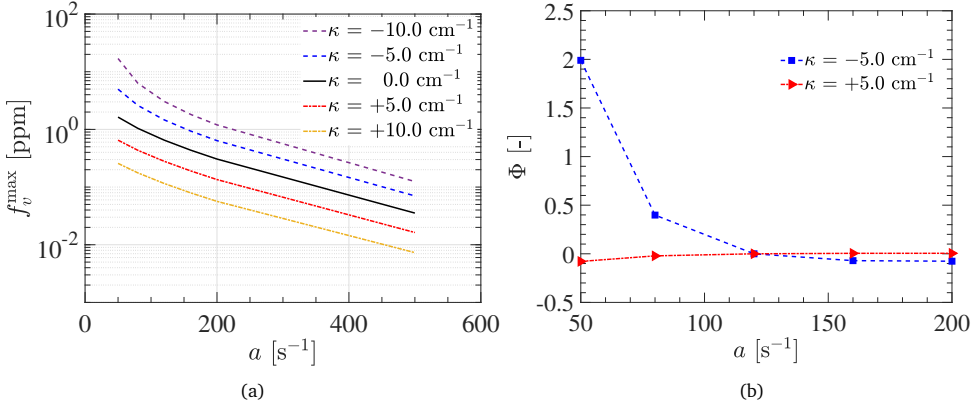
Figure 4.12: Variation of f_v^{max} against strain rate at different curvatures for the target flame (a), variation of synergy parameter (Φ) for negative and positive curvature against strain rate (b).

where $\hat{f}_\kappa(\kappa)$ and $\hat{f}_a(a)$, respectively, denote the fractional change in f_v^{max} for the variation in curvature at a reference strain rate $a_0 = 120\,\mathrm{s}^{-1}$, and for the variation in strain rate of the flat flame ($\kappa = 0$). The first term, $\hat{f}(\kappa, a)$ in the Φ expression refers to the actual change observed in the f_v^{max} compared to the baseline case ($a = a_0$, $\kappa = 0$). On the other hand, the second term signifies the expected change in f_v^{max} as a consequence of variation in curvature and strain rate by considering their individual effects through multiplication. The values of the synergy parameter (Φ) observed under negative and positive curvatures are plotted against the strain rate in Fig. 4.12. The analysis of the synergistic response suggests that the sensitivity of an increment in f_v^{max} by negative curvature is enhanced on lowering the strain rate. Positive curvature, on the other hand, hardly shows any significant sensitivity of f_v^{max} reduction to strain rate. Moreover, the synergistic effects are found to be substantially lowered in negatively curved flames for an increment in strain rate. Such an effect can be partially attributed to the decrease in flame thickness δ_f at higher strain rates, causing a reduction in dimensionless curvature $\kappa\delta_f$, which essentially lowers the tendency of the flame structure to be affected through curvature effects [98].

4.4 Simulations of unsteady flames

In this section, we analyze the dynamic response of soot formation in the target flame to unsteady curvature. The curvature unsteadiness was introduced with a sinusoidal function of the form:

$$\kappa = \Delta\kappa \cdot \sin\left(2\pi f_\kappa t\right) \tag{4.12}$$

97

where $\Delta\kappa$ is the amplitude, and f_κ the frequency of the curvature oscillations. In addition, to understand the effects of simultaneous strain-curvature oscillations on the soot formation, sinusoidal-type fluctuations were imposed on the applied strain rate. The strain rate oscillations were assumed to have a form:

$$a = a_0 + \Delta a \cdot \sin\left(2\pi f_a t\right) \tag{4.13}$$

where Δa is the amplitude, and f_a the frequency of the imposed strain rate oscillations, and $a_0 = 120\,\mathrm{s}^{-1}$ is the strain rate of the steady-state flame solution. Initially, the flame is planar and at a steady state, upon which the subsequent oscillations are imposed. At $t = 0$, the curvature and strain rate begins to fluctuate according to Eq. 4.12 and Eq. 4.13, respectively. It was noticed in [183] that the response of soot and PAH to the imposed strain rate fluctuation is quasi-steady for low frequencies. At higher frequencies, on the other hand, the time scales of soot formation became larger than the time scales of flow field fluctuations, and thus the imposed oscillations could not impact the response of the soot formation process. In the present analysis, the frequencies chosen for strain and curvature fluctuations are in the range of 1-1000 Hz. Furthermore, $\Delta\kappa$ and Δa are selected such that for the limits of unsteady curvature and strain rate variation, steady-state results are also available. To quantify the unsteady effects of separate, and simultaneous curvature and strain rate fluctuations, a wide range of conditions were simulated.

4.4.1 Dynamic response of soot to fluctuating curvature at constant strain rate

Variation in the frequency of imposed oscillations

Because of the relatively large characteristic time scale of soot formation/oxidation, the soot formation response is very sensitive to the flame unsteadiness [183]. Therefore, unsteadiness imposed through curvature oscillations is expected to strongly affect the dynamic behavior of soot. To elucidate this, the dynamic response of peak soot volume fraction (normalized with the steady-state value) at different values of f_κ is presented in Fig. 4.13. For reference, the imposed profiles of curvature oscillation are also shown. The time is non-dimensionalized with the period ($\tau_\kappa = f_\kappa t$) of the imposed curvature oscillations. Note that the transient simulations were conducted until a limit cycle is reached. However, for the readability of figures, the results for the f_v^{max} response are conveniently presented for the first few periods.

As can be noticed from Fig. 4.13a, the dynamic response of soot is strongly influenced by the frequency of the imposed curvature oscillations. The amplitude of the induced oscillations in peak soot volume fraction rapidly decreases with an increase in the imposed frequency. This essentially indicates that at higher frequencies, the dynamic response of soot tends to get attenuated. The amplitude variation also exhibits strong asymmetric behavior about the steady-state value. Furthermore, the phase-shift ob-
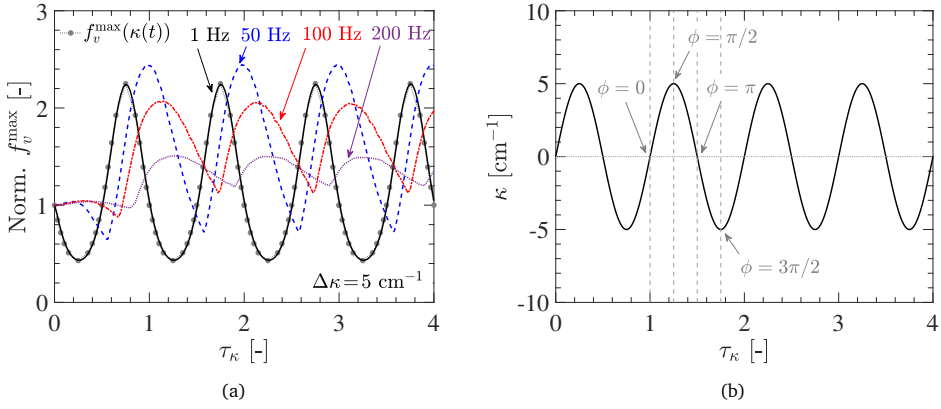
Figure 4.13: The dynamic response of normalized peak values of soot volume fraction $f_v^{\max}$ (a), and imposed curvature oscillations (b) at several frequencies with $\Delta\kappa = 5\,\mathrm{cm}^{-1}$. Time is normalized by the period of curvature oscillations ($\tau_\kappa = f_\kappa t$).

served in the $f_v^{\max}$ response is negligible for $f_\kappa = 1\,\mathrm{Hz}$, indicating the quasi-steady type response. On the contrary, with an increase in f_κ, the phase-lag between imposed oscillations and soot volume fraction response becomes substantial.

To enable a clear comparison with the steady-state response, the transient variation of normalized $f_v^{\max}$ within an induced oscillation cycle is represented against the instantaneous curvature in Fig. 4.14. The dotted gray curve in the plot refers to the $f_v^{\max}$ values obtained in steady-state conditions. The large departure from the steady-state conditions, indicating decoupling between imposed oscillations and the soot response, is more evident at higher f_κ. In other words, at high frequency, the curvature fluc-
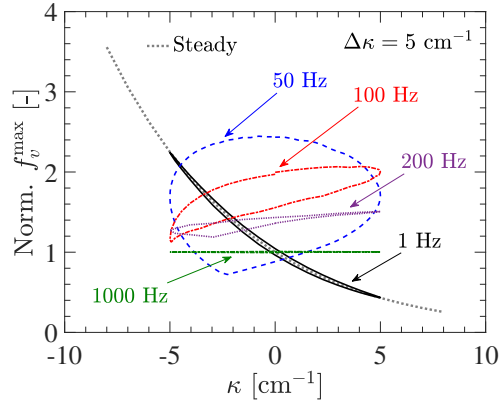
Figure 4.14: Unsteady trajectories (limit cycle) of normalized $f_v^{\max}$ at several oscillation frequencies versus the flame curvature. The dotted gray curve represents the steady-state response.

tuations have a very small effect on the induced amplitude of f_v^{max} response. As a consequence, $f_\kappa = 1000\,\mathrm{Hz}$ shows no dynamic effects on the soot formation. In contrast, the deviation from the steady-state trajectory becomes insignificant as the imposed frequency is lowered to 1 Hz, indicating a quasi-steady response.

The soot response to sinusoidal curvature fluctuations can be further illustrated by comparing soot profiles at different temporal positions. Figure 4.15 depicts the instantaneous profiles of soot volume fraction at four phases (ϕ) of the limit cycle for different f_κ, along with the quasi-steady flame solution (gray symbols). These phase positions correspond to: zero fluctuation and increasing curvature ($\phi = 0$), maximum curvature ($\phi = \pi/2$), zero fluctuation and decreasing curvature ($\phi = \pi$), and minimum curvature ($\phi = 3\pi/2$) (refer to Fig. 4.13b). It is evident from Fig. 4.15 that the curvature unsteadiness strongly modifies the shape of the soot profile during the oscillations. From soot volume fraction profiles it can be observed that, within a period of oscillation, the peak of f_v is periodically formed in the soot formation zone ($Z \sim 0.15$ to 0.3) and transported towards the stagnation plane. It is important to reflect on the fact that, the imposed oscillations in curvature tend to induce fluctuations in the convective and diffusive transport of soot. Therefore, unsteady curvature is expected to have a strong impact on the overall soot formation process. As the frequency of imposed oscillations is increased, the rate at which the soot formation process responds is somewhat reduced as the time scales associated with the faster oscillations become smaller than the characteristic time scales of soot formation, leading to a phase-lag. Such phase-lagged response of peak f_v at higher f_κ can be noticed from its relative positions in Z-space during the evolution.
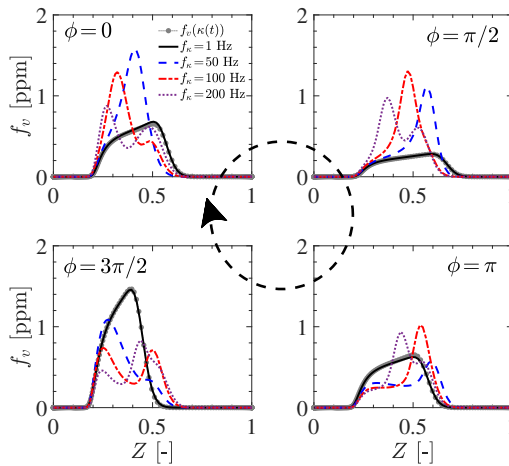
Figure 4.15: Instantaneous soot volume fraction profiles at several phase positions in the limit cycle for different f_κ. Dotted gray symbols represent the quasi-steady profile.
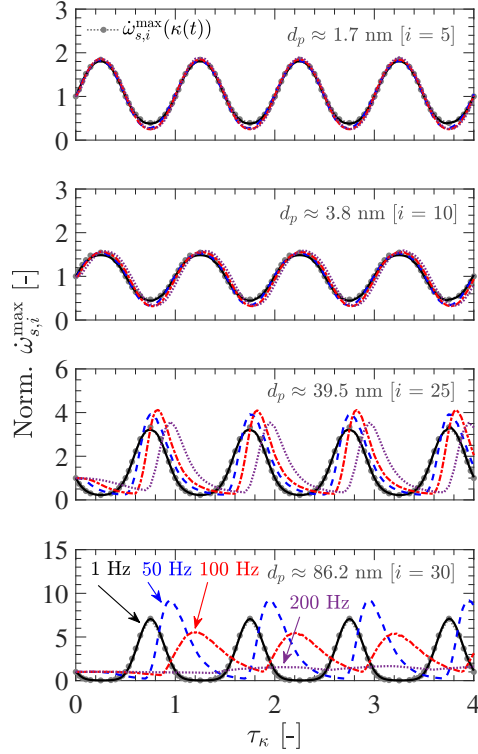
Figure 4.16: The dynamic response of normalized peak soot mass growth rate ($\dot{\omega}_{s,i}^{\max}$) in different sections for variation in the frequency of imposed curvature oscillations. The amplitude of imposed oscillations is $\Delta\kappa = 5\,\text{cm}^{-1}$. The peak values are normalized with the corresponding steady-state flat flame result.

The mechanism governing the dynamic behavior of soot under unsteady curvature can be better explained by comparing the response of the sectional soot mass growth rates. It is also important to emphasize that the characteristic time scales for soot chemistry also increase with the size of soot particles [43]. Therefore, the transient variation of normalized peak soot mass growth rates for soot particles with different sizes ($\dot{\omega}_{s,i}^{\max}$) is presented in Fig. 4.16. It is clear from the results that the phase-lag and damping noticed in the $f_v^{\max}$ (Fig. 4.13a) oscillations are mainly correlated to the dynamic response of $\dot{\omega}_{s,i}^{\max}$ at higher sections. Since larger-sized soot particles mainly contribute to the overall soot volume fraction, the dynamic response of peak $f_v^{\max}$ is predominantly affected by the unsteady behavior of larger particles under the imposed curvature oscillations. Rodrigues et al. [43] reported that the characteristics time scales of the collision phenomena such as coagulation and condensation increase with particle size. Owing to their large characteristic time scales, larger-sized soot particles do not get sufficient time to respond to the rapid changes in the unsteady hydrodynamics of the diffusion flame, induced by the imposed high-frequency curvature fluctuations. This essentially leads to a time-shift between the imposed curvature

oscillations and induced soot oscillations, resulting in the larger phase-lag. When the curvature fluctuations are imposed at lower frequencies, the changes in convective and diffusive transport are more prominently felt by the larger-sized soot particles. The soot formation process in the larger sections then responds to the slowly evolving hydrodynamics in a quasi-steady-like manner, leading to smaller phase-lag and smaller damping, as evident in Fig. 4.16 for 1 Hz.

To quantitatively illustrate the arguments discussed above, in Fig. 4.17, the phase-lag between the quasi-steady and induced oscillations of $\dot{\omega}_{s,i}^{\max}$ for different sized particles is compared against the phase-lag observed in the global $f_v^{\max}$ response at different f_κ values. It can be observed that the phase-lag increases with the soot particles' size, and with the increase in the imposed frequency, the phase-lag for a particular size of particles, enhances. Furthermore, it is evident from the results that the phase-lag observed in the $f_v^{\max}$ response is approximately equivalent to the phase-lag noticed in the $\dot{\omega}_{s,i}^{\max}$ response of larger-sized particles. Therefore, it can be affirmed that the dynamic response of $f_v^{\max}$ at unsteady curvatures in terms of phase and amplitude maintains a hierarchical relationship with the dynamic response of the sectional soot mass growth rates. Nevertheless, the phase-lag observed in the $\dot{\omega}_{s,i}^{\max}$ response of $d_p \approx 86$ nm under 200 Hz is significantly higher than the phase-lag for $f_v^{\max}$. Such a discrepancy is mainly attributed to the fact that the amount of soot in this section is too low for the phase-lag to reflect in the global $f_v^{\max}$ response.

In summary, the dynamic response of soot to curvature fluctuations suggests that when the oscillation frequency (f_κ) is increased, the soot formation time for bigger-sized particles tends to become larger than or comparable to the oscillation time. As a result, the larger-sized soot particles do not get enough time to respond to the imposed oscillations, which leads to their delayed response, causing a large phase shift
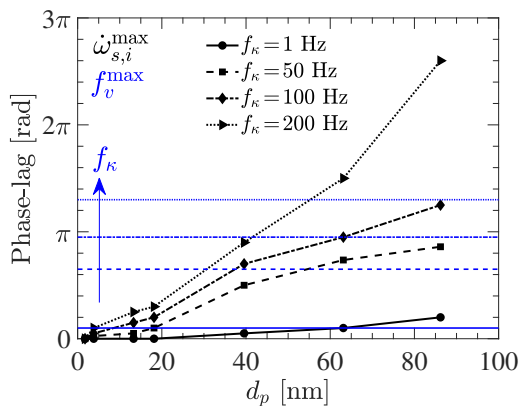
Figure 4.17: Variation of phase-lag between the quasi-steady and induced oscillations of peak soot mass growth rates ($\dot{\omega}_{s,i}^{\max}$) for different particle sizes at several oscillation frequencies. Horizontal blue lines indicate the phase-lag observed in the normalized $f_v^{\max}$ response.

in the soot response. In contrast, at lower frequencies, the characteristic formation time scales of larger-sized soot particles are smaller than the time scales of imposed oscillations. Therefore, the phase shift observed in the induced soot response tends to be smaller. It is also important to note that the flame curvature also impacts the characteristic time scales of soot formation for different sizes of soot particles, which further influences the dynamic response of soot formation to the imposed curvature oscillations.

Variation in the amplitude of imposed oscillations

In addition to frequency, the amplitude of the imposed curvature oscillations is expected to have a strong influence on the soot dynamics [43,183]. Therefore, to study the response of soot to the variation in amplitude at constant f_κ, additional computations have been performed for $f_\kappa = 50\,\text{Hz}$ with $\Delta\kappa = 2\,\text{cm}^{-1}$ and $8\,\text{cm}^{-1}$. Figure 4.18 shows the dynamic response of $f_v^{\max}$ against time for different values of $\Delta\kappa$. From the numerical results, it is evident that the value of the induced amplitude of $f_v^{\max}$ depends strongly on the amplitude of the imposed oscillations in the flame curvature. The observed dynamic response of $f_v^{\max}$ at different amplitudes translates from the strong increment in soot concentration under negative curvatures as noticed in Section 3.1. This is because, when the amplitude of imposed oscillation is increased, the flame encounters a larger range of negative curvature during the transient evolution. As a consequence, the soot mass growth rate is accelerated, which essentially reflects in the increased amplitude of the $f_v^{\max}$ response. Moreover, larger imposed amplitudes lead to a larger asymmetry in the induced amplitudes with respect to the steady-state values. However, the phase-lag is hardly affected by the amplitude of the imposed curvature oscillations.
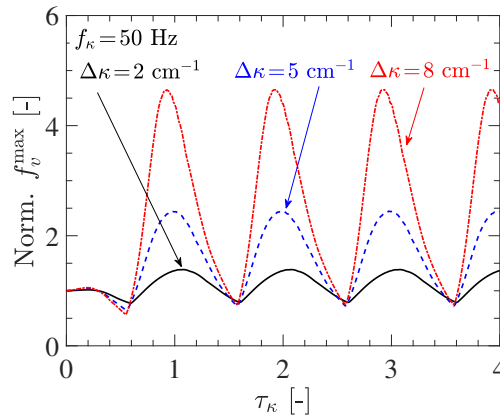
Figure 4.18: The dynamic response of normalized (on the steady-state value of flat flame) peak soot volume fraction ($f_v^{\max}$) at several amplitudes of imposed curvature oscillations for $f_\kappa = 50\,\text{Hz}$.

4.4.2 Dynamic response of soot to fluctuating curvature and strain rate

During the steady flames analysis in Section 3.2, it was identified that the sensitivity of soot formation in the presence of flame curvature is greatly influenced by the strain rate variation. Therefore, it is interesting to investigate the dynamic response of soot formation to the simultaneously imposed fluctuations of strain rate and curvature.

Variation in strain rate oscillation frequency for the flat flame

Prior to studying the effects of simultaneous curvature and strain rate fluctuations, it is important to briefly highlight the dynamic behavior of soot for the flat flames ($\kappa = 0$) under the strain rate oscillations. Accordingly, the response of f_v^{max} (normalized by steady flat flame value) is compared against the time of imposed strain rate oscillations (normalized by the period $\tau_a = f_a t$) in Fig. 4.19 for $\Delta a = 50\,\mathrm{s}^{-1}$ at $f_a = 50\,\mathrm{Hz},\ 100\,\mathrm{Hz}$. In Fig. 4.19 it can be observed that the induced oscillations of f_v^{max} are significantly damped and phase-lagged for an increase in the frequency of imposed strain rate oscillations. These observations are aligned with the findings reported elsewhere [43, 121, 183].

It is ratified in previous studies [183, 192], that the strain rate oscillations mainly impact the thickness of the diffusion layer of the flame, and hence, influence the diffusion time of different species. Since a finite time is required for the species to be transported to the main reaction zone, the reaction zone essentially responds with a time lag when faster perturbations are introduced to the flow field by increasing oscillation frequency. Therefore, a larger phase-lag is expected at a higher frequency owing to the larger diffusion time of different species compared to the oscillation period. As
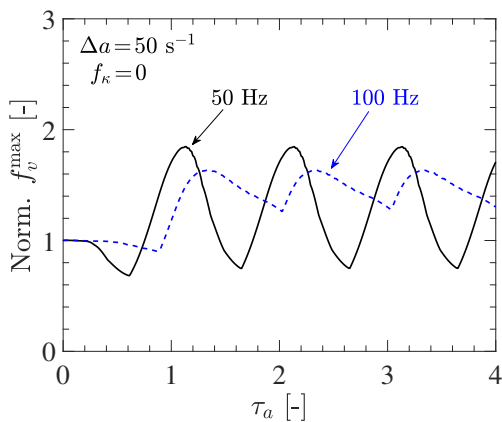
Figure 4.19: The dynamic response of f_v^{max} at different frequencies of imposed strain rate oscillations for $f_a = 50\,\mathrm{Hz},\ 100\,\mathrm{Hz}$. Time is normalized by the period of oscillations ($\tau_a = f_a t$).
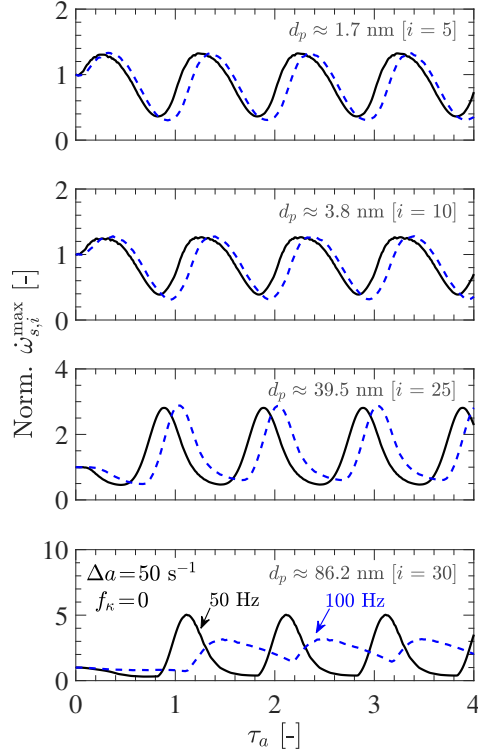
Figure 4.20: The dynamic response of normalized peak soot mass growth rate ($\dot{\omega}_{s,i}^{\max}$) in different sections for variation in frequency of imposed strain-rate oscillations. The peak values are normalized with the steady flat flame result.

a consequence, a hierarchical behavior between temperature, soot precursors, and soot sections is observed [43] regarding the phase-lag in their temporal responses. Furthermore, the overall soot response under strain rate fluctuations is found to be governed by the slow chemistry of larger-sized soot particles [43].

To demonstrate the validity of this correlation, the dynamic response of $\dot{\omega}_{s,i}^{\max}$ is presented in Fig. 4.20 for different particle size sections. It is evident that the phase-lag between imposed and induced oscillations is stronger at the higher sections (hence larger-sized soot particles). Therefore, similar to the case of curvature fluctuations discussed earlier, variability in the dynamic response of $f_v^{\max}$ can also be attributed to the transient response of $\dot{\omega}_{s,i}^{\max}$ for different particle sizes owing to the large disparity in their time scales. However, it is interesting to note that the phase-lag observed in the $\dot{\omega}_{s,i}^{\max}$ response at lower sections (e.g. $i = 5$, 10) for pure strain rate fluctuations is slightly larger than the same noticed under pure curvature fluctuations. It further suggests that the soot response in terms of the phase-lag is more sensitive to strain rate fluctuations as compared to curvature fluctuations at the same frequencies.

105

Curvature and strain rate oscillations imposed at the same frequency

In this section, we compare the dynamic response of soot in flames subjected to simultaneous curvature and strain rate oscillations at identical frequencies. Accordingly, in Fig. 4.21, the response of $f_v^{\max}$ under simultaneous strain rate and curvature fluctuations at $f_\kappa = f_a = 50\,\mathrm{Hz}$ is compared against its response for the pure curvature fluctuations ($f_a = 0$, $f_\kappa = 50\,\mathrm{Hz}$) and pure strain rate fluctuations ($f_\kappa = 0$, $f_a = 50\,\mathrm{Hz}$). The dotted gray curve in Fig. 4.21 represents the expected $f_v^{\max}$ after multiplying the effects of pure curvature fluctuations and pure strain rate fluctuations. Since the imposed oscillations of curvature and strain rate have identical frequencies (in-phase), the curvature and strain rate fluctuate simultaneously.

It is recognized from the analysis of steady flames (refer to Section 4.3.2) that under the decreasing strain rate, the presence of negative curvature tends to synergistically enhance the formation of soot. During the combined strain and curvature fluctuations, the flame encounters simultaneously decreasing strain rate and increasing negative curvature in every oscillation cycle. The flame with $f_\kappa = f_a$, therefore, presents the local conditions favorable for soot formation during their transient evolution. As a result, the amplitude of $f_v^{\max}$ fluctuations is found to be synergistically increased in the $f_\kappa = f_a$ case compared to the $f_\kappa = 0$ and $f_a = 0$ flames. Note that during the simultaneous strain and curvature oscillations, the flame is also subjected to increased strain rate and positive curvature, which tend to lower the soot formation. However, the sensitivity of soot formation suppression to positive curvature at higher strain rates was observed to be marginal (refer to Section 4.3.2). Therefore, the amplitude enhancement of $f_v^{\max}$ response in the presence of simultaneously fluctuating strain and curvature shows strong asymmetric behavior, with the peak increasing faster than the reduction of the trough.
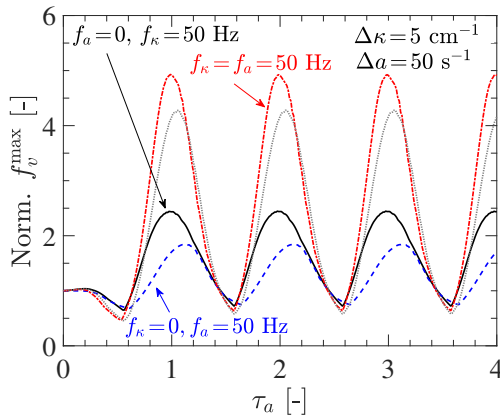
Figure 4.21: The dynamic response of peak soot volume fraction for simultaneously imposed, in-phase strain rate and curvature fluctuations. Time is normalized by the period of strain rate oscillations ($\tau_a = f_a t$).
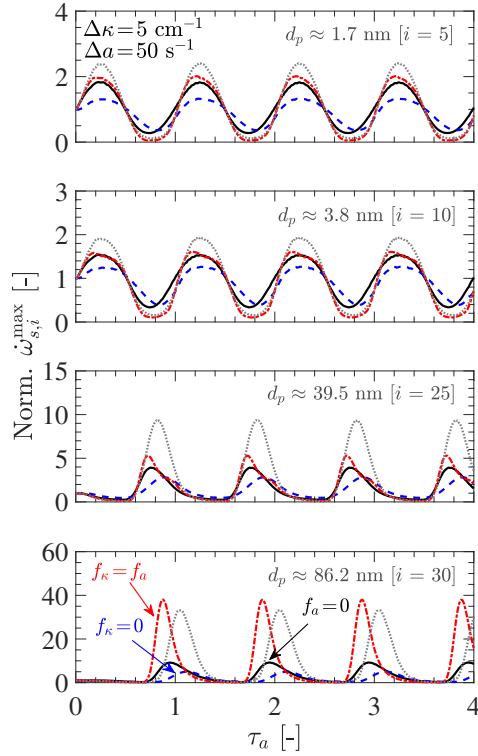
Figure 4.22: The dynamic response of normalized peak soot mass growth rate ($\dot{\omega}_{s,i}^{\max}$) in different sections for separate and simultaneous curvature and strain rate oscillations. The peak values are normalized with the steady-state flat flame result.

To understand the aforementioned observation better, the dynamic response of peak $\dot{\omega}_{s,i}^{\max}$ for different-sized particles is presented in Fig. 4.22. The profiles of expected $\dot{\omega}_{s,i}^{\max}$ by multiplying the effects of $f_\kappa = 0$ and $f_a = 0$ cases are plotted with the dotted gray curve. The $\dot{\omega}_{s,i}^{\max}$ response under simultaneous strain rate and curvature fluctuations reveals that the synergistic effect of strain and curvature variation starts to appear for larger particle size. For instance, in section $i = 30$, the amplitude enhancement under combined strain and curvature fluctuation is found to be higher than expected. As mentioned previously, the dynamic response of soot volume fraction is governed by the larger-sized soot particles, therefore, synergistic behavior noticed in soot mass growth rates for higher sections is also reflected in $f_v^{\max}$ variation.

Note that, for larger-sized particles, the observed phase-shift in the $\dot{\omega}_{s,i}^{\max}$ response under the presence of simultaneous strain and curvature fluctuations is substantially different than the one noticed in the algebraically predicted response (gray curve) based on the separate effects. As a consequence, the disparity in actual and algebraically predicted phase-shift in the $f_v^{\max}$ response is observed in Fig. 4.21. Furthermore,

107
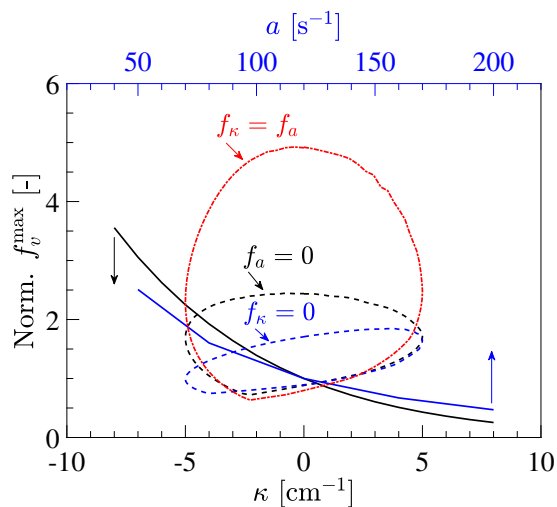
Figure 4.23: Unsteady trajectories (limit cycle) of normalized peak values of soot volume fraction under separate and simultaneous fluctuations of strain rate and curvature versus the flame curvature (bottom abscissa) and strain rate (top abscissa). The solid curve represents the steady-state response for curvature (black) and strain rate variation (blue).

compared to the flames subjected to pure curvature and pure strain rate oscillations, the $\dot{\omega}_{s,i}^{\max}$ response for the flame with simultaneously fluctuating strain and curvature tends to display a small phase-gain.

The dynamic response of $f_v^{\max}$ under separate and simultaneous fluctuations of strain rate and curvature can be summarized in the combined plot of the unsteady limit cycle, as shown in Fig. 4.23. The solid curves in the figure correspond to the variation of $f_v^{\max}$ with curvature (bottom abscissa) and strain rate (top abscissa) under steady conditions. The transient variation of $f_v^{\max}$ against the strain rate for $f_\kappa = 0$, and against curvature for $f_a = 0$ are compared with the unsteady limit cycle obtained under their simultaneous fluctuations at $f_a = f_\kappa$. It is evident that, when curvature and strain rate oscillations are imposed simultaneously at the same frequency (in phase), the amplitude of induced oscillations in $f_v^{\max}$ increases with a significant synergistic effect. Furthermore, for a given frequency, the response of soot tends to be more 'decoupled' from the imposed strain rate oscillations (indicated by the smaller amplitude of induced oscillations and large phase-lag) as compared to curvature oscillations. It further suggests that the cut-off frequency, beyond which the decoupling between soot chemistry and hydrodynamics occurs, would be higher for curvature than strain rate oscillations (as found earlier).

To highlight the impact of curvature and strain rate fluctuations on gas-phase quantities, the dynamic response of temperature and key chemical species is compared in Fig. 4.24. The induced oscillations of peak temperature hardly show any phase lag for the pure strain rate and pure curvature fluctuations. For identical imposed
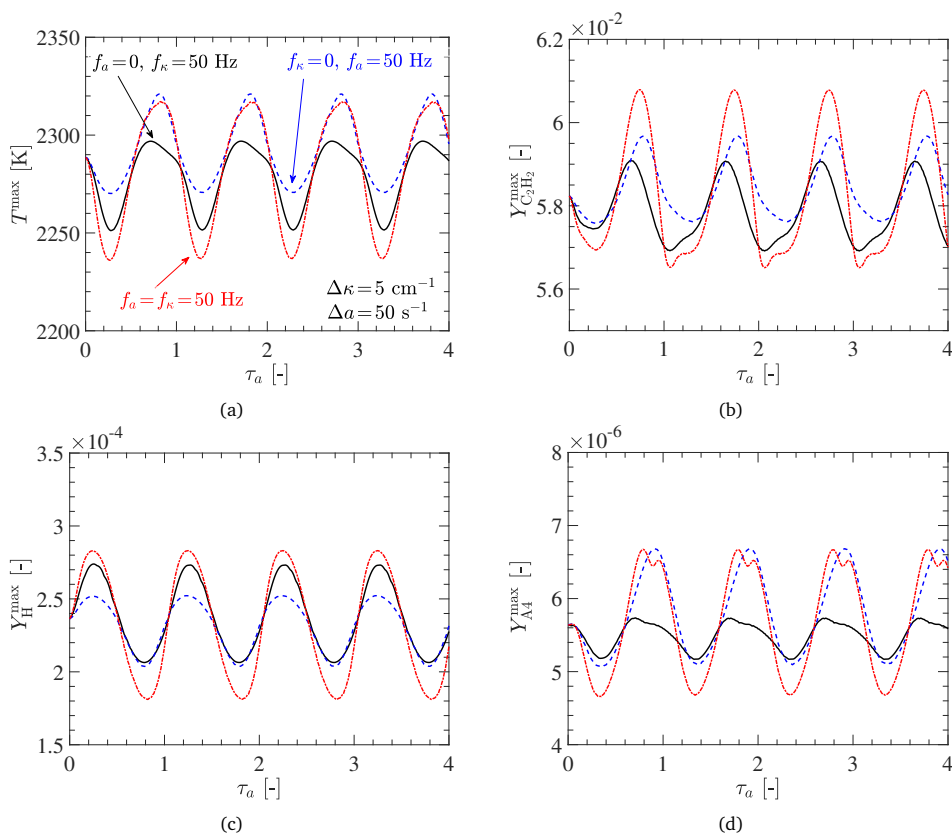
Figure 4.24: The dynamic response of peak values of temperature (a), C_2H_2 (b), H (c), and A4 (d) for separate and simultaneous curvature and strain rate oscillations. Color blue: strain oscillation; black: curvature oscillations; red: both strain and curvature oscillations. Time is normalized by the period of curvature oscillations ($\tau_a = f_a t$).

frequencies, a phase-lag in the transient response of C_2H_2 for pure strain rate fluctuations is larger compared to the one for pure curvature fluctuations. It implies its stronger sensitivity to strain rate oscillations as compared to curvature oscillations. The observed sensitivity of gas-phase species to strain rate and curvature oscillations stems from the characteristic time scales governing their chemistry. As a result, for H radicals, which are characterized by fast chemical time scales, the impact of curvature and strain rate oscillations appear quasi-steady. On the other hand, for A4 owing to its slower characteristic reaction time scales, the phase lag can be noticed in the induced oscillations.

Curvature and strain rate oscillations imposed at non-identical frequencies

We further extend the analysis to compare the dynamic response of soot formation under unsteady curvature and strain rate fluctuations varying at different frequencies. For this analysis, two possible scenarios are considered based on the relative frequencies of curvature and strain rate oscillations. These include:

1. $f_\kappa < f_a$: ($f_\kappa = 50\,\text{Hz}$, $f_a = 100\,\text{Hz}$)

2. $f_\kappa > f_a$: ($f_\kappa = 75\,\text{Hz}$, $f_a = 50\,\text{Hz}$)

The dynamic response of $f_v^{\max}$ is compared in Fig. 4.25 for the aforementioned cases. In addition, the transient evolution of $f_v^{\max}$ for $f_\kappa = f_a$ is also presented for reference. The numerical results demonstrate that, when curvature fluctuations are imposed in addition to the strain rate fluctuations, the overall soot formation process is strongly affected by the relative tendencies of curvature and strain rate to enhance or diminish the soot formation. For example, it is noticed that when the frequency of curvature and strain rate oscillations is identical ($f_\kappa = f_a$), the amplitude of the induced $f_v^{\max}$ fluctuations is maximum. On the other hand, for the cases, in which the strain rate fluctuates at a frequency distinct from the frequency of curvature, multiple peaks are detected in the induced $f_v^{\max}$ response.

For the case in which strain rate fluctuates faster than curvature ($f_\kappa < f_a$), close observation of $f_v^{\max}$ response and imposed curvature-strain rate oscillations indicates that the first maximum in the $f_v^{\max}$ response occurs when the flame is subjected to a lower strain rate along with decreasing positive curvature, while the second maximum occurs when both strain rate and curvature tend to reduce, with the latter being negative. Since for the first peak, the curvature is positive, the $f_v^{\max}$ value for the first
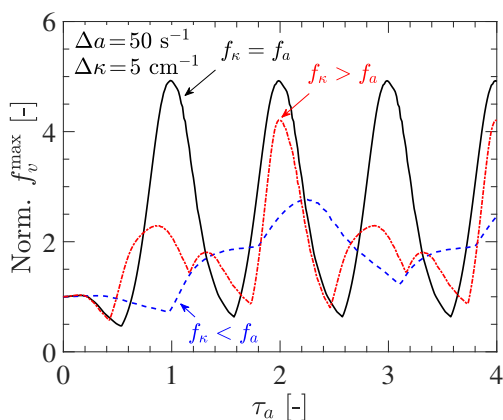
Figure 4.25: The dynamic response of peak values of soot volume fraction ($f_v^{\max}$) at simultaneous curvature and strain rate oscillations. Time is normalized by the period of strain rate oscillations ($\tau_a = f_a t$).

peak is found to be smaller than the one observed for the second peak. Furthermore, a higher strain rate frequency tends to enhance the phase-lag and damping of f_v^{max} amplitude as compared to its response under in-phase conditions ($f_\kappa = f_a$).

On the other hand, when the frequency of the imposed curvature oscillations is higher than that of the strain rate fluctuations ($f_\kappa > f_a$), the number of extrema in the f_v^{max} response increases. This is because when the frequency of curvature oscillation is increased, the number of curvature cycles per strain rate cycle is enlarged. As a result, the flame is subjected to multiple conditions that either assist or impede the rates of soot formation. Accordingly, for the ($f_\kappa > f_a$) case considered here, three maxima are noticed in the f_v^{max} evolution. These peaks in f_v^{max} arise, respectively, as a consequence of the following instances:

- when both strain and curvature tend to decrease, with the strain rate reduction being slower than the curvature, while curvature being on the positive side.

- when the strain rate is on the low side and curvature tends to decrease from positive towards negative.

- when both strain and curvature decrease with the strain rate drop being faster than the curvature decrement.

The maximum peak observed in the overall f_v^{max} response is mainly the reflection of the last condition. Note that the aforementioned observation is specific to the chosen values of f_κ and f_a. In a general sense, the dynamic response of f_v^{max} under simultaneous strain rate and curvature fluctuations indicates an additive effect of separately imposed strain rate and curvature oscillations. In other words, during the transient evolution, soot concentration (indicated by f_v^{max}) is found to be enhanced when a flame encounters local conditions favorable for soot formation (e.g. negative curvature at a low strain rate), while the soot formation is found to be reduced for the adverse local conditions (e.g. positive curvature at a high strain rate). The competition between local strain rate and curvature essentially determines the number of extrema (and their amplitudes) in the induced soot response.

From numerical results, it can be argued that, under simultaneously fluctuating curvature and strain rate, the variability in values of the induced f_v^{max} amplitudes strongly depends on the frequency difference between the imposed oscillations. In principle, the amplitude of induced soot response is found to be largest when imposed curvature and strain rate frequencies are identical (in-phase). On the contrary, the amplitude of induced oscillations attains the lowest value for the curvature and strain rate oscillations being in anti-phase (not shown here). For the frequency of curvature oscillations distinct from that of strain rate oscillations, the number of extrema and their corresponding values in induced soot response are governed by the magnitude and balance between the imposed frequencies.

4.5   Summary

The response of soot formation to curvature in an SF type counterflow flame was numerically investigated under steady and unsteady conditions using detailed kinetics and a discrete sectional method-based soot model. A detailed analysis of various soot sub-processes was conducted to acquire insights into the associated mechanism. The dynamic response of soot to externally imposed fluctuating curvature was successively studied in a wide range of conditions. The present numerical study revealed some interesting findings which can be summarized as follows:

The numerical results for steady counterflow flames showed that in presence of curvature, due to a change in the surface area along the flame, the velocity of soot particles is significantly altered. For negatively curved (center of curvature lies in the fuel-rich side of the flame front) flames, the soot particle velocity is found to be lowered compared to that in a flat flame. The lowered soot velocity leads to an enhanced residence time in the soot formation zone and consequently contributes to higher soot volume fractions. Furthermore, the flame curvature strongly affects the differential transport of soot particles with respect to the gas phase, due to their high Schmidt numbers. For negative curvature, soot particles are differentially transported towards the lower mixture fractions, leading to their accumulation within the soot formation zone (characterized by region in Z-space with large rates of soot sub-processes). Soot displaced towards the soot formation zone grows predominantly by surface reactions leading to increased soot mass and volume fractions. Subsequent to surface growth, the curvature-induced transport of large-sized particles also promotes their coagulation which further contributes to the increase in the soot surface area available for surface growth reactions. Positive curvature on the other hand exhibits the opposite behavior causing lowered soot concentration. Negative curvature leads to a synergistic increment in soot volume fractions at lower strain rates compared to their flat flame counterparts, indicating strong complementary effects of strain rate and curvature. On the contrary, in positively curved flames, such synergistic effects are hardly exhibited.

The imposed curvature oscillations tend to increase the soot concentration compared to steady-state conditions. Curvature fluctuations significantly impact the distribution of soot within the flame. At lower frequencies the response of soot to curvature oscillations is quasi-steady. At intermediate oscillation frequencies, the dynamic response of soot is phase-lagged, and the phase-shift in the induced oscillations tends to increase with frequency. The overall response of soot volume fraction is recognized to be predominantly governed by the evolution of larger-sized particles owing to their large chemical time scales. With an increase in the imposed frequency, the dynamic response of soot gets attenuated leading to the lowered amplitudes of the induced oscillations. When the frequency of imposed fluctuations is sufficiently large, soot particles do not adequately respond to the faster curvature fluctuations, and the soot response becomes decoupled from curvature. A more complex flow-flame-soot

interaction is observed when the flame is subjected to simultaneous strain rate and curvature fluctuations. For in-phase strain rate-curvature oscillations, the soot formation is enhanced due to the complementary effects of strain and curvature. At unequal frequencies, on the other hand, the locally adverse/favorable conditions encountered by the soot formation process during transient evolution govern the overall dynamic response of the soot.

In conclusion, the present work demonstrates that the soot response in curved counterflow flames is strongly correlated to the residence time of soot particles in the soot formation zone and differential diffusion effects. The discrete sectional method-based model provides important insights into the curvature effects on the soot particle size distribution. Furthermore, the sectional model facilitates the investigation of the damped and delayed response of soot to oscillating curvature in correlation with the variability in the response of different-sized soot particles.

It is important to recognize that, although the retained soot modeling approach is state-of-the-art, due to the lack of reliable experimental validation, it may still present certain undiscovered limitations in capturing physics related to curvature effects in its entirety, and thus, to establish the general consensus about the presented conclusions. Therefore, the analysis concerning the role of different soot sub-processes in curvature effects may depend on the employed soot model in conjunction with the gas-phase kinetics. Moreover, it is worth highlighting that although a simplified 1-D analysis was conducted to study curvature unsteadiness, the chosen frequency modes or curvature values in the counterflow setup were not explicitly analyzed concerning the turbulent combustion regime. Hence, a direct correlation of this laminar flame study to turbulent combustion is unexplored at the moment, and further fundamental studies are therefore still necessary. Nevertheless, the analysis of unsteady curvature effects on soot can be recognized as a step forward for a better understanding of the interactions between soot kinetics and fluid dynamics to guide further modeling efforts.

5

Coupling of sectional soot model with FGM chemistry

Discrete sectional method (DSM) based soot models are computationally demanding since several transport equations are required to be solved for sectional soot variables using large chemical kinetic mechanisms. To achieve computationally efficient chemistry reduction for combustion simulations, in this chapter, the sectional soot model is coupled with the Flamelet Generated Manifold (FGM) tabulated chemistry. Different approaches are explored for incorporating soot-gas phase coupling with FGM chemistry, and a comprehensive assessment of these FGM-DSM approaches is conducted for their predictive accuracy and computational performance in simulations of laminar ethylene counterflow flames. The content of this chapter is published in Combustion and Flame [193] as 'An assessment of the sectional soot model and FGM tabulated chemistry coupling in laminar flame simulations'.

5.1   Introduction

In addition to soot concentration, the central focus of future emission norms will be on regulating the soot particle size and number density. Therefore, in recent years, there is a great interest in the advancement of detailed soot models to capture the accurate size distributions of soot particles in combustion processes. The accurate description of the collision phenomenon associated with the soot particles is a critical and computationally intensive aspect of detailed soot modeling. To effectively capture particle dynamics, several numerical techniques such as the method of moments (MOM) [14, 65, 194], discrete sectional methods [35, 39, 68, 71, 72], Monte Carlo (MC) [195, 196] have been proposed in the literature. In the discrete sectional method, the accuracy of particle size description can be improved by increasing the number of sections used. However, adding more sections also increases the number of transport equations to be solved for soot variables (mass fraction/number density). Hence, the trade-off between computational cost and approximate accuracy becomes

an important factor in the application of sectional models to multi-dimensional combustion simulations.

Besides particle dynamics, the detailed modeling of soot formation processes demands accurate predictions of gas-phase soot precursors. Therefore, to correctly predict the concentrations of soot precursors and other major species associated with the soot growth and oxidation processes, detailed kinetic schemes involving hundreds of species and thousands of elementary reactions are required in combustion simulations. However, solving combustion chemistry by transporting such a large number of species poses a principal challenge in terms of computational cost. Therefore, the use of detailed kinetic mechanisms is practically not feasible in large-scale combustion simulations considering their computational grid requirements. Moreover, a wide range of time scales associated with the formation of chemical species and fluid mixing introduces additional complexities in their numerical treatment. In this context, the flamelet-based tabulated chemistry approaches have proved to be effective and widely used chemistry-reduction strategies to simulate flames in terms of reduced computational cost and good precision level.

Over the past decade, in many of the numerical simulations investigating soot formation, various approaches of modeling flamelet-based tabulated chemistry with semi-empirical and detailed soot models have been proposed [36, 65, 73, 197–199]. In an earlier study, Dorey et al. [197] adopted FPI (Flame Prolongation of ILDM) tabulated chemistry coupled with a semi-empirical, two-equation soot model for estimating soot formation in ethylene premixed flames. In their approach, the mass exchange between the soot and gas phase was incorporated by transporting additional equations for the species involved in the soot model. Dupoirieux and Bertier [199] later validated this strategy in LES of the DLR burner used by Geigle et al. [200]. In LES of swirl-stabilized ethylene-air flames, Franzelli et al. [201] compared the performance of the full tabulation approach and the hybrid method proposed by Lecocq et al. [202], using a two-equation soot model. Besides steady flamelet-based models, unsteady/interactive flamelet-based techniques [35, 203] have also been explored for modeling sooting flames and have shown good agreement with experiments. However, many of the existing flamelet-based tabulated chemistry approaches employed for soot modeling, have been examined under turbulent flame conditions. Therefore it is of interest to assess the performance of tabulated chemistry-based soot modeling methods in more simplified canonical configurations by isolating the influence of additional complexities induced by turbulence. Such analysis is critical to identify the limitations of specific approaches and underlying mechanisms behind the disparity in the accuracy associated with them before extending to turbulent conditions.

Concerning detailed soot models, Mueller and Pitsch [65, 66] applied an integrated kinetics-based LES approach with the Hybrid Method of Moments (HMOM)-based soot model, and Radiation Flamelet Progress Variable (RFPV) tabulated chemistry for soot prediction in a gas turbine combustor. In their strategy, an additional transport equation was introduced to model the PAH during the soot formation by assuming

a quasi-steady state of PAH dimers. This lumped PAH transport approach is widely used when considering tabulated chemistry models for sooting flames. It has also been extended to the sectional methods-based soot model by Rodrigues et al. [73]. Recently, Wick et al. [204] conducted a combined a-priori and partial a-posteriori analysis of errors in soot predictions associated with the flamelet-based combustion model FPV [81], using DNS data of a temporally evolving turbulent jet diffusion flame. The quantitative uncertainties in soot predictions were mainly related to the accuracy of the chemical mechanism in capturing the PAH formation and modeling the PAH source term for PAH-based processes (nucleation and condensation).

Although many flamelet-based techniques have been applied for modeling sooting flames and are even widely used, there is still no general agreement about the best approach. Hence, it is of interest to devote further efforts in identifying alternative strategies to accurately model the contributions of soot-related processes with somewhat different tabulated chemistry methods. In this regard, modeling sooting flames with FGM tabulated chemistry would be of interest. There have been limited studies on coupling FGM tabulated chemistry with soot models for applications to diffusion flames [97,205] and spray combustion [206]. Notably, Zimmer [97] explored various strategies for storing soot information in the FGM database for application to laminar diffusion flames. The approach of storing the rates associated with individual soot processes showed a good qualitative agreement between the FGM and detailed chemistry solutions. However, these studies were based on semi-empirical soot models and thus, emerge as inadequate in terms of capturing particle size distributions. The coupling of the FGM tabulated chemistry with a sectional method-based soot model has not been fully explored, which essentially motivates the current study.

This chapter aims to present different approaches for coupling the FGM tabulated chemistry with the sectional soot model and assess their performance for the accuracy of soot prediction and the overall CPU time. The soot characteristics obtained from proposed FGM-DSM strategies are compared against the experimental measurements from the literature and corresponding detailed chemistry solutions to examine their predictive capabilities for the soot formation in laminar counterflow flames. Furthermore, the accuracy of FGM-DSM coupling approaches is evaluated for variations in strain rate and reactants composition. The effects of preferential diffusion on the soot prediction in a laminar counterflow diffusion flame are investigated by employing different transport modeling approaches. Moreover, the dynamic response of soot formation to unsteady conditions is investigated for various FGM-DSM approaches.

5.2 Numerical methodology

5.2.1 Flamelet Generated Manifold chemistry

The FGM approach proposed by van Oijen and de Goey [184,207,208] based on the classical flamelet concept [209] is used for the tabulated chemistry. In FGM, a low-

dimensional manifold is generated from the solutions of one-dimensional flamelet equations. The thermo-chemical variables of the system are then stored in the manifold as functions of suitable controlling variables (ϕ). During the numerical simulation, the transport equations are solved for these control variables altogether with the fluid flow and state equations, while the thermo-chemical parameters are retrieved from the generated manifold [184]. Therefore, conducting sooting flame simulations with FGM chemistry involves the following key steps.

Computation of flamelets and manifold generation

In the first step, 1-D laminar flamelets (steady and unsteady) suitable for the combustion system under consideration (premixed/non-premixed) are computed with a detailed chemistry model. Based on the FGM-DSM coupling strategy, which will be discussed later, partial or entire soot kinetics can be included in the flamelet computation. The second step consists of building a manifold from the computed flamelets to describe the thermochemical structure of the flame via control variables. In FGM, the choice of representative flamelets and control variables depends on the combustion system to which it is being applied. For non-premixed flames, the mixture fraction Z, and reaction progress variable $\mathcal{Y}$, are considered as the most relevant control variables, describing mixing and chemical reaction processes, respectively. Here, the mixture fraction Z is expressed in terms of the element mass fractions following Bilger's [188] definition

$$Z = \frac{Z^* - Z_o^*}{Z_f^* - Z_o^*} \quad \text{with} \quad Z^* = 2\frac{Z_\text{C}}{W_\text{C}} + \frac{1}{2}\frac{Z_\text{H}}{W_\text{H}} - \frac{Z_\text{O}}{W_\text{O}}, \tag{5.1}$$

where Z_j and W_j denote, respectively, the elemental mass fractions and atomic weights of element j. The subscripts f and o represents quantities for fuel and oxidizer, respectively.

For the reaction progress variable $\mathcal{Y}$, the necessary constraint is that it should be monotonous from the unburned state to the chemical equilibrium state to facilitate an unambiguous mapping of dependent variables. For the present study, a suitable progress variable is chosen as a linear combination of species mass fractions Y_j with

$$\mathcal{Y} = \sum_j \alpha_j Y_j \tag{5.2}$$

where α_j are weight factors for the species j. The choice of α_j is not unique, and several combinations resulting in monotonous $\mathcal{Y}$ definition are possible [184]. The values of α_j are often determined following the guess-and-check approach or using optimization methods [210]. Important thermo-chemical parameters $\psi(Z, \mathcal{Y})$ of the system are then mapped onto these control variables and stored in the flamelet database, following the procedure described in van Oijen et al. [184].

Coupling with soot model (FGM-DSM)

After the creation of the database manifold, FGM tabulated chemistry is linked to a CFD code. During the run-time, first, the FGM database is loaded into memory. Subsequently, transport equations are solved for the control variables, together with continuity, momentum, and sectional soot mass fractions. Transport of enthalpy can be avoided by tabulation of h in the manifold. The transport equations for Z and $\mathcal{Y}$ can be expressed as:

$$\frac{\partial(\rho Z)}{\partial t} + \nabla \cdot (\rho \boldsymbol{u} Z) - \nabla \cdot \left(\frac{\lambda}{c_p} \nabla Z\right) = \nabla \cdot (\mathcal{D}_Z \nabla Z) \tag{5.3}$$

$$\frac{\partial(\rho \mathcal{Y})}{\partial t} + \nabla \cdot (\rho \boldsymbol{u} \mathcal{Y}) - \nabla \cdot \left(\frac{\lambda}{c_p} \nabla \mathcal{Y}\right) = \nabla \cdot (\mathcal{D}_{\mathcal{Y}} \nabla \mathcal{Y}) + \dot{\omega}_{\mathcal{Y}} \tag{5.4}$$

where $\dot{\omega}_{\mathcal{Y}} = \sum_j \alpha_j \dot{\omega}_j$ denote source term for progress variable. The first term on the right-hand side represents the preferential diffusion flux and is assumed to be only a function of the gradient of the main control variable (Z here). This is a model simplification based on the 1-D flamelet assumption. The preferential diffusion coefficient $\mathcal{D}_\phi$ for control variable (ϕ) is modeled as:

$$\mathcal{D}_\phi = \left[\sum_j -\rho \alpha_j \boldsymbol{V_j} Y_j - \left(\frac{\lambda}{c_p} \nabla \phi\right)\right] \Big/ \nabla Z \tag{5.5}$$

The terms $\mathcal{D}_\phi$ are computed from the laminar flamelets. Besides source terms and preferential diffusion coefficients, thermo-chemical parameters (e.g. ρ, c_p, λ) required for the solution of the transport equations are retrieved from the FGM database.

For sooting flame simulations, the concentrations of essential gas phase species (e.g. A4, C_2H_2, H_2, O_2, OH, etc.) involved in soot formation processes are also included in the FGM database. The retrieved species and thermo-chemical parameters are subsequently provided as an input to the soot model for computations of the source terms in the sectional soot transport equations:

$$\frac{\partial(\rho Y_{s,i})}{\partial t} + \nabla \cdot (\rho(\boldsymbol{u} + \boldsymbol{V_T}) Y_{s,i}) = \nabla \cdot (\rho D_{s,i} \nabla Y_{s,i}) + \dot{\omega}_{s,i} \quad \forall \quad i \in [1, N_{sec}] \tag{5.6}$$

Since the soot particles are formed from the processes involving contributions from various gas-phase species, the concentrations of these gas-phase species also get affected as a result of soot formation. Therefore, including this two-way coupling of the soot and gas phase is a critical aspect of soot modeling in combustion simulations. In the case of detailed chemistry, transport equations for all the gas-phase species are solved. Thus, the consumption of gas phase species associated with the soot formation can be straightforwardly incorporated in the chemical source terms of their transport equations. On the other hand, in a tabulated chemistry approach such as FGM, the species data is looked-up from a pre-computed manifold. Consequently, a special

Table 5.1: Key features of the soot model and chemistry coupling approaches.

Coupling type	Contribution of soot to gas phase	Soot processes included in flamelets	Soot transport
Detailed	Fully included during the run-time	Not applicable	Yes
FGM-Unc	Not included	None	Yes
FGM-Tran	Partially included by transporting PAH	None	Yes
FGM-Nuc	Partially included in the manifold	Nucleation	Yes
FGM-Full	Fully included in the manifold	All sub-processes	Yes

treatment is required to include the soot-gas phase coupling, which can influence the predictive capabilities of the soot model. Concerning this, different approaches of FGM-DSM coupling, listed in Table 5.1, are investigated for their predictive accuracy and computational performance. The key features of these approaches can be summarized as:

- **FGM-Unc**: In the FGM-Unc approach, the FGM database is generated using gas-phase flamelets without soot formation kinetics. Concentrations of relevant gas-phase species (e.g., A4, C_2H_2, H_2, O_2, OH, etc.) are retrieved from the manifold, and transport equations are solved for sectional soot mass fractions. However, the coupling between the soot and gas-phase for the mass exchange of concerned species is not considered. Since the nucleation process is modeled through PAH dimerization, the soot prediction is particularly sensitive to the concentration of PAH. The unaccounted consumption of gas-phase PAH associated with soot nucleation and condensation results in its surplus, and may lead to the overprediction of soot.

- **FGM-Tran**: The DNS study of Bisetti et al. [41] revealed that the unsteady mixing in turbulent flows tends to affect the PAH concentrations significantly. Therefore the dependence of PAH on turbulence-chemistry interactions needs to be appropriately modeled. Species with relatively slow chemistry, such as PAH, show a delayed response to rapid changes in the turbulent flow field. As a result, the slower time scales of PAH formation compared to other gas-phase species often violate the fast chemistry assumption in flamelet-based tabulated chemistry approaches [204]. To model the unsteady effects, an additional transport equation is generally solved for PAH species following the approach proposed by Ihme and Pitsch [211] for NO chemistry. The PAH transport equation used here is given by:

$$\frac{\partial(\rho Y_{\text{PAH}}^{\text{tran}})}{\partial t} + \nabla \cdot \left(\rho \boldsymbol{u} Y_{\text{PAH}}^{\text{tran}}\right) - \nabla \cdot \left(\frac{\lambda}{c_p Le_{\text{PAH}}} \nabla Y_{\text{PAH}}^{\text{tran}}\right) = \dot{\omega}_{\text{PAH}} \qquad (5.7)$$

where Le_{PAH} is computed from the mixture-averaged diffusivity of PAH species and stored in the manifold as a function of Z and $\mathcal{Y}$. The chemical source term of the PAH transport equation can be generally expressed as:

$$\dot{\omega}_{\mathrm{PAH}} = \dot{\omega}_{\mathrm{PAH}}^{\mathrm{gas}} + \dot{\omega}_{\mathrm{PAH}}^{\mathrm{soot}} \tag{5.8}$$

where the first term on the right-hand side, $\dot{\omega}_{\mathrm{PAH}}^{\mathrm{gas}}$, indicate the contribution from gas-phase reactions, and the second term, $\dot{\omega}_{\mathrm{PAH}}^{\mathrm{soot}}$, denotes the consumption of PAH though soot formation processes (nucleation and condensation). The $\dot{\omega}_{\mathrm{PAH}}^{\mathrm{gas}}$ term is computed through tabulated (tab superscript) production ($\dot{\omega}_{\mathrm{PAH}}^{\mathrm{gas},+}$) and consumption ($\dot{\omega}_{\mathrm{PAH}}^{\mathrm{gas},-}$) rates as:

$$\dot{\omega}_{\mathrm{PAH}}^{\mathrm{gas}} = \left[\dot{\omega}_{\mathrm{PAH}}^{\mathrm{gas},+}\right]^{\mathrm{tab}} + \left(\frac{Y_{\mathrm{PAH}}^{\mathrm{tran}}}{Y_{\mathrm{PAH}}^{\mathrm{tab}}}\right)\left[\dot{\omega}_{\mathrm{PAH}}^{\mathrm{gas},-}\right]^{\mathrm{tab}} \tag{5.9}$$

where the consumption rate $\dot{\omega}_{\mathrm{PAH}}^{\mathrm{gas},-}$ is linearized with the tabulated ($Y_{\mathrm{PAH}}^{\mathrm{tab}}$) and transported ($Y_{\mathrm{PAH}}^{\mathrm{tran}}$) values of PAH (A4) mass fraction since A4 consumption via gas-phase reactions usually scales linearly with A4 concentration. The term $\dot{\omega}_{\mathrm{PAH}}^{\mathrm{soot}}$ in Eq. 5.8, representing the contribution from soot formation processes can be treated in different ways. In some of the studies [65, 73, 204], tabulated rates of dimer formation have been used as an additional consumption term in the PAH transport equation to include the influence of PAH-based soot growth processes. However, in the present study, we compute $\dot{\omega}_{\mathrm{PAH}}^{\mathrm{soot}}$ during the simulation run-time as done in the detailed chemistry case. The $\dot{\omega}_{\mathrm{PAH}}^{\mathrm{soot}}$ term, thus, includes the contributions from the soot nucleation and PAH condensation processes. Note that the number density of PAH required for the computations of nucleation and condensation rates is calculated based on transported PAH mass fractions. The linearization of $\dot{\omega}_{\mathrm{PAH}}^{\mathrm{soot}}$ term is not applied as in previous studies, because it is computed during run-time and not retrieved from the database. For the FGM-Tran approach, the manifold is built from the gas-phase flamelets without soot formation (same as the FGM-Unc case).

- **FGM-Nuc**: Solving additional transport equations to account for the soot-gas coupling can lead to increased computational cost. Therefore, the FGM-Nuc approach is proposed in this study to partially include the effect of gas-phase PAH extraction by the soot model. It is observed that the change in PAH concentration due to soot processes is substantially higher compared to other major species such as C_2H_2, O_2, H_2O. Hence, to avail the advantage in terms of model accuracy at a lower computational cost, the consumption of PAH through the soot nucleation process is accounted for in the manifold generation step. Accordingly, for the FGM-Nuc approach, the contribution of soot nucleation to PAH and H_2 concentrations are included in their respective transport equations while simulating flamelets for the manifold creation. Subsequently, the resulting PAH mass fractions are stored in the FGM table. During run-time, the tabulated

PAH concentration is directly used in the soot model for the computation of nucleation and condensation rates. Since the soot nucleation source term only depends on gas-phase, soot modeling is not required in the manifold generation stage. It is to be noted that in addition to nucleation, the condensation process also leads to the consumption of PAH. However, the condensation rates also depend on soot parameters such as soot number density. Its inclusion, thus, increases the duration of manifold generation, as additional transport equations need to be solved during flamelets creation to compute related soot parameters. Therefore, the contribution from soot nucleation alone is considered, for the computational simplicity of the manifold generation stage.

- **FGM-Full**: In the FGM-Full approach, the contribution of soot in the consumption of all the relevant gas-phase species is included in the manifold generation step. Therefore, in addition to gas-phase species, transport equations for soot mass fractions are also solved during the flamelet simulations with the same soot model parameters as employed for the detailed chemistry simulations. The concentrations of important gas-phase species related to the soot formation process are then tabulated in the FGM table. Since the soot model is included in its entirety during the flamelet generation, the tabulated concentrations of gas-phase precursors species reflect their more accurate prediction. During the FGM simulation run, the tabulated concentrations of these species are looked-up from the FGM database and used as an input to the soot model for the computations of soot source terms. With the FGM-Full approach, the accuracy of soot prediction is expected to improve as the tabulated gas-phase species concentrations are predicted with a higher level of accuracy. However, since contributions from all the soot processes are included in the flamelets, the manifold generation process becomes computationally more intensive to some extent.

- **FGM-Read**: In the FGM-Read approach, flamelets are solved with the complete sectional soot model (as done in the FGM-Full case), and in addition to relevant gas-phase species, the values of sectional soot mass fractions, $Y_{s,i}$, are stored in the manifold. Due to the inclusion of the full soot model in the manifold generation stage, the concentrations of gas-phase species relevant to the soot model are well predicted in FGM-Read, as their consumption through soot formation processes is incorporated in the manifold. Moreover, during FGM simulation run-time, the values of sectional soot mass fractions ($Y_{s,i}$) are looked-up directly from the manifold. Since the soot mass fraction values are explicitly retrieved from the manifold, no additional transport equations are required to be solved for sections when the FGM-Read approach is applied. As a result, a significant reduction in computational time can be achieved.

A schematic of the FGM-DSM coupling (except for FGM-Read) is presented in Fig. 5.1. In the schematic diagram, ϕ_j, $\dot{\omega}_{\phi_j}$ represent control variables and their source terms, respectively. The flamelet database of thermochemical variables is denoted as ψ, while Y_k represents gas phase species k, and $Y_{s,i}$ are sectional soot mass fractions.
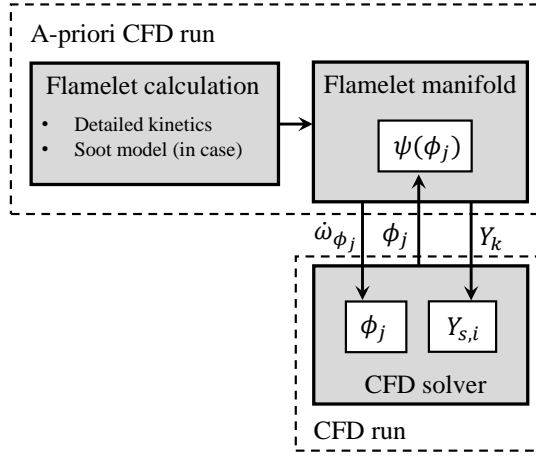
Figure 5.1: Schematic representation of the FGM-CDSM method.

5.2.2 Investigated flames

In total, six ethylene counterflow flames are simulated for the assessment of the FGM-DSM coupling strategies. The potential flow approximation is used for the boundary conditions in the quasi-1-D formulation of the counterflow configuration. The details of the studied flames are summarized in Table 5.2. The chosen target flames also facilitate the variation of strain rate and the change in reactants composition for additional verification of the FGM-DSM coupling approaches. The detailed kinetic mechanism, KAUST Mech 2.0 (KM2) [105], is retained for all the simulations reported in the present study. A mixture-averaged approximation is used for modeling species diffusion transport during flamelet generation as well as sooting flame simulations.

Table 5.2: Description of target flames modeled.

Flame	Fuel $X_{C_2H_4}$ / X_{N_2}	Oxidizer X_{O_2} / X_{N_2}	a [s^{-1}]	Reference
CDF-1	1.0 / 0.0	0.25 / 0.75	120	Wang et al. [27]
CDF-2	1.0 / 0.0	0.25 / 0.75	90	Wang and Chung [113]
CDF-3	1.0 / 0.0	0.25 / 0.75	150	Wang and Chung [113]
CDF-4	1.0 / 0.0	0.25 / 0.75	180	Wang and Chung [113]
CDF-5	0.8 / 0.2	0.25 / 0.75	120	Wang and Chung [114]
CDF-6	1.0 / 0.0	0.30 / 0.70	120	Xu et al. [115]

5.2.3   Manifold verification

In the FGM simulations, the choice of progress variable is of great importance as it essentially determines the soundness of the mapped thermodynamic state of the mixture in the manifold. Hence, prior to discussing the results for FGM-DSM coupling approaches, the important features of thermo-chemical parameters stored in FGM manifolds are illustrated. In the present study, the definition of progress variable $\mathcal{Y}$ (Eq. 5.2) is obtained through a guess and check method, mainly based on previous experience. Here, $\mathcal{Y}$ is defined based on H_2O, CO_2, CO, O_2, H_2, and A4 species mass fractions with their corresponding weight factors $\alpha_{H_2O} = 0.0555$, $\alpha_{CO_2} = 0.0228$, $\alpha_{H_2} = 0.3$, $\alpha_{CO} = 0.0357$, $\alpha_{A4} = 0.0988$, $\alpha_{O_2} = -3.13 \times 10^{-3}$. In general, the standard definitions of $\mathcal{Y}$ are expressed by the major combustion product species such as H_2O, CO_2, CO, H_2. However, since A4 is the PAH species in the current soot model, the contribution of A4 is considered in the present progress variable definition to improve the mapping of its chemical source term evolution. The current choice of $\mathcal{Y}$ facilitates the unique mapping of the thermo-chemical variables in the Z–$\mathcal{Y}$ space. The influ-
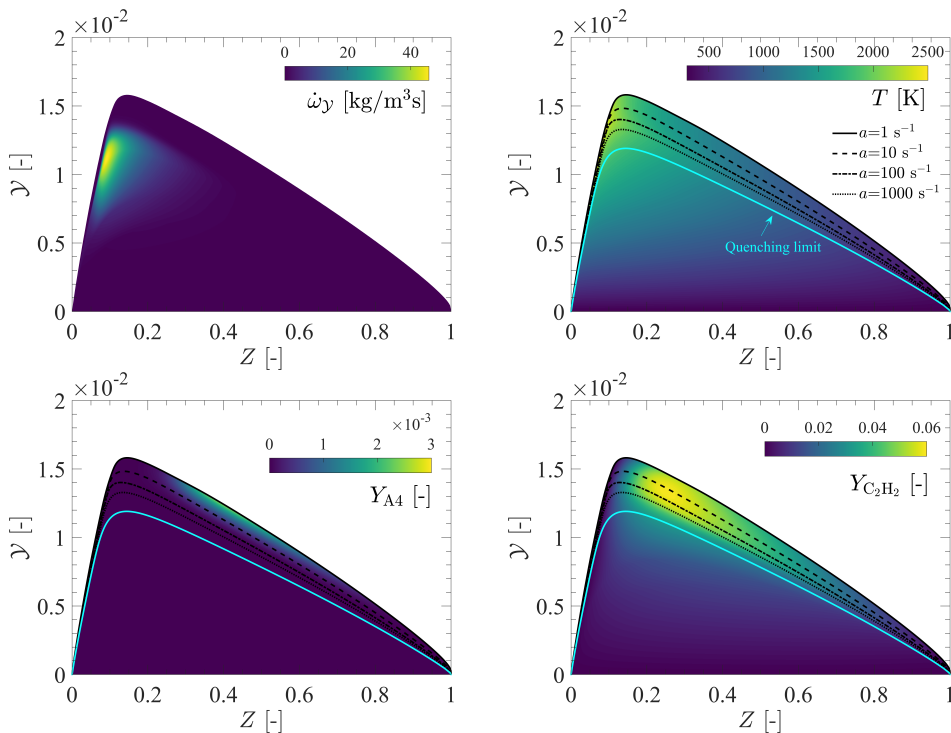
Figure 5.2: Manifold visualization for progress variable source term $\dot{\omega}_{\mathcal{Y}}$, temperature, A4 mass fractions, and C_2H_2 mass fractions as function of Z and $\mathcal{Y}$ for the CDF-1 flame. Results of Z and $\mathcal{Y}$ reconstructed from detailed flamelets are presented for the strain rate of $1\,\mathrm{s}^{-1}$, $10\,\mathrm{s}^{-1}$, $100\,\mathrm{s}^{-1}$, $1000\,\mathrm{s}^{-1}$ and $2800\,\mathrm{s}^{-1}$ (quenching limit).
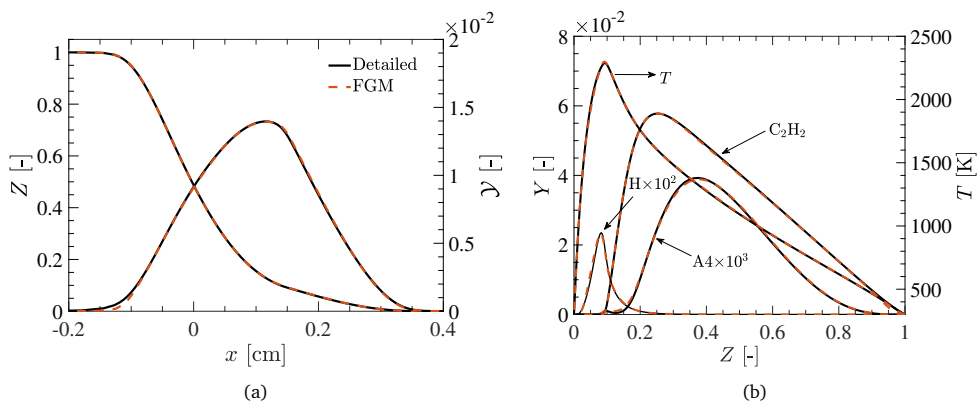
Figure 5.3: Comparison of FGM and detailed solutions for mixture fraction Z and $\mathcal{Y}$ profiles (a), and key chemical species mass fractions and temperature (b) in the CDF-1 flame (without the soot formation).

ence of $\mathcal{Y}$ definition on the accuracy of soot prediction by FGM-DSM approaches is highlighted in Section 5.3.

The manifold is constructed from the solutions of steady and unsteady adiabatic counterflow diffusion flamelets. The steady flamelets are simulated by varying the applied strain rate (a) from a very low value ($a = 1\,\mathrm{s}^{-1}$) representing the composition state close to chemical equilibrium until an extinction limit ($a \rightarrow 2800\,\mathrm{s}^{-1}$). Since the counterflow diffusion flamelets extinguish beyond the extinction strain rate, the composition space between the most strained flamelet and the quenched mixing limit is covered by using an unsteady formulation of flamelets. The time-dependent solutions of flamelets are thus stored until the solution reaches the mixing limit (where there is no reaction). The FGM database is stored using a $400{\times}400$ rectilinear discretization of the normalized Z–$\mathcal{Y}$ space. Important thermo-chemical parameters $\psi(Z, \mathcal{Y})$ of the system are then mapped onto these two control variables using linear interpolation. For simplicity and robustness, a bilinear interpolation procedure is used to look up the thermo-chemical variables from the manifold during simulation run-time. Figure 5.2 presents the progress variable source term $\dot{\omega}_{\mathcal{Y}}$, temperature, C_2H_2, and A4 mass fractions stored in the manifold as a function of Z and $\mathcal{Y}$ for the CDF-1 flame. The contours of temperature and progress variable source terms show a peak near the oxidizer side (Z close to zero), whereas the A4 concentration is more prominent near the sooting zone ($Z \simeq 0.3$–0.5) for flamelets at very low strain rates. Besides, the flamelets for the strain rates ranging from $1\,\mathrm{s}^{-1}$ to $1000\,\mathrm{s}^{-1}$ demonstrate the monotonicity of the progress variable necessary for the unique mapping of stored variables in the Z–$\mathcal{Y}$ space. The higher concentrations of C_2H_2 within strain rates $1\,\mathrm{s}^{-1}$ to $100\,\mathrm{s}^{-1}$ denote the composition space pertinent to a higher amount of soot formation. Note that the A4 mass fraction distribution is very narrow in the FGM composition space, which indicates that the evaluation of PAH-based processes is particularly sensitive to the accurate retrieval of A4 mass fractions during simulation run-time.

Furthermore, an analysis is conducted to verify the solutions of control variable transport equations obtained from the FGM approach. Accordingly, the profiles of mixture fraction (Z), progress variable ($\mathcal{Y}$), and temperature obtained from FGM solutions for CDF-1 flame (without soot) are compared against the detailed chemistry counterparts in Fig. 5.3. It can be observed that the FGM simulations reproduce the detailed chemistry solutions for the control variables (Z, $\mathcal{Y}$) and temperature with good accuracy. Moreover, the profiles of species involved in the soot formation process are reproduced well by FGM chemistry. Only a marginal deviation is observed in detailed and FGM profiles of progress variable near $x \simeq -0.15$ cm ($Z \simeq 1$), as the mixture composition approaches pure fuel conditions. This essentially underlines the good capability of the FGM in predicting the thermo-chemical composition space of the manifold relevant to the soot formation.

5.3 Assessment of FGM-DSM coupling: steady flames

5.3.1 Comparison of different FGM-DSM approaches

In this section, the performance of various FGM-DSM coupling strategies described in Section 5.2.1 is examined for the accuracy of soot prediction in the target flames. First, the results obtained through the FGM-Unc coupling approach for the CDF-1 flame are evaluated, to identify the impact of neglecting gas phase consumption of PAH on the overall soot formation prediction. In Fig. 5.4, the computed profiles of soot volume fraction, number density, and particle size for the FGM-Unc approach are presented along with the detailed chemistry solution and experimental measurements. It can be observed that the soot volume fractions are overpredicted by almost an order of magnitude compared to their measured values and detailed chemistry counterparts. Such a drastic deviation in the predicted soot concentration is expected since the consumption of gas-phase species (PAH in particular) due to soot formation is not included in the FGM-Unc approach. The overpredicted PAH concentration significantly increases the soot nucleation rate, number density, and consequently, the overall soot concentration. The obtained results essentially emphasize the need for appropriate treatment of soot-gas phase coupling in tabulated chemistry solutions. As evident, the FGM-Unc approach fails to accurately capture the soot formation. Henceforth, the FGM-Unc results are not discussed further.

Next, the FGM-Tran and FGM-Nuc approaches are examined, in which the feedback of PAH consumption to the gas phase is partially accounted for by solving a transport equation for PAH, and via the inclusion of soot nucleation during manifold generation respectively. In Fig. 5.5, the computed profiles of soot parameters for CDF-1 flame with different FGM-DSM coupling strategies are compared with the detailed chemistry results and experimental measurements. Both FGM-Tran and FGM-Nuc approaches show an overestimation of soot quantities. Besides flamelet-induced errors, such a quantitative disparity is mainly a consequence of intrinsic differences in strate-
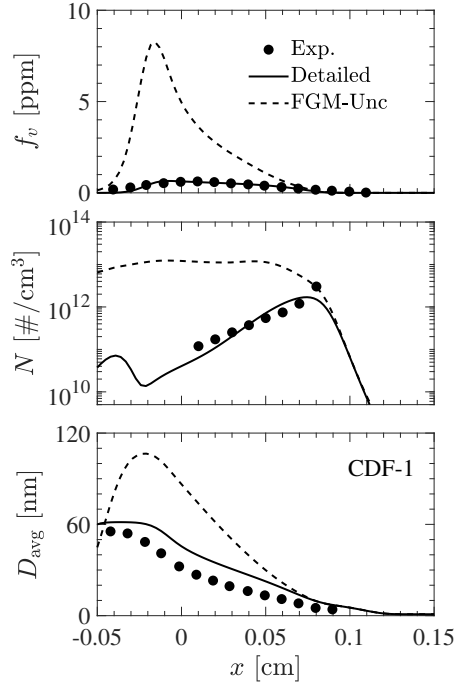
Figure 5.4: Measured and computed profiles of soot volume fraction, soot number density, and soot particle diameter (c) for the CDF-1 flame with the FGM-Unc approach.

gies employed for including soot-gas coupling in them. Note that, in the FGM-Nuc approach, the consumption of PAH, and production of H_2 due to nucleation is accounted for during the manifold generation step. On the other hand, in FGM-Tran, the consumption of PAH through soot nucleation and condensation is introduced during the run-time by solving the PAH transport equation. However, the FGM-Nuc approach appears to show a better prediction of soot concentration compared to the FGM-Tran approach. The important factors responsible for such behavior can be explained through mass fraction distributions of A4 and C_2H_2 species involved in the soot model (refer to Fig. 5.6).

From Fig. 5.6a it can be observed that the concentration of PAH (A4) predicted by FGM-Tran is somewhat higher than the one obtained in FGM-Nuc. To identify the extent of disparity in the PAH concentrations predicted by FGM-Tran and FGM-Nuc, the results for A4 mass fractions, obtained for detailed chemistry and FGM-Tran cases without the inclusion of PAH condensation process, are compared in Fig. 5.7. Note that in FGM-Tran, the contributions of both nucleation and PAH condensation are included in the chemical source term of the PAH transport equation (Eq. 5.8). Therefore FGM-Tran is expected to predict the PAH concentration better than FGM-Nuc, wherein only the contribution of soot nucleation is included. However, it can be observed from
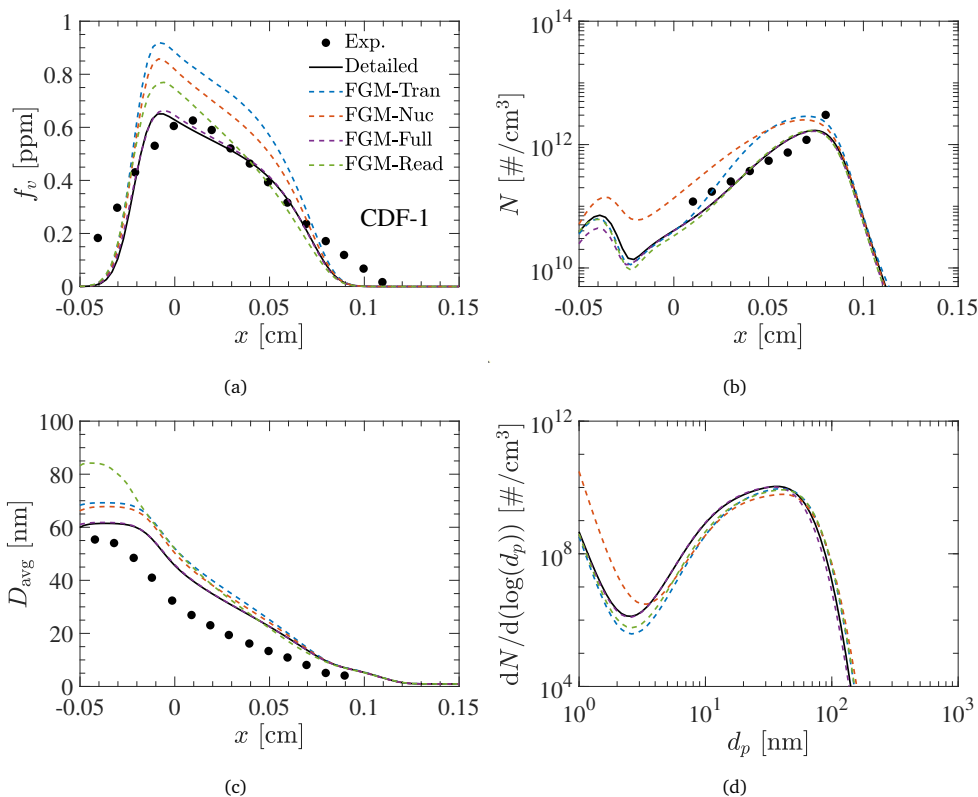
Figure 5.5: Measured and computed profiles of soot volume fraction (a), number density (b), average particle diameter (c), and particle size distribution function (PSDF) (d) for the CDF-1 flame with FGM-DSM coupling approaches. PSDF is taken at the maximum f_v position.

Fig. 5.7 that the concentration of PAH in FGM-Tran after consumption through both the PAH-related processes (nucleation and PAH condensation) is slightly higher than the PAH concentration obtained in FGM-Nuc. It essentially indicates that solving a transport equation for the PAH, although provides a partial coupling for gas and soot phase, its accuracy of the PAH prediction is somewhat inferior compared to when the entire process of soot nucleation is computed during the flamelet generation stage. In addition to the numerical accuracy in the retrieval of various thermo-chemical parameters associated with the PAH transport equation under the FGM chemistry, the discrepancies in the prediction of PAH for FGM-Tran could be associated with the following factors:

i) In the FGM-Tran method, the $\dot{\omega}_{\mathrm{PAH}}^{\mathrm{soot}}$ is computed from the transported PAH mass fractions. Therefore, the effect of PAH consumption through the soot process on the detailed kinetics associated with its formation in the gas phase can not be well captured. In other words, the effect of PAH consumption through soot processes on its

(a)   (b)
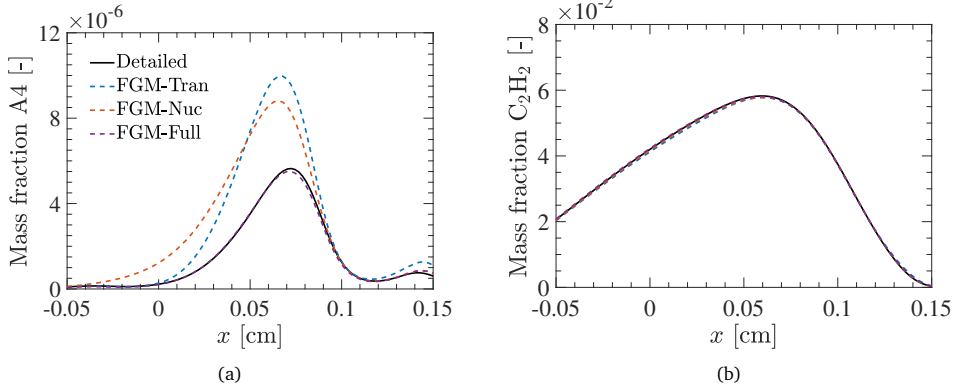
Figure 5.6: Computed profiles of A4 (a), and C_2H_2 (b) mass fractions for the CDF-1 flame under different FGM-DSM coupling approaches.
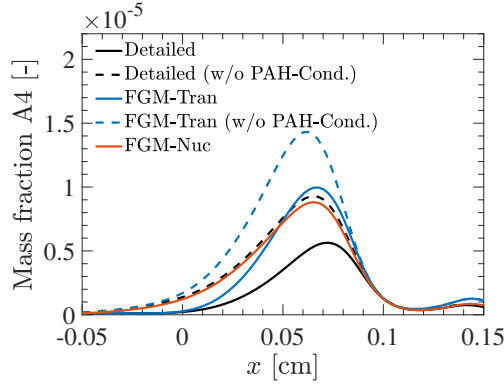
Figure 5.7: Comparison of the A4 mass fractions predicted by FGM-Tran and detailed chemistry with and without the inclusion of the PAH condensation process against the FGM-Nuc approach.

gas-phase dynamics can not be accurately reproduced with tabulated chemical production and consumption rates. Considering the fact that the consumption of PAH also affects its gas-phase kinetics, the proposed FGM-Tran method thus only ensures partial two-way coupling, which results in the overestimation of PAH compared to detailed chemistry results.

ii) The mere application of the linear scaling approach for PAH consumption rate can not fully reproduce their concentrations as the production rates of large aromatics (such as PAH) are found to be proportional to smaller aromatics which exhibit transient effects [175]. Therefore, the assumption of constant production rates for PAH, employed in FGM-Tran during tabulation, may not be entirely appropriate. As a consequence, the simplified approach used in the PAH transport equation for modeling the chemical source term could not reproduce the correct PAH concentrations. On
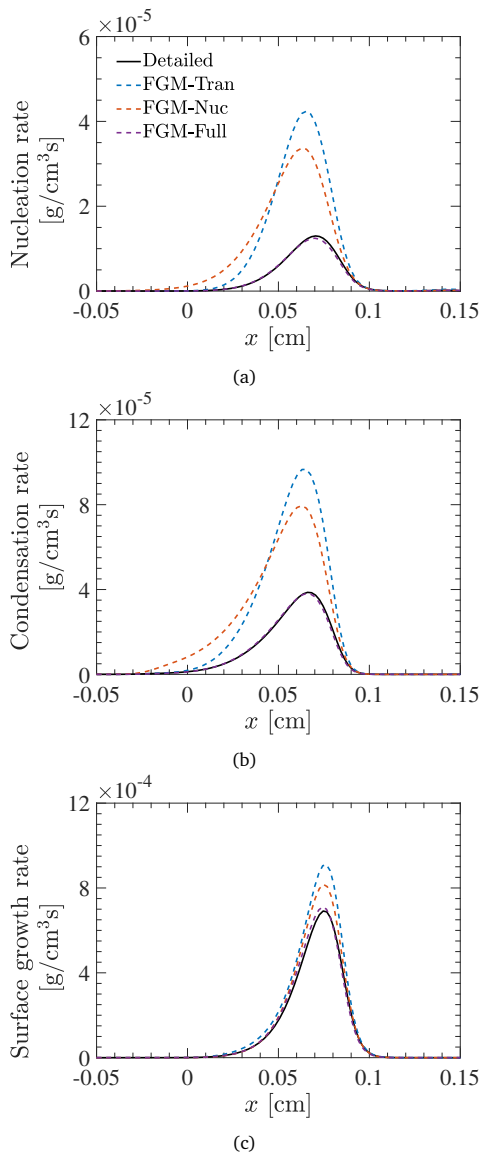
Figure 5.8: Computed profiles of soot nucleation rate (a), condensation rate (b), and surface growth rate (c) for the CDF-1 flame with different FGM-DSM coupling approaches.

the other hand, for FGM-Nuc, since the complete model of soot nucleation is solved in the flamelet generation stage, the change in PAH species concentration through its detailed gas-phase kinetics, and soot-to-gas mass exchange, is well captured. The existing overprediction of PAH in FGM-Nuc compared to detailed chemistry is a direct consequence of neglecting the contribution of PAH-condensation.

The effect of predicted species concentrations on various processes related to soot formation can be elucidated through their rate distributions in Fig. 5.8. A slightly higher A4 concentration in FGM-Tran over FGM-Nuc is reflected in enhanced soot nucleation rates since the nucleation rate is proportional to the square of A4 concentration in the present soot model. The higher nucleation rate in FGM-Tran causes an increment in the number density of soot particles within the region $x \simeq 0.05$–$0.1\,\text{cm}$ in Fig. 5.5b. However, near the flame stagnation region ($x \simeq 0$–$0.02\,\text{cm}$), the A4 concentration is found to be higher for the FGM-Nuc approach than for the FGM-Tran method. Therefore, the soot number density is seen to be overpredicted by the FGM-Nuc approach near the stagnation region, which is essentially reflected in the deviation of the power-law mode of the PSDF in Fig. 5.5d. The overestimation of PAH concentration and soot number density, lead to increased condensation rates for the FGM-Tran approach against the FGM-Nuc, as observed in Fig. 5.8b. Furthermore, higher soot surface growth rates are observed in Fig. 5.8c for the FGM-Tran approach compared to FGM-Nuc. The profiles of C_2H_2 mass fractions (Fig. 5.6b) responsible for surface growth under the HACA mechanism show no substantial deviation for FGM-Tran or FGM-Nuc. Therefore the observed difference in surface growth rates can be attributed to the effect of the increased surface area of soot particles as a consequence of increased number density induced by higher PAH prediction. In brevity, both FGM-Tran and FGM-Nuc approaches, show quantitative discrepancies in the accurate prediction of soot characteristics, due to ad-hoc techniques employed for the inclusion of mass transfer feedback from soot processes to the gas-phase. However, the findings discussed above suggest that the proposed FGM-Nuc strategy serves equally well (or better) in comparison with the FGM-Tran approach.

Concerning the performance of FGM-Full, and FGM Read approaches, from Fig. 5.5 it can be observed that the FGM-Full approach shows a good agreement with the detailed chemistry solutions for various soot parameters, including PSDF. The accurate prediction of soot quantities stems from the fact that, for the FGM-Full approach, a soot model is included in its entirety during the flamelets generation, as discussed in Section 5.2.1. Therefore, the mass exchange between the soot and gas phase, associated with the sub-processes akin to the soot formation, is implicitly included in the manifold. As a result, the concentration profiles of soot precursor species in Fig. 5.6 are found to be accurately reproduced by the FGM-Full approach. With the correct prediction of gas-phase species, the rates of various sub-processes associated with the soot formation are also predicted with a great level of accuracy in Fig. 5.8, as expected. To that end, the FGM-Full stands out as a superior strategy in terms of accuracy of soot prediction amongst the FGM-DSM coupling approaches investigated.

The FGM-Read approach is the most trivial and the simplest of all since no additional transport equations are solved for soot mass fractions in the FGM application stage. Instead, the values of sectional soot mass fractions are stored in the manifold and retrieved directly during the simulation. Figure 5.5 shows that the FGM-Read approach captures the trends in soot number density and particle size considerably well. How-
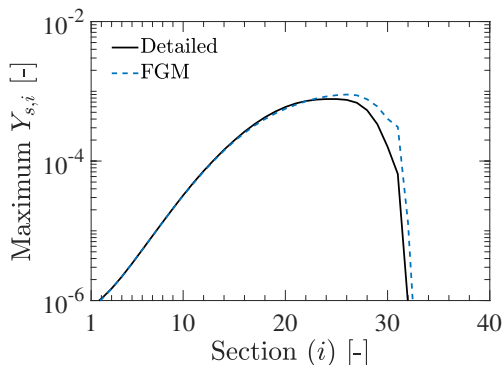
Figure 5.9: Comparison of the maximum sectional soot mass fractions ($Y_{s,i}^{\max}$) against sections (i) for FGM-Read and detailed chemistry simulations in the CDF-1 flame.

ever, it slightly overpredicts the soot formation compared to the detailed and FGM-Full solutions. The deviation in the soot volume fraction profile can be attributed to flamelet-induced errors in the retrieval of soot mass fractions in larger sections. To illustrate this, the values of peak sectional soot mass fractions $Y_{s,i}^{\max}$ predicted by FGM-Read are compared against the detailed chemistry results in Fig. 5.9.

It can be observed that the mass fraction values for higher sections ($i > 20$) are not very well reproduced. The overestimation of soot mass fractions for large-sized sections has a negligible influence on the soot number density, but, it can directly reflect in the overprediction of soot volume fractions. Such discrepancies in the retrieval are commonly encountered for species that evolve at a slower rate when compared to other species in the manifold [97]. A close observation of stored sectional mass fractions in the FGM database showed steep gradients for their values in the Z–$\mathcal{Y}$ composition space, especially for higher sections, where soot production is more prominent. Such steep gradients in stored values of sectional mass fractions also lead to interpolation errors during their retrieval. It is further observed that by modifying the progress variable definition marginally, the prediction of soot under FGM-Read can be improved to some extent for certain flames (refer Section 5.3). However, such improvements in the accuracy of FGM-Read are only limited to steady conditions and do not reflect in the dynamics of soot evolution in unsteady simulations. Therefore it is reasonable to state that the extremely small difference in Z–$\mathcal{Y}$ mapping of the sectional soot mass fractions influences the accuracy of a direct look-up based approach such as FGM-Read. Hence, solving transport equations for soot mass fractions would be the ideal choice to improve the accuracy of results, as we noticed in the case of the FGM-Full approach. Nonetheless, soot number density is better predicted by the FGM-Read as compared to FGM-Tran or FGM-Nuc approaches.

5.3.2 Variation in strain rates

To demonstrate the effect of strain rate variation, CDF-2, CDF-3, and CDF-4 flames are simulated under different FGM-DSM coupling approaches. Since the reactant composition in these flames is identical to the WRC15 flame, the same manifolds generated in the CDF-1 flame cases are used for the FGM chemistry simulations in CDF-2, 3, and 4 flames. In Fig. 5.10, the soot characteristics for the CDF-2, 3, and 4 flames with various FGM-DSM approaches are compared against their detailed chemistry solutions and measured values.

It is evident from Fig. 5.10 that the qualitative trends of reduction in soot volume fraction, number density, and soot particle size with strain rate are captured considerably well with all the FGM-DSM approaches. The predictive capability of the FGM-DSM coupling approaches under varied strain rate conditions is, thus, encouraging. Furthermore, the FGM-Nuc approach shows a better prediction of soot concentration than the FGM-Tran approach at all the strain rates, as noticed earlier for the CDF-1 flame. The FGM-Full approach is found to capture the trends in soot quantities with great accuracy. However, the FGM-Read approach shows a significant overprediction of soot in CDF-3 and CDF-4 flames, whereas, for the CDF-2 flame, the distribution of soot volume fraction is well captured. Such large discrepancies in the prediction of soot volume fractions essentially suggest that the accuracy of the FGM-Read approach is influenced by the strain rates. However, it is primarily a consequence of its sensitivity to the mapping of sectional mass fractions in the FGM database for the selected progress variable.
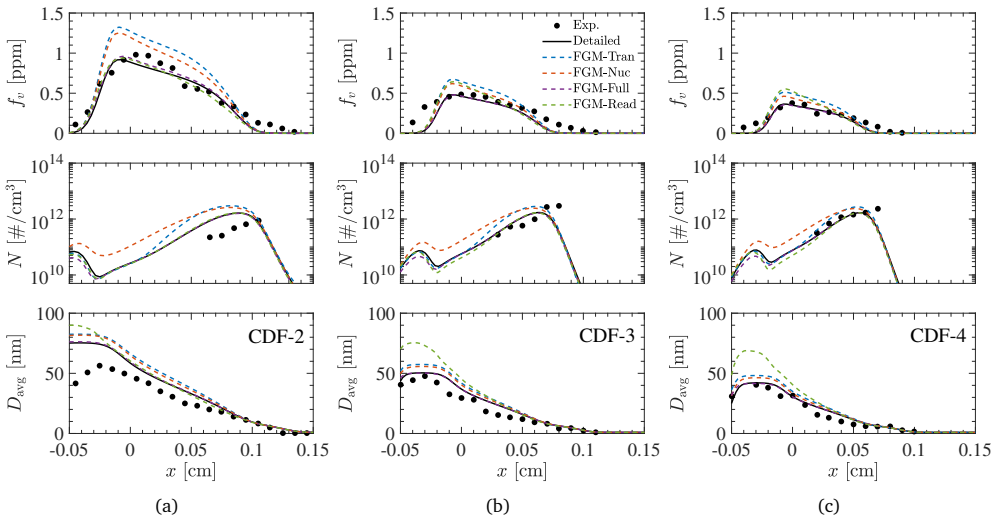
Figure 5.10: Computed and measured profiles of soot volume fraction, number density, and average particle size for different FGM-DSM coupling approaches in CDF-2 (a), CDF-3 (b), and CDF-4 (c) flames.

5.3.3 Variation in reactants composition

Next, to assess the capabilities of FGM-DSM coupling approaches for variation in mixture composition, CDF-5, and CDF-6 flames are simulated. Separate manifolds are generated for CDF-5, and CDF-6 flames as the reactant compositions in them are different from those of CDF-1 flame. In Fig. 5.11, the soot volume fraction profiles for various FGM-DSM coupling approaches are compared against the detailed chemistry solution and experiments in CDF-5, and CDF-6 flames. In the CDF-6 flame, the oxygen concentration in the oxidizer is increased, thus overall soot volume fraction is increased compared to the CDF-1 flame. This increment is qualitatively captured well by all the FGM-DSM approaches. Similarly, in the CDF-5 flame, ethylene is diluted with N_2 causing a reduction in soot concentration over the CDF-1 flame. This reduction in soot volume fraction is also captured with FGM-DSM coupling approaches in Fig. 5.11a.

As identified earlier, in both the flames, FGM-Tran and FGM-Nuc approaches overpredict the soot concentration, whereas the FGM-Full approach gives a more accurate prediction of soot parameters. In contrast, the FGM-Read approach shows a significant deviation in soot prediction for the CDF-5 flame, while the prediction is better for the CDF-6 flame. It is important to note that the reported observations for FGM-Read are related to the definition of the progress variable chosen in the analysis. Therefore, the conclusions regarding the level of accuracy for FGM-Read can not be generalized. Nevertheless, the modeling results indicate that the FGM-DSM coupling qualitatively captures the trends in the distribution of soot volume fractions when the reactive system is subjected to changes in mixture composition, although quantitative discrepancies still exist.

To quantify the precision levels of the different FGM-DSM coupling approaches, the values of peak soot volume fractions in the target flames obtained from simulations
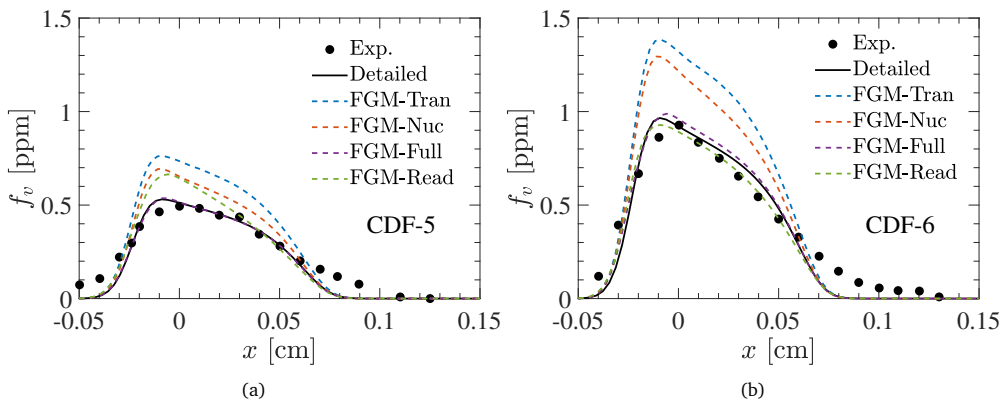
Figure 5.11: Computed and measured profiles of soot volume fraction for different FGM-DSM coupling approaches in CDF-5 (a), and CDF-6 (b) flames.
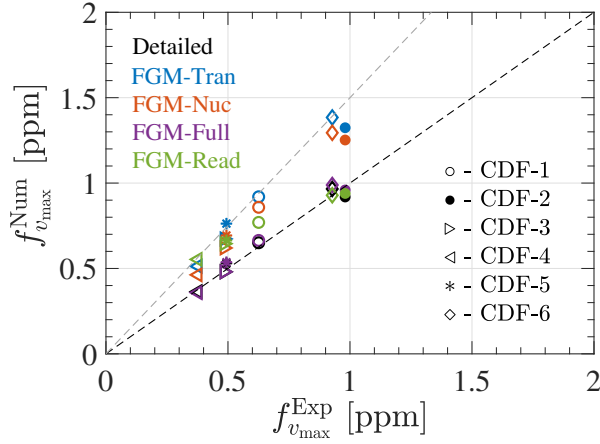
Figure 5.12: Comparison of the simulated ($f_{v_{\max}}^{\mathrm{Num}}$) and measured ($f_{v_{\max}}^{\mathrm{Exp}}$) values of maximum soot volume fractions for different FGM-DSM coupling approaches in the set of simulated flames from Table 5.2. Type of FGM-DSM coupling is denoted by colors such as; black: detailed chemistry, blue: FGM-Tran, orange: FGM-Nuc, purple: FGM-Full, green: FGM-Read. The dashed gray line indicates the 50% overestimation.

($f_{v_{\max}}^{\mathrm{Num}}$), are compared against their measured ($f_{v_{\max}}^{\mathrm{Exp}}$) counterparts in Fig. 5.12. In FGM-Tran and FGM-Nuc approaches, the peak f_v values for the modeled flames are overpredicted by approximately 30-50%, with FGM-Nuc being more accurate. The accuracy of FGM-Read is recognized to be susceptible to large deviations for the prediction of lower values of soot volume fractions ($f_{v_{\max}} \sim 0.5\,\mathrm{ppm}$), whereas, the same is found to be increased for a higher amount of soot concentration ($f_{v_{\max}} \sim 1.0\,\mathrm{ppm}$). However, although not presented extensively in the current study, with a somewhat different choice of progress variable, the accuracy of soot prediction for FGM-Read can be found improved for flames yielding lower soot concentrations. Therefore, the rationale behind better accuracy of FGM-Read at higher soot volume fractions is the result of the chosen progress variable and may not correspond to a particular physical phenomenon associated with the soot formation. Such discrepancies can be recognized as the main drawback of direct look-up-based methods such as FGM-Read. On the other hand, in all the target flames, the FGM-Full approach showed excellent agreement with the detailed chemistry results. The precision level of the FGM-Full approach is found to be almost equivalent to the detailed chemistry solutions.

While understanding the quantitative inconsistencies in the soot prediction by FGM-DSM approaches against the detailed chemistry, it is important to recall that the accuracy of soot prediction strongly depends on local concentrations of the gaseous species and soot precursors such as C_2H_2, H_2, A4, etc. Since these values are read from a pre-computed manifold, multiple factors including the choice of progress variables, method of soot-gas phase coupling, and interpolation errors during lookup, can influence the overall soot prediction in FGM chemistry approaches. Therefore, quantitative discrepancies between detailed and tabulated chemistry results are not

surprising. Nevertheless, it is evident that the FGM-DSM approaches can predict the amount of soot within the factor of 1.5 from the detailed chemistry results for the present steady cases, which can still be considered promising considering the complexities of the soot formation process.

5.3.4   Influence of progress variable definition

As highlighted in Section 5.2.3, the definition of progress variable $\mathcal{Y}$ used in the reported FGM-DSM simulations (Eq. 5.2) is determined based on a trial and error approach. Accordingly, an appropriate $\mathcal{Y}$ definition has been chosen based on preliminary analysis, which leads to a unique mapping of the thermo-chemical variables in the Z–$\mathcal{Y}$ space to recover their tabulated quantities. The results for six different progress variable definitions are analyzed to examine the influence of the progress variable on the prediction of global soot quantities. Table 5.3 summarizes the weight factors (α_j) for the progress variable definitions selected for the analysis. All the other species have $\alpha_j = 0$.

To demonstrate the effect of various $\mathcal{Y}$ definitions on the overall soot prediction, the variation of normalized peak soot volume fractions for CDF-1 flame under different FGM-DSM approaches are compared in Fig. 5.13. It can be observed that the accuracy of FGM-Tran, FGM-Nuc, and FGM-Full approaches, in which transport equations are solved for the soot mass fractions, is insignificantly affected by the choice of progress variable $\mathcal{Y}$. However, the progress variable definition has a substantial impact on the accuracy of the FGM-Read approach in which sectional soot mass fractions are directly looked-up from the manifold. Reducing the weight factor of O_2 by an order of magnitude changes the accuracy of FGM-Read drastically. From the performance of various $\mathcal{Y}$ definitions, it can be observed that by modifying progress variable definitions to $\mathcal{Y}_5$ the prediction for FGM-Read becomes slightly better than compared to $\mathcal{Y}_6$ (which is used currently). Therefore, it is noticed that the look-up of sectional soot mass fractions is particularly sensitive to its mapping in Z–$\mathcal{Y}$ space in the FGM database. Given that FGM-Read results can be improved with a better $\mathcal{Y}$ definition to a certain extent, its accuracy is limited only to steady-state flames. For unsteady conditions, FGM-Read

Table 5.3: Weight factors for $\mathcal{Y}$ definitions under analysis

$\mathcal{Y}$	α_{H_2O}	α_{CO_2}	α_{H_2}	α_{CO}	α_{A4}	α_{O_2}	$\alpha_{C_2H_2}$
$\mathcal{Y}_1$	0.0555	0.0228	0.5	0.0357	0	-3.13×10^{-2}	0
$\mathcal{Y}_2$	0.0555	0.0228	0.5	0.0357	0.0988	-3.13×10^{-2}	0
$\mathcal{Y}_3$	0.0555	0.0228	0.2	0.0321	0.0988	0	0.0461
$\mathcal{Y}_4$	0.0555	0.0228	0.5	0.0357	0	-3.13×10^{-3}	0
$\mathcal{Y}_5$	0.0555	0.0228	0.1725	0.0357	0.0988	-3.13×10^{-4}	0
$\mathcal{Y}_6$	0.0555	0.0228	0.3	0.0357	0.0988	-3.13×10^{-3}	0
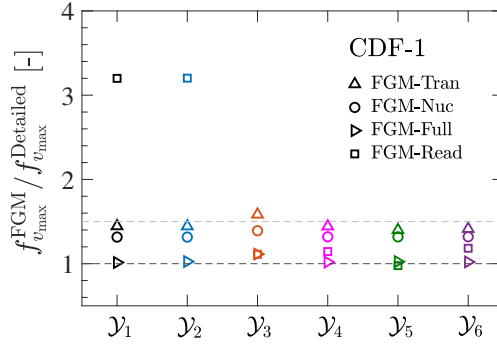
Figure 5.13: Comparison of the normalized values of maximum soot volume fractions for various FGM-DSM coupling approaches against different progress variable ($\mathcal{Y}$) definitions from Table 5.3. The dashed red line indicates the 50% overestimation level. The maximum soot volume fraction values are normalized with the detailed chemistry results.

can not capture the dynamics of soot evolution for any of the $\mathcal{Y}$ choices, as will be discussed in the later sections.

5.3.5   Effects of preferential diffusion

In many turbulent combustion models employing tabulated chemistry approaches, unity Lewis numbers are generally assumed for chemical species since their diffusion transport is presumed to be controlled by turbulent mixing. However, some of the species (PAHs) associated with soot formation exhibit strong preferential diffusion effects as they diffuse from the reaction zone to the soot formation zone. In particular, for non-premixed sooting flames, the relative positions of the reaction zone and soot formation zone essentially influence the overall soot formation characteristics. Therefore, neglecting preferential diffusion effects could lead to an erroneous prediction of soot precursors, and consequently, the overall soot concentration in numerical simulations. Hence, the effects of preferential diffusion on the soot prediction with FGM-DSM approaches are investigated by employing different transport models.

In the first approach (referred to as MIXAVG), the species mass diffusion coefficients (D_i) are calculated through a mixture averaged approximation using the Hirschfelder and Curtiss [92] expression. In the second approach (referred to as CONLEW), constant (but different) values of species Lewis numbers (Le) are assumed. The Lewis numbers are obtained by taking the diffusion flux weighted average of mixture-averaged diffusion coefficients. The third approach (referred to as UNILEW) assumes unity Lewis numbers for all the gas-phase species. In the fourth approach, (referred to as MIXUNI), the flamelets are computed with a mixture-averaged transport model, while the contribution of the preferential diffusion term is neglected ($\mathcal{D}_\phi = 0$) in transport equations for control variables (Eqs. 5.3, 5.4). The key characteristics of the aforementioned transport models are summarized in Table 5.4.

137

Table 5.4: Features of diffusion transport models.

Model	Le_i in flamelets	$\mathcal{D}_\phi$ in CFD
MIXAVG	$\frac{\lambda}{\rho c_p D_i} \quad \forall \, i \, \in \, [1, N_s]$	$\left[\sum_j -\rho\alpha_j \boldsymbol{V_j} Y_j - \left(\frac{\lambda}{c_p}\nabla\phi\right)\right] \Big/ \nabla Z$
CONLEW	fixed constants	$\left[\sum_j \left(\frac{1}{Le_j} - 1\right)\frac{\lambda}{c_p}\nabla\phi\right] \Big/ \nabla Z$
UNILEW	1	neglected
MIXUNI	$\frac{\lambda}{\rho c_p D_i} \quad \forall \, i \, \in \, [1, N_s]$	neglected

For the analysis of preferential diffusion effects, CDF-1 flame is considered. The computed and measured profiles of soot characteristics in the CDF-1 flame for various diffusion transport models are compared in Fig. 5.14. It can be observed that the unity Lewis number assumption (UNILEW) results in severe under-prediction of soot
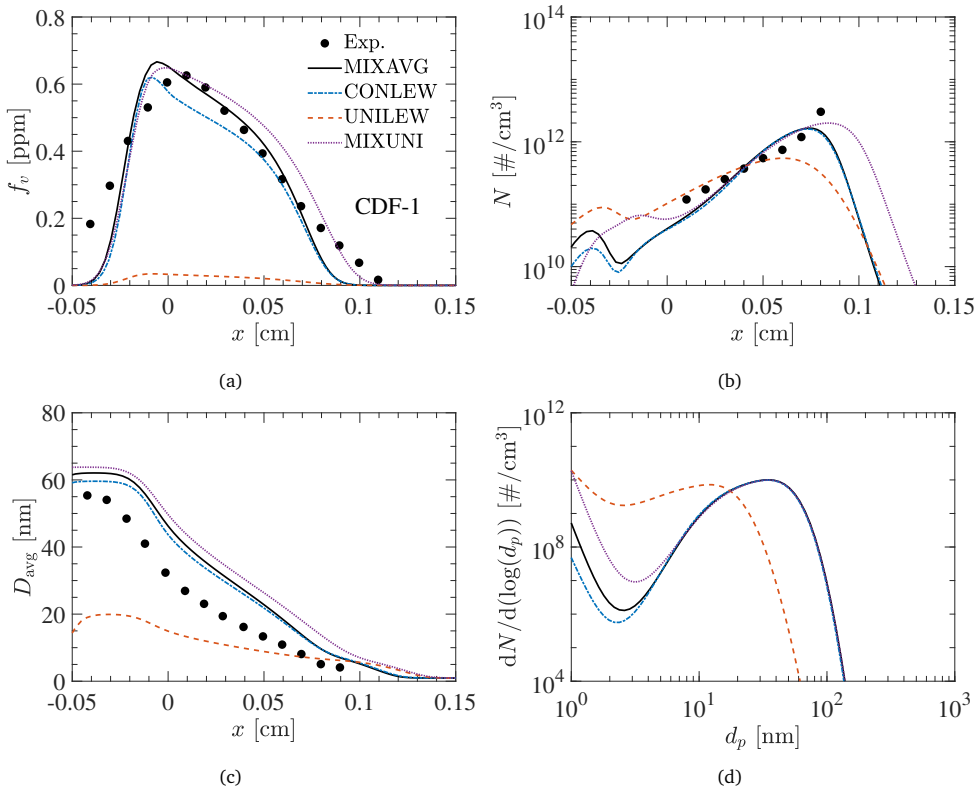
Figure 5.14: Measured and computed (FGM-Full) profiles of soot volume fraction (a), number density (b), particle diameter (c), and PSD for the CDF-1 flame with various transport models.
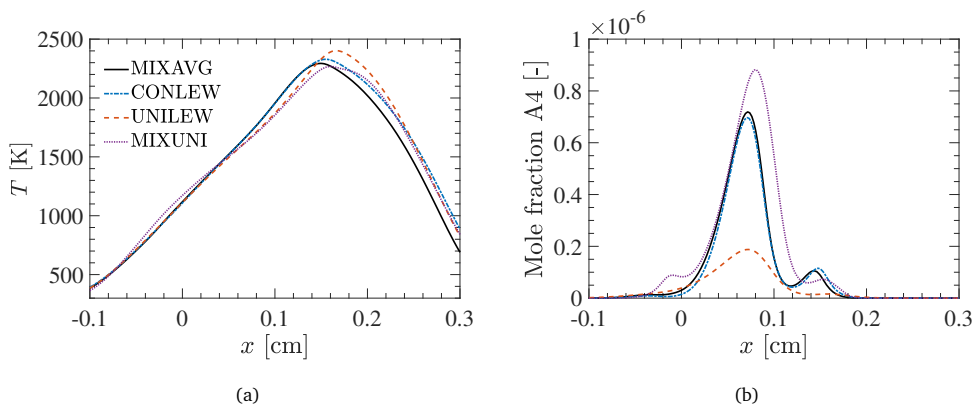
Figure 5.15: Computed profiles (FGM-Full) of temperature (a), and mole fractions of A4 (b) for the CDF-1 flame with different transport models.

concentration. In contrast, the mixture-averaged (MIXAVG) and constant Lewis number (CONLEW) based approaches show close agreement with experimental measurements. The noticed discrepancies in the prediction of soot can be explained through the computed profiles of temperature and A4 (PAH here) mole fractions in Fig. 5.15. It is evident from Fig. 5.15b that, the A4 concentration is significantly underpredicted under the unity Lewis numbers approximation. In addition to lower PAH, a reduction in temperature within the sooting zone ($x \simeq 0$–0.1 cm) tends to decrease the soot nucleation rates. Hence, a lower soot yield is obtained with the UNILEW transport approximation. Conversely, for the CONLEW model, the peak A4 concentration is marginally affected compared to the MIXAVG model, thus, only a slight variation is observed in the overall soot prediction. Despite neglecting the preferential diffusion term in the transport equations of the control variables, the quantitative and qualitative profiles of soot characteristics predicted by MIXUNI are in good agreement with the MIXAVG results. However, temperature and PAH profiles in Fig. 5.15 for MIXUNI exhibit marked deviations from the MIXAVG profiles.

It is evident from the soot volume fraction profiles for the laminar flames presented in this study that the assumption of unity Lewis numbers for gas-phase species during flamelet generation leads to significant underprediction of soot. On the other hand, including the preferential diffusion term in transport equations of control variables can increase computational costs in large-scale simulations. In this context, the MIX-UNI approach can be a suitable alternative for large-scale simulations.

5.4 Assessment of FGM-DSM coupling: unsteady flames

The main purpose of employing tabulated chemistry is to facilitate computationally efficient chemistry reduction in large-scale turbulent as well as laminar conditions.

In turbulent reacting flows, the flamelet structures are subjected to time-dependent strain rates as they evolve in the flow field. Hence, it is essential to assess the capabilities of FGM-DSM approaches for soot prediction under the influence of unsteady hydrodynamics. To investigate this, the following unsteady scenarios are examined:

- **Case 1:** Unsteady simulations at a constant strain rate ($a = a_0$), with a steady-state gas-phase flame solution without soot as an initial condition ($Y_{s,i}(t=0) = 0$) in which soot evolves from gas-phase. This case is considered to study the performance of FGM-DSM approaches in capturing the evolution of soot from the gas phase.

- **Case 2:** Unsteady simulations with an increasing strain rate (from $120\,\text{s}^{-1}$ to $720\,\text{s}^{-1}$), with a steady-state sooting flame solution as an initial condition ($Y_{s,i}(t=0) = Y_{s,i}^{\text{ss}}$). The strain rate increase is modeled with a hyperbolic tangent profile with gradual and sharp transitions in time.

- **Case 3:** Unsteady simulations at a sinusoidally varying time-dependent strain rate ($a = f(t)$), with a steady-state sooting flame solution as an initial condition ($Y_{s,i}(t=0) = Y_{s,i}^{\text{ss}}$). This case is considered to investigate the capabilities of FGM-DSM in capturing the dynamic response of soot formation under fluctuating strain rates.

The CDF-1 flame is considered the baseline case for the assessment of the FGM-DSM coupling for unsteady conditions.

5.4.1   Case 1: Constant strain rate with no-soot initial condition

In the first case, simulations are carried out at a strain rate of $120\,\text{s}^{-1}$ for all the FGM-DSM approaches. In these simulations, the time-dependent evolution of soot concentration from an initial condition without soot is studied. To capture the dynamics of soot evolution, all the simulations are initialized with the gas-phase flame solution without soot. In Fig. 5.16 the distributions of soot volume fraction in the CDF-1 flame at different time instants for various FGM-DSM approaches are compared against the detailed chemistry solutions. In soot formation (SF) type flame such as CDF-1, the soot particles nucleate in the region with high PAH concentration on the fuel side of the flame and are convected by the flow towards the flame stagnation location. During this process, soot particles grow in size through surface reactions and particle-particle coagulation, such that their number density decreases. As a result, the shape of soot volume fraction profiles becomes somewhat skewed towards the flame stagnation location.

Figure 5.16 reveals that the temporal evolution of soot from its inception to the steady-state is qualitatively captured well by FGM-Tran, FGM-Nuc, and FGM-Full approaches. The FGM-Full approach predicts the progress of soot formation under unsteady conditions with great accuracy when compared with the detailed chemistry response. The
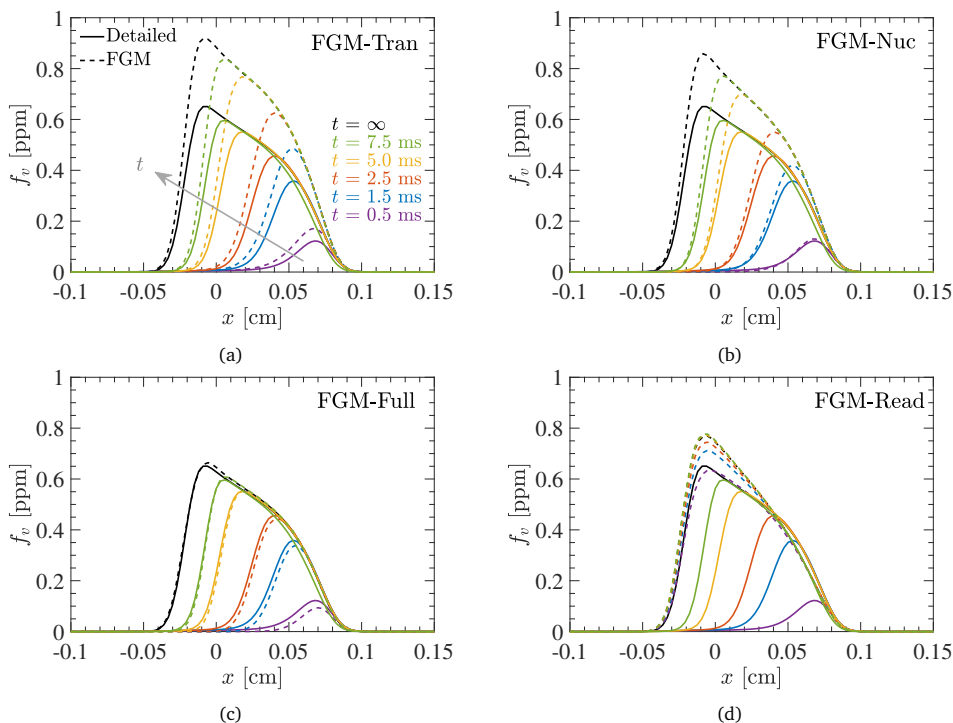
Figure 5.16: Comparison of computed profiles of soot volume fraction in CDF-1 flame at various time instances for unsteady conditions with FGM-Tran (a), FGM-Nuc (b), FGM-Full (c), and FGM-Read (d) approaches. Solid lines represent a detailed chemistry solution and dashed lines denote FGM solution. Plot colors indicate distinct time instances from purple: $t = 0.5$ ms to black: steady-state solution.

FGM-Tran and FGM-Nuc approaches, on the other hand, show quantitative overprediction in instantaneous soot concentration, with the latter being better. All the approaches, except the FGM-Read one, predict the correct dynamics of soot formation. The FGM-Read approach fails to capture the trends in soot formation for obvious reasons. This is because, in the FGM-Read approach, the soot mass fractions are directly looked-up from the manifold based on distributions of the control variables. The control variables are in a steady state in this flame. Therefore, the time-dependent response of soot formation is not captured well in FGM-Read, as transport equations for their evolution are not explicitly solved. It emerges as the major limitation of the FGM-Read method in predicting soot formation under unsteady conditions.

5.4.2 Case 2: Time-dependent strain rate with steady soot initial condition

In turbulent flows, the strain rates can change rapidly, and their fluctuations could vary by order of magnitude [212]. However, the soot evolution occurs at a relatively

slow chemical time scale. Hence it is imperative to investigate the capabilities of various FGM-DSM coupling approaches in capturing the dynamic response of soot formation to rapid strain rate fluctuations. For this reason, the applied strain rate is temporally varied as per the function:

$$a = a_0 + \left(\frac{a_f - a_0}{2} \right) \left[1 + \tanh\left(\frac{t - t_s}{\xi t_f} \right) \right] \tag{5.10}$$

with $a_0 = 120\,\mathrm{s^{-1}}$, $a_f = 720\,\mathrm{s^{-1}}$, $t_f = 20\,\mathrm{ms}$, $t_s = t_f/2$ and ξ is the profile parameter. Two different values, $\xi = 0.01$ and $\xi = 0.1$ are chosen for the profile parameter to mimic a rapid and gradual variation, respectively, in the temporal distribution of the strain rate.

In this case, the steady-state sooting flame solutions corresponding to the respective FGM-DSM approaches are used as initial conditions for unsteady simulations. To understand the overall response of soot formation to temporal variation of strain rate, the time evolution of the peak soot volume fractions in various FGM-DSM approaches are compared in Fig. 5.17. The qualitative trends of decrease in the peak soot concentrations for rapid and gradual increments in strain rates are captured well by FGM-Tran, FGM-Nuc, and FGM-Full approaches. The FGM-Full approach shows a good agreement with the detailed chemistry solutions as expected. The FGM-Read approach, on the other hand, could not reproduce the trends in the soot volume fraction evolution well. Note that for the $\xi = 0.01$ case, the strain rate increases drastically (within 1 ms). Therefore, a sharp change in the evolution of soot volume fractions can be noticed at 10 ms. Furthermore, relatively slow time scales associated with the soot formation cause a lag between the response of soot to the strain rate variation. The FGM-Read approach, however, could not capture this behavior since the trends shown by FGM-Read qualitatively follow the course of progress variable evolution

Figure 5.17: Temporal evolution of peak f_v for FGM-DSM approaches and detailed chemistry under the time-dependent variation of strain rate with $\xi = 0.01$ (a), and $\xi = 0.1$ (b) in the CDF-1 flame.

considering that the soot mass fractions are retrieved directly from the FGM database as a function of the progress variable. The analysis hence justifies that the FGM-DSM approaches (except for FGM-Read) can qualitatively reproduce the dynamic response of soot formation to the drastic strain rate variations.

5.4.3 Case 3: Sinusoidal strain rate with steady soot initial condition

The transient response of non-premixed flames to the unsteadiness is often modeled by imparting harmonic oscillations to the flow field in laminar counterflow diffusion flames [183, 192]. Following this feasible approach, sinusoidal oscillations are introduced to the applied strain rate with varying frequencies and amplitudes. The response of flame to the strain rate fluctuations is analyzed in terms of induced oscillations of the peak soot volume fractions for various FGM-DSM approaches. The strain rate oscillations are assumed to have the following form:

$$a = a_0 + \Delta a \cdot \sin\left(2\pi f t\right) \tag{5.11}$$

where Δa is the semi-amplitude, f is the frequency of the imposed oscillations and $a_0 = 120\,\mathrm{s}^{-1}$ is the strain rate of steady-state flame solution. Since the soot formation is usually a slow process, the soot field could not respond to the imposed oscillations at higher frequencies ($\gg$100 Hz) [121]. Therefore, for illustration, two different values of frequencies ($f = 50$ and $100\,\mathrm{Hz}$) and semi-amplitudes ($\Delta a = 20$ and $50\,\mathrm{s}^{-1}$) are chosen. Similar to Case 3, all the cases (Detailed and FGM-DSM) are initialized from their corresponding steady-state solutions at a_0 with soot formation. The numerical results obtained for the detailed chemistry and FGM-DSM cases in terms of the evolution of peak soot volume fractions against the number of oscillation cycles are shown in Fig. 5.18.

It is evident that when low-frequency oscillations are imposed, the induced amplitudes for the soot field become large, and the symmetry around their mean value is lost [183]. For the same frequency, with an increase in the amplitude of the imposed oscillations, the value of the observed amplitude in soot volume fractions also increases. On the contrary, at higher frequencies, the amplitude of the induced oscillations is reduced for an identical amplitude of imposed oscillations. These characteristics can be witnessed from the dynamic response of peak soot volume fractions to the strain rate oscillations in Fig. 5.18. The FGM-Full coupling shows a good agreement with the detailed chemistry results, whereas FGM-Tran and FGM-Nuc predict the qualitative trends reasonably well. Note that the shift in the 'steady-state' value leads to offset in transient profiles. The departure from the detailed-chemistry values for peak soot volume fractions follows the sequence: FGM-Tran > FGM-Nuc > FGM-Full. On the other hand, the FGM-Read fails to capture the qualitative trends of soot evolution. Besides, a significant phase-lag exists in the temporal evolution of peak soot volume fractions. Such a tendency is mainly observed in FGM-Read since the soot
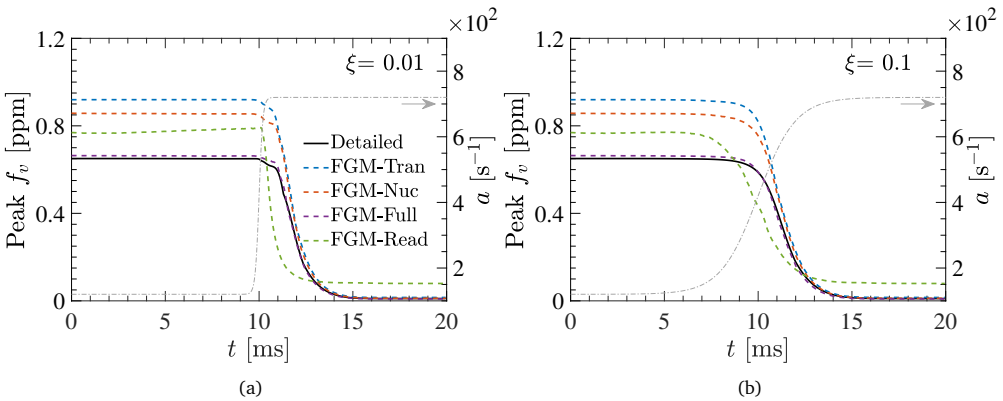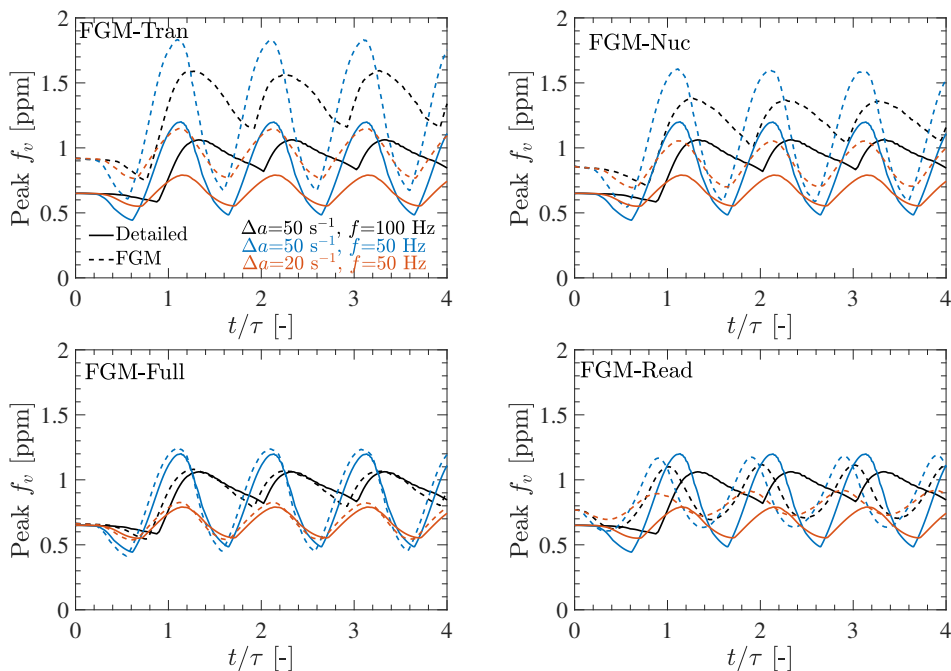
Figure 5.18: Temporal evolution of peak f_v for FGM-DSM approaches and detailed chemistry under the oscillating strain rates in the CDF-1 flame. Time is normalized with the period of oscillations ($\tau = 1/f$).

mass fractions are retrieved directly from the table. As a result, time scales associated with the transport of soot mass fractions are not captured. Unlike other approaches, the FGM-Read, therefore, does not have a phase lag in the temporal evolution of soot for the imposed sinusoidal oscillations of the strain rates.

It is interesting to note that, for imposed sinusoidal fluctuations, the response of FGM-Full shows a slight phase deviation compared to the detailed chemistry results. To elucidate this, in Fig. 5.19, the temporal evolutions of normalized maximum progress variable, PAH (A4) mass fractions, and soot volume fractions are presented for the detailed chemistry and FGM-Full simulations. From the detailed chemistry results, it can be noticed that a phase-lag arises between the progress variable and PAH as a consequence of the time scales associated with the slower chemistry of PAH formation. In contrast, since PAH mass fractions are directly looked-up from the manifold in the FGM-Full approach, the phase difference between the PAH and progress variable can not be captured. Given that the PAH concentration directly influences the overall soot formation process, the phase difference associated with the progress variable and PAH also reflects in the response of soot volume fractions. The skewness in the temporal profiles of f_v indicates fast soot formation at peak A4, followed by its slow removal owing to longer convective time scales. The time scales associated with soot formation are, however, significantly slower than the progress variable transport.
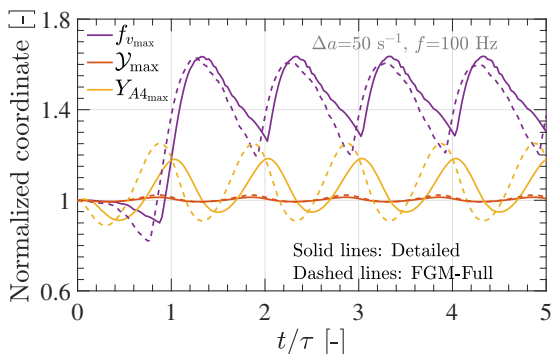
Figure 5.19: Temporal evolution of normalized maximum progress variable ($\mathcal{Y}_{\mathrm{max}}$), peak A4 mass fraction ($Y_{A4_{\mathrm{max}}}$), peak soot volume fraction ($f_{v_{\mathrm{max}}}$) for detailed chemistry (solid lines), and FGM-Full approach (dashed lines) under the oscillating strain rate ($\Delta a = 50\,\mathrm{s}^{-1}$, $f = 100\,\mathrm{Hz}$) in CDF-1 flame. Time is normalized with the period of oscillations ($\tau = 1/f$). The quantities are normalized with their corresponding steady-state values at $t = 0$.

The present analysis also shows that although the evolution of PAH species is slightly slower compared to the progress variable, its influence on the overall dynamics of soot leads to a phase lag of less than 10% of the period for the detailed chemistry and FGM-DSM approaches (except for FGM-Read). Therefore it is more crucial to capture the dynamics of soot evolution compared to the dynamics of PAH when the FGM chemistry is employed. Accordingly, including sectional transport equations for soot prediction in FGM-DSM approaches is critical (as opposed to FGM-Read). Hence, it can be argued that as long as the concentration of PAH is accurately predicted, the FGM-DSM approaches characterized by the transport of soot mass fractions, can yield considerably good accuracy of quantitative and qualitative soot prediction.

It is worth mentioning that since the goal of the present chapter is to assess the performance of FGM-DSM coupling approaches. Based on the presented analysis, it can be argued that the influence of unsteady hydrodynamics on soot formation is qualitatively captured by FGM-DSM approaches, with FGM-Full being relatively accurate, although quantitative discrepancies exist because PAH delay is not accounted for. The assessment of FGM-DSM coupling under a range of unsteady conditions provides confidence in their relevance for turbulent conditions.

5.5 Computational performance of FGM-DSM methods

The most important aspect of chemistry-reduction methods such as FGM is the computational advantage gained compared to detailed kinetics. Hence, it is imperative to analyze the computational performance of different FGM-DSM modeling approaches for studied cases. In sectional methods, increasing the number of sections for capturing particle size distribution enlarges the CPU time since additional transport equations are required to be solved. In this context, the total CPU time needed to per-

form time-dependent simulations for a period of 1 ms is compared in Fig. 5.20a for a varied number of sections in different FGM-DSM approaches. The simulations are performed with identical soot model parameters on Intel(R) Core(TM) i7-8700 CPU @ 3.20 GHz processor. In the simulations, a fully implicit time integration with an adaptive time step is used. Each of the FGM-DSM cases is initialized with an identical gas-phase flame solution at a strain rate of $90\,\mathrm{s}^{-1}$. The initialization from a flamelet at a lower strain rate is done intentionally, to provide slightly different initial values of thermo-chemical variables from their desired final solution. The total CPU time, thus, encompasses two important aspects. First, the transport of sectional soot mass fractions, and second, the adjustment to the flow field strain. The chosen initial conditions, thus, inherently control the extent of the computational advantage that can be attained with the FGM-DSM approaches compared to detailed chemistry.

From Fig. 5.20a, it can be observed that the total CPU time reduces by approximately an order of magnitude when the FGM-DSM coupling strategy is applied. This speed-up is mainly caused by a drastic reduction in the number of transport equations needed to be solved for the evolution of gas-phase species. This is because, in CHEM1D, the CPU time for matrix factorization generally scales with N^3, while the overall solution time scales approximately as N^2 for N transported variables. Furthermore, the FGM-DSM strategy provides the advantage of larger time steps since smaller time scales associated with the gas-phase chemistry are eliminated. Therefore, the total computational time of FGM-DSM coupling approaches is found to be significantly lower than the detailed chemistry. On comparing different FGM-DSM approaches, relative differences can be seen in the evolution of their CPU time with the number of sections. In the FGM-Tran approach, an additional transport equation is solved for PAH. As a result, the CPU time for FGM-Tran is higher compared to FGM-Nuc. The FGM-Tran

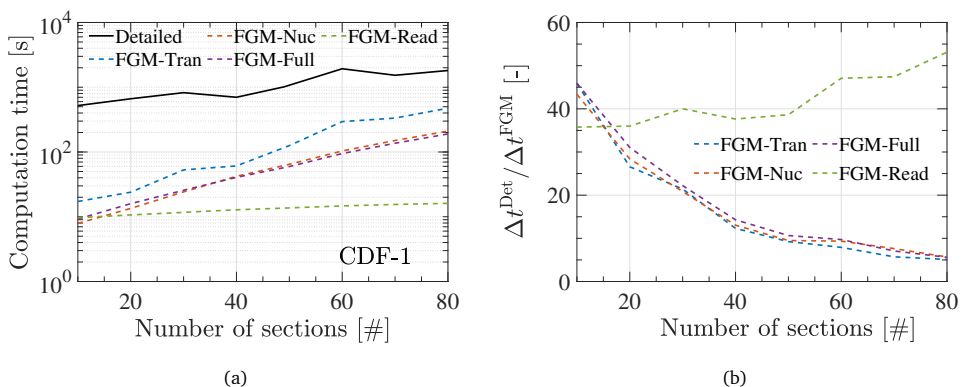| (a) | (b) |

Figure 5.20: Variation of CPU time with the number of sections for different FGM-DSM coupling approaches under unsteady simulations till 1 ms (a), variation of the ratio of CPU time per time-step in detailed (Δt^{Det}) and FGM (Δt^{FGM}) chemistry simulations with the number of sections for different FGM-DSM coupling approaches (b) in the CDF-1 flame.

approach is found to be about 10 equivalent sections slower compared to FGM-Nuc and FGM-Full. This stems from the fact that the simulation time steps in FGM-Tran become relatively smaller as a consequence of the PAH transport equation, leading to an increment in the number of iterations and CPU time. The results also suggest that simulations with the FGM-Full approach progress somewhat comparable to the FGM-Nuc one. Only a marginal reduction in CPU time is observed for a higher number of sections. On the other hand, the CPU time for the FGM-Read approach is significantly lower and hardly affected by an increment in the number of sections. For a higher number of sections, the FGM-Read approach gives a faster solution by almost two orders of magnitude compared to detailed chemistry. Such a strong reduction in CPU time is expected since no additional equations are solved for sectional soot mass transport in the FGM-Read approach.

The extent of CPU time reduction can be further elucidated through the analysis of the total time required per time-step. In Fig. 5.20b the ratios of CPU time per time-step in detailed (t_{ts}^{Det}) and FGM (t_{ts}^{FGM}) chemistry cases are plotted against the number of sections. It is observed that the iteration time of the FGM-DSM computations (except FGM-Read) can be reduced by approximately 6 to 40 times depending on the number of sections employed. Note that in the present analysis, an implicit time integration scheme is used, and the computational advantage is expected to improve further for explicit time integration methods [207].

It is obvious that constructing an FGM table for one-dimensional simulations is rather inefficient, considering the total time taken in manifold creation. However, the reduction in CPU time achieved by using FGM in large-scale, multidimensional combustion simulations, could be orders of magnitude larger than the time required for manifold construction. Moreover, for a given reactant composition, the manifold needs to be created only once and can be used in multiple simulations. The use of FGM thus facilitates efficient simulations for design optimization.

5.6   Summary

To facilitate the use of FGM tabulated chemistry for soot modeling in turbulent flames, it is important to validate and assess the suitable strategies of coupling FGM with the soot model over a range of conditions in a canonical, laminar one-dimensional flame configuration. In this regard, five different approaches for coupling FGM tabulated chemistry with the sectional model namely FGM-Unc, FGM-Tran, FGM-Nuc, FGM-Full, and FGM-Read were examined in six target flames to evaluate their performance in terms of accuracy of soot prediction and computational advantage. The main conclusions of the present assessment are:

1. The prediction of soot properties with the FGM-Nuc and FGM-Tran approaches is encouraging, considering the expected discrepancies associated with the lack of full coupling of the gas-soot phase. Both FGM-Nuc and FGM-Tran approaches

predicted soot volume fractions within a factor of 1.3-1.5 against the experimental values for investigated flames. However, the FGM-Nuc emerged as a superior approach compared to the FGM-Tran in terms of accuracy and computational time.

2. The FGM-DSM coupling approaches recover the distributions of the soot parameters with reasonable accuracy against detailed chemistry solutions and experimental measurements when mass exchange from the soot processes to gas-phase species is appropriately incorporated. Accordingly, the FGM-Full approach, in which full soot model solutions were used for the manifold generation, showed an excellent agreement with the detailed chemistry results. On the other hand, the accuracy of the FGM-Read approach, in which soot mass fractions are retrieved directly from the manifold, is found to be influenced by the mapping of sectional soot mass fractions in mixture fraction and progress variable space.

3. Numerical results revealed that the FGM-DSM coupling approaches predict the qualitative trends in soot formation for variations in strain rate and reactant compositions reasonably well. Moreover, the proposed FGM-DSM coupling approaches (except FGM-Read) can capture the dynamic response of soot evolution under unsteady conditions considerably well. The accuracy of the FGM-Read approach is found to be significantly compromised in unsteady conditions, making it unsuitable for use in turbulent combustion simulations.

4. Computational time analysis suggests that the FGM-DSM modeling strategies can reduce the CPU time by 1 to 2 orders of magnitude compared to the detailed chemistry simulations. For unsteady simulations under the implicit time integration method, the FGM-DSM approaches facilitated up to 40 times reduction in the CPU time per time-step, based on the number of sections used.

Even though numerical analysis in one-dimensional flames can not exactly predict the actual performance of FGM-DSM coupling in simulations of turbulent flames, it can be concluded that FGM-DSM is a promising technique for soot prediction in non-premixed flames with a reasonable level of accuracy at enormously reduced computational efforts. Especially, for approaches in which transport equations are solved, the unsteady dynamics of soot formation are captured reasonably well. This essentially highlights the encouraging capabilities of FGM-DSM approaches to characterize the flame conditions that are different from the steady flamelets used for building the FGM database. Therefore, except for FGM-Read, the FGM-DSM approaches proposed would be suitable for predicting soot formation under more complex environments.

It should be noted that based on the complexity of combustion phenomena, FGM chemistry relies on user knowledge for the suitable choice of flamelets, and it is sometimes required to increase the dimensions of the manifold to account for additional physics (e.g., heat loss effects). Therefore, it is reasonable to state that the effectiveness of FGM-DSM approaches for soot prediction in more complex cases will also depend on the physical processes that are considered during the manifold generation.

However, it is unexplored at this point how the FGM-DSM approaches can be integrated into the simulations involving subgrid-scale modeling (LES, RANS), and will be discussed in later chapters. Despite a significant reduction in CPU time through FGM chemistry, still many soot sections need to be transported in the FGM-DSM strategies discussed in this chapter. To address this, another computationally efficient method of FGM-DSM coupling is proposed in the next chapter, and its performance is evaluated for accuracy and CPU cost.

6

Efficient approach for FGM-DSM coupling with clustering

In the previous chapter, various strategies coupling the sectional soot model with FGM chemistry were investigated. In this chapter, a novel approach for the prediction of soot formation in combustion simulations, referred to as FGM-CDSM, is proposed. This approach concern use of tabulated source terms followed by clustering of soot sections. A comparative assessment of FGM-CDSM is conducted in laminar diffusion flames for its accuracy and computational performance against the detailed kinetics-based classical sectional model. The content of this chapter refers to an article in-press for publication in Combustion and Flame [213] as 'A computationally efficient approach for soot modeling with discrete sectional method and FGM chemistry'.

6.1 Introduction

To facilitate the accurate description of the dynamics of soot particles and the evolution of their size distributions, the role of detailed models in the development of numerical tools predicting soot formation has become pivotal. The state-of-the-art detailed soot models primarily include discrete sectional methods [35, 71, 73, 94], method of moments (MOM) [37, 64, 65], and stochastic methods such as Monte Carlo (MC) [61, 214]. MC-based models are computationally expensive and therefore mainly limited to canonical 0-D and 1-D configurations. For multi-dimensional simulations, MOM-based soot models, which can adequately describe soot morphology at a low computational cost, are often employed [66, 75]. However, the re-construction of PSDF with MOM approaches necessitates closure models for unsolved higher-order moments, which increases their mathematical complexity. On the other hand, DSM-based soot models enable a discretized representation of the soot PSDF in the particles' volume/mass space. Hence, a complete (discretized) PSDF can be accurately reproduced through the transport of soot scalars (mass fraction/number density) for each representative particle size (section). However, DSM-based models require a large number of sections (typically ranging from 30-100) to resolve the soot PSDF ad-

equately, which makes them computationally demanding for multi-dimensional cal-culations. In addition, a large number of chemical species and reactions need to be included in the kinetic mechanism to describe the evolution of gaseous phase soot precursors. Hence soot modeling with detailed kinetics becomes very expensive, and its application in multi-dimensional simulations is rather impractical.

In the context of CPU-efficient combustion simulations with detailed chemistry, ana-lytically reduced, optimized kinetic schemes along with systematic automation are at-tractive. However, the solution of the soot phase remains an additional computational challenge, that supersedes the reduction achieved in the gas-phase description. De-spite the progress in multicore architectures and CPU accelerators, the application of such reduced-order kinetic schemes becomes unaffordable for conditions of potential interest [88]. New machine-learning-based models [87] and virtual chemistry [88] techniques have been recently proposed for soot formation prediction in laminar and turbulent flames. While these methods were able to predict the first moments of the distribution (soot volume fraction and number density), the evolution of the soot particle size distribution was not examined. On the other hand, flamelet-based mod-els are popular and often employed in multi-dimensional sooting flame simulations, to efficiently represent the combustion chemistry. In particular, MOM-based models coupled with tabulated chemistry have been widely applied in simulations of sooting flames [66, 84]. Owing to the limitations of MOM-based models in capturing the soot PSDs, there have been efforts in integrating DSM-based soot models with tabulated chemistry within the RANS [36] and LES [73] frameworks. However, in the DSM-based simulations, although a significant reduction in CPU time can be achieved by employing flamelet-based tabulated chemistry, a large number of additional transport equations with the corresponding soot source terms integration are still required to represent the soot PSDF. In consequence, the reduction in CPU time achieved by the use of tabulated chemistry is lost if a large number of sectional transport equations are to be solved. Hence, for an effective application of DSM-based models in large-scale simulations, it becomes critical to develop computationally efficient approaches that can facilitate remarkable reductions in CPU time with minimum compromise on accuracy.

Different subprocesses associated with soot formation involve non-linear correlations between the gas-phase thermo-chemical states and soot variables. Hence, while cou-pling sectional models with tabulated chemistry, the dependence of soot source terms on the sectional soot variables is often explicitly accounted for during CFD calcula-tion. Owing to the physical consistency regarding soot source term computation and the overall accuracy of soot prediction, computation of soot reaction rates is preva-lent in the literature [36, 73]. The performance of such a method in connection to FGM chemistry is studied in the previous chapter. In the method relying on run-time computation of soot reaction rates, however, the CPU speedup is mainly due to the re-duction of gas-phase kinetics, as soot source term calculation remains computationally intensive. On the other hand, the tabulation of soot reaction rates in flamelet-based

models has been investigated in earlier works [97, 215] for semi-empirical soot models. In the complete tabulation of soot reaction rates, the non-linear dependence of soot source terms on local soot variables is neglected, and soot formation is assumed to follow the characteristics of flamelets. Although the tabulation of soot source terms presents limitations in terms of the accuracy of soot prediction, it offers an interesting approach to reduce the computational cost for sooting flame calculations.

Against this background, a new approach of coupling the DSM-based soot model with FGM tabulated chemistry [193], referred to as FGM-CDSM (Clustered-DSM), is proposed in this study to reduce the computational cost (CPU time, memory use) of tabulated source term based sectional soot modeling approaches. The rationale behind the FGM-CDSM model is to take one step further and assess if the complete tabulation of source terms followed by clustering of soot sections can yield reasonable results in terms of the prediction of global soot quantities, and evolution of soot PSD. This approach essentially considers a low dimensional representation of the soot PSDF by employing clustering of sections during simulation run-time, and a re-construction of the detailed PSDF in a post-processing stage based on PSDFs from the laminar flamelets. The proposed FGM-CDSM offers a good balance between accuracy and computational cost, as only a few transport equations are to be solved, making this model highly suitable for large-eddy simulations.

In this chapter, the FGM-CDSM formalism is first introduced and the clustering of soot sections is explained, followed by the assessment of its performance concerning the accuracy of soot prediction in laminar diffusion flames under steady, and unsteady conditions. In this assessment, the FGM-CDSM approach is first validated against numerical results for global soot quantities (volume fraction, number density) and PSDs using the detailed model and with source term tabulation, but without clustering. Subsequently, global soot characteristics predicted by FGM-CDSM with clustering are compared against their no-clustering counterparts for a series of non-premixed ethylene flames. Moreover, as a step towards application to more realistic, multi-dimensional flow configurations, the assessment of the FGM-CDSM is extended to a two-dimensional laminar coflow diffusion flame. Subsequently, the computational performance of the proposed FGM-CDSM method is evaluated. Finally, the predictive capabilities of the FGM-CDSM methods relying on the tabulation of soot source terms are compared against the FGM-Full strategy (introduced in Chapter 5), which involves run-time computation of soot source terms. The primary focus of this work is to investigate the capabilities of the proposed FGM-CDSM strategy in capturing soot formation characteristics and identifying possible deficiencies associated with its application to more general conditions. Hence, the present study is limited to laminar flame simulations, as soot prediction in turbulent conditions presents additional challenges related to the closure of soot-turbulence-chemistry interactions and the sensitivity of the results to different models employed, which are investigated in Chapter 7.

6.2   FGM-CDSM methodology

In FGM, a manifold representing the thermophysical and chemical space, parametrized by relevant control variables, is constructed from the flamelet solutions. The manifold is subsequently coupled to a flow solver through the transport of controlling variables that describe the manifold structure in composition space, so a cost-efficient method for solving multi-dimensional reactive flow simulations is defined [184]. The FGM-CDSM strategy essentially uses the soot chemistry information obtained by the flamelets and recovers the original PSD during run-time (or post-CFD) by transporting only a few clustered sections. The non-linear dependence of different soot sub-processes with sectional soot mass fractions is not explicitly solved in CFD calculation but included in flamelet computations. Therefore, the description of soot formation and PSD in multidimensional flames is assumed to follow their flamelet response, as the inter-sectional dependence of soot formation rates is implicitly accounted for in the flamelet stage. On the premise of this approach, modeling soot formation with FGM-CDSM involves four key steps:

1. Computation of flamelets including detailed soot kinetics

2. Creation of a manifold

3. Coupling the manifold to a CFD solver

4. Re-construction of the soot PSDF

These steps are explained in the following sections.

6.2.1   Computation of flamelets including detailed soot kinetics

In the first step, 1-D laminar flamelets suitable for the combustion system under consideration (premixed/non-premixed) are computed with a detailed kinetics and DSM-based soot model. In the DSM soot model, a range of soot particle volume is discretized into a finite number of sections (N_{sec}). Transport equations for soot mass fraction ($Y_{s,i}$) of section i are solved along with equations for the conservation of mass, momentum, and energy. Under a steady formulation, the 1-D description of the conservation equations for $Y_{s,i}$ read:

$$\frac{\partial(\rho u Y_{s,i})}{\partial x} = \frac{\partial}{\partial x}\left(-\rho V_T Y_{s,i} + \rho D_s \frac{\partial Y_{s,i}}{\partial x}\right) + \dot{\omega}_{s,i} \quad ; \quad \forall\, i \in [1, N_{sec}] \qquad (6.1)$$

The sectional soot source terms ($\dot{\omega}_{s,i}$) are computed by considering the contributions of soot nucleation, PAH condensation, surface growth, oxidation, and coagulation sub-processes as described in Chapter 2.

6.2.2 Creation of a manifold

In the second step, a manifold is constructed from the computed flamelets to describe the thermochemical evolution of the flame and the soot chemistry. Important thermo-chemical parameters $\psi(\phi_j)$ of the system are then mapped onto the control variables (ϕ_j) and stored in the flamelet manifold, following the procedure described by van Oi-jen et al. [184]. As mentioned earlier, the FGM-CDSM method relies on the tabulation of soot source terms. Therefore, the soot source terms for the clusters are stored in the database as functions of the manifold control variables (typically mixture fraction and progress variable) in addition to the transport properties, and relevant gas-phase species.

In the FGM-CDSM method, the number of sections N_{sec} utilized during the computa-tion of the flamelets are combined into a set of clusters N_{clust} for the transport of soot in the CFD simulation. The soot mass fraction ($Y_{s,c}^c$) in cluster c is, thus, the sum of $Y_{s,i}$ from the original sections that are grouped together in c:

$$Y_{s,c}^c = \sum_{i=i_c^{\min}}^{i_c^{\max}} Y_{s,i} \tag{6.2}$$

where $i_c^{\min}$ and $i_c^{\max}$ are, respectively, the lower and upper limit of the sections i that are clustered. The clustering of sections relies on the assumption that soot particles within the cluster preserve the intra-sectional distribution of soot mass exhibited by associated original sections. In other words, this assumption means that the evolu-tion of the full soot PSD partially depends on the CFD (through the transport of soot clusters) and the FGM tabulation (via re-construction).

For a preliminary assessment of the FGM-CDSM, a uniform clustering of sections is employed. The schematic presentation of the uniform clustering approach is depicted in Fig. 6.1. Accordingly, the sectional limits of cluster c are given by:

$$i_c^{\max} = c \cdot (N_{sec}/N_{clust}) \quad ; \quad N_{sec}/N_{clust} \in \mathbb{N} \tag{6.3a}$$

$$i_c^{\min} = i_{c-1}^{\max} + 1. \qquad \forall \, c \in [1, N_{clust}] \tag{6.3b}$$

To parameterize the reduction in sectional dimensions, a clustering factor $\mathcal{R}$ is intro-duced as:

$$\mathcal{R} = 1 - (N_{clust}/N_{sec}) \quad ; \qquad \mathcal{R} \in [0,1) \tag{6.4}$$

which is zero when no clustering is applied, and approaches unity when all sections are grouped into a single cluster.

Owing to the long characteristic time scales of soot formation compared to the fuel-oxidation chemistry, the steady-state assumption of soot chemistry can lead to its inaccurate prediction by flamelet-based approaches [204], yielding non-physical, sur-plus consumption of soot. To prevent this, a linear relaxation is applied to the soot
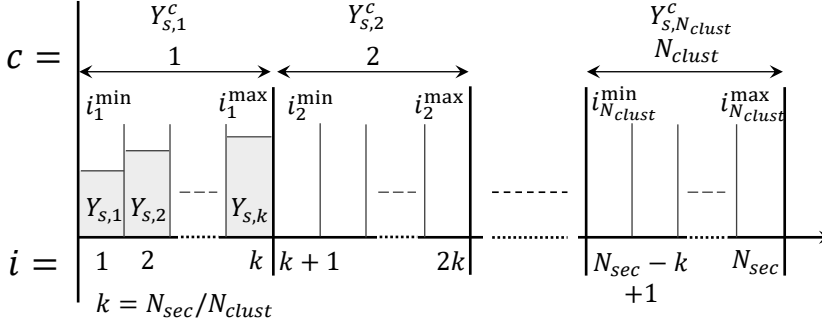
Figure 6.1: Schematic diagram of the uniform clustering in the FGM-CDSM method.

consumption rate term. Consequently, the chemical source terms for the cluster are recast as:

$$\dot{\omega}_{s,c}^c = \left[\dot{\omega}_{s,c}^{c,+}\right]^{\text{tab}} + \left(Y_{s,c}^c\right)^{\text{tran}} \left[\frac{\dot{\omega}_{s,c}^{c,-}}{Y_{s,c}^c}\right]^{\text{tab}} \qquad (6.5)$$

where superscripts tran and tab refer to transported and tabulated quantities, respectively. The terms, $\dot{\omega}_{s,c}^{c,+}$ and $\dot{\omega}_{s,c}^{c,-}$ for the cluster are given by:

$$\dot{\omega}_{s,c}^{c,+} = \sum_{i=i_c^{\min}}^{i_c^{\max}} \max(\dot{\omega}_{s,i}, 0), \qquad (6.6a)$$

$$\dot{\omega}_{s,c}^{c,-} = \sum_{i=i_c^{\min}}^{i_c^{\max}} \min(\dot{\omega}_{s,i}, 0). \qquad (6.6b)$$

The choice of the linear relaxation stems from the fact that in the retained soot model, rates of different soot subprocesses scale distinctly with soot mass fraction, in a linear (condensation, surface growth, oxidation) and a quadratic manner (coagulation). Since soot oxidization is the dominant subprocess in overall soot mass consumption, a linear relaxation model appears to be a reasonable approximation for soot consumption rates. Note that no relaxation model is applied to soot production terms, thus soot formation rates are approximated to be correlated with control variables only, following their flamelet values. In this approximation, the non-linear dependence of the soot source term on the soot variable is fully accounted for in the flamelet calculations, instead of CFD This approximation is carefully verified here for its applicability/deficiencies in several conditions, which will be discussed later. Furthermore, as a modeling choice, in Eq. 6.5, contributions of the net soot source term are preferred over individual subprocesses. However, it is also possible to isolate the rates of various subprocesses in the tabulation.

6.2.3 Coupling the manifold to a CFD solver

During the CFD calculation, transport equations are solved for momentum, continuity, enthalpy, manifold control variables (ϕ_j), and the mass fraction of soot in N_{clust} clusters. The transport equation for the clustered soot mass fraction derived from Eqs. (7.30) and (6.2), can be expressed in a general form as:

$$\frac{\partial\left(\rho Y_{s,c}^c\right)}{\partial t} + \nabla \cdot \left(\rho[\boldsymbol{u} + \boldsymbol{V_T}]Y_{s,c}^c\right) = \nabla \cdot \left(\rho D_s \nabla Y_{s,c}^c\right) + \dot{\omega}_{s,c}^c \qquad \forall\, c \in [1, N_{clust}] \quad (6.7)$$

The source term $\dot{\omega}_{s,c}^c$ is calculated following Eq. (6.5). The thermochemical variables (ψ) required for the solution of the transport equations are retrieved from the flamelet manifold as a function of the computed control variables.

6.2.4 Re-construction of the soot PSDF

After the calculation of the chemical states in the CFD, the distribution of soot mass fraction within the N_{sec} sections is re-constructed from the tabulated $Y_{s,i}$ and the computed $Y_{s,c}^c$, via the expression:

$$Y_{s,i}^{re} = [\mathcal{F}_i(\phi_j)]^{\text{tab}} \cdot Y_{s,c}^c \tag{6.8}$$

with $\mathcal{F}_i$ the mass fraction of section i in cluster c given by:

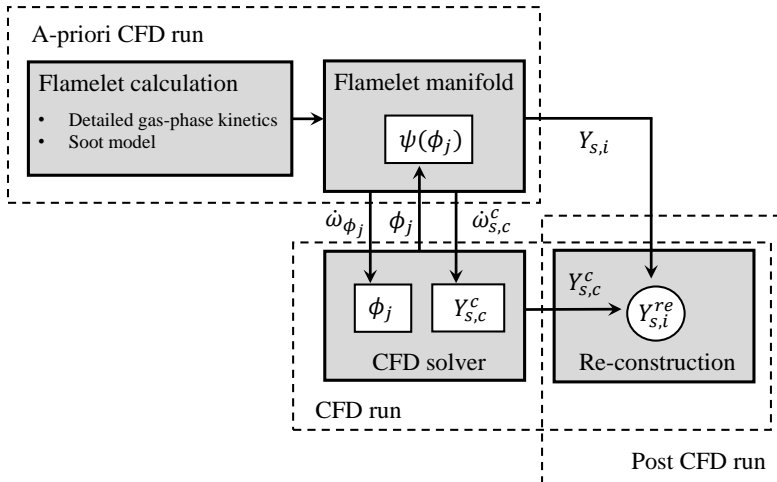$$\mathcal{F}_i = \frac{Y_{s,i}}{\sum_{i=i_c^{\min}}^{i_c^{\max}} Y_{s,i}}. \tag{6.9}$$

Figure 6.2: An overview of the key steps in the FGM-CDSM method.

157

This fraction is assumed to be a function of the control variables (ϕ_j) only and is provided in the database as a lookup variable for the re-construction of the sectional soot mass fractions. Subsequently, relevant soot quantities such as number density, mean particle diameter, and PSDF can be derived from the re-constructed sectional soot mass fractions $Y_{s,i}^{re}$ using appropriate relations (Ref. [94]). Note that the re-construction of soot PSDF can be achieved in a post-processing step or in run-time. A schematic of the aforementioned steps is presented in Fig. 6.2.

6.3 Assessment of FGM-CDSM for 1-D laminar flames

The performance of the FGM-CDSM approach is first evaluated in simulations of 1-D laminar counterflow diffusion flames under steady and unsteady conditions.

6.3.1 Flamelet tabulation approach

In all the 1-D laminar flames investigated in the present study, the same strategy is employed for manifold construction. A series of strained steady flamelets including soot chemistry are computed with $N_{sec} = 60$ using the code CHEM1D [108]. To generate a steady branch of the manifold, the applied stain rate is varied from lower values (close to chemical equilibrium) until the extinction limit for the corresponding flame. Subsequently, the composition space between the extinction limit and the mixing solution is covered by simulating unsteady extinguishing flamelet, which is also embedded in the manifold as a continuation of the steady branch. The detailed kinetic scheme KM2 of Wang et al. [105], involving 202 species and 1351 reactions, is used for the gas phase chemistry during the computation of flamelets. The diffusion transport of species is modeled using a mixture-averaged approximation [92].

Here non-premixed flames are considered for the assessment of the FGM-CDSM strategy. Therefore, for FGM simulations, the mixture fraction (Z) and reaction progress variable ($\mathcal{Y}$) are selected as suitable control variables. The Z definition follows the work of Bilger [188], while $\mathcal{Y}$ is represented by a linear combination of H_2O, CO_2, CO, O_2, H_2, and A4 species ($\mathcal{Y} = \sum_j \alpha_j Y_j$) with their corresponding weight factors $\alpha_{H_2O} = 0.0555$, $\alpha_{CO_2} = 0.0228$, $\alpha_{H_2} = 0.173$, $\alpha_{CO} = 0.0357$, $\alpha_{A4} = 0.0988$, and $\alpha_{O_2} = -3.13 \times 10^{-4}$. The progress variable definition is determined using a guess-and-check approach based on previous experience, and this selection should be taken with care. This definition has been applied in previous work [193] and shown to preserve the unique mapping of $\mathcal{Y}$ in composition space. The inclusion of slow chemical species such as A4 in $\mathcal{Y}$ is shown to improve the mapping of its chemical source term evolution in FGM [193], therefore, the aforementioned $\mathcal{Y}$ definition is retained here. Nevertheless, it is also noticed that in the case of the tabulation of soot source terms (FGM-CDSM), the accuracy of soot prediction is almost insensitive to the inclusion of A4 species in $\mathcal{Y}$. The manifolds are discretized with 400×400 equally-spaced grid points in the Z and $\mathcal{Y}$ directions, respectively.

Table 6.1: Investigated counterflow flames.

Flame	Fuel	Oxidizer	Reference
	$X_{C_2H_4} / X_{N_2}$	X_{O_2} / X_{N_2}	
CDF-1	1.0 / 0.0	0.25 / 0.75	Wang et al. [27]
CDF-2	0.8 / 0.2	0.25 / 0.75	Wang and Chung [114]
CDF-3	1.0 / 0.0	0.30 / 0.70	Xu et al. [115]

6.3.2 Steady non-premixed counterflow flames

The FGM-CDSM approach is applied to 1-D steady counterflow diffusion flames from literature [27, 114, 115]. This is generic but a crucial step in the context of identifying the lookup-related errors, and examining the suitability of control variable definitions. The details of the target flames considered for the assessment are summarized in Table 6.1. Owing to the different compositions of reactants, individual flamelet manifolds are created for the different flames in Table 6.1.

Comparisons in soot volume fraction (f_v) between the experimental measurements, detailed chemistry (DC), and FGM-CDSM are presented in Fig. 6.3 for the target flames. The numerical prediction of f_v for both DC and FGM agrees well with the experimental measurements on the different cases. The f_v profiles computed with FGM-CDSM favorably reproduce their DC counterparts, and the change in clustering factor $\mathcal{R}$ shows only a marginal impact on the accuracy of FGM-CDSM. To illustrate the merits of the FGM-CDSM in detail, key global soot quantities computed with DC and FGM are compared in Fig. 6.4 as a function of Z for the CDF-1 flame. The profiles of soot number density (N) and average particle diameter (D_{avg}) reconstructed through
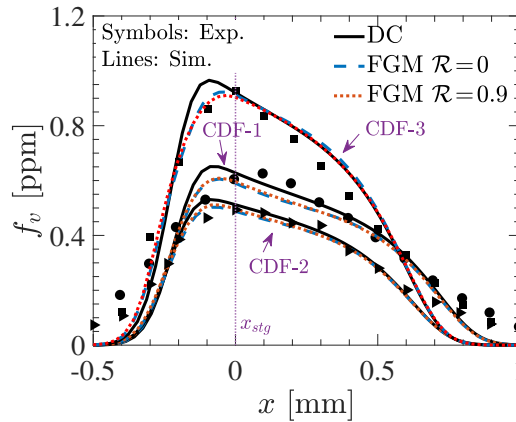
Figure 6.3: Comparison of numerical results of soot volume fraction f_v with DC and FGM-CDSM against experiments [27, 114, 115].
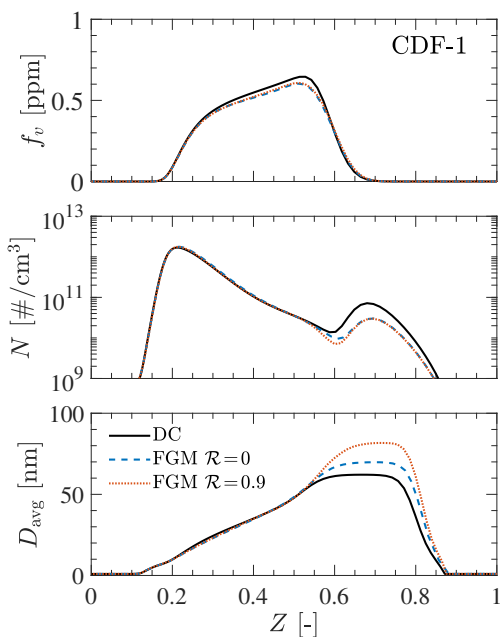
Figure 6.4: Comparison of soot quantities f_v, N, and D_{avg} predicted by DC and FGM-CDSM simulations.

FGM-CDSM exhibit a good agreement with DC results. The departure from DC solutions for $\mathcal{R} = 0$ (no clustering) essentially highlights the role of FGM chemistry. Such discrepancies mainly arise from the progress variable definition and interpolation-related errors introduced during the retrieval of manifold quantities, especially the soot source terms. Note that, the departure from DC results for $Z > 0.6$ are the result of a small peak in the PAH predicted by the employed chemical kinetic scheme [173].

As part of the assessment, it is imperative to verify the assumption of PSD preservation within the soot clusters. To address this, the Z–d_p distribution of re-constructed soot number density for $\mathcal{R} = 0.9$ is compared against the DC results in Fig. 6.5a. As can be noticed, the FGM-CDSM approach reproduces the N distribution of the DC simulations well. In addition, the locations of f_v^{max} in Z–d_p space are also well captured by FGM-CDSM. Finally, the evolution of soot PSDF reconstructed from FGM-CDSM is compared against DC solutions for different Z positions in Fig. 6.5b. The evolution of soot PSDF predicted by the FGM-CDSM approach is in good agreement with the DC and no-clustering solutions. Moreover, the transition from unimodal to the bimodal shape of PSDF with increasing Z is well reproduced by the re-constructed soot sections. It is also clear from the numerical results that the accuracy of soot prediction is only slightly impacted by the application of clustering. Overall, the analysis of predicted soot quantities and size distributions for steady 1-D flames exemplify the favorable ability of the clustering approach in reproducing the evolution of not only the global soot quantities but also the PSDF of the original sections.

(a)

(b)
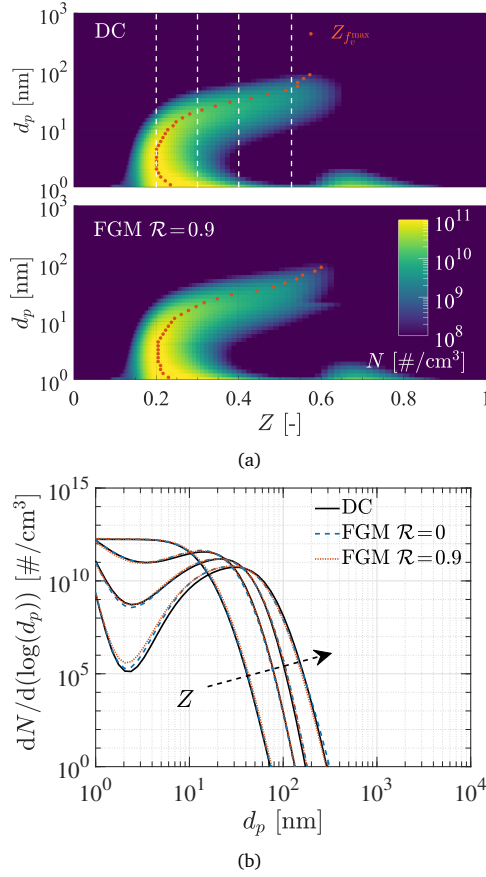
Figure 6.5: Comparison of N distributions in $Z\text{–}d_p$ space (a), and profiles of soot PSDFs at $Z = 0.2$, 0.3, 0.4, $Z_{f_v^{\max}}$ positions (b) for DC and FGM-CDSM. The position of maximum f_v in $Z\text{–}d_p$ space is marked by orange dots in subplot (a) and dashed white lines correspond to Z locations of PSDFs.

Note that the uniform clustering considered in the current work is an operational choice. Therefore, it is also interesting to investigate the impact of clustering distribution on the accuracy of FGM-CDSM. To address this, a non-uniform clustering of sections is formulated with identical $\mathcal{R} = 0.9$ (6 clusters). The distribution of particle sizes in uniform (referred to as CL-1) and non-uniform (referred to as CL-2) clusters is shown in Fig. 6.6. As can be observed, the cluster size is smaller near the small particle sizes for CL-2 (where soot number density is typically higher) and progresses approximately with a geometrical fraction. The profiles of f_v are compared in Fig. 6.7a for different clustering distributions at several strain rates (a). The qualitative prediction of f_v response to strain rate variation with FGM-CDSM is encouraging. However, discrepancies between FGM and DC solutions can be noticed for the lowest strain rate. Furthermore, slight differences in the f_v profiles are apparent for different clustering
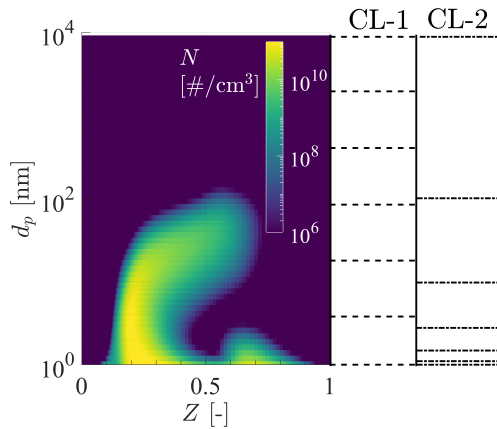
Figure 6.6: Distributions of soot number density in Z–d_p space (left panel), and the size limits of sections considered in uniform (CL–1) and non-uniform (CL–2) clustering (right panel).

distributions. For the CL-2 distribution, the f_v profiles are somewhat underpredicted compared to CL-1 and DC. The sensitivity of FGM-CDSM to clustering distribution may be attributed to a coarser representation of sections that predominantly contributes to the overall soot volume fraction. For instance, in the case of CL-2, the sections corresponding to $d_p > 10$ nm are represented by 2 clusters, while for CL-1, the same range of particle size encompasses approximately 4 clusters. The difference in cluster sizes may lead to discrepancies in the retrieval of the net soot source term of the cluster and, eventually, the soot volume fraction. At lower strain rates, the soot source terms are primarily concentrated within larger sections owing to higher residence time and facilitating sustained growth of soot particles. Hence, higher sensitivity of FGM-CDSM to clustering distribution is found at lower strain rates.
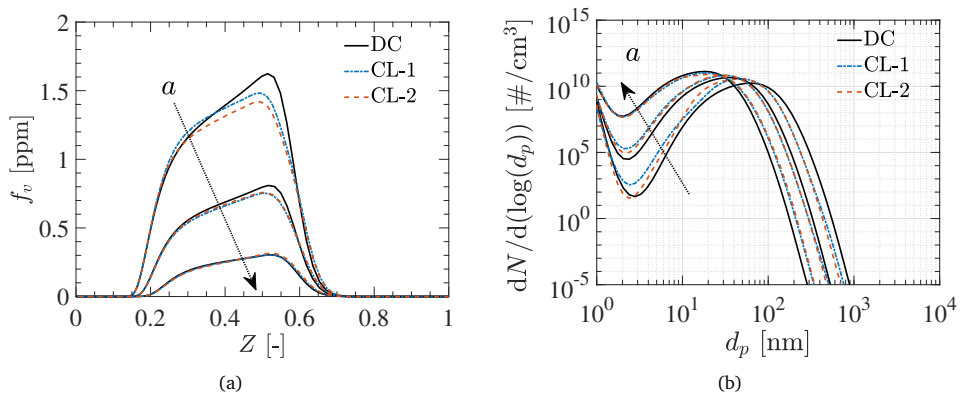
Figure 6.7: Profiles of f_v (a), and particle size distribution function (PSDF) at peak f_v position (b) for CL-1 and CL-2 clustering at $a = 50$, 100, and 200 $\mathrm{s^{-1}}$. Arrow points in the increasing direction of a.

In addition to the soot volume fraction, it is also essential to examine the impact of clustering distribution on the re-constructed soot PSDF. Hence, the profiles of soot PSDF at maximum f_v position are compared for the two clustering distribution types in Fig. 6.7b. It can be observed that the clustering distribution influences the prediction of soot PSDF. Under the CL-2 distribution, the PSDFs show close agreement with DC profiles near the trough of the PSDF for a range of strain rates as compared to the CL-1 distribution. As mentioned earlier, the finer distribution of clusters in the lower particle sizes for CL-2 tends to improve the accuracy of PSDF prediction within the power-law mode of the PSDF. The analysis suggests that the accuracy of FGM-CDSM is impacted by the clustering distribution, especially at lower strain rates. Although the uniform clustering appears to perform fairly well for different $\mathcal{R}$, a more sophisticated non-uniform clustering facilitating fine cluster sizes within smaller sooting sections might improve the accuracy of the FGM-CDSM. In the context of practical applications, the qualitative agreement between FGM and DC for different clustering distributions seems reasonable. Hence, a dedicated study on the optimization of clustering distribution is not considered in the present work.

6.3.3   Unsteady non-premixed counterflow flames

Tabulated chemistry methods are commonly applied to simulations of turbulent flames, which are inherently unsteady and often manifest strong variations of local strain rates. Therefore, it is important to investigate the predictive capabilities of FGM-CDSM in capturing the dynamic evolution of soot in such transient conditions. Two unsteady conditions are considered for this assessment. These cases are described in the following subsections.

Flames with oscillating strain rates

To represent an important aspect of unsteady flow evolution, simulations are carried out for non-premixed counterflow flames subjected to oscillations of strain rate. Such an unsteady configuration essentially mimics the fluctuating flow field through imposed strain rate oscillations. The sufficiently fast fluctuations of the flow field lead to an almost instantaneous variation of local stretch rate in a counterflow burner, and gas-phase chemistry as well as soot chemistry tend to adjust to the transient conditions. Hence, the counterflow flame configuration with imposed harmonic oscillations in the strain rate has been conveniently used to investigate the effects of hydrodynamic unsteadiness on the soot and PAH formation in previous works [43, 121, 216]. Here, this configuration is retained to examine the capabilities of FGM-CDSM in predicting the dynamic response of soot to flow unsteadiness when a flame that is in a steady-state is subjected to strain rate fluctuations.

The laminar counterflow flames experimentally investigated by Li et al. [120] are considered for this assessment. In these flames, the fuel stream is pure ethylene, and the oxidizer is composed of 25%-75% O_2-N_2 on a volume basis. The strain rate

unsteadiness is introduced by imposing sinusoidal fluctuations to the fuel and oxidizer velocities at frequency f with an amplitude A_u around a mean global strain rate. The strain rate unsteadiness is introduced by imposing sinusoidal fluctuations to the fuel and oxidizer velocities at frequency f with an amplitude A_u around a mean global strain rate K_{g} (Eq. 2.90). The velocity fluctuations imposed to the oxidizer stream have the following form:

$$u_{\mathrm{o}}(t) = u_{\mathrm{o}}^{\mathrm{st}}[1 + A_u \sin(2\pi f t)], \tag{6.10}$$

where $u_{\mathrm{o}}^{\mathrm{st}}$ is the steady-state value of the inlet velocity of the oxidizer stream. The profile for fuel stream fluctuations is obtained by fitting their measured values. Initially, the flame is in a steady state at $K_{\mathrm{g}} = 144\,\mathrm{s}^{-1}$, and the corresponding solution presents the initial condition for the application of the sinusoidal oscillations.

In Fig. 6.8, the dynamic response of soot volume fraction peak values (f_v^{max}) is presented against the dimensionless time for DC and FGM simulations. In addition, mea-
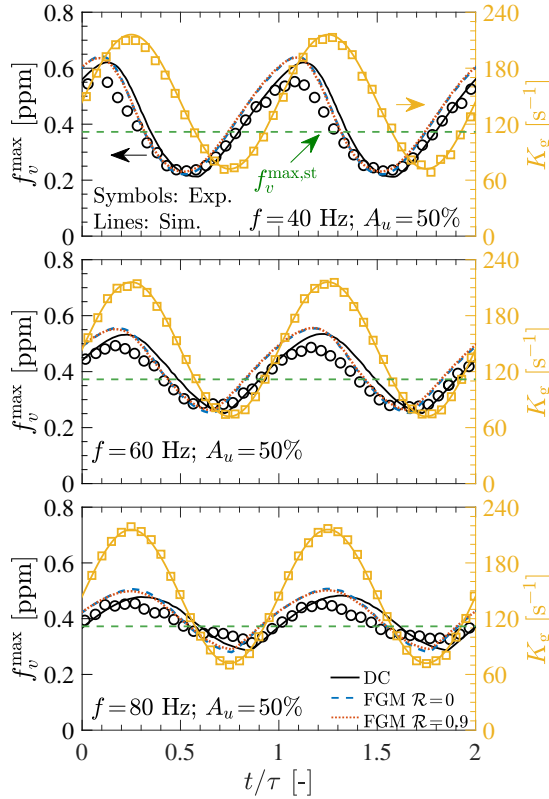

Figure 6.8: Measured (symbols) and computed (lines) temporal evolution of K_{g} and maximum soot volume fraction (f_v^{max}) as a function of dimensionless time (with $\tau = 1/f$) in unsteady counterflow flames.
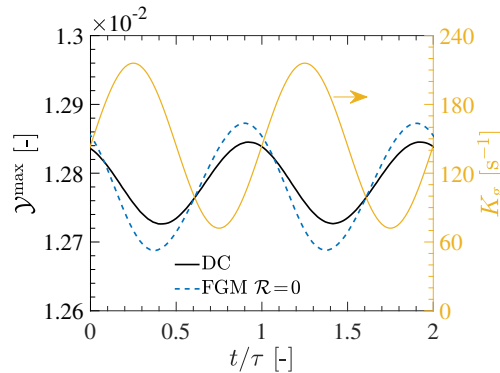
Figure 6.9: Comparison between DC and FGM solutions for evolution of peak $\mathcal{Y}$ for $f = 60\,\mathrm{Hz}$ case.

sured values of unsteady f_v^{max} and K_g are plotted for comparison. Consistent with previous studies [121], for an increase in the imposed frequency, the amplitude of induced oscillations of soot volume fraction tends to decrease, while the phase-lag between imposed oscillations and soot response becomes larger. It can be observed that DC results show very good agreement with measurements for the transient soot response. The maximum and minimum values of the induced soot oscillations quantitatively match well with their experimental values, although a slight phase-lag can be observed for the simulation. In addition to DC, the dynamic response of soot is also reproduced reasonably well by the FGM-CDSM method. The amplitude and the peak values of the induced oscillations agree well with the DC and experimental results. It is also evident that the FGM profiles for soot response with clustering ($\mathcal{R} = 0.9$) are almost identical to the one achieved without the inclusion of clustering, see Fig. 6.8. Nevertheless, the transient variation of f_v^{max} for FGM chemistry is found to be in better agreement with experiments, while DC tends to overpredict the phase-lag.

In FGM simulations, variation in local flame structure with unsteady strain rate is essentially represented through the response of control variables to the imposed fluctuations. Since control variables are used to parameterize various thermochemical parameters from the manifold that is generated from steady flamelets at different strain rates, (and extinguishing flamelets) the unsteady phase-lag and soot attenuation are consequences of the flamelet behavior of soot source terms (through the progress variable) along with transport. To elucidate this argument, the transient evolution of the progress variable for the DC and FGM is shown in Fig. 6.9. The phase-lagged response of the progress variable can be noticed in DC results compared to FGM, which essentially translates into phase-lag in the unsteady evolution of f_v^{max}. In the current FGM-CDSM framework, manifolds are constructed through steady and extinguishing flamelets. An extension of the manifold generated from fluctuating flamelets with additional parametrization, as proposed in the work of Delhaye et al. [217], or an unsteady flamelet formulation, introduced by Pitsch and Imhe [218] can also be considered to improve the accuracy of soot prediction in the unsteady conditions.
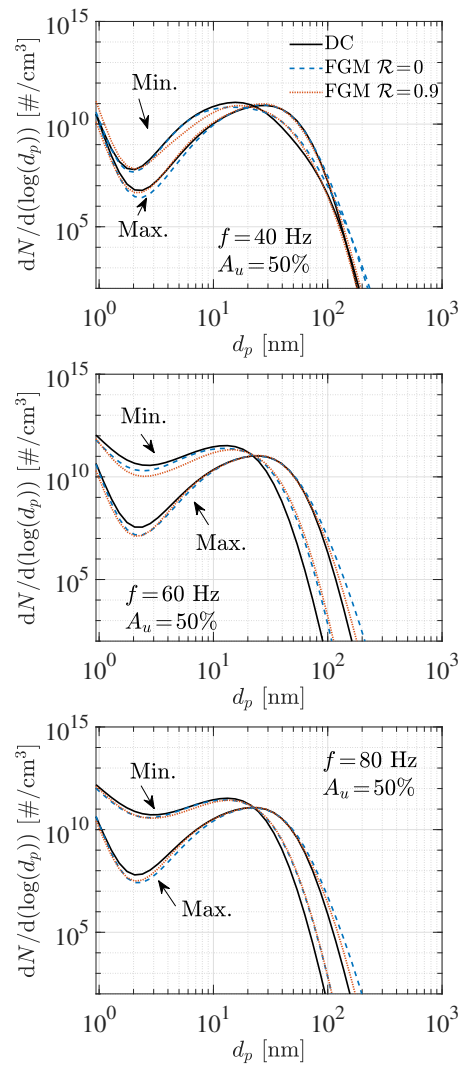
Figure 6.10: Comparison of soot PSDFs for maximum and minimum values of the induced response taken at $f_v^{\max}$ locations for DC and FGM chemistry under different frequencies.

To demonstrate the ability of FGM-CDSM in predicting unsteady soot evolution, the instantaneous profiles of re-constructed PSDF are compared against DC solutions in Fig. 6.10. The PSDFs are taken at the times of the maximum and minimum induced soot response and at the spatial location of the maximum soot volume fraction for different imposed frequencies. In a counterflow configuration, a decrease in strain rate tends to increase the residence time of soot particles, which enhances their growth through surface reactions and coagulation. Consequently, the log-normal mode of
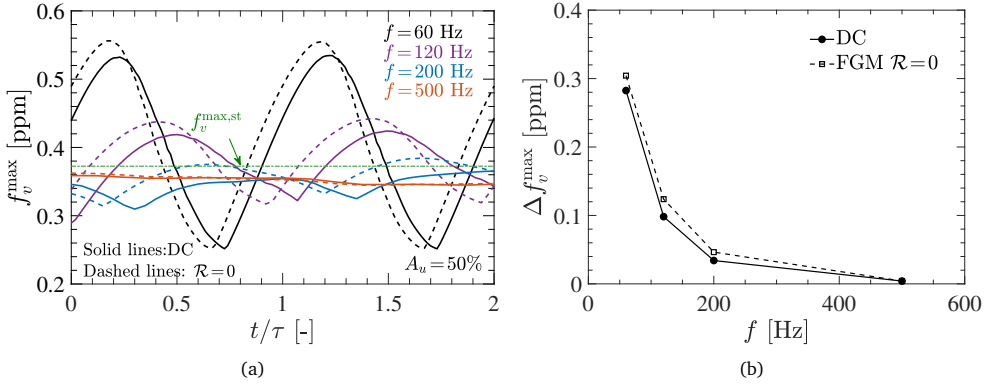
Figure 6.11: Comparison between FGM and DC solutions for transient response of maximum soot volume fraction (f_v^{max}) (a), and amplitude of induced f_v^{max} oscillations (b) in unsteady counterflow flames.

PSDF shifts towards larger particle diameters while the trough of the PSDF moves toward lower particle number densities. The opposite occurs for the increase in the strain rate. It is evident from Fig. 6.10 that the FGM-CDSM qualitatively reproduces the PSDF shape from DC. The application of clustering reproduces well the unsteady PSDF evolution when compared to the case without clustering, which displays the potential of FGM-CDSM to capture the dynamic evolution of the soot PSDF.

Given the modest range of frequency (30-80 Hz) used in the experiments [120], the attenuation observed in soot response is relatively small. Hence computations are performed for higher frequencies of imposed strain rate oscillations. The comparison of peak f_v response between FGM-CDSM ($\mathcal{R} = 0$) and DC for several frequencies is presented in Fig. 6.11a. The phase-lag in the response of soot to the imposed fluctuations is prominent at higher frequencies, accompanied by a drastic reduction in the amplitude of the soot oscillations. Such strong attenuation of soot oscillations at substantially higher frequencies is captured well by the FGM-CDSM approach. As can be observed in Fig. 6.11b, the amplitude of induced oscillations in peak soot volume fractions ($\Delta f_v^{\mathrm{max}}$) obtained with FGM-CDSM agree well with their DC counterparts, which demonstrate good capabilities of FGM-CDSM in capturing soot formation under unsteady conditions. It is worth highlighting that at very high frequencies (e.g. 500 Hz) the oscillation times are very small. These flow oscillations introduce rapid variations in radical formation due to strain effects but occur at smaller time scales than those of the soot chemistry. As the frequency of the perturbations increases, the amplitude of the response in soot formation reduces to zero. While this tendency is well predicted, certain discrepancies appear concerning the dynamic response to flow oscillations. A phase-lag between DC and FGM solutions can be distinguished in Fig. 6.11a. This response is associated with the strategy used for flamelet tabulation and manifold generation. The impact of the tabulation strategy on unsteady soot formation requires a detailed investigation, which is left for future work.

Unsteady soot evolution from gas phase

In the FGM-CDSM approach, the soot source terms are calculated and stored for soot mass fractions (and other variables) in a steady state. Therefore, the chemical trajectories concerning the formation of soot from the gas phase to the steady state are not explicitly retained in the FGM manifold. Hence, it is also interesting to investigate the capabilities of FGM-CDSM in predicting the unsteady formation of soot from the pure gas phase. The time-dependent evolution of soot volume fraction from an initial condition pure gas-phase initial solution (i.e. steady solution with $Y_{s,i} = 0$) for $\mathcal{R}=0$ and $\mathcal{R} = 0.9$ are compared against the DC counterparts in Fig. 6.12a for the CDF-1 flame investigated earlier in Section 6.3.2. It can be observed that the soot evolution at the early stage is not very well captured by the tabulation of the soot source terms ($\mathcal{R} = 0$). However, the influence of clustering ($\mathcal{R} = 0.9$) on f_v profiles at different time instances is found to be negligible.

At smaller time intervals (0.005 to 0.1 ms), the comparison between FGM-CDSM and DC profiles in Fig. 6.12b shows a significant overprediction (up to a factor of 4) of soot volume fraction by FGM-CDSM. However, the clustering of sections accurately reproduces the soot volume fraction profiles of their no-clustering counterparts. Apart from the quantitative differences, the soot volume fraction profiles in the region $0.2 < Z < 0.3$ are found to be more skewed for FGM-CDSM than DC. This response can be attributed to the fact that the soot source term is obtained from steady flamelets, resulting in an overprediction of growth within $0.2 < Z < 0.3$. In contrast, for DC, soot inception is more prevalent in earlier times, resulting in more distributed f_v profiles in the mixture fraction space, with higher f_v in $0.2 < Z < 0.3$ compared to FGM-CDSM. This overprediction of soot volume fraction is not unexpected given the lack of information on the chemical trajectories from the gas phase to the steady-state soot evolution in the flamelet database.

(a)   (b)
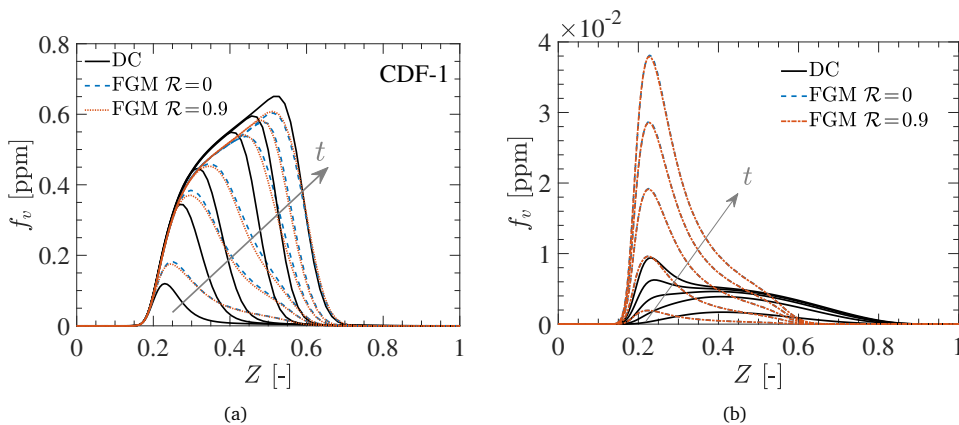
Figure 6.12: Evolution of f_v from steady gas-phase solution for DC and FGM chemistry.   Gray arrow indicates time $t = 0.5, 1.5, 2.5, 5, 7.5, \infty$ ms (a), and $t = 0.005, 0.01, 0.05, 0.075, 0.1$ ms (b).

The departure from DC results for f_v is primarily related to the tabulation of soot source terms. For flame initially at steady state without soot, the direct look-up of soot production rate in the clustered section ($\dot{\omega}_{s,c}^{c,+}$) is overestimated, while the linearized consumption rate ($\dot{\omega}_{s,c}^{c,-}$) is underestimated. Especially, near $Z = 0.5$, the f_v values are overpredicted as compared to the DC solutions. This is because, in a counterflow flamelet, the low residence time of soot enhances soot particle size (and volume fraction) as particle approach the stagnation plane (the fuel-rich side for the current case). As a result, the discrepancy in soot profiles is particularly evident near higher mixture fractions. The agreement between DC and FGM-CDSM results for f_v tends to be better as the soot formation progress toward a steady state. Naturally, an extension of FGM to incorporate the chemical trajectories of soot formation (from the gas phase to the steady state) would require computations of complementary unsteady flamelets (at every level of scalar dissipation rate), which would also require an additional controlling variable to entirely encapsulate the reaction progress of soot, leading to a complex manifold generation. However, adhering to the scope of the present work, further investigation is necessary to fully address this aspect. Note that the simulation starting from no-soot is a special case considered here to demonstrate the limitations of the soot source term tabulation approach. Nevertheless, in simulation applications where the unsteady evolution of soot quantities is not of interest, the no-soot initialization can be replaced with a steady-state soot initial condition.

6.4   Application of FGM-CDSM to 2-D laminar flames

As a next (intermediate) step towards real burner configurations, a laminar coflow diffusion flame is considered to evaluate the performance of FGM-CDSM. The burner configuration is a 2-D planar channel in which the fuel jet is injected from the central rectangular slot, while a coflow is introduced on the sides. The 2-D burner configuration is modeled with the computational domain as shown in Fig. 6.13. The dimensions in the computational domain are $L_h = 10\,\text{cm}$, $L_j = 2.5\,\text{cm}$, $L_c = 7.5\,\text{cm}$, and $L_r = 0.5\,\text{cm}$. A structured grid with approximately 0.26 mm element size is used for the simulations. The burner is enclosed with adiabatic, no-slip side walls and maintained at atmospheric pressure. For the jet and coflow inlets, uniform velocity profiles are specified, and a small recession is provided to mimic a developed laminar velocity profile at the jet lip ($y = 0$). The fuel is pure ethylene, and the oxidizer is composed of O_2 and N_2 (25/75 by volume, respectively). The fuel and oxidizer are injected at 15 cm/s and 300 K temperature.

The sooting flame simulations with both detailed chemistry and FGM-CDSM are carried out using the multi-physics code Alya [219]. The code Alya has been successfully applied for the investigation of laminar and turbulent flames using tabulated and finite rate chemistry [220–222], and will be used here as a platform for comparing the different approaches for FGM-CDSM. The kinetic mechanism ABF of Appel et al. [23], containing 101 species and 544 elementary reactions, is employed for the de-
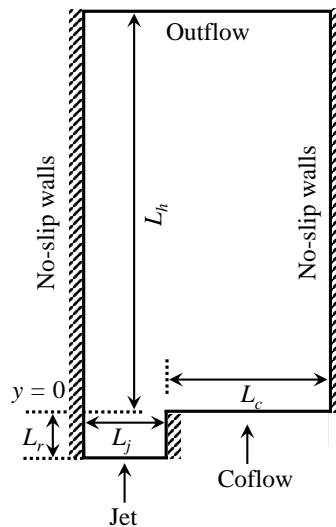
Figure 6.13: Schematic of 2-D slot burner configuration (not to scale).

tailed chemistry simulation and the computation of the diffusion flamelets. The FGM database is constructed using steady and unsteady quenching counterflow flamelets following the strategy mentioned in Section 6.3.1. The progress variable definition employed in 1-D flame simulations (presented in section 6.3.1) is retained for 2-D simulations. The ABF mechanism is selected solely to reduce the cost of the detailed flame simulations. To further minimize the cost of calculations, $N_{sec} = 40$ sections are considered. The differential diffusion effects are important in sooting flames as demonstrated in earlier works [223,224] and can be included, but for the sake of simplicity in the DC vs FGM comparison, the unity Lewis number assumption is retained here for diffusion transport of gaseous species. The performance of FGM-CDSM has been investigated for non-unity Lewis transport in 1-D cases.

The steady-state fields of temperature are compared in Fig. 6.14a for DC and FGM-CDSM cases. A good agreement between the numerical solutions is shown for the temperature distribution, which probes the ability of the FGM chemistry to capture the flame position. In addition, mass fraction profiles of the key gas-phase species at stream-wise location $y = 4$ cm predicted by detailed kinetics and FGM are presented in Fig. 6.14b. The numerical profiles of different species obtained with the FGM chemistry are in good agreement with the detailed simulation. The comparisons of temperature and gas-phase species, confirm that the flame structure is fairly well reproduced by the FGM chemistry in this planar flame configuration.

Subsequent to the verification of the flame structure, the contours of soot volume fraction predicted by DC and FGM-CDSM, are presented in Fig. 6.15 for $\mathcal{R} = 0$ and $\mathcal{R} = 0.9$. The overall distribution of f_v is well reproduced by FGM-CDSM. Early-stage
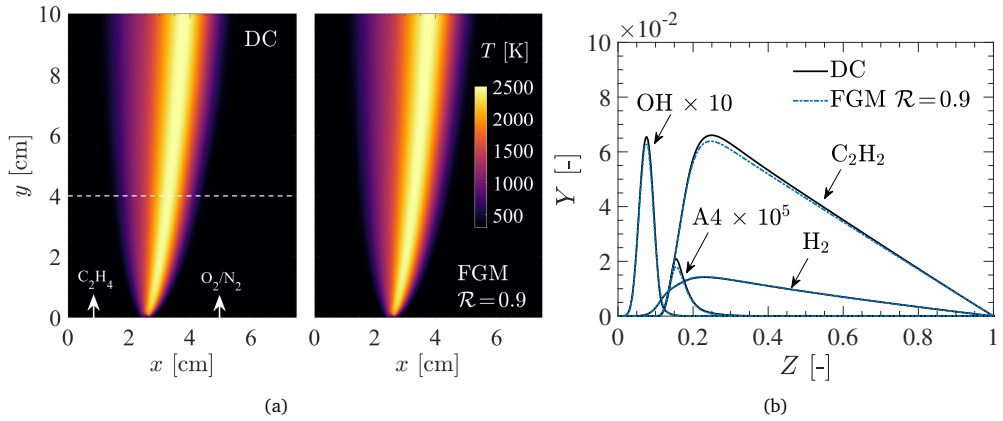
Figure 6.14: Comparison between DC and FGM-CDSM solutions for temperature fields (a), and mass fractions of important gas-phase species at $y = 4\,cm$ (b).

soot formation near the upstream region is captured well by FGM solutions. However, the FGM-CDSM shows a slight tendency to under-predict peak f_v compared to the DC solution as the flame develops downstream. The profiles of f_v and PSDF at several downstream positions are compared in Fig. 6.16 for a more quantitative illustration of the accuracy of FGM-CDSM. The qualitative agreement between DC and FGM-CDSM for the prediction of f_v distribution in Z-space is encouraging. Furthermore, the evolution of the soot PSDF along several downstream locations and their bi-modality is re-constructed with reasonable accuracy by FGM-CDSM. However, a quantitative deviation between the DC and FGM-CDSM solutions can still be observed. The f_v profiles predicted by FGM-CDSM tend to exhibit wider distributions in Z-space compared to
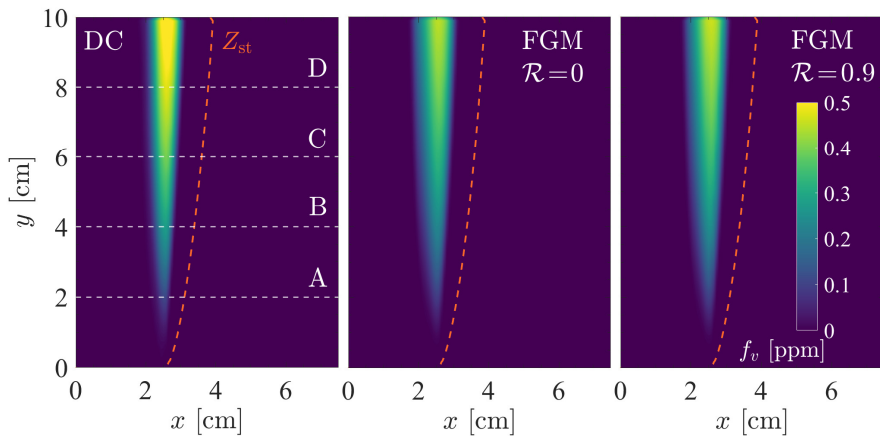
Figure 6.15: Comparison between DC and FGM-CDSM solutions for soot volume fraction fields.

171
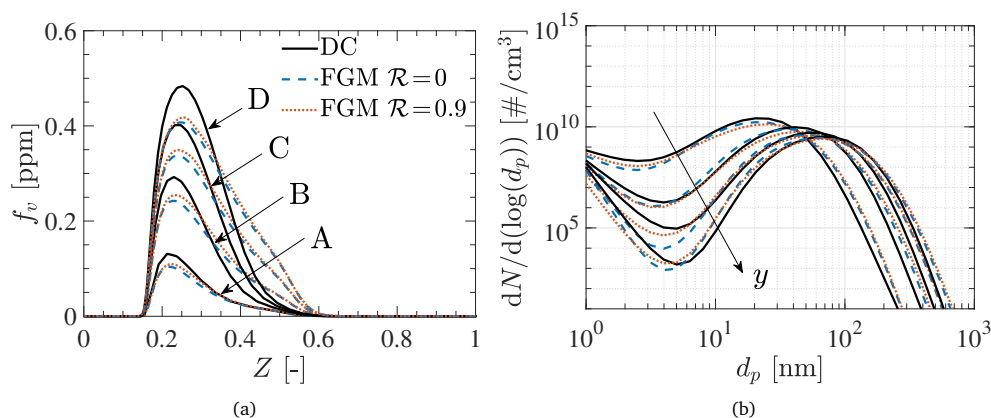
Figure 6.16: Comparison between DC and FGM-CDSM solutions for profiles of f_v (a), and PSDF (at $f_v^{\max}$) along $y = 2, 4, 6, 8\,\mathrm{cm}$ (denoted by A, B, C, D, respectively in Fig. 6.15) positions (b).

DC. However, the results clearly show, that the introduction of clustering ($\mathcal{R} = 0.9$) only does not impact the overall accuracy of FGM-CDSM compared to the case transporting all the sections ($\mathcal{R} = 0$). Therefore, the noticed departure from DC solutions suggests the limitation of tabulated source terms to exactly reproduce the chemistry of the soot formation.

It is important to highlight that the FGM database here is generated using steady and unsteady quenching formulations of representative counterflow flamelets. In FGM the soot source terms are calculated and stored for soot mass fractions (and other variables) in a steady state. In contrast, in the coflow case, the soot mass fractions are initially much lower and slowly increase toward steady-state values. Therefore, the chemical trajectories concerning the formation of soot from the gas phase to the steady state are not explicitly retained in the FGM manifold. As already noticed in the results for unsteady soot evolution for 1-D counterflow flame (refer Fig. 6.12a) the early-stage reaction progress of soot is not well captured by the FGM-CDSM method. Especially, near $Z = 0.5$, the f_v values are overpredicted compared to the DC solutions. A similar trend is also translated near $Z = 0.5$ for the f_v profiles in the 2-D coflow case. Nevertheless, considering the challenges associated with the numerical prediction of soot formation in multi-dimensional flames, the performance of the novel FGM-CDSM approach in capturing soot formation is remarkable.

6.5 Comparison of FGM-CDSM and FGM-Full strategy

The main objective of the present work is to introduce a computationally efficient FGM-DSM coupling through the tabulation of soot source terms followed by the clustering of soot sections. The limited capability of this method in capturing the chemical history effects of soot formation is evident from the discussion of the results presented
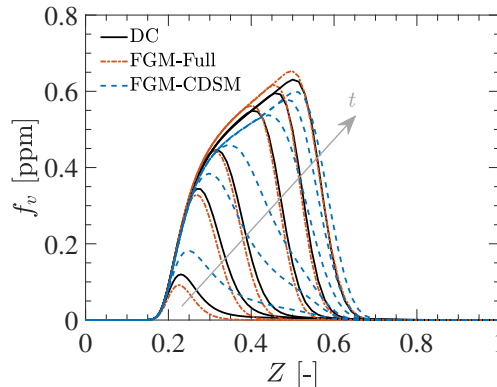
Figure 6.17: Profiles of unsteady evolution of f_v from steady gas-phase solution for DC, FGM-CDSM (with $\mathcal{R} = 0$), and FGM-Full approaches. The gray arrow indicates time $t = 0.5, 1.5, 2.5, 5, 7.5, 12.5$ ms.

here. Hence, it is interesting to illustrate the differences between run-time source term computation and source term tabulation (FGM-CDSM) in predicting soot history effects. The FGM-DSM coupling approach involving run-time soot source term computation has been introduced in the previous chapter [193] under the term FGM-Full method. In the FGM-Full method, the sectional soot source terms are computed during the simulation run by using tabulated gas-phase species mass fractions and thermochemical parameters relevant to the soot model.

A test counterflow flame configuration (introduced in Section 6.3.3) describing the unsteady evolution of soot from the pure gas-phase initial solution toward the steady solution is retained for this comparative assessment. The instantaneous profiles of soot volume fraction are compared for FGM-Full and FGM-CDSM ($\mathcal{R} = 0$) in Fig 6.17. As can be noticed, the profiles of soot volume fraction obtained from DC are well reproduced with the FGM-Full strategy. Such a favorable unsteady response of FGM-Full can be attributed to the fact that the separation of soot formation and gas-phase chemistry time scales (with the former being much slower than the latter) is effectively achieved during soot source term computation, as opposed to their tabulation from steady-state flamelets.

The comparison of FGM-CDSM and FGM-Full strategies for unsteady flames with oscillating strain rates (introduced in Section 6.3.3) is presented in Fig. 6.18 for different frequencies. It can be observed that the dynamic response of peak soot volume fraction predicted by FGM-Full, shows a close agreement with DC in terms of phase difference as compared to FGM-CDSM. Since the intra-sectional dependence of soot source terms on soot variables is included in the FGM-Full method, the chemical time scales of soot formation are favorably captured in the FGM-Full method. On the other hand, FGM-CDSM follows the chemical time scales of soot formation based on the tabulated source terms, which are strongly correlated to the dynamic evolution of the progress variable along with soot transport. Despite slight discrepancies when com-

173
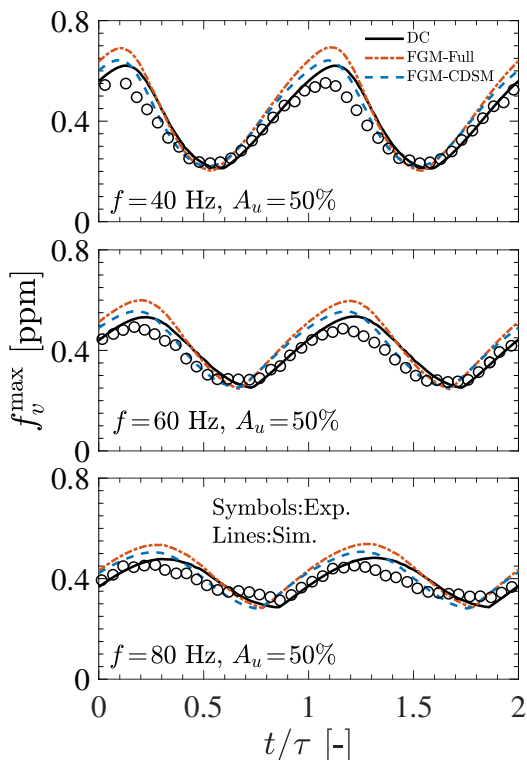
Figure 6.18: Comparison between DC, FGM-CDSM (with $\mathcal{R} = 0$), and FGM-Full solutions for transient evolution of peak soot volume fraction.

pared with FGM-Full, the accuracy of FGM-CDSM in capturing dynamic responses of soot is encouraging, considering several assumptions surrounding its formulation.

The 2-D laminar configuration introduced earlier (in Section 6.4) is similar to this 1-D time-dependent case where unsteady soot evolution is translated into streamwise spatial evolution. In Fig. 6.19, the steady-state soot volume fraction fields obtained with DC are compared against FGM-CDSM (with $\mathcal{R} = 0$) and FGM-Full solutions. It can be observed that the distribution of f_v within fuel-rich regions is somewhat better reproduced with the FGM-Full method as compared to FGM-CDSM method. For a more quantitative illustration, the f_v profiles and PSD (at the peak f_v) obtained with the FGM-Full and FGM-CDSM methods at several downstream positions are compared against their DC counterparts in Fig. 6.20. Compared to FGM-CDSM, the f_v profiles in composition space and PSDs predicted by the FGM-Full approach show good qualitative agreement with DC solutions. Moreover, the diffusion of soot noticed in the fuel-rich region for the FGM-CDSM case is prevented in the FGM-Full approach, as the chemical trajectories of soot formation from the gas phase are captured well in the latter approach.
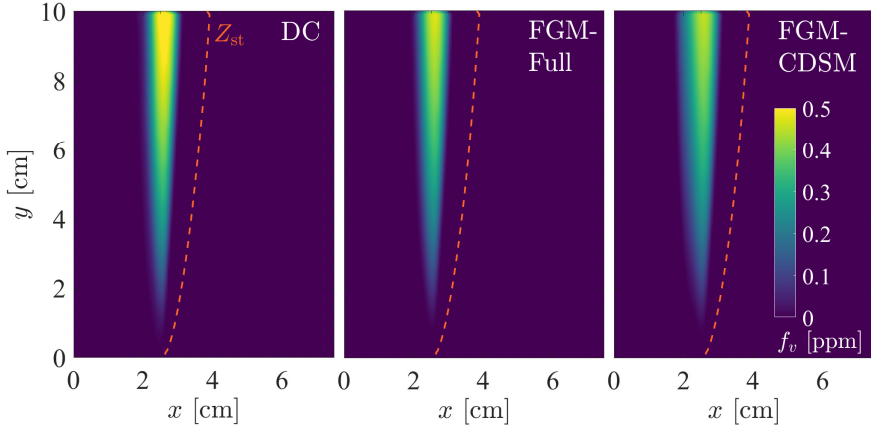
Figure 6.19: Comparison between DC, FGM-CDSM (with $\mathcal{R} = 0$), and FGM-Full solutions for soot volume fraction fields.

From the comparison between soot prediction with the FGM-CDSM and FGM-Full methods, it is evident that the use of tabulated soot chemistry from steady flamelets for an essentially unsteady soot formation process will not be very accurate. An alternative approach for FGM-CDSM can be suggested to isolate time scales associated with different subprocesses which involve run-time computation for the coagulation process in conjunction with a priori-tabulation of source terms of other soot subprocesses. However, the computational speed-up gained with this approach will be very marginal compared to the FGM-Full method. The calculation of the 2-D coflow flame showed that compared to the run-time computation of the soot source term (FGM-Full), the use of FGM-CDSM yields a speed-up of about 14 (from 40 sections). This
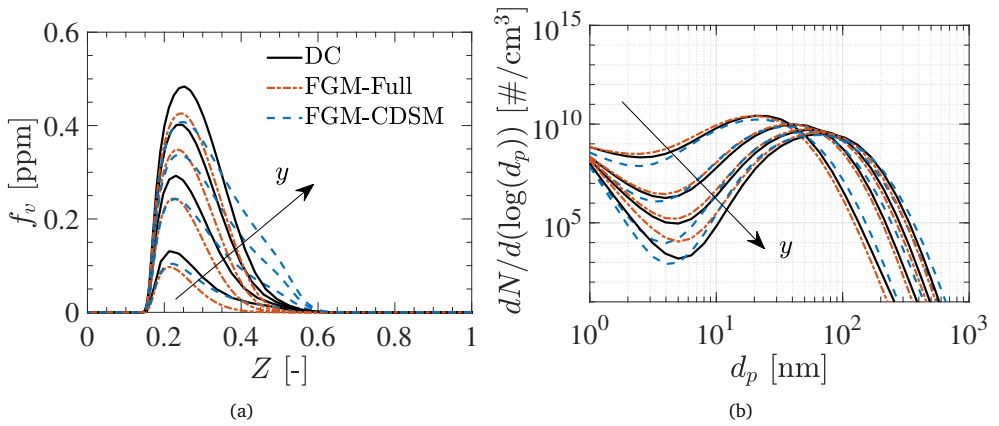
Figure 6.20: Comparison between DC, FGM-CDSM (with $\mathcal{R} = 0$), and FGM-Full solutions for profiles of f_v (a), and PSDF (at $f_v^{\max}$) along $y = 2, 4, 6, 8 \, \text{cm}$ downstream positions (b).

speed-up can be further increased by a factor of approximately 60 through the clustering level $\mathcal{R} = 0.9$. The present approach is therefore very useful in the context of the simulation of practical systems.

In terms of implementation within a CFD solver, the FGM-CDSM strategy is relatively straightforward compared to FGM-Full. The FGM-CDSM approach allows for a simpler extension of the general FGM framework for transport equations to accommodate a few clustered sections, as the source terms of clusters are directly looked up from the manifold. Besides, the re-construction of sectional soot mass fractions can also be performed in the post-CFD stage, eliminating the need for additional programs to perform the runtime reconstruction. On the contrary, for the FGM-Full method, an additional program is required to calculate the contributions of different soot subprocesses to the soot source terms based on the local concentrations of gas-phase species. This additional program needs to be integrated into the CFD solver, introducing the extra complexity of model implementation. In this context, the FGM-CDSM model offers an efficient and simplistic approach for implementing soot formation prediction capabilities within CFD solvers.

6.6 Computational performance

An important aspect of the FGM-CDSM method is its computational efficiency. The efficiency is evaluated here from the computing time required to perform time-dependent simulations of laminar flames for a period of 1 ms. The solutions from FGM-CDSM and DC are compared in Fig. 6.21. In CHEM1D, a fully implicit 2nd-order time integration scheme with an adaptive time step strategy is considered for simulations of laminar counterflow flames. On the other hand, in Alya, an explicit 3rd-order Runge-Kutta time integration scheme with a constant time step is employed for the assessment of CPU time.
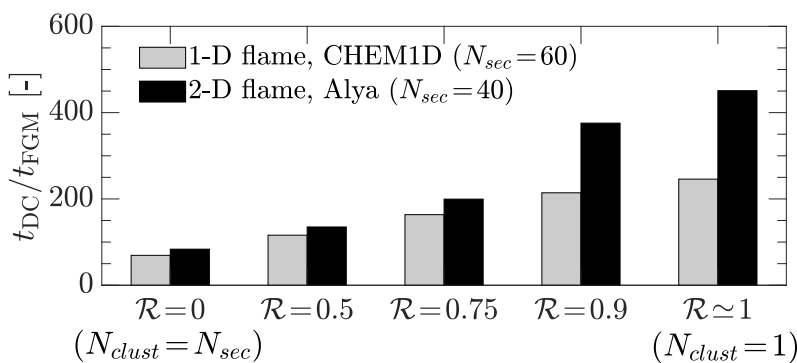
Figure 6.21: Computational speed-up with FGM-CSDM for laminar flame simulations in solvers CHEM1D and Alya.

Figure 6.21 shows that the FGM-CDSM enables a reduction in CPU time by two orders of magnitude compared to detailed chemistry with the same number of sections ($\mathcal{R} = 0$). Clustering of sections leads to further reduction of the computational cost. For instance, in 1-D calculations, a factor 10 reduction in the number of clusters ($\mathcal{R} = 0.9$) leads to speed-up factors of 3 and 215 compared to $\mathcal{R} = 0$ and DC respectively. In the 2-D FGM calculations, a speed-up of 4.5 is achieved for an increase in clustering factor from $\mathcal{R} = 0$ to $\mathcal{R} = 0.9$. In addition, the calculation of 2D coflow flame showed that compared to the run-time computation of soot source term (FGM-Full), the use of FGM-CDSM yields a speed-up of about 14 (from 40 sections).

Understandably, the extensive computational speed-up is primarily the consequence of a drastic reduction in the number of transport equations needed to be solved for the gas-phase species (through FGM) and sectional soot mass fractions (through clustering). In addition, the tabulation of the soot source terms avoids the computationally intensive calculation of the soot particle dynamics (coagulation process). Although the impact of clustering on the overall speed-up is somewhat moderate compared to the use of FGM, it facilitates a significant reduction in the memory consumption of the FGM database and post-processed variables. Therefore, the FGM-CDSM approach tends to deliver a drastic advantage in terms of the memory footprint of the CFD simulations besides the aforementioned reduction in computational cost.

6.7   Summary

A computationally efficient strategy to predict the formation of soot and the evolution of its PSD is proposed by integrating the discrete sectional method-based soot model and Flamelet Generated Manifold chemistry and is referred to as FGM-CDSM. The FGM-CDSM comprises clustering of soot sections to enable the low dimensional description of PSD and minimize the computational cost. In this work, FGM-CDSM is applied to simulations of laminar non-premixed flames for the assessment of its accuracy and computational performance against a detailed kinetics-based sectional soot model.

Numerical results revealed that the FGM-CDSM tends to reproduce the global soot quantities and their dynamic response captured by detailed kinetics reasonably well. Moreover, the introduction of clustering demonstrated a minimal effect on the overall accuracy of soot prediction, apart from slight discrepancies in quantitative prediction. Computational performance analysis indicated that the application of FGM-CDSM facilitates the reduction of CPU time by approximately two orders of magnitude compared to the detailed chemistry-based simulations.

Although the assumption of soot following its steady flamelet behaviour may not have physical evidence, the current study demonstrates it to be a reasonably good approximation to reproduce the soot formation in steady and unsteady conditions while proposing an efficient modeling strategy (clustering) for sooting flame simulations.

The results presented here show certain limitations of the model to capture accurately the soot formation during the onset and early stages of the soot process. In fact, when information on soot evolution from the gas phase to the steady state is not included in the manifold, the model's performance is affected. However, this issue is primarily related to the flamelet generation rather than the tabulated soot chemistry or the clustering strategy. In this context, the development of a consistent relaxation model for soot source terms, and effective treatment of the chemical history of soot formation in the manifold can be of interest towards application to multidimensional unsteady flames. Finally, it is observed that the accuracy of FGM-CDSM is slightly impacted by clustering distribution. Therefore, further improvements can be sought to establish a more sophisticated distribution of sections in clustering.

In conclusion, the good predictive accuracy, decent computational efficiency along with low memory footprint, make the FGM-CDSM approach a promising candidate for large-scale simulations of turbulent sooting flames. However, further research is required to investigate the performance of FGM-CDSM under turbulent conditions, which constitutes the main focus of the next chapter.

7

Modeling of soot formation in turbulent flames with FGM-DSM

In this chapter, the soot modeling framework with FGM chemistry and DSM-based soot model is introduced within the Large Eddy Simulation (LES) approach. The LES formalism is subsequently applied to the simulation of a turbulent non-premixed ethylene jet flame and examined for its predictive capabilities with the experimental soot measurements. Soot formation and evolution of the PSD are analyzed in the context of soot-turbulence-chemistry interaction treatment, preferential diffusion effects, hydrogen addition effects, and thermal radiation effects. The content of this chapter partially refers to an article under review for publication in Combustion and Flame.

7.1 Introduction

As discussed in Chapter 1 soot modeling in turbulent flames remains a great challenge owing to its complex multi-physical nature, characterized by an intricate coupling between flow parameters, gas-phase chemistry, and soot properties. Hence numerical prediction of soot in turbulent conditions necessities adequate characterization of the flame behavior as well as different physico-chemical phenomena involved in soot formation. Turbulent flows are characterized by a wide range of flow scales from energy-containing large scales to the smallest Kolmogorov scales [90]. In comparison, the time scales of soot formation are typically even larger than the integral flow time scales. This disparity makes the prediction of soot formation in turbulent flames a challenging task. Considering the uncertainties in soot chemistry, aerosol dynamics, and their interaction with turbulence, quantitative modeling of soot formation in turbulent combustion is still beyond the frontier of current modeling advancements [89]. Although significant efforts have been made to describe turbulent-chemistry interaction, the effect of turbulence on soot formation is still an open subject. At the same time, state-of-the-art soot models, if used judiciously in conjunction with a better prediction of the turbulent flow structure, can provide partial solutions to the practical problems of interest.

The prediction of soot formation in turbulent flames using the aforementioned soot modeling approaches is preferable to be conducted in the context of Direct Numerical Simulations (DNS), where a full description of all the temporal and spatial scales associated with turbulence and chemistry is available. However, the high computational cost required to resolve the coupled phenomena associated with the scales of turbulence, chemistry, and particle dynamics limits the DNS investigation to selected cases [41, 204, 212]. On the other end, Reynolds Averaged Navier-Stokes (RANS)-based methods that solve the time-averaged equations, provide information on the mean properties of the flow and soot at much affordable simulation costs. The RANS approach has been extensively used to predict soot formation in turbulent conditions, especially in industry-relevant IC engines and gas turbine model combustors [39]. However, the RANS approach hardly provides information on the transient phenomena of flow, flame dynamics, and soot formation. Large Eddy Simulation (LES) technique being an intermediary approach between DNS and RANS, can capture transient features of flow and flame as the large scales are the predominant energy-containing scales of the flow, with subgrid models needed for accounting for interactions on small scales. In fact, LES has been applied very successfully for a wide range of problems including jet, swirl, or spray flames [73, 85, 220, 225–229] and it generally shows a good trade-off between accuracy and computational cost. Therefore, the development of reliable soot models for LES is essential for the study of soot formation in both fundamental and industrial configurations. In recent years, LES has been adopted to investigate soot formation in turbulent flames, departing from semi-empirical methods [201, 230, 231] and evolving towards more detailed soot modeling approaches [66, 73, 75, 226, 232, 233]. However, due to limitations in terms of computational overhead, primarily the method of moments [66] and, to a certain extent, sectional methods [73] are employed in large-scale flame simulations. Compared to the moments-based approach, the discrete sectional method has the advantage that it directly provides local information on soot PSD. However, due to its higher computational cost, it is employed to a smaller extent in LES. Therefore, exploring efficient strategies offering a compromise between accuracy and computational cost by combining an LES approach with a sectional model would be instrumental.

LES of turbulent sooting flames relies on three aspects: an accurate description of gas-phase chemistry, modeling of the dynamics of soot particle population, and integration of models for capturing interactions between soot-turbulence-chemistry. For reliable prediction of soot formation in turbulent combustion, a detailed understanding of gas-phase kinetics is necessary to properly capture the flame structure and formation of gas-phase species participating in the soot processes (such as polycyclic aromatic hydrocarbons (PAHs) or unsaturated hydrocarbons such as acetylene). However, using detailed kinetic schemes involving hundreds of species is impractical in LES employing finite-rate chemistry-based methods. As a result, tabulated chemistry methods [66, 73], reduced kinetic schemes [79], and globally optimized chemistry [234] are often used instead. Concerning the soot-phase description, although quantitative modeling of soot formation in turbulent combustion is still beyond the frontier of cur-

rent modeling advancements [89], the state-of-the-art soot models can still offer valuable qualitative and semi-quantitative information on soot formation when employed judiciously along with accurate predictions of the turbulent flow structures. Another challenge in LES of turbulent sooting flames is modeling the subgrid-scale interactions between soot and turbulence, as soot chemistry involves non-linear interactions between the gas and solid phases. Different strategies have been proposed to model soot-turbulence interactions in mono-dispersed and moment-based models [66, 75] and more recently in sectional models [73, 226]. Although closure models for soot-turbulence interactions are important in the detailed description of the soot formation process, their impact on the overall prediction of global soot quantities appears less prominent compared to the sensitivity of soot production to model parameters involved in soot subprocesses [89]. As a result, in some cases [36, 233], interactions between turbulence and soot are neglected.

Earlier studies on the LES of turbulent sooting flames have been primarily focused on moment-based soot models. El-Asrag and Menon [235] employed the Linear Eddy Model (LEM) in combination with the moment method for soot prediction with LES. Later, Mueller and Pitsch [66, 236] combined the moment-based soot model with an extended Flamelet/Progress Variable (FPV) [81] model by including lumped-PAH inception kinetics. In this LES approach, the presumed-PDF method was used to account for subgrid-scale interactions between turbulence and soot. Xuan and Blanquart [84] proposed an alternative approach to the lumped-PAH inception kinetics, where the filtered transport equations for aromatic species were solved with closure based on a PAH relaxation model. This aromatic chemistry-turbulence interaction was found to be important in accurately reproducing soot yield in turbulent flames. To obtain the information on particle size distribution in LES, the FPV presumed-PDF model of Mueller and Pitsch [236] was extended to a sectional method by Rodrigues et al. [73]. The qualitative trends in soot formation were reproduced in their work while providing detailed information on the evolution of local soot PSD. The decoupling of soot and gas-phase species in the LES presumed-PDF approach leads to narrow profiles of the mean soot volume fraction. Hence, transported joint PDF (JPDF) method, which allows for a more accurate representation of the turbulence-chemistry interactions by directly coupling the full scalar space, is applied to the sectional model by Tian et al. [232]. Encouraging agreement was obtained with experimental measurements for soot quantities in turbulent non-premixed flames.

Besides flamelet-based methods, several other combustion models have been investigated in the LES framework to model soot formation in turbulent flames. The Conditional Moment Closure (CMC) approach was applied to a sectional soot model by Gkantonas et al. [85] to study soot formation and predict their size distribution in a lab-scale swirl Rich-Quench-Lean (RQL) combustor. In LES of lifted non-premixed turbulent flames with the sectional method, Grader et al. [237] used a finite-rate chemistry model, that requires no assumptions concerning the combustion regime. A good prediction of soot evolution was achieved in their study enabling detailed inves-

tigations of soot formation and oxidation processes. Sewerin and Rigopoulos [238] adapted the stochastic fields method to the LES of sooting flames, which recently extended to the sectional method by Sun and Rigopoulos [226] to predict the soot particle size distribution in turbulent non-premixed flames. Concerning sectional method-based approaches, simplifying the gas-phase kinetics by the use of various combustion models in the LES can reduce CPU time, but the calculation of the soot source term remains computationally expensive. Recent research has explored different approaches to improve computational efficiency, including a three-equation model of Franzelli et al. [201] based on mono-disperse closure of source terms. Machine learning models and virtual chemistry have also been proposed [88] for predicting soot formation, but they do not provide information on size distributions. While efficient tabulated soot chemistry has been investigated with semi-empirical soot models [215], detailed soot models [213] in laminar flames, accurately modeling soot formation rates in turbulent conditions remains a challenge due to the nonlinear interaction between gas-phase thermochemistry, soot particle dynamics, and turbulence. Overall, developing detailed, and at the same time computationally efficient methods for predicting soot formation is crucial for their application in industrially relevant conditions.

Given the aforementioned challenges in accurately predicting soot formation in turbulent conditions, in this chapter, the LES approach is combined with a discrete sectional soot model and FGM chemistry for the prediction of soot formation in turbulent flames. The LES formalism is first introduced along with model approximations. An assessment of filtered soot source term treatment is conducted to investigate its impact on the prediction of global soot quantities and the evolution of soot PSDs. The extension of the FGM-DSM approach discussed in earlier chapters to the LES of turbulent jet flames constitutes one of the major objectives of this work. The focus is given to the assessment of this tabulated soot chemistry approach to predict the complex interactions between the gas phase and the soot particles in turbulent conditions. In addition, the computationally efficient clustered-sections method (FGM-CDSM) introduced in the previous chapter is verified in turbulent flame conditions for its accuracy and computational performance. The impact of differential diffusion of PAHs species on soot prediction in turbulent conditions is studied using a simplified approach. As a progressive step to the analysis conducted in Chapter 3 on laminar flames, the present LES study is extended to understand the influence of hydrogen addition to fuel on soot formation in turbulent conditions. Finally, the impact of thermal radiation on the predictive capabilities of the FGM-DSM framework is investigated.

The following section outlines the LES-FGM-DSM formalism for modeling the formation and evolution of soot in turbulent non-premixed combustion.

7.2   LES formalism for turbulent sooting flames

Turbulent flows are characterized by chaotic unsteady motions over a broad range of spatio-temporal scales. In LES, large scales of the turbulent flow are resolved using

filtering operation, which essentially filters out the eddies whose scales are smaller than the filter width, while effects of un-resolved small scales are modeled by employing sub-grid models. Since, with the LES technique, the large scales governing transient features of the flow are captured at reasonably affordable CPU cost, it is an excellent approach for understanding the soot production and its interaction with local turbulence in complex configurations.

In the typical LES formalism, the filter quantity $\overline{f}$ for variable $f(\boldsymbol{x}, t)$ is obtained by the convolution product between the instantaneous variables and the normalized filter G with the characteristic length Δ as:

$$\overline{f}(\boldsymbol{x}, t) = \int f(\boldsymbol{x}', t) G(\boldsymbol{x} - \boldsymbol{x}') d\boldsymbol{x}' \tag{7.1}$$

Since combustion processes are characterized by density variations, the Favre-filtered or density-weighted description of variables is often preferred in the context of LES. The Favre-decomposition of a variable $f(\boldsymbol{x}, t)$ into its mean $\widetilde{f}$ (resolved) and fluctuating f'' (unresolved) component is described as:

$$f = \widetilde{f} + f'' \quad \text{with} \quad \widetilde{f''} = 0 \tag{7.2}$$

where Favre-filtering operation $\widetilde{(\cdot)}$ on f is defined as:

$$\widetilde{f} = \frac{\overline{\rho f}}{\overline{\rho}} \tag{7.3}$$

In LES, the filtered formalism of conservation equations is used for computations of turbulent reacting flows with several approximations. The following section outlines the retained LES formalism for modeling soot formation in turbulent combustion.

7.2.1 Filtered conservation equations

Under low-Mach number approximation, and by neglecting external forces, Favre-filtered conservation equations for mass, momentum, and total enthalpy are obtained as follows [90]:

$$\frac{\partial \overline{\rho}}{\partial t} + \nabla \cdot (\overline{\rho} \widetilde{\boldsymbol{u}}) = 0 \tag{7.4}$$

$$\frac{\partial (\overline{\rho} \widetilde{\boldsymbol{u}})}{\partial t} + \nabla \cdot (\overline{\rho} \widetilde{\boldsymbol{u}} \widetilde{\boldsymbol{u}}) = -\nabla \overline{p} + \nabla \cdot [\overline{\boldsymbol{\tau}} - \overline{\rho} (\widetilde{\boldsymbol{u}\boldsymbol{u}} - \widetilde{\boldsymbol{u}} \widetilde{\boldsymbol{u}})] \tag{7.5}$$

$$\frac{\partial \left(\overline{\rho} \widetilde{h} \right)}{\partial t} + \nabla \cdot \left(\overline{\rho} \widetilde{\boldsymbol{u}} \widetilde{h} \right) = \frac{\overline{Dp}}{Dt} - \nabla \cdot \left[\overline{\boldsymbol{q}} + \overline{\rho} \left(\widetilde{\boldsymbol{u}h} - \widetilde{\boldsymbol{u}} \widetilde{h} \right) \right] + \nabla \cdot (\overline{\boldsymbol{\tau}\boldsymbol{u}}) + \overline{\dot{\mathcal{Q}}} \tag{7.6}$$

In the conservation equations, the overline operator denotes the Reynolds-filtering, and the tilde represents the Favre-filtering operations. Under low Mach number ap-

proximation, the material derivative of pressure is generally neglected ($\overline{Dp/Dt} = 0$). Furthermore, the viscous heating effects (term $\nabla \cdot (\overline{\boldsymbol{\tau u}})$) are considered to be relatively small and neglected in the enthalpy equation.

Unclosed expressions occur as a result of filtering operation which requires modeling. In the momentum equation, the filtered laminar viscous stress tensor $\overline{\boldsymbol{\tau}}$ is modeled using Stoke's assumption as:

$$\overline{\boldsymbol{\tau}} \approx \widetilde{\mu} \left[\nabla \widetilde{\boldsymbol{u}} + (\nabla \widetilde{\boldsymbol{u}})^T - \frac{2}{3} (\nabla \cdot \widetilde{\boldsymbol{u}}) \boldsymbol{I} \right] \tag{7.7}$$

while the subgrid-scale (SGS) stresses in the momentum equation are closed using the turbulent viscosity approximation of Boussinesq [90].

$$\bar{\rho}(\widetilde{\boldsymbol{uu}} - \widetilde{\boldsymbol{u}}\widetilde{\boldsymbol{u}}) \approx -\mu_t \left[\nabla \widetilde{\boldsymbol{u}} + (\nabla \widetilde{\boldsymbol{u}})^T - \frac{2}{3} (\nabla \cdot \widetilde{\boldsymbol{u}}) \boldsymbol{I} \right]. \tag{7.8}$$

The Vreman model [239] with modeling constant $c_k = 0.1$ is adopted for the SGS turbulent viscosity μ_t. The filtered heat flux $\overline{\boldsymbol{q}}$ is modeled as:

$$\overline{\boldsymbol{q}} \approx -\overline{\frac{\lambda}{c_p}} \nabla \widetilde{h} = -\bar{\rho} \widetilde{D} \nabla \widetilde{h} \tag{7.9}$$

with $\widetilde{D}$ as thermal diffusion coefficient. The SGS enthalpy flux term is closed using the classical gradient diffusion assumption:

$$\bar{\rho} \left(\widetilde{\boldsymbol{u}h} - \widetilde{\boldsymbol{u}}\widetilde{h} \right) \approx -\frac{\mu_t}{Pr_t} \nabla \widetilde{h} \tag{7.10}$$

where Pr_t is the turbulent Prandtl number. Guided by the previous studies using the same numerical methods [220, 221], the turbulent Prandtl number Pr_t set constant with a value of 0.7.

7.2.2   Combustion modeling

Reliable prediction of soot formation in the combustion process relies on an accurate description of fuel oxidation, and soot precursor species (such as acetylene and PAHs). Given the tractability of combustion models in terms of CPU cost and complexity of the closure, the combustion process is assumed to occur in the flamelet regime in this study. Therefore, turbulent combustion is modeled with the Flamelet Generated Manifold (FGM) [80, 184] approach. In FGM, the thermochemical state of the flame can be described from a pre-computed flamelet database parameterized by a reduced set of control variables. In the context of non-premixed combustion, mixture fraction Z and progress variable $\mathcal{Y}$ are selected as the control variables representing mixing and combustion progress, respectively. To describe the combustion process during LES calculations, transport equations are solved for the filtered mixture fraction $\widetilde{Z}$

and filtered progress variable $\widetilde{\mathcal{Y}}$ in the form:

$$\frac{\partial \left(\bar{\rho}\widetilde{Z} \right)}{\partial t} + \nabla \cdot \left(\bar{\rho}\widetilde{\boldsymbol{u}}\widetilde{Z} \right) = \nabla \cdot \left(\overline{\rho D \nabla Z} \right) - \nabla \cdot \bar{\rho} \left(\widetilde{\boldsymbol{u}Z} - \widetilde{\boldsymbol{u}}\widetilde{Z} \right) \tag{7.11}$$

$$\frac{\partial \left(\bar{\rho}\widetilde{\mathcal{Y}} \right)}{\partial t} + \nabla \cdot \left(\bar{\rho}\widetilde{\boldsymbol{u}}\widetilde{\mathcal{Y}} \right) = \nabla \cdot \left(\overline{\rho D \nabla \mathcal{Y}} \right) - \nabla \cdot \bar{\rho} \left(\widetilde{\boldsymbol{u}\mathcal{Y}} - \widetilde{\boldsymbol{u}}\widetilde{\mathcal{Y}} \right) + \bar{\bar{\omega}}_{\mathcal{Y}} \tag{7.12}$$

The unclosed laminar diffusive fluxes are modeled by the gradient diffusion assumption as:

$$\overline{\rho D \nabla Z} \approx \bar{\rho}\widetilde{D}\nabla\widetilde{Z} \qquad \text{and} \qquad \overline{\rho D \nabla \mathcal{Y}} \approx \bar{\rho}\widetilde{D}\nabla\widetilde{\mathcal{Y}} \tag{7.13}$$

where $\widetilde{D}$ denotes the diffusion coefficient, which is evaluated under the assumption of a unity Lewis number and included as a lookup quantity in the manifold. Similarly, the unresolved turbulent flux terms appearing in control variable transport equations after the LES filtering are closed using a gradient diffusion approach as:

$$\bar{\rho} \left(\widetilde{\boldsymbol{u}Z} - \widetilde{\boldsymbol{u}}\widetilde{Z} \right) \approx -\frac{\mu_t}{Sc_t}\nabla\widetilde{Z} \tag{7.14}$$

and

$$\bar{\rho} \left(\widetilde{\boldsymbol{u}\mathcal{Y}} - \widetilde{\boldsymbol{u}}\widetilde{\mathcal{Y}} \right) \approx -\frac{\mu_t}{Sc_t}\nabla\widetilde{\mathcal{Y}} \tag{7.15}$$

where Sc_t is the turbulent Schmidt number, fixed at 0.7 following previous studies [220]. The term $\bar{\bar{\omega}}_{\mathcal{Y}}$ in Eq. 7.12 refers to the filtered progress variable source term.

For convenient tabulation and retrieval from the manifold, a scaled progress variable $\mathcal{C}$ is defined as:

$$\mathcal{C} = \frac{\mathcal{Y} - \mathcal{Y}_{\min}(Z)}{\mathcal{Y}_{\max}(Z) - \mathcal{Y}_{\min}(Z)} \tag{7.16}$$

where $\mathcal{Y}_{\max}$ and $\mathcal{Y}_{\min}$ are, respectively the values of $\mathcal{Y}$ in the lowest strain rate flamelet and unburnt (mixing) state. The closure for tabulated filtered variables (species mass fractions) and chemical source terms (e.g. $\bar{\bar{\omega}}_{\mathcal{Y}}$) is discussed in the following section.

7.2.3 Turbulence-chemistry interactions

In turbulent conditions, the scalar variables are exposed to spatio-temporal fluctuations that can not be resolved with the LES filter length, given in this case by the mesh size. Therefore, the flamelet database incorporating laminar flamelet solutions must be extended to account for the effect of turbulence on subgrid levels. Different methods for the modeling of these turbulence-chemistry interactions exist in the liter-

ature. In this study, the stochastic approach based on the presumed-shape Probability Density Function (PDF) is employed to account for subgrid-scale turbulence-chemistry interactions in LES. In the present LES, only the fluctuations in Z and $\mathcal{C}$ are considered while describing the statistical impact of turbulence on the flame. Therefore, a filtered thermochemical variable $\widetilde{\psi}$, convoluted over the joint PDF of Z and $\mathcal{C}$, can be expressed as:

$$\widetilde{\psi} = \int \int \psi(Z,\mathcal{C}) P(Z,\mathcal{C}) dZ d\mathcal{C} \tag{7.17}$$

Commonly, statistical independence between Z and $\mathcal{C}$ is assumed. Thus, the joint PDF $P(Z,\mathcal{C})$ can be modeled using individual presumed distributions of Z and $\mathcal{C}$. Accordingly, a Favre-filtered variable $\widetilde{\psi}$ and Reynolds-Averaged variable $\overline{\psi}$ are obtained from integration with marginal PDFs of Z, and $\mathcal{C}$ as:

$$\widetilde{\psi} = \int \int \psi(Z,\mathcal{C}) P(Z) P(\mathcal{C}) dZ d\mathcal{C} \tag{7.18}$$

$$\overline{\psi} = \left[\left(\widetilde{\frac{1}{\rho}} \right) \right]^{-1} \int \int \left(\frac{\psi(Z,\mathcal{C})}{\rho(Z,\mathcal{C})} \right) P(Z) P(\mathcal{C}) dZ d\mathcal{C} \tag{7.19}$$

where ψ refers to any quantity defined in the flamelet solutions. A presumed β-function PDF is used to characterize the distribution of mixture fraction and progress variable. For a general control variable ϕ ($\in [0,1]$), a β-PDF function is defined as:

$$P(\phi) = \frac{\Gamma(a+b)}{\Gamma(a)\Gamma(b)} \, \phi^{a-1} (1-\phi)^{b-1} \tag{7.20}$$

where a and b parameters are calculated as:

$$a = \widetilde{\phi} \left(\frac{\widetilde{\phi}(1-\widetilde{\phi})}{\widetilde{\phi''^2}} - 1 \right) \tag{7.21}$$

$$b = \left(\frac{1-\widetilde{\phi}}{\widetilde{\phi}} \right) a \tag{7.22}$$

with the constraint of a, $b > 0$. In Eq. 7.21, $\widetilde{\phi''^2}$ represents the variance of control variable ϕ.

For the application in LES, the thermochemical parameters of the mixture are mapped on four non-dimensional coordinates in the FGM database Ψ as:

$$\widetilde{\psi} = \Psi \left(\widetilde{Z}, \mathcal{S}_Z, \widetilde{\mathcal{C}}, \mathcal{S}_\mathcal{C} \right) \tag{7.23}$$

where $\mathcal{S}_\phi$, called the segregation factor, represents the normalized variance of quantity ϕ, required in the β-PDF model. For $\mathcal{S}_\phi = 0$ the variance $\widetilde{\phi''^2}$ is zero, which leads to

$\widetilde{\psi}(\widetilde{\phi}) = \psi(\phi)$. The segregation factors for variables Z and $\mathcal{C}$, are given as:

$$S_Z = \frac{\widetilde{Z''^2}}{\widetilde{Z}\left(1 - \widetilde{Z}\right)} \quad \text{and} \quad S_{\mathcal{C}} = \frac{\widetilde{\mathcal{C}''^2}}{\widetilde{\mathcal{C}}\left(1 - \widetilde{\mathcal{C}}\right)} \tag{7.24}$$

The variance of scaled progress variable $\widetilde{\mathcal{C}''^2}$ is related to its unscaled variance $\widetilde{\mathcal{Y}''^2}$ through [240]:

$$\widetilde{\mathcal{C}''^2} = \frac{\widetilde{\mathcal{Y}''^2} + (\widetilde{\mathcal{Y}})^2 - \widetilde{(\mathcal{Y}_{\min})^2} - 2\widetilde{\mathcal{C}}\left[\widetilde{(\mathcal{Y}_{\min}\mathcal{Y}_{\max})} - \widetilde{(\mathcal{Y}_{\min})^2}\right]}{\widetilde{(\mathcal{Y}_{\max} - \mathcal{Y}_{\min})^2}} - \widetilde{\mathcal{C}}^2 \tag{7.25}$$

In this work, transport equations are solved for the closure of subgrid-scale variances of mixture fraction and progress variable. The transport equations for $\widetilde{Z''^2}$ and $\widetilde{\mathcal{Y}''^2}$ are given by [220, 241]:

$$\frac{\partial\left(\bar{\rho}\widetilde{Z''^2}\right)}{\partial t} + \nabla \cdot \left(\bar{\rho}\widetilde{u}\widetilde{Z''^2}\right) - \nabla \cdot \left[\left(\bar{\rho}\widetilde{D} + \frac{\mu_t}{Sc_t}\right)\nabla\widetilde{Z''^2}\right] = 2\frac{\mu_t}{Sc_t}\left|\nabla\widetilde{Z}\right|^2 - \bar{\rho}\widetilde{\chi_Z} \tag{7.26}$$

$$\frac{\partial\left(\bar{\rho}\widetilde{\mathcal{Y}''^2}\right)}{\partial t} + \nabla \cdot \left(\bar{\rho}\widetilde{u}\widetilde{\mathcal{Y}''^2}\right) - \nabla \cdot \left[\left(\bar{\rho}\widetilde{D} + \frac{\mu_t}{Sc_t}\right)\nabla\widetilde{\mathcal{Y}''^2}\right] = 2\frac{\mu_t}{Sc_t}\left|\nabla\widetilde{\mathcal{Y}}\right|^2 - \bar{\rho}\widetilde{\chi_{\mathcal{Y}}}$$
$$+ 2\left(\widetilde{\mathcal{Y}\dot{\omega}_{\mathcal{Y}}} - \widetilde{\mathcal{Y}}\bar{\dot{\omega}}_{\mathcal{Y}}\right) \tag{7.27}$$

where χ_Z and $\chi_{\mathcal{Y}}$ respectively denote the subgrid turbulent scalar dissipation rates for mixture fraction and progress variable, modeled as:

$$\widetilde{\chi_Z} = \left(\frac{\varepsilon}{k}\right)\widetilde{Z''^2} \quad \text{and} \quad \widetilde{\chi_{\mathcal{Y}}} = \left(\frac{\varepsilon}{k}\right)\widetilde{\mathcal{Y}''^2} \tag{7.28}$$

where k is the unresolved turbulent kinetic energy and ε is its dissipation rate. To close $\widetilde{\chi_Z}$ and $\widetilde{\chi_{\mathcal{Y}}}$, the ratio of ε and k is defined following the expression of Both et al. [241]

$$\frac{\varepsilon}{k} = \left(\frac{C_\varepsilon^2 \mu_t |\boldsymbol{S}|^2}{\bar{\rho}\Delta^2}\right)^{1/3} \quad \text{with} \quad \boldsymbol{S} = \frac{1}{2}\left[\nabla\widetilde{u} + (\nabla\widetilde{u})^T\right] \tag{7.29}$$

where $\boldsymbol{S}$ is the stress tensor, model parameter $C_\varepsilon = 1.8$, and Δ is the LES filter size (taken as the cube root of the volume of the grid element).

7.2.4 Filtered sectional soot equations

For modeling soot formation and evolution in LES, the filtered equations for sectional soot mass fractions are obtained as:

$$\frac{\partial\left(\bar{\rho}\widetilde{Y}_{s,i}\right)}{\partial t} + \nabla \cdot \left(\bar{\rho}\left[\widetilde{\boldsymbol{u}} + \widetilde{\boldsymbol{V_T}}\right]\widetilde{Y}_{s,i}\right) = \nabla \cdot \left(\overline{\rho D_{s,i}\nabla Y_{s,i}}\right) - \nabla \cdot \bar{\rho}\left(\widetilde{\boldsymbol{u}Y_{s,i}} - \widetilde{\boldsymbol{u}}\widetilde{Y}_{s,i}\right) + \bar{\dot{\omega}}_{s,i}$$

$$\forall\, i\, \in [1, N_{sec}] \tag{7.30}$$

The thermophoretic velocity $\widetilde{\boldsymbol{V_T}}$ is modeled following [99], as:

$$\widetilde{\boldsymbol{V_T}} = C_{th}\bar{\nu}\frac{\nabla\widetilde{T}}{\widetilde{T}} \qquad \text{with} \qquad C_{th} = -0.554 \tag{7.31}$$

The unclosed laminar diffusive fluxes are modeled by the gradient diffusion assumption as:

$$\overline{\rho D_{s,i}\nabla Y_{s,i}} \approx \bar{\rho}\widetilde{D}_{s,i}\nabla\widetilde{Y}_{s,i} \tag{7.32}$$

The SGS soot flux is modeled using a classical gradient diffusion assumption:

$$\bar{\rho}\left(\widetilde{\boldsymbol{u}Y_{s,i}} - \widetilde{\boldsymbol{u}}\widetilde{Y}_{s,i}\right) \approx -\frac{\mu_t}{Sc_t}\nabla\widetilde{Y}_{s,i} \tag{7.33}$$

The closure of filtered source term $\bar{\dot{\omega}}_{s,i}$ for soot sections is presented in the following.

7.2.5 Closure of soot source terms

The soot source term $\dot{\omega}_{s,i}$ includes the contribution of the main sub-processes of soot formation and evolution. Therefore $\dot{\omega}_{s,i}(\phi_g, \phi_s)$ involves the non-linear correlations between the gas-phase thermo-chemical variables (ϕ_g) as well as soot variables (ϕ_s). Typically, variables $\phi_g = \{Y_k(Z, \mathcal{C}), T, \rho\}$ and $\phi_s = \{Y_{s,i}\}$. The filtered source term $\bar{\dot{\omega}}_{s,i}$ poses closure problems requiring models to account for subgrid-scale soot-chemistry-turbulence interactions. There have been notable attempts [73, 226] to accomplish subgrid closure for filtered soot source terms in the context of sectional method-based models. However, there is no consensus about the most accurate approach and, therefore, this is an open area of research. In several numerical works, e.g. [36, 233], the correlations involving the unresolved fluctuations of soot variables are neglected. In this study, two different strategies are considered to treat the filtered soot source terms and subsequently, their influence on the soot prediction in turbulent flames is assessed.

Run-time calculation without subgrid-scale model

In the first approach, the sectional soot source term is computed during the simulation run by using tabulated filtered thermochemical parameters and gas-phase species mass fractions relevant to the soot model. Therefore, the subgrid-scale interaction between soot and turbulence is neglected in this formulation. The filtered source term with this model can be written as:

$$\overline{\dot{\omega}}_{s,i} = \dot{\omega}_{s,i}\left(\widetilde{\phi}_g, \widetilde{\phi}_s\right) \tag{7.34}$$

Moreover, because the gas-phase consumption of precursor species due to soot formation is accounted for during the flamelet generation step, no additional transport equation is solved for the description of gas-phase species in the LES. For brevity, this approach, in which the soot source terms are *computed* on-the-fly is referred to as FGM-C here. Additionally, an alternative variant of the FGM-C approach with a slightly different formulation for filtered soot source term is evaluated. This variant involves tabulating the gas-phase rate of the filtered chemical soot source term instead of calculating it from local gas-phase species concentrations. A comprehensive analysis of this approach is provided in Section 7.3.3.

Tabulation with presumed PDF model

The second model concerns the closure of the filtered soot source term through the presumed PDF approach. In a general form, the filtered soot source term convoluted with presumed PDF is written as:

$$\overline{\bar{\dot{\omega}}}_{s,i} = \bar{\rho} \int \int \frac{1}{\rho} \dot{\omega}_{s,i}(\phi_g, \phi_s) P(\phi_g, \phi_s) d\phi_g d\phi_s \tag{7.35}$$

where ϕ_g and ϕ_s are gaseous and soot scalars, respectively. Using Bayes' theorem, the joint PDF can be split into two marginal PDFs for the thermochemical variable and for the soot variable such that $P(\phi_g, \phi_s) = P(\phi_g)P(\phi_s|\phi_g)$. In this model, the soot source terms are parameterized through control variables and tabulated in the manifold ($\phi_g = \{Z, \mathcal{C}\}$). The marginal PDF $P(\phi_g)$ is assumed to have β-PDF function for Z and $\mathcal{C}$, while the conditional PDF of soot variable $P(\phi_s|\phi_g)$ is treated as a delta (δ) function. Under this approximation, turbulence-soot interaction is partially accounted for by including the effect of subgrid-scale fluctuations in mixture-fraction and progress variables on filtered soot source terms. Besides, the assumption of δ-PDF function (neglecting subgrid-scale fluctuations) for $P(\phi_g)$ is also evaluated to understand the impact of PDF integration on the performance of the tabulated soot chemistry, which will be explained later.

The approach employed for the tabulated soot chemistry in Chapter 6, is extended for turbulent flame simulations. Accordingly, the soot source term for the soot section is split into production ($\dot{\omega}_{s,i}^{+}$ or $\dot{\omega}_{s,i}^{\mathrm{prod}}$) and consumption parts ($\dot{\omega}_{s,i}^{-}$ or $\dot{\omega}_{s,i}^{\mathrm{cons}}$). The con-

sumption part is linearized by soot mass fraction to avoid the un-physical consumption of soot when $\widetilde{Y}_{s,i} = 0$. The filtered soot source term is modeled as:

$$\bar{\dot{\omega}}_{s,i} = \bar{\dot{\omega}}^+_{s,i} + \bar{\dot{\omega}}^-_{s,i} \approx \left[\bar{\dot{\omega}}^+_{s,i}\right]^{\text{tab}} + \widetilde{Y}_{s,i} \left[\overline{\frac{\dot{\omega}^-_{s,i}}{Y_{s,i}}}\right]^{\text{tab}} \tag{7.36}$$

where the production and linearized consumption terms are parameterized through gas-phase thermochemical variables and tabulated (denoted by the superscript tab) in the manifold. This approach does not consider the separation of gas and soot parts for the soot production term. However, with the linearization of consumption terms, the partial separation of gas and soot time scales can be achieved.

In general, soot concentrations are negligible in lean mixture fraction ($\widetilde{Z} < Z_{st}$) regions, as soot particles are oxidized through reactions with OH, whose concentration is high near the stoichiometric mixture fraction. In this model, since soot source terms are obtained from the flamelet solutions, the filtered consumption term $\bar{\dot{\omega}}^-_{s,i} \approx 0$ in lean regions. This can lead to the spurious existence of soot (during transport) in lean mixture factions if soot oxidation is not properly accounted for during the soot chemistry tabulation. To avoid this issue, the soot oxidation contribution, in the
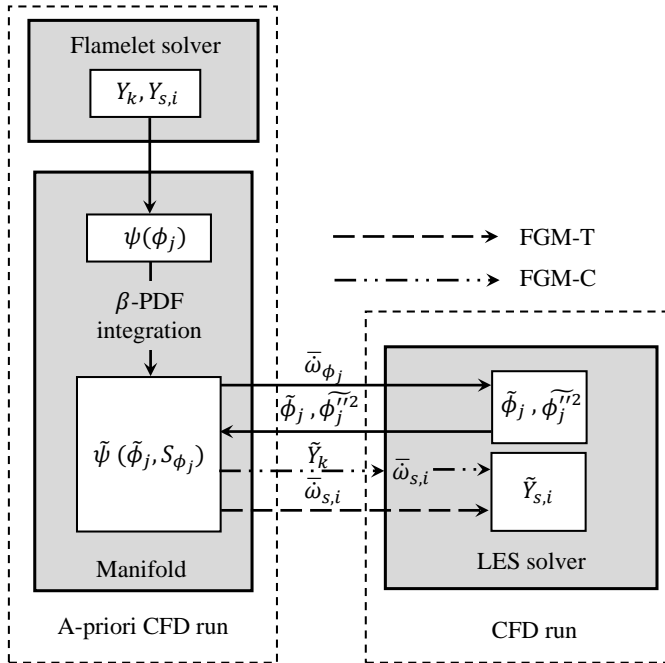

Figure 7.1: An overview of the LES-FGM-DSM implementation. Symbols are explained in the main text.

linearized consumption term in Eq. 7.36 is further approximated as:

$$\overline{\dot{\omega}}_{s,i}^{-} \approx \widetilde{Y}_{s,i} \left[\overline{\left(\frac{\dot{\omega}_{s,i}^{-} - \dot{\omega}_{s,i}^{-;\mathrm{ox}}}{Y_{s,i}} \right) + \left(\frac{d\dot{\omega}_{s,i}^{-;\mathrm{ox}}}{dY_{s,i}} \right)} \right]^{\mathrm{tab}} \tag{7.37}$$

where $\dot{\omega}_{s,i}^{-;\mathrm{ox}}$ denotes the sectional soot consumption rate by oxidation subprocesses. For computational efficiency, the coagulation process of soot particles is not explicitly solved at runtime, but the inter-sectional mass transfer due to the coagulation process (or other subprocesses) is included in the flamelet computation. This approach, in which the soot source term is *tabulated*, is referred to as FGM-T from hereon. The schematic illustration of the LES-FGM-DSM implementation is shown in Fig. 7.1.

7.3 LES of turbulent piloted diffusion flame

7.3.1 Flame configuration and modeling setup

The LES formalism with FGM-DSM is applied to the simulation of soot production in a turbulent piloted jet flame. The piloted jet flame offers an ideal combustion environment to analyze the evolution of soot formation sub-processes, such as nucleation (near to burner) followed by soot growth (within flame mid-height), and soot oxidation (near the flame tip). Hence, the assessment of the LES-FGM-DSM framework described earlier is carried out on the turbulent non-premixed ethylene-air piloted jet flame, experimentally investigated at Sandia National Laboratories [242]. This flame is also one of the target flames from the International Sooting Flame (ISF) workshop [124]. The selected flame presents well-characterized exit conditions for various nozzles. It provides an extensive experimental database of soot measurements, which justifies the appropriateness of this flame for soot model assessment and validation. Unfortunately, measurements for the velocity field and/or mixing are not available for the selected flame, which presents an additional challenge in the validation of the turbulent flow field in simulations. The details of the experimental configuration and simulation setup are presented below:

Experimental configuration

The selected non-premixed jet flame features a burner with a central jet of pure C_2H_4 and low-speed pilot injection of fully reacted C_2H_4-air pre-mixture at an equivalence ratio of 0.9. The pilot tube (with an inner diameter of 15.2 mm, and an outer diameter of 19.1 mm) comprises an insert, which provides 64 small pilot flames for the stabilization of the main flame. The spacing and number of pilot flames have been designed to produce a uniform flow rate of burned products near the burner exit plane. The global mass flow rate of the pilot corresponds to 1.77×10^{-4} kg/s. Fuel (C_2H_4) is injected at 294 K with a bulk velocity of 54.7 m/s, resulting in a Reynolds number

of 20000 (based on the diameter of the main jet $d_j = 3.2$ mm) at the fuel nozzle exit. The pilot is surrounded by a co-flow of air at a bulk velocity of 0.6 m/s. Additional details on the experimental conditions can be found in Ref. [242].

Numerical set-up

Based on the experimental observation of the visible flame height, the computational domain is designed to be 1 m×0.3 m×2π in axial (z), radial (r) and circumferential directions, respectively. The computational domain is discretized via 384×192×64 cells in the axial, radial, and circumferential directions, respectively. A schematic illustration of the computational domain and grid is given in Fig. 7.2. Typically Kolmogorov length scale is related to macro-scale $\mathcal{L}$ (taken as $d_j/2$) and Reynolds number Re as

$$\eta/\mathcal{L} \sim \mathrm{Re}^{-3/4} \tag{7.38}$$

For the present flame, the Kolmogorov scales are in the order of 1×10^{-3} mm in the near jet region. Furthermore, it is important to have the reaction zone resolved in LES. For the preliminary assessment, the grid is selected such that the typical cell size near the fuel exit is ≈ 0.1 mm. This essentially yields a resolution of approximately 100 times the Kolmogorov length. The grid is stretched in the axial and radial directions while the circumferential direction is uniformly spaced. In the radial direction, the grid is non-uniformly concentrated in the shear layers between the different injection streams. The structured grid is made of approximately 5 million hexahedral elements. The mesh has been also verified for Pope's criteria [243] in Fig. 7.3. More than 90% of the grid cells show a ratio of resolved to total kinetic energy ($\mathcal{M}$) larger than 0.8, indicating the kinetic energy is sufficiently resolved with the selected mesh.
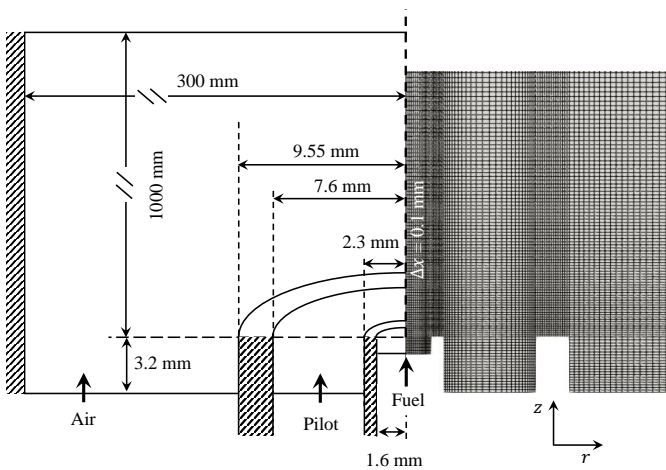

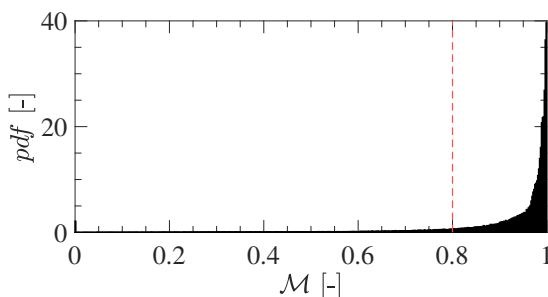Figure 7.2: Illustration of the computational domain and grid.

Figure 7.3: Probability density function of the $\mathcal{M}$ parameter in Pope's criteria for the LES grid.

The mean axial velocity at the fuel inflow is set to the power-law profile with an exponent of 1/7. The turbulent inlet with a turbulence intensity (I_t) of 5% extracted from a separate fully-developed periodic pipe flow simulation is imposed for the fuel jet boundary. The theoretical turbulent intensity for fully developed turbulent pipe flow is related to the Reynolds number [244]:

$$I_t^{\text{th}} = 0.16 \, \text{Re}^{-1/8} \tag{7.39}$$

For the current case, I_t^{th} is approximately 4.6%, close to the value selected for the LES. The velocity inlet profiles for the pilot and coflow air streams are treated as uniform. The velocity of the air stream is specified as 0.6 m/s while the bulk velocity of the pilot is adjusted to impose the mass flow rate satisfying the experimental condition. No-slip adiabatic wall conditions are imposed at the injector boundaries. The pilot inlet is assumed to have a composition close to the equilibrium state of an ethylene-air mixture at an equivalence ratio of 0.9 ($\widetilde{Z} = 0.0577$, $\widetilde{C} = 1.0$) and temperature of 2256 K. The fuel and coflow inlet temperatures are maintained at 294 K.

For the creation of the FGM database, a series of 1-D non-premixed counterflow flamelets are calculated with detailed chemistry including soot kinetics. The detailed kinetic scheme KM2 [105] is retained for the gas-phase chemistry during the computation of flamelets. In the LES simulations, 30 soot sections are transported to describe particle size distribution, hence the flamelets including soot kinetics are also computed with 30 sections. This value is selected considering the compromise between accuracy and limited CPU over-cost of LES simulations. To cover the composition space from chemical equilibrium to frozen mixing in the flamelet database, first, a series of strained steady counterflow flamelets are computed by varying the applied stain rate from very low values (close to chemical equilibrium) until the extinction limit. Subsequently, the composition space between the extinction limit and the mixing solution is covered by simulating unsteady quenching flamelets at the extinguishing strain rate. Considering the large Reynolds number of the turbulent jet, turbulent diffusivities are expected to be higher compared to molecular diffusivities. Hence a unity-Lewis diffusion model is considered for the species transport in the

flamelet computation. The progress variable is defined based on H_2O, CO_2, CO, O_2, H_2, and A4 species mass fractions (same as the one introduced in Chapter 6) for the mapping of thermochemical variables. The thermochemical variables are stored in the FGM database with a non-uniform (refined near stoichiometric and equilibrium regions) resolution of $101 \times 11 \times 101 \times 11$ grid points in $\widetilde{Z}$, $\mathcal{S}_Z$, $\widetilde{\mathcal{C}}$, and $\mathcal{S}_\mathcal{C}$ space respectively. In the assessment of the filtered source term treatment in FGM-DSM coupling, the thermal radiation effects from gas and soot are neglected for simplicity.

The simulations are carried out in a Cartesian coordinate system using the multiphysics code Alya [219], developed at the Barcelona Supercomputing Center (BSC). In the Alya code, a second-order conservative finite element scheme is used for spatial discretization, while an explicit third-order Runge-Kutta scheme is employed for the time integration. A low-dissipation scheme based on the fractional step algorithm proposed by Both et al. [221] is used for continuity and momentum equations under a low-Mach number approximation of reacting flows. The simulations are performed using the Hawk cluster equipped with AMD EPYC 7742 processors at the High-Performance Computing Center Stuttgart. The temporal statistics for the quantities are performed for a period of approximately 250 ms after the simulations have reached a statistically steady state.
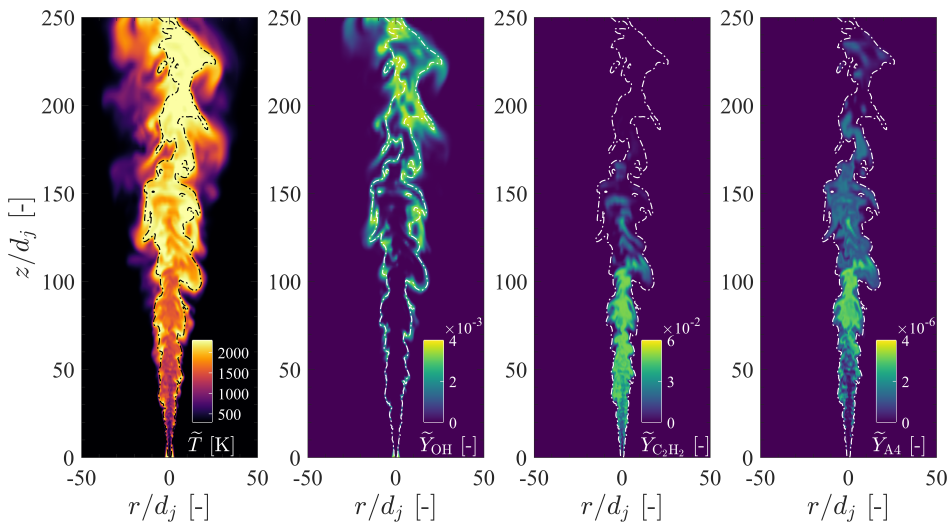
7.3.2 Modeling results

Figure 7.4: Instantaneous 2-D fields of temperature, OH mass fraction, C_2H_2 mass fraction, A4 mass fraction. The stoichiometric mixture fraction is shown with dashed iso-lines. The instantaneous results correspond to the FGM-C case.

Gas-phase characteristics

To describe the main combustion features of the piloted turbulent jet flame, the instantaneous fields of temperature, and key species involved in soot chemistry are presented in Fig. 7.4. An iso-contour of stoichiometric mixture fraction ($\widetilde{Z} = Z_{st}$) characterizing the flame front is also shown. The flame is found to be stabilized by the pilot and attached to the burner. Under turbulent conditions, the flame reaction zones (indicated by OH contours) show local extinction events within the shear layers. The formation of PAH (A4) and C_2H_2 is predominant in the fuel-rich region. However, a systematic lag can be noticed in the spatial locations of A4 formation compared to C_2H_2 as the relatively large time scales governing A4 formation reflect in its downstream spatial evolution. The production of A4 is observed to initiate mainly after $z/d_j \simeq 50$, while C_2H_2, a precursor species responsible for surface growth is found to occur closer to the burner exit ($z/d_j \simeq 20$). Furthermore, the regions of higher OH concentration, in which soot oxidation is dominant, are shown to be prominent in the region beyond $z/d_j \simeq 170$.
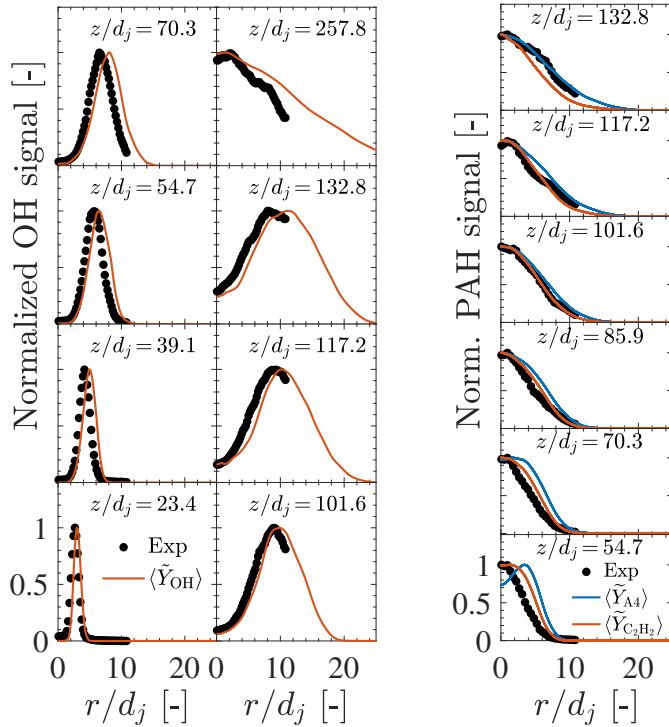

Figure 7.5: Comparison of radial profiles for computed mean mass fractions (normalized with maximum) against measured signals for OH (left panel), PAH (right panel) at different axial locations. The gas-phase results correspond to the FGM-T case.

Gas-phase validation

For the preliminary validation of gas-phase, computed time-averaged radial profiles of mean OH mass fractions at different downstream heights are shown in Fig. 7.5 along with the experimentally measured OH signal. In addition, a comparison of the PAH signal against computed profiles of mean C_2H_2 and A4 mass fractions at several axial locations is presented in Fig. 7.5. Overall, the computed profiles show fair qualitative agreement with the experiments in terms of downstream evolution, suggesting that the turbulent combustion models applied can favorably capture the main features of the flame structure in the gas phase. A slight overprediction of the jet spreading rate is observed in the radial direction at downstream positions leading to a wider spread in the species profile. This however is found to have a minor effect on the quantitative prediction of soot formation.

7.3.3 Characterization of soot formation

Instantaneous fields

To investigate the effects of tabulating the source terms and include the PDF integration on the evolution and distribution of soot, the instantaneous fields of soot volume fraction and soot formation rates (split into production $\overline{\omega}_s^{\mathrm{prod}}$ and consumption $\overline{\omega}_s^{\mathrm{cons}}$ parts) obtained with FGM-C and FGM-T approaches are compared in Fig. 7.6. From the soot volume fraction fields, it is evident that soot is mainly formed in the fuel-rich zones beyond $z/d_j > 50$, characterized by high A4 mass fractions (see Fig. 7.4). Soot inception is predominant near the flame base, leading to the formation of small-sized particles and, consequently, low values of soot volume fraction. From Fig. 7.6, it can be observed that the soot production rate (dominated by surface growth primarily) is concentrated in the middle of the flame. Therefore, a high amount of soot volume fraction is noticed in the middle region of the flame, where incepted particles grow. On the other hand, consumption rates (oxidation) are prominent at the tip region of the flame, and near the stoichiometric iso-contour where particles are oxidized due to a high concentration of OH. Similar trends are noticed in the previous numerical studies [73, 175]. In presence of turbulent fluctuations, the soot formation is highly intermittent, forming sporadic pockets that detach from the fuel-rich zone and are convected downstream where soot oxidation takes place.

The FGM-T method results in a higher soot volume fraction in the middle region of the flame compared to FGM-C. Additionally, the FGM-T model predicted soot formation further upstream than the FGM-C model. This is because the soot production rate in FGM-T is higher near the flame base ($z/d_j \simeq 50$) and in the middle region ($z/d_j \simeq 100$) than compared to FGM-C, causing higher soot concentration. For a more quantitative illustration of soot formation characteristics between FGM-C and FGM-T methods, the scatter plots of the soot volume fraction and soot formation rates fields are compared in Fig. 7.7 (for the results from Fig. 7.6). The scatter plots are colored with the temper-
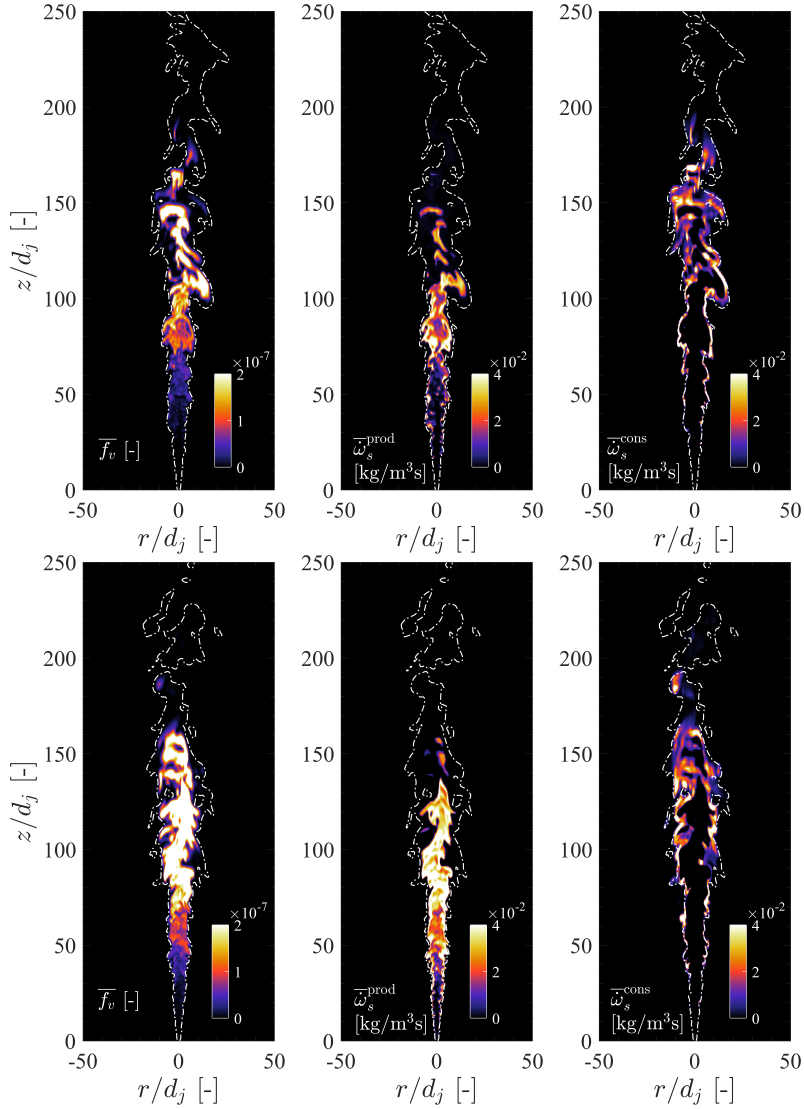
Figure 7.6: Instantaneous fields of soot volume fraction, soot production rate, and soot consumption rate for the FGM-C (top panel) and FGM-T (bottom panel) method. The dashed iso-lines are Z_{st}.

ature. It is clear that soot formation is predominant in the fuel-rich regions spanning $0.1 \leqslant \widetilde{Z} \leqslant 0.4$. Within this sooting region of composition space, higher values of soot production rates are evident for FGM-T as compared to FGM-C, which explains the higher f_v values predicted by the FGM-T method. Below the stoichiometric mixture fraction (Z_{st}), almost all the soot is consumed for both methods since soot oxidation is predominant in the composition space close to the stoichiometric value. However, the
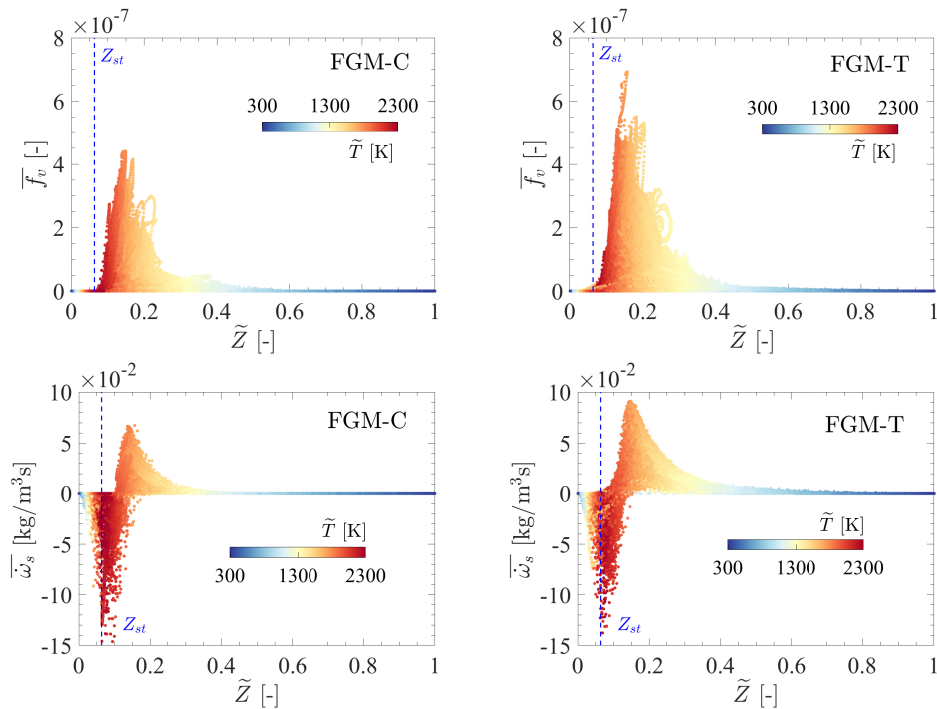
Figure 7.7: Scatter plots of instantaneous soot volume fraction (top panel) and (bottom panel) soot formation rates for FGM-T and FGM-C methods.

distribution of soot consumption rates is found to be qualitatively and quantitatively somewhat similar in both the FGM-C and FGM-T approaches. Therefore, the noticed discrepancies in the quantitative prediction of soot with FGM-C and FGM-T methods are primarily the consequence of differences in the soot production rates.

Soot volume fraction fluctuations

Scatter plots of soot volume fraction (colored by temperature) against mixture fraction at different positions along the axial direction are compared in Fig. 7.8. The scatter represents instantaneous values collected at several time instants. The conditional means of soot volume fraction are included for reference. It can be observed that a large extent of soot is present in fuel-rich mixture fractions while below the stoichiometric values, no soot is observed, as it is rapidly oxidized on the lean side. At lower heights, soot volume fraction samples span a large range of mixture fractions and temperatures. With an increase in axial location, higher values of soot volume fraction are detected, however, the spread in mixture fraction space tends to gradually decrease. The decreasing branch of soot volume fraction in mixture fractions beyond 0.2, vanishes at the downstream position, due to enhanced mixing leading to

lower mixture fraction values. The qualitative trends of soot volume fraction scatter are similar in FGM-C and FGM-T simulations. However, more soot production is evident for FGM-T, especially at higher mixture fractions than their FGM-C counterparts. Far downstream of the flame ($z/d_j \simeq 180$), a lower soot volume fraction is found in FGM-T compared to FGM-C.

The correlation between mixture fraction and soot volume fraction can be further analyzed through conditional probability density functions ($P(\overline{f_v}|\widetilde{Z})$) of soot volume fractions in Fig. 7.9. The PDFs are examined for three fuel-rich intervals. The $P(\overline{f_v}|\widetilde{Z})$ at different axial positions indicate that fluctuations in soot volume fraction are mainly concentrated within rich regions, identified by $2Z_{st} < \widetilde{Z} < 3Z_{st}$. Moreover, a substantial amount of soot also exists in highly rich regions $\widetilde{Z} \geqslant 3Z_{st}$. The mean values of f_v are lower for FGM-C as compared to FGM-T. For mixture fractions below $2Z_{st}$, the peak value of $P(\overline{f_v}|\widetilde{Z})$ approaches zero, confirming a minimal amount of soot in these regions, as soot oxidation is prominent within lean regions. In the FGM-C

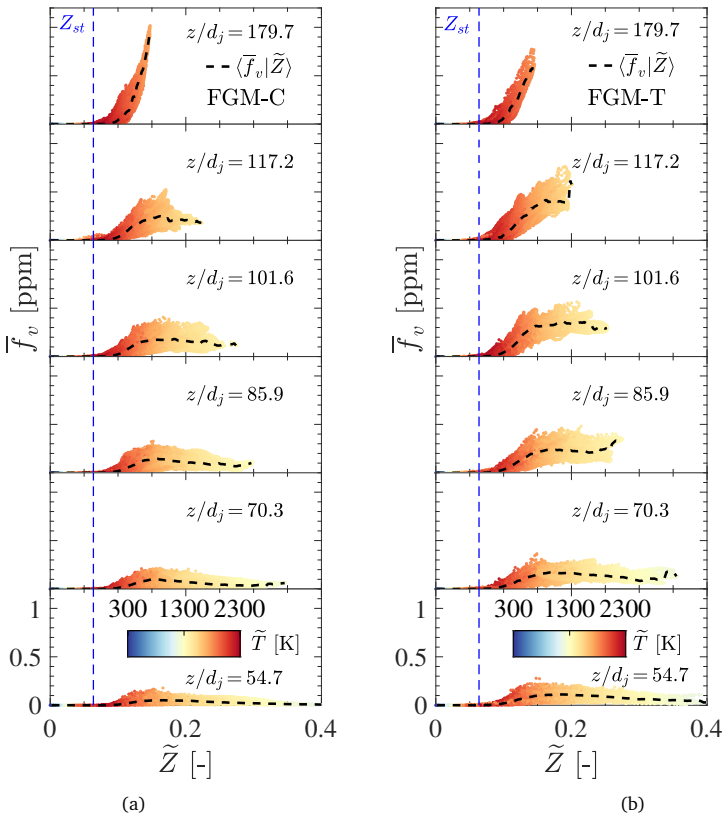Figure 7.8: Comparison of scatter plots of soot volume fraction colored by temperature along with conditional means of $\langle \overline{f}_v|\widetilde{Z}\rangle$ (dashed lines) at different axial locations for FGM-C (a) and FGM-T (b) approaches.
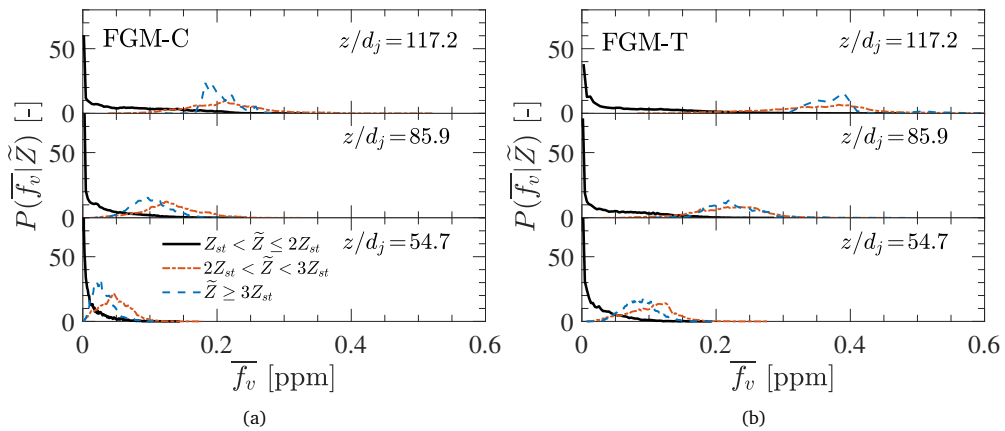
Figure 7.9: Comparison of soot volume fraction PDF conditioned on the mixture fraction at different axial locations along the flame for FGM-C (a), and FGM-T (b).

method, fluctuations in soot volume fraction primarily arise from resolved fluctuations in the flamelet independent variables (Z, $\mathcal{C}$) and turbulent transport of soot. In FGM-T, besides fluctuations in flamelet independent variables, and turbulent transport of soot, fluctuations in the chemical source term of soot sections are taken into account through the presumed-PDF integration during tabulation.

The fluctuations in soot volume fraction are often characterized by soot intermittency (I_s). The soot intermittency is defined experimentally as the probability of observing an instantaneous value of soot volume fraction lower than 0.03 ppm [73]. In Fig. 7.10 the numerical and experimental intermittency profiles are shown for sampled data at several time instants. The intermittency profiles are favorably captured beyond $z/d_j > 120$ confirming the good prediction of soot particle oxidation and turbulent
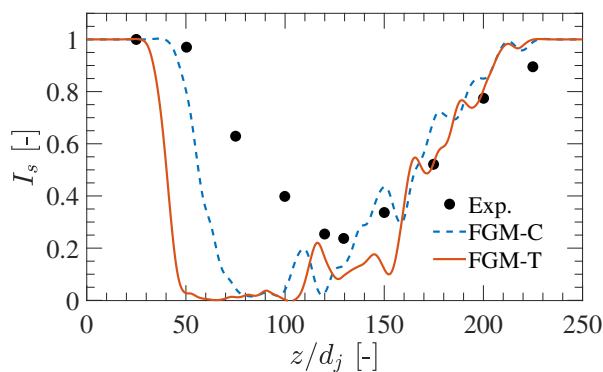
Figure 7.10: Comparison of soot intermittency I_s profiles along the centerline for FGM-C and FGM-T approaches (lines) with measurements (symbols).

fluctuations (resolved). The simulation results tend to underestimate the intermittency close to the burner. The discrepancies in the simulation results compared to the experiment are more pronounced at lower heights for the FGM-T approach where soot volume fraction values are higher as evident in Fig. 7.6. Nevertheless, the upstream translation with an underestimation is also noticed in several other numerical works [88, 226], hence the overall performance of the current LES-FGM-DSM approaches is quite reasonable in the context of the current state of the art in modeling turbulent sooting flames.

Mean soot profiles

The time-averaged fields of soot volume fraction obtained from LESs with FGM-C and FGM-T models are compared in Fig. 7.11a. As can be observed, soot is predominantly restricted to fuel-rich regions within the stoichiometric mean mixture fraction iso-contour, while the peak soot volume fraction locations are found approximately $z/d_j \simeq 125$. Because of the soot oxidation (predominantly through OH species near stochiometric conditions) and flow fluctuations, soot particles do not exist over the complete mixture fraction space. For the FGM-T model, substantial soot concentration is observed at locations close to the burner exit ($z/d_j \simeq 30$), while the soot formation is somewhat delayed in FGM-C simulations. For a more quantitative illustration, the radial profiles of computed mean and RMS soot volume fraction at several heights are compared against the measurements in Fig. 7.11b. The RMS for computed soot volume fraction is calculated as:

$$f_v^{\mathrm{RMS}} = \sqrt{\langle \overline{f_v}^2 \rangle - \langle \overline{f_v} \rangle^2} \tag{7.40}$$

The qualitative trends in the experimental data are reasonably reproduced in the simulations. The normalized RMS profiles of soot volume fraction show very good agreement with measurements for both approaches, however, the magnitude of the soot volume fraction is underpredicted. The peaks observed in the soot volume fraction in the lean region away from the jet ($r/d_j \simeq 5$) are not well captured in the simulations. Contrary to measurements, soot almost ceases to exist beyond $z/d_j \simeq 180$ in the computed results. The underprediction of soot volume fraction in far downstream regions could be attributed to either the overprediction of OH oxidation rates or the underprediction of the overall flame length in simulations.

The axial profiles of mean and RMS soot volume fraction along the centerline axis are compared in Fig. 7.12. In the present turbulent jet flame, the overall prediction of soot formation along the centerline is mainly controlled by surface growth (in the middle region) and oxidation (due to OH) as shown in [226]. A reasonable agreement between simulated and measured soot volume fraction profiles is obtained, but the peak value of $\langle \overline{f_v} \rangle$ is under-predicted by a factor of two in the simulations. The prediction of RMS fluctuations of soot volume fraction is similar in magnitude to the mean with approximately a factor 2 lower. This underprediction is aligned with the state-of-the-
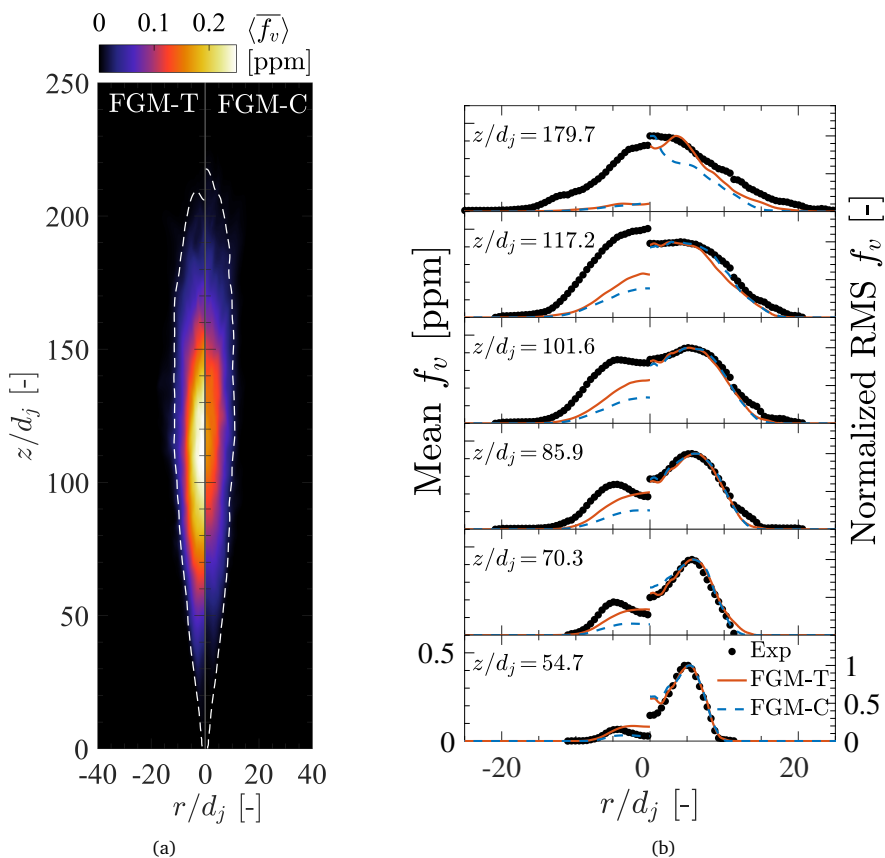
Figure 7.11: Time-averaged fields of soot volume fraction for FGM-T, and FGM-C closure models (a), and a comparison between experimental (symbols) and numerical (line) data for mean and normalized RMS of soot volume fraction profiles at several axial heights (b).

art results from this flame, where a comparable under/over prediction is found with other approaches [73, 84, 226, 232]. From the present LES results, it can be inferred that the FGM-DSM formalism can fairly capture the soot volume fraction distribution under turbulent conditions. Nevertheless, the early formation of soot is evident for the FGM-T approach compared to the FGM-C approach. Besides, for both approaches, the position of the peak soot volume fraction is slightly shifted upstream compared to experiments, indicating that the soot consumption is predicted early in simulations. Nevertheless, an early formation of soot is evident for the FGM-T approach compared to FGM-C.

In the current LESs, soot mass fractions slowly increase while going downstream from the inlet toward a statistically steady state from the initial no-soot condition. Therefore, capturing the chemical trajectories of soot evolution (from the gas-phase to the steady state) becomes crucial in the accurate prediction of soot formation. In the
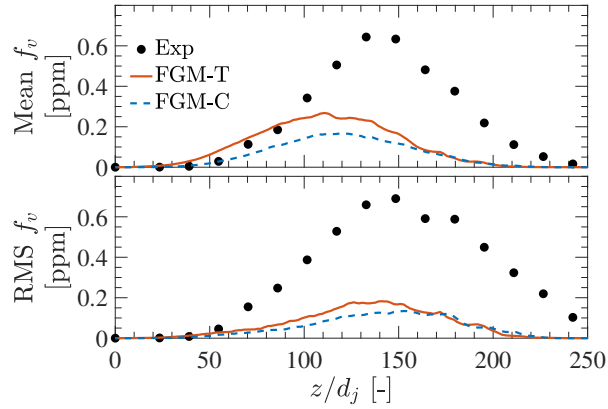
Figure 7.12: Comparison between experimental (symbols) and numerical (line) data for mean and RMS of soot volume fraction profiles at the centerline.

FGM-C approach, soot subprocesses are explicitly computed using the local soot mass fractions. This yields a better qualitative description of unsteady soot evolution in LES. On the contrary, in FGM-T soot source terms are calculated and stored for soot mass fractions in a steady-state flamelet, therefore, the chemical trajectories concerning the formation of soot from the gas-phase to the steady state are not explicitly retained in the FGM tabulation strategy (as highlighted in Chapter 6). Moreover, the non-linear dependency of soot production rates on soot variables is not included in the present FGM-T formulation. Hence, the direct look-up of soot production rates may lead to their overestimation. As a result, higher soot volume fractions are noticed at lower axial positions for FGM-T compared to FGM-C. Nevertheless, the results for both approaches are overall in good agreement with the current state-of-the-art of this flame
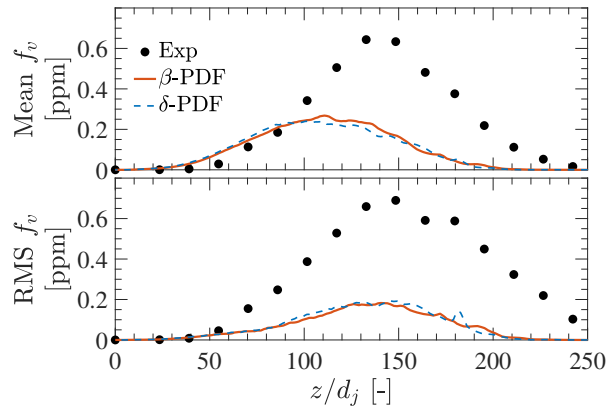

Figure 7.13: Comparison between experimental (symbols) and numerical (line) data for mean and RMS of soot volume fraction profiles at the centerline.

and the FGM-T approach shows high potential for LES due to the high computational efficiency. This aspect will be addressed later.

As previously mentioned, the FGM-T model accounts for the subgrid-scale chemistry-soot-turbulence interactions, as the tabulated source terms are integrated with the presumed β-PDF function. To investigate the impact of the presumed-PDF model on soot prediction with FGM-T, additional simulation is carried out by neglecting the influence of subgrid-scale fluctuations on tabulated soot source terms by using a δ-PDF. In Fig. 7.13, the axial profiles of mean and RMS soot volume fraction along the centerline are compared for the two PDF functions. The soot volume fraction profiles are only marginally influenced by the exclusion of the presumed-PDF treatment accounting for subgrid-scale interactions on soot source terms. Such a response of soot formation can be elucidated by analyzing the spatial distribution of soot volume fraction and mixture fraction variance (which characterize the influence of turbulence fluctuations on scalar mixing). The time-averaged fields of soot volume fraction (with δ-PDF) and mixture fraction variance are shown in Fig. 7.14. As expected, the high variance of mixture fraction is primarily found in the shear layers generated by strong velocity gradients between the main jet and coflow. In the base region of the flame, close to the burner, the mixture fraction variance is significant. However, soot formation is not predominant in this region. On the contrary, the soot formation zone
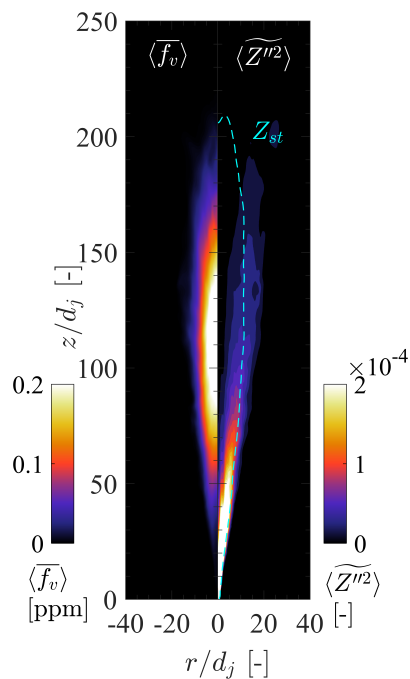

Figure 7.14: Time averaged fields of mean soot volume fraction and mixture fraction variance (range adjusted for better visualization) for FGM-T case with δ-PDF integration applied to tabulated soot rates.

is mainly spanned in the mid-flame region, where mixture fraction gradients are low (leading to low variance). As a result, the subgrid-scale fluctuations only slightly affect the soot source terms. Consequently, overall soot formation is found to be only marginally affected by subgrid-scale turbulent fluctuations in the present flame.

Time-averaged particle size distributions

The coupling of an LES approach with a sectional method provides information on the spatio-temporal evolution of the soot PSD. Hence, the calculated time-averaged PSDs at different axial locations along the flame centerline are plotted in Fig. 7.15 for FGM-T and FGM-C methods. The evolution of the PSD along its trajectory in the flame is strongly correlated to the particle history characterized by a succession of
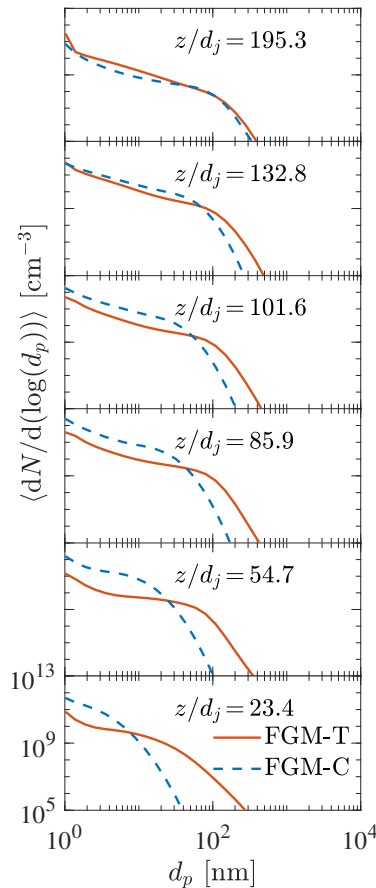

Figure 7.15: Time-averaged soot PSDs at different axial locations along the centerline for FGM-T and FGM-C approaches.

205

chemical and collisional processes associated with soot formation. The time-averaged soot PSDs feature mainly unimodal shapes for FGM-C and FGM-T approaches. The number density of larger-sized particles increases during this process as nucleated soot particles grow primarily through surface reactions. For FGM-T, the shift of PSD towards large diameters is observed as compared to FGM-C, which translates into higher soot volume fractions predicted by the FGM-T. Beyond $z/d_j \approx 150$, the number density starts to drop due to the soot oxidation accompanied by fuel-lean conditions. As noticed earlier in Fig. 7.12 for both FGM-T and FGM-C, the soot concentration is almost negligible at around $z/d_j \approx 200$ since large soot particles are oxidized. This leads to a reduction in the number density of larger-sized soot particles downstream of the flame (as can be observed for $z/d_j \approx 195$ in Fig. 7.15).

In general, both FGM-T and FGM-C demonstrate similar qualitative features of soot PSD evolution in this turbulent jet flame. The quantitative discrepancies in PSD profiles can be attributed to differences in the formation and unsteady evolution of soot in both approaches. For instance, in FGM-C, the coagulation of soot particles is explicitly computed, contrary to the FGM-T model.

Extension of FGM-C model

Besides the two methods mentioned in Section 7.2.5 for soot source term closure, an additional model is considered as an extension of the FGM-C approach. Similar to FGM-C, this model relies on the run-time computation of soot source terms while tabulating the pre-computed gas-phase rate contribution in the FGM database. However, the filtered soot source term formulation is slightly different from the FGM-C approach, as discussed below. In a more general form, the sectional soot source term can be expressed as:

$$\dot{\omega}_{s,i} = \sum_j \dot{\omega}_{s,i}^j(\phi_g, \phi_s) \tag{7.41}$$

$$= \sum_j k_g^j(\phi_g)\zeta_i^j(\phi_g)\Gamma_i^j(\phi_s) \qquad \forall\, i \in [1, N_{sec}] \tag{7.42}$$

where j refers to the soot sub-process (e.g. nucleation), k_g is the gas-phase factor independent of i, the ζ_i term depends on the section (e.g. collision frequency factor), while Γ_i is a function of soot scalars (e.g. number density). The closure of filtered soot source term is achieved using the presumed-PDF approach:

$$\overline{\dot{\omega}}_{s,i} = \sum_j \bar{\rho} \int \int \frac{1}{\rho} k_g^j(\phi_g)\zeta_i^j(\phi_g)\Gamma_i^j(\phi_s) P(\phi_g, \phi_s)d\phi_g d\phi_s \tag{7.43}$$

Since the time scales associated with the evolution of the thermochemical state are typically smaller than the time scales of soot production [66], the independence be-

tween gas and soot phases is assumed, as discussed in Refs. [66, 73], which gives:

$$\overline{\dot{\omega}}_{s,i} = \sum_j \underbrace{\left[\bar{\rho} \int \frac{1}{\rho} k_g^j(\phi_g) P(\phi_g) d\phi_g \right]}_{\overline{k_g^j}} \underbrace{\left[\int \zeta_i \left(\widetilde{\phi_g} \right)^j \Gamma_i^j(\phi_s) P(\phi_s|\phi_g) d\phi_s \right]}_{\Xi_i^j \left(\widetilde{\phi_g}, \widetilde{\phi_s} \right)} \tag{7.44}$$

where $\overline{k_g^j}$ represents the filtered rates for the soot subprocesses, and depend only on the gas phase. The $\overline{k_g^j}$ terms are tabulated in the manifold as a function of control variables $\widetilde{Z}$ and $\widetilde{C}$. The second term Ξ_i^j in Eq. 7.44 depends on the soot variable $(\widetilde{\phi_s} = \widetilde{Y}_{s,i}$ here). This term is computed at runtime. For model simplicity, the ζ_i term, which depends on the sectional soot properties (e.g. volume) and gas-phase variables (e.g. temperature) is computed during simulation. To account for subgrid-scale turbulence-chemistry interactions, the gas-phase contribution, $\overline{k_g^j}$, is modeled with the presumed-PDF approach. The marginal PDF $P(\phi_g)$ is assumed to have a β function. The conditional PDF of solid phase contribution $P(\phi_s|\phi_g)$ is treated as a δ function. For brevity, this method is referred to as FGM-CR hereon.

It is important to note that FGM-C and FGM-CR methods primarily differ in the treatment of the gas-phase contribution in the closure of soot source terms. In the FGM-C case, $\overline{k_g^j}$ is computed on-the-fly using tabulated filtered gas-phase quantities $\widetilde{\phi_g}$. On the other hand in the FGM-CR, the filtered $\overline{k_g^j}$ is a-computed *a-priori* from flamelets and directly tabulated in the manifold. Since $\overline{k_g^j(\phi_g)} \neq k_g^j(\widetilde{\phi_g})$, the FGM-CR model essentially facilitates a more physically consistent treatment of subgrid-scale fluctuations of gas-phase variables, as compared to the FGM-C approach. At the same time, similar to FGM-C, subgrid-scale turbulence-soot interactions are not accounted for in the FGM-CR approach. This strategy, therefore, can be regarded as an extension of the FGM-C model.

The fields of mean soot volume fraction are compared in Fig. 7.16a for the FGM-CR and FGM-C models. In general, the soot formation zones in FGM-CR and FGM-C show similarities in the spatial distribution as well as the magnitude of the soot volume fraction. A slight reduction in soot volume fraction is noticed near the flame tip. For more quantitative illustration, the radial profiles of mean and RMS (normalized with peak) soot volume fraction at several heights are compared against the measurements and FGM-C model in Fig. 7.16b. The results obtained with the FGM-T method are also presented for reference. It can be observed the radial distribution of soot volume profiles for FGM-CR case exhibit qualitative similarities with FGM-C results. In the far downstream region, (close to the flame tip) where soot oxidation is prevalent, the slightly lower soot volume fraction is predicted by the FGM-CR strategy, as compared to FGM-C. The overall shape and peak location of the soot volume fraction obtained with FGM-CR agree closely with FGM-C. However, slight deviations between FGM-C and FGM-CR are evident in the downstream regions. The strong intermittency is evident (Fig. 7.6) in downstream regions where soot pockets detach near the flame
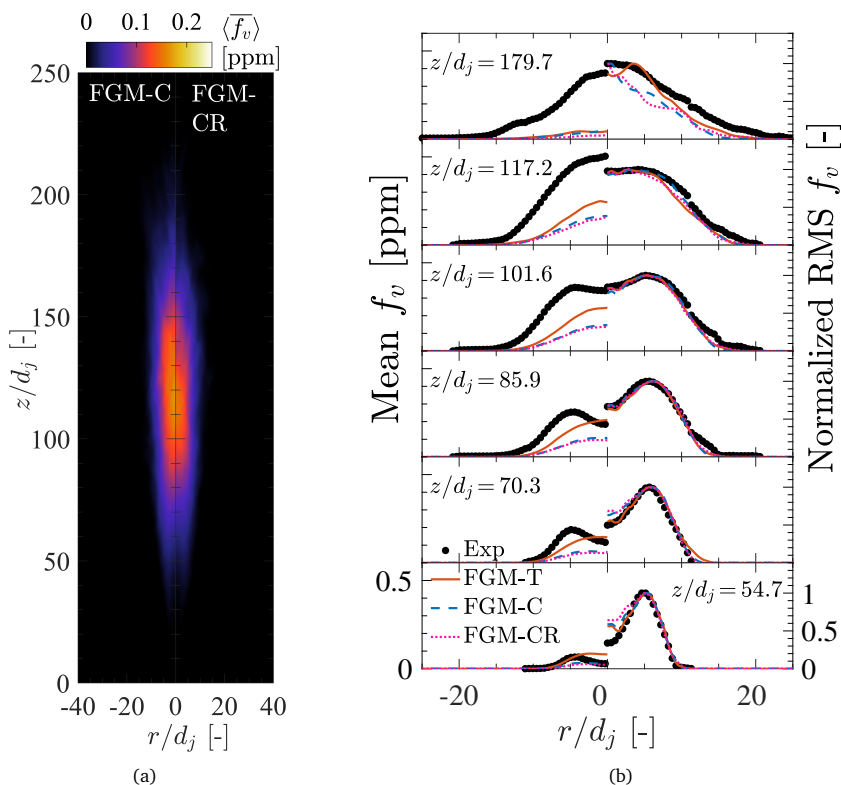
Figure 7.16: Time-averaged fields of soot volume fraction for FGM-C, and FGM-CR closure models (a), and a comparison between experimental (symbols) and numerical (line) data for mean and normalized RMS of soot volume fraction profiles at several axial heights (b).

tip. This intermittent behavior is captured differently during soot source term filtering in the FGM-C and FGM-CR models. As a result, deviations are also seen in the soot volume fraction.

Remark on computational performance

Besides the gas-phase chemistry, in sooting flame simulations with the sectional method, the greatest CPU overhead is due to the computation of soot source terms. Especially the particle dynamics (coagulation) takes almost half of the total CPU time. Employing FGM chemistry leads to a significant reduction in CPU cost for gas-phase reactions. However, computation of soot source terms during run-time remains a CPU-intensive task, which is alleviated here with tabulation of the sectional source term in the FGM-T approach. In the current LESs with 30 soot sections, the FGM-T approach yields a factor 3 reduction in CPU time per time-step as compared to FGM-C. The computational speedup with FGM-T for a higher number of sections can be even more

significant since the computational time scales non-linearly with N_{sec}. For instance, the FGM-T approach provides a computational speed-up of about a factor 7 compared to FGM-C when 60 soot sections are considered.

In summary, it is evident from the LES results that the modeling of filtered soot source terms strongly influences the soot formation prediction in turbulent flames. The complete tabulation of soot chemistry (FGM-T) tends to effectively capture the experimentally observed features of soot distribution in turbulent conditions. Compared to the FGM-C method, in which soot chemistry is calculated during runtime, the FGM-T method overpredicts (by factor 2) soot concentration. Considering the state-of-the-art in the numerical prediction of soot formation in turbulent flames, the discrepancy in quantitative prediction by factor 2 is still acceptable. It is also important to emphasize the good computational efficiency of FGM-T within the context of the sectional method which makes it an attractive alternative to the FGM-C.

However, as already highlighted, the complete tabulation of the soot chemistry has certain limitations, for example, soot-independent treatment of the soot production term, and a lack of information on the gas-to-soot history effects in flamelets. Therefore, in simulation applications where the unsteady evolution of soot quantities is not of interest, the FGM-T approach is more suitable to predict the soot formation. Especially, in simulations of practical combustion systems, the FGM-T is an excellent strategy to gain an understanding of soot formation and information on size distribution, at affordable computational cost. On the other hand, for more fundamental and parametric studies, the FGM-C method is recommended as accounts for the non-linear interactions between the soot and gas phase, without any modeling assumptions, and can be more reliable for highly transient cases.

7.4 Assessment of FGM-DSM clustering method (in turbulent flames)

A computationally efficient integration of FGM chemistry with DSM through clustering (FGM-CDSM) was introduced in the previous chapter. However, the assessment of the clustering method was conducted on laminar flames. The FGM-CDSM approach is essentially the FGM-T method discussed in this study. Hence, the verification of the clustering approach in the context of turbulent flame simulations is a relevant progressive step. The FGM-CDSM method is applied in the simulation of turbulent piloted jet flame to investigate its capabilities for soot formation prediction in turbulent conditions. For the comparative assessment of the clustering method, a reference simulation without clustering ($\mathcal{R} = 0$) is considered by transporting soot mass in 30 sections (FGM-T case). Subsequently, an LES simulation is carried out with 6 clustered sections ($\mathcal{R} = 0.8$) by employing a uniform grouping of soot sections.

In Fig. 7.17a the time-averaged field of soot volume fraction obtained from LES with clustering ($\mathcal{R} = 0.8$) is compared against the no-clustering solution. As can be ob-

served, qualitative features of the mean f_v field including the region of higher soot yield obtained with clustering solution agree well with the no-clustering counterpart. For a more quantitative illustration, the radial profiles of computed mean and RMS (normalized with peak) soot volume fraction at several heights are compared against the measurements in Fig. 7.17b. The computed profiles of f_v with clustering show very good agreement with the solutions without clustering. Furthermore, the qualitative features of RMS profiles are favorably captured on clustering.

It is important to note that in FGM-T formulation, Eq. 7.37, considered for the treatment of soot oxidation, presents limitations in computing the soot consumption rate term for the clustered section. However, since the soot oxidation (predominantly by OH) occurs near stoichiometric mixture fraction region, the oxidation-corrected consumption term (Eq. 7.37) is applied only in regions $\widetilde{Z} \leqslant Z_{st}$, while the filtered soot source term (Eq. 7.36) is considered in rich mixture fractions. Therefore, dis-
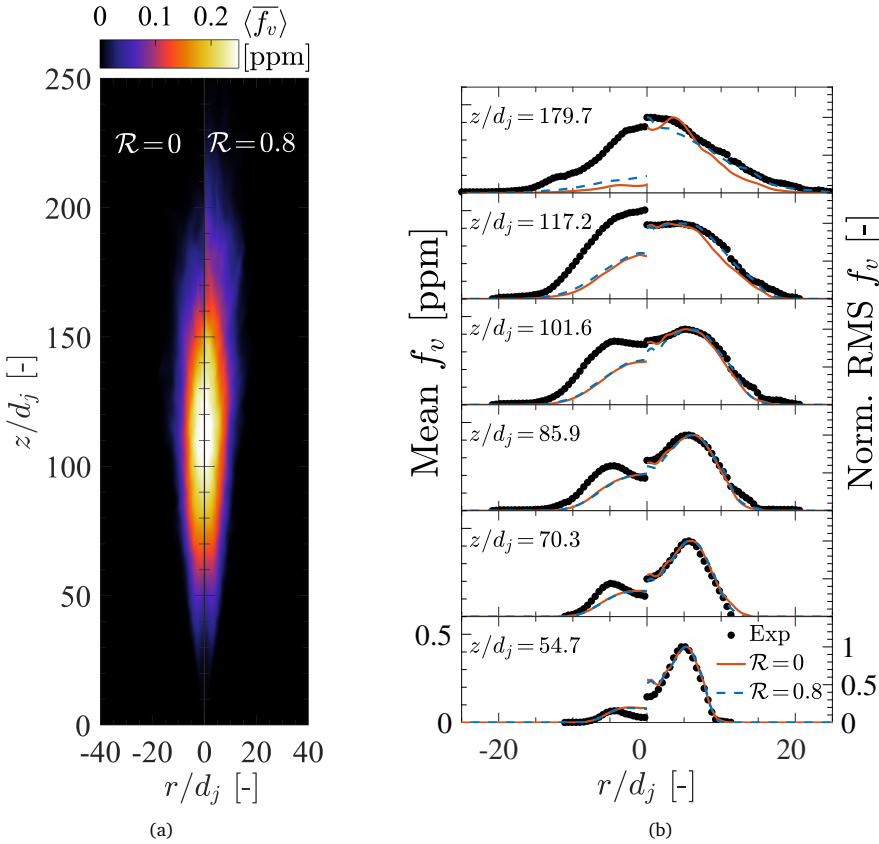

Figure 7.17: Time-averaged fields of soot volume fraction (a), and comparison between experimental (symbols) and numerical (line) data for mean and RMS of soot volume fraction profiles at several downstream heights for $\mathcal{R} = 0$ and $\mathcal{R} = 0.8$ cases (b).
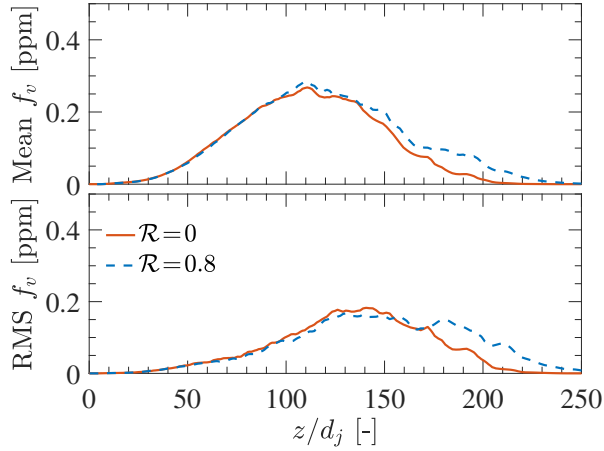
Figure 7.18: Comparison between experimental (symbols) and numerical (line) data for mean and RMS of soot volume fraction profiles at the centerline for $\mathcal{R} = 0$ and $\mathcal{R} = 0.8$ cases.

crepancies noticed in soot profiles at the downstream position ($z/d_j \simeq 179.7$) are mainly attributed to the limitation of clustering formulation in capturing soot oxidation in lean mixture fraction zones. The axial profiles of mean and RMS soot volume fraction along the centerline are compared in Fig 7.18. Overall, the qualitative and quantitative agreement is encouraging. The agreement between clustering and non-clustering-based solutions is very good, which suggests that the FGM-CDSM approach can favorably reproduce the soot volume fraction distribution in turbulent conditions.

The time-averaged soot PSD distributions on the centerline at several heights are compared in Fig. 7.19. The PSDFs obtained with re-constructed (Rec.) soot mass fractions, and with 6 clusters before the reconstruction step, are presented. As can be observed, the downstream evolution and shape of PSDF profiles are reasonably well reproduced by the reconstructed sections in Fig. 7.19. The coarse PSD distribution (No-Rec.) obtained with a few transported clustered sections also predicts the general shape of its no-clustering counterparts. However, unlike laminar simulations (refer to Chapter 6), the reconstruction in turbulent flames tends to show discontinuities at the sectional boundaries, especially for the PSDFs far downstream of the soot formation region. The discrepancies in PSDF prediction could be associated with errors introduced during the reconstruction of filtered sections followed by averaged statistics.

In the clustering method, the sub-cluster distribution of soot mass fraction (parameterized by $\mathcal{F}_i$) is governed by the Z and $\mathcal{Y}$ evolution, since $\mathcal{F}_i$ parameter is tabulated in the manifold. Due to its oxidation, soot ceases to exist in lean-mixture fraction regions in the flamelets. As a result, the soot mass is almost uniformly distributed in sub-clusters leading to steep sub-cluster PSDs for lean regions. Besides, the strong intermittency in soot formation may lead to deviations in the evolution of soot mass in clustered sections compared to their steady-state tabulated values. Nevertheless,
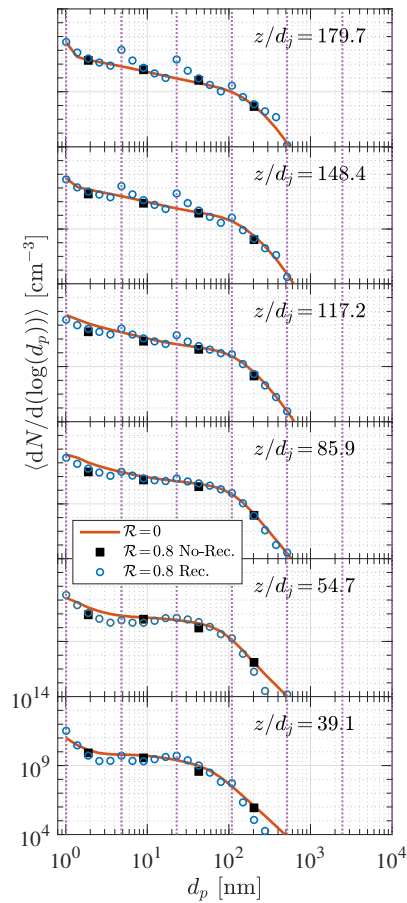
Figure 7.19: Comparison between mean soot PSD solutions at several axial positions on the centerline for $\mathcal{R} = 0$ and $\mathcal{R} = 0.8$ cases. Dotted vertical lines indicate the boundaries of clustered sections.

considering the complexities of flow-flame-soot interactions associated with turbulent flames, the agreement between PSD profiles predicted by the clustering-based FGM-T method is promising. The results, therefore, indicate that the FGM-CDSM can capture PSD with qualitative features considerably well, at a significantly reduced level of transported soot variables.

Concerning the computational performance of FGM-CDSM in the present LES computations, for A factor 5 reduction (from 30 sections) in the total number of soot sections to 6, the CPU cost per time step (with a constant time step size) is found to be reduced by a factor of 1.8. Moreover, for the LES with 6 clustered sections, the FGM database memory size is reduced by 70% compared to the one required for the LES with 30 soot sections. However, PSD reconstruction required additional variables to be stored in the database, limiting the overall memory reduction to 20%.

7.5 Influence of hydrogen addition on soot formation

In Chapter 3, the soot-inhibiting effects of hydrogen addition to fuel were investigated in laminar counterflow flames. Here, the study is extended to understand the influence of hydrogen addition on soot formation in turbulent conditions. For this study, the ethylene fuel is blended with 10% (by volume) H_2. Due to the change in fuel composition, a new flamelet database is created with the unity-Lewis transport model and the same soot model parameters. The flow conditions are kept identical to the Sandia ISF case, as described in Section 7.3.1. In the LES, the FGM-C method is employed for the soot source term closure (to maintain a consistent strategy as used in laminar flame studies).

In Fig. 7.20c the fields of mean soot volume fraction are compared for baseline (pure ethylene fuel) and H_2-addition case. As noticed in the laminar flame study (Chapter 3), the soot production is found to be lowered in the case of hydrogen addition. Also, the soot formation region is found to be slightly shorter near the flame tip in the presence of hydrogen. The centerline profiles of mean temperature and soot volume
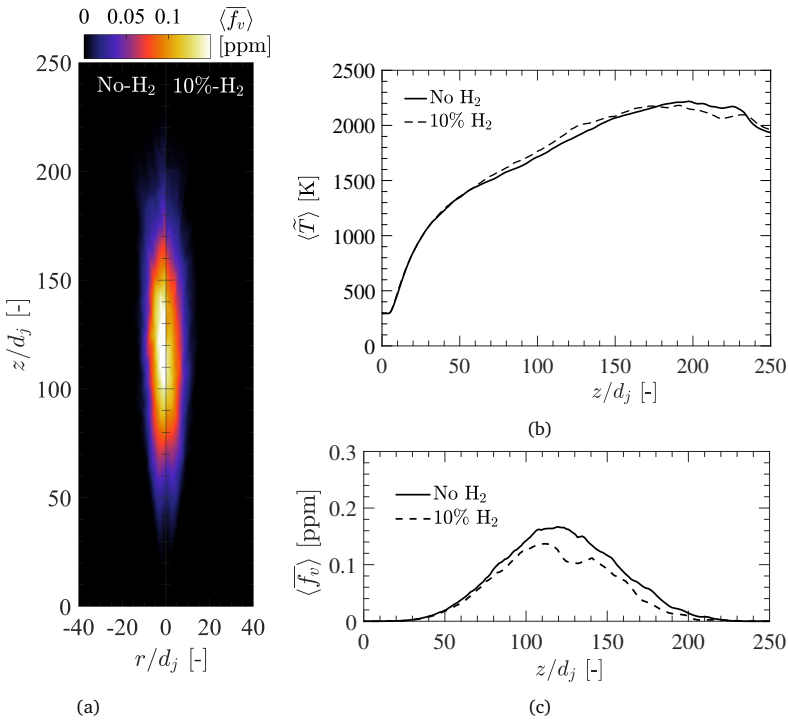

Figure 7.20: Time-averaged fields of soot volume fraction for FGM-C with and without H_2 addition to the fuel (a), comparison between mean temperature (b) and soot volume fraction (c) profiles along the centerline .
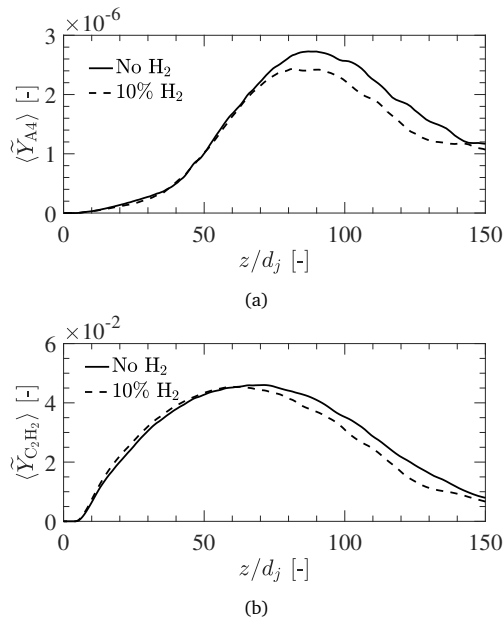
Figure 7.21: Computed centerline profiles of mean A4 (a), and C_2H_2 (b) mass fraction for baseline and hydrogen-enriched conditions.

fraction are compared in Fig. 7.20b. The temperature shows a slight increase in the middle region of the flame for the H_2 addition case. The increase in the temperature for hydrogen-enriched fuel is also noticed in the laminar flame study. Moreover, consistent with the observations in laminar counterflow flames, the soot volume fraction is decreased in the presence of H_2.

The observed soot-inhibiting response of soot under hydrogen addition conditions can be mainly attributed to the influence of H_2 on the prediction of key soot precursors A4 and C_2H_2, responsible for nucleation and surface growth respectively. To illustrate this, the mean centerline profiles of A4 and C_2H_2 mass fractions are compared in Fig. 7.21. In the case of hydrogen addition, the formation of A4 and C_2H_2 is found to be slightly reduced in the middle region of the flame as compared to the baseline case. The reduction in the precursor formation leads to lowered rates of soot subprocesses such as nucleation and surface growth. For the 10% H_2 addition level, the peak soot volume fraction is reduced by approximately 20%. In laminar flames studied in Chapter 3, the peak soot volume fraction reduction is found to be lowered by about 30% for 10% of H_2 addition. The soot-inhibiting effect of hydrogen addition, recognized in the laminar flames, is also observed in turbulent flames. The LES results confirm that soot formation is lowered by hydrogen addition to fuel for turbulent jet flame conditions.

7.6 Influence of preferential diffusion effects

In turbulent combustion simulations, the unity-Lewis number transport model is often employed since the diffusion of chemical species is presumed to be controlled by turbulent mixing. However, as demonstrated in Chapter 5 the quantitative prediction of soot formation is strongly influenced by the preferential diffusion effects associated with PAH species [224]. To assess the impact of the diffusion transport of species on soot formation in turbulent conditions, an additional FGM database is created from the flamelets computed with the mixture-averaged transport model of Hirschfelder and Curtiss [92]. In the LES, however, the control variables $\widetilde{Z}$ and $\widetilde{\mathcal{Y}}$ are transported with the unity-Lewis number approximation. For this assessment, the FGM-T strategy involving tabulated soot chemistry is considered for LESs with $N_{sec} = 30$.
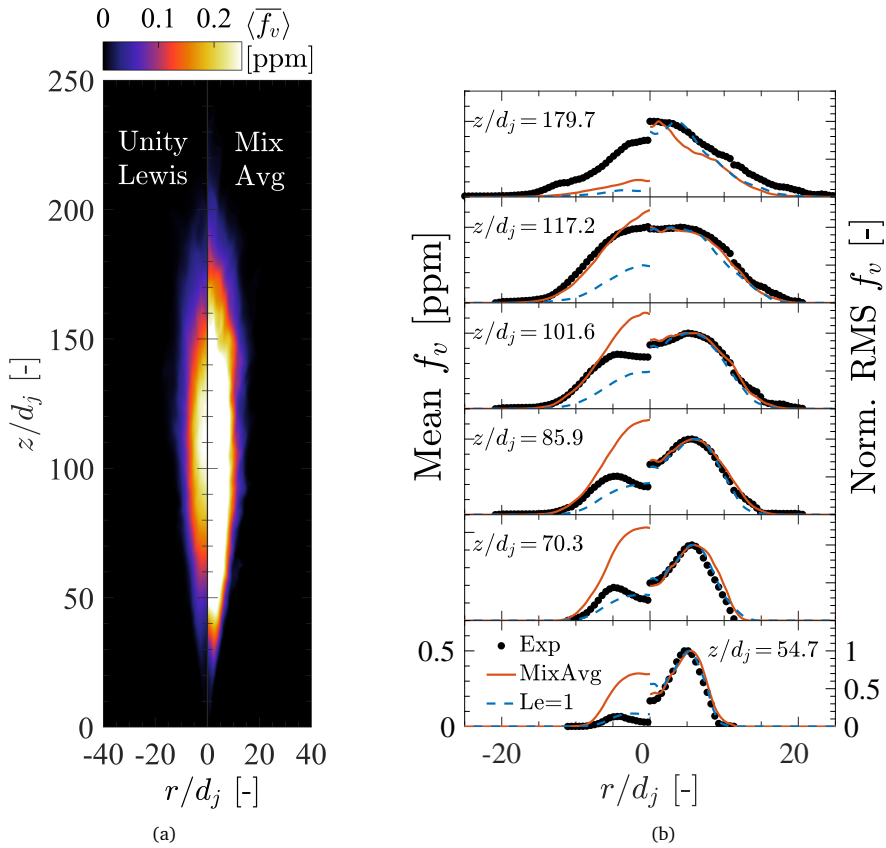

Figure 7.22: Time-averaged fields of soot volume fraction for FGM-T with unity-Lewis and mixture-averaged transport (a), comparison between experimental (symbols) and numerical (line) data for mean and normalized RMS of soot volume fraction profiles at several axial heights (b).

215

The time-averaged field of soot volume fraction obtained from LES with manifolds based on the unity-Lewis ($Le = 1$) transport model and mixture-averaged transport model (MixAvg for brevity) are compared in Fig. 7.22a. As can be observed, the soot volume fraction values are almost a factor 2 higher for the mixture-averaged flamelet-based manifold as compared to the one created with the unity-Lewis transport model. The radial profiles of computed mean and RMS (normalized with peak value) soot volume fraction at several heights are compared against the measurements in Fig. 7.22b. The computed profiles of f_v with mixture-averaged transport-based FGM show significant overprediction of soot compared to the one with the unity-Lewis model. Besides, the f_v profiles are widened in the radial direction for the strategy based on mixture-averaged flamelets as compared to the unity-Lewis approach.

Since soot formation rates are looked-up, the noticed disparity in quantitative prediction can be attributed to differences in their values stored in the manifold. To illustrate this, the manifold visualizations of net soot mass growth rates are compared for flamelets computed with mixture-averaged and unity-Lewis transport models in Fig. 7.23. It can be observed that soot mass growth rates are approximately 5 times higher for the flamelets created with the mixture-averaged transport model as compared to their unity-Lewis model counterparts. The noticed trends in soot mass growth rates are translated in the f_v prediction. The response of soot formation to preferential diffusion treatment in turbulent flames is qualitatively consistent with the one obtained for laminar counterflow flames in Section 5.3.4, where soot formation is enhanced for the non-unity Lewis transport models. The PAH species responsible for soot nucleation and H_2 involved in the HACA growth mechanism, exhibit strong pref-
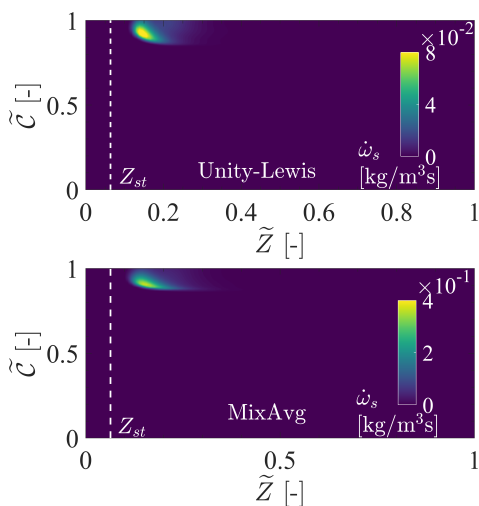

Figure 7.23: Manifold visualizations of net soot mass growth rate $\dot{\omega}_s$ for flamelets computed with unity-Lewis (top panel) and mixture-averaged transport (bottom panel) models. These manifold slices correspond to $\mathcal{S}_Z = \mathcal{S}_C = 0$.

erential diffusion effects as they diffuse from the reaction zone to the soot formation zone. The unity-Lewis approximation essentially underpredicts the concentration of PAH leading to lowered overall soot formation.

It is important to note that, in the current assessment, the non-unity Lewis number effects are not explicitly considered in the transport of control variables for simplicity [245]. However, from the LES results, it is clear that the inclusion of preferential diffusion effects in flamelet calculation can substantially impact the soot formation prediction. Therefore, the use of non-unity Lewis transport should be considered in turbulent flames for a more accurate quantitative prediction of soot formation. In this context, more consistent models in which control variables are transported with non-unity Lewis numbers (e.g. Ref. [225]) can be also considered to account for preferential diffusion effects in sooting flame simulations.

7.7 Influence of radiative heat transfer effects

For accurate predictions of temperature, accounting for radiation and wall heat losses can be crucial [211]. In the context of sooting flames, due to temperature sensitivity, the important role of radiative heat transfer in the prediction of soot and gaseous properties has been demonstrated in earlier works [99, 246, 247]. Therefore, the influence of radiative heat transfer on the prediction of soot formation in turbulent sooting flame is also investigated in the present work. Several approaches for modeling radiative heat transfer properties of gas and soot with varied levels of complexity exist [246]. In this work, the radiative heat transfer model introduced in Chapter 2 based on the optically thin approximation is considered for its application to LES.

7.7.1 Non-adiabatic manifold generation

To include non-adiabatic effects due to radiative heat transfer in the FGM chemistry framework, the method employed in previous works [228, 240] is considered here. Accordingly, the FGM database is augmented with solutions of strained diffusion flamelets with a radiative heat sink term (which accounts for the optically thin radiation of CO, CO_2, CH_4, and H_2O species and soot) in the enthalpy equation. In this approach, the local enthalpy deficit is obtained through a radiative heat term scaled with a factor c_R without changing the inlet temperature of the reactants. This approach facilitates a relatively simple tabulation process. The effect of the scaling of the gas-phase radiative source term on the peak temperature can be observed in Fig. 7.24. The $c_R = 0$ curve corresponds to the solution of the steady flamelet equations without radiative heat losses for several strain rates (parameterized by stoichiometric scalar dissipation rate χ_{st}), while $c_R = 1$ curve represents flamelets with radiative heat loss. In flamelets, the concentrations of key radiating gases CO_2 and H_2O peak near the stoichiometric regions where temperature exhibits the maximum value. Therefore, a significant reduction (e.g. about $600\,K$ for $\chi_{st} = 0.1$) in the peak temperature is ob-
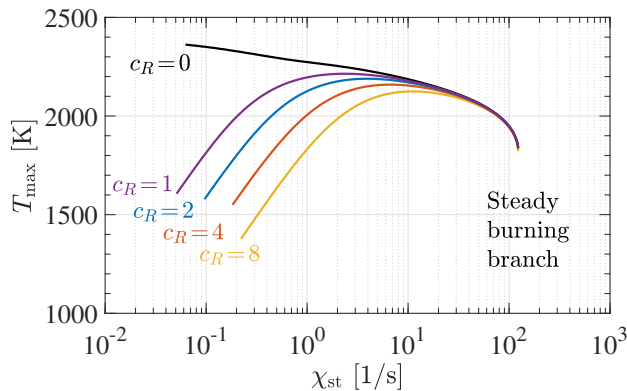
Figure 7.24: S-curve of the maximum temperature against scalar dissipation rate at stoichiometric position χ_{st} at different c_R scaling of the radiation source term.

served for flamelets when thermal radiation is included. The influence of radiative heat transfer is predominant at lower scalar dissipation rates. Moreover, to cover the enthalpy space beyond the $c_R = 1$, an additional enthalpy deficit can be obtained in the flamelet solutions by increasing the scaling parameter c_R.

Figure 7.25 illustrates the flamelets with ($c_R = 1$) and without ($c_R = 0$) radiative heat loss in Z-$\mathcal{Y}$ space. Each flamelet is colored by the corresponding value of enthalpy. As can be observed, the enthalpy loss due to radiative heat transfer is higher as the composition approaches the long residence time. Due to the change in chemical composition, the progress variable needed to be adopted to facilitate the monotonic mapping of flamelets for adiabatic and non-adiabatic flamelets. After a guess and check method, the new progress variable is obtained to parameterize the manifold. The

Figure 7.25: Evolutions of the progress variable $\mathcal{Y}$ and enthalpy (h) against the mixture fraction Z in flamelets for heat loss parameter $c_R = 0$ (a), and $c_R = 1$ (b).

updated progress variable is defined as:

$$\mathcal{Y} = \alpha_{H_2O}Y_{H_2O} + \alpha_{CO_2}Y_{CO_2} + \alpha_{CO}Y_{CO} + \alpha_{H_2}Y_{H_2} + \alpha_{C_2H_2}Y_{C_2H_2} + \alpha_{A4}Y_{A4} \qquad (7.45)$$
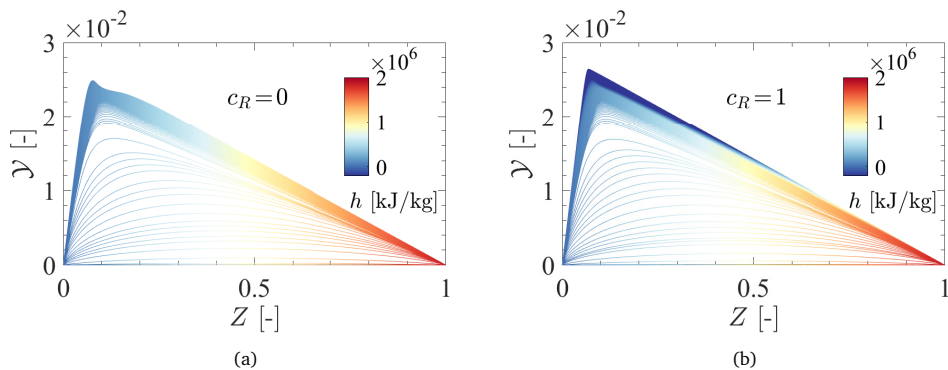
where $\alpha_{H_2O} = 0.111$, $\alpha_{CO_2} = 0.09088$, $\alpha_{CO} = 0.0357$, $\alpha_{H_2} = 0.496$, $\alpha_{C_2H_2} = -0.0384$ and $\alpha_{A4} = 9.888$. To parameterize the enthalpy deficit in the tabulation process, the scaled enthalpy $\mathcal{H}$ is considered. The $\mathcal{H}$ is computed from the enthalpy h as:

$$\mathcal{H} = \frac{h - h_{\min}(Z, \mathcal{C})}{h_{\max}(Z, \mathcal{C}) - h_{\min}(Z, \mathcal{C})} \qquad (7.46)$$

where $h_{\max}$ and $h_{\min}$ denote the maximum and minimum enthalpy levels in the low-dimensional manifold for each mixture fraction and reaction progress.

In the present non-adiabatic manifold, a Favre-filtered variable $\widetilde{\psi}$ and Reynolds-averaged variable $\overline{\psi}$ are obtained from integration with marginal PDFs of Z, $\mathcal{C}$ and $\mathcal{H}$ as:

$$\widetilde{\psi} = \int \int \psi(Z, \mathcal{C}, \mathcal{H}) P(Z) P(\mathcal{C}) P(\mathcal{H}) dZ d\mathcal{C} d\mathcal{H} \qquad (7.47)$$

In the simulations of non-adiabatic conditions, the β-PDF is used to model the mixture fraction distribution. The statistical distribution conditioned on Z of scaled reaction progress variable $\mathcal{C}$ and scaled enthalpy $\mathcal{H}$ are represented by the δ functions. The four controlling variables ultimately describe the chemical state of the turbulent flame in the manifold:

$$\widetilde{\psi} = \Psi\left(\widetilde{Z}, \mathcal{S}_Z, \widetilde{\mathcal{C}}, \widetilde{\mathcal{H}}\right) \qquad (7.48)$$

In the LES, the transport equations are solved for controlling variables $\widetilde{Z}$, $\widetilde{Z''^2}$, $\widetilde{\mathcal{Y}}$ and $\widetilde{h}$. Then, $\mathcal{S}_Z$, $\widetilde{\mathcal{C}}$, and $\widetilde{\mathcal{H}}$ are evaluated using Eq. 7.24, Eq. 7.16 and Eq. 7.46, respectively. The thermochemical variables are stored in the FGM database with a non-uniform resolution of $101 \times 11 \times 101 \times 21$ grid points in $\widetilde{Z}$, $\mathcal{S}_Z$, $\widetilde{\mathcal{C}}$, and $\widetilde{\mathcal{H}}$ space respectively. In the enthalpy transport equation, the filtered radiative source term is approximated by neglecting subgrid-scale turbulence-radiation interactions:

$$\overline{\mathcal{Q}}_{\mathrm{rad}} \simeq \dot{\mathcal{Q}}_{\mathrm{rad}}^{\mathrm{gas}}\left(\widetilde{Y}, \widetilde{T}\right) + \dot{\mathcal{Q}}_{\mathrm{rad}}^{\mathrm{soot}}\left(\widetilde{Y}_s, \widetilde{T}\right) \qquad (7.49)$$

The implementation methodology and validation of the radiation model in the Alya solver are presented in Appendix D.

7.7.2 Instantaneous fields

The instantaneous fields of temperature, soot volume fraction, and soot number density obtained with the non-adiabatic manifold (Non-Ad. for brevity) are compared against their adiabatic counterparts in Fig. 7.26. The FGM-C approach is employed

in the LES. This method explicitly accounts for the temperature dependence of different soot subprocesses in the filtered source term calculation. From the temperature field, it can be observed that thermal radiation significantly reduces the temperature in the downstream regions of the flame $z/d_j > 150$. The radiative heat loss occurs predominantly near high-temperature regions (close to stoichiometric conditions) al-
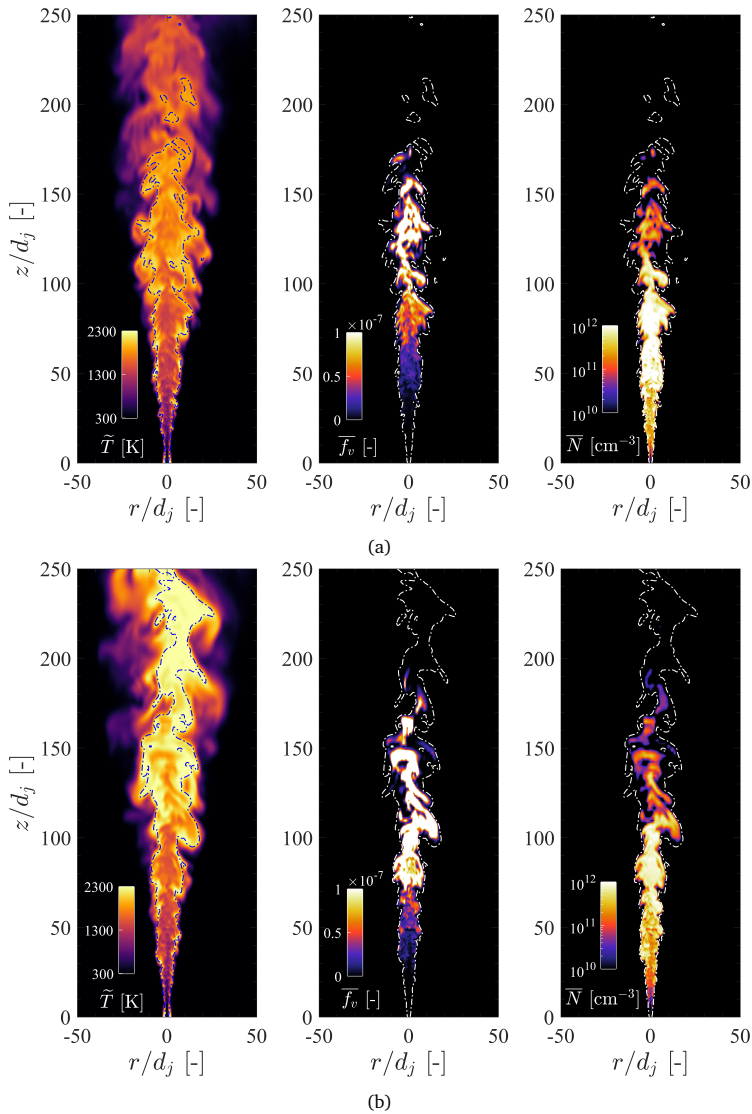

Figure 7.26: Instantaneous fields of temperature, soot volume fraction, and soot number density for non-adiabatic (a), and adiabatic (b) conditions. The stoichiometric mixture fraction is shown with dashed iso-lines. The instantaneous results correspond to the FGM-C cases.

together with the presence of radiative combustion products such as CO_2, H_2O. The inclusion of thermal radiation in the simulations highly impacts the soot formation. The soot volume fraction values are substantially reduced (approximately by a factor of 2) in the presence of thermal radiation. Moreover, in the presence of radiative heat transfer, the overall number density of soot particles is increased near the flame base ($z/d_j \simeq$ 20-50). However, both adiabatic and non-adiabatic cases, show similar qualitative features as the soot formation zone is mainly present in the middle region of the flame within the richer mixtures.

7.7.3 Mean profiles

The computed axial temperature profiles for adiabatic and non-adiabatic cases are shown in Fig. 7.27b. In the region close to the burner, the temperature profiles are quite similar as thermal radiation is almost negligible in this region. However, the temperature decreases drastically (about 300-500 K) compared to the adiabatic case around $z/d_j \simeq$ 100 for the non-adiabatic case. The centerline profiles of the mean radiative source term, indicative of radiation intensity, are presented in Fig. 7.27b. The profile for radiative power shows an initial increase with axial position and then drops with further downstream distance. The radiative source term peaks near $z/d_j \simeq$ 150. The numerical results are consistent with the observation in experiments for the localization of radiative intensity [124]. Figure 7.27a presents the comparison of radial mean and RMS temperature with experiments for adiabatic and non-adiabatic simulations. A substantial decrease in temperature can be observed in the non-adiabatic simulations, as a result of radiative heat loss through the gas and soot phase. The numerical profiles for LES with thermal radiation show close agreement with measurements, as compared to the adiabatic results.

In Fig. 7.28a, the field of mean soot volume fraction for the non-adiabatic LES is compared against the adiabatic case. The soot formation zone is found to be shorter in the non-adiabatic case compared to the adiabatic case. The radial profiles of mean and RMS (normalized with peak) soot volume fraction at several heights are compared against the measurements and adiabatic results in Fig. 7.28b. As can be observed the radial distribution of soot volume profiles for non-adiabatic cases exhibit qualitative similarities with the adiabatic results. The centerline profiles of mean and RMS, shown in Fig. 7.29 also demonstrate that the overall shape and peak location of soot volume fraction, obtained with non-adiabatic cases show close agreement with the adiabatic case. However, the soot volume fraction values in the non-adiabatic case are approximately a factor 2 lower than in the adiabatic case.

The numerical prediction of soot formation is very sensitive to the concentration of soot precursors. Hence, the observed response of soot under non-adiabatic conditions can be attributed to the prediction of key soot precursors A4 and C_2H_2, responsible for nucleation and surface growth respectively. To illustrate this, the mean centerline profiles of A4 and C_2H_2 mass fractions are compared in Fig. 7.30. In presence of
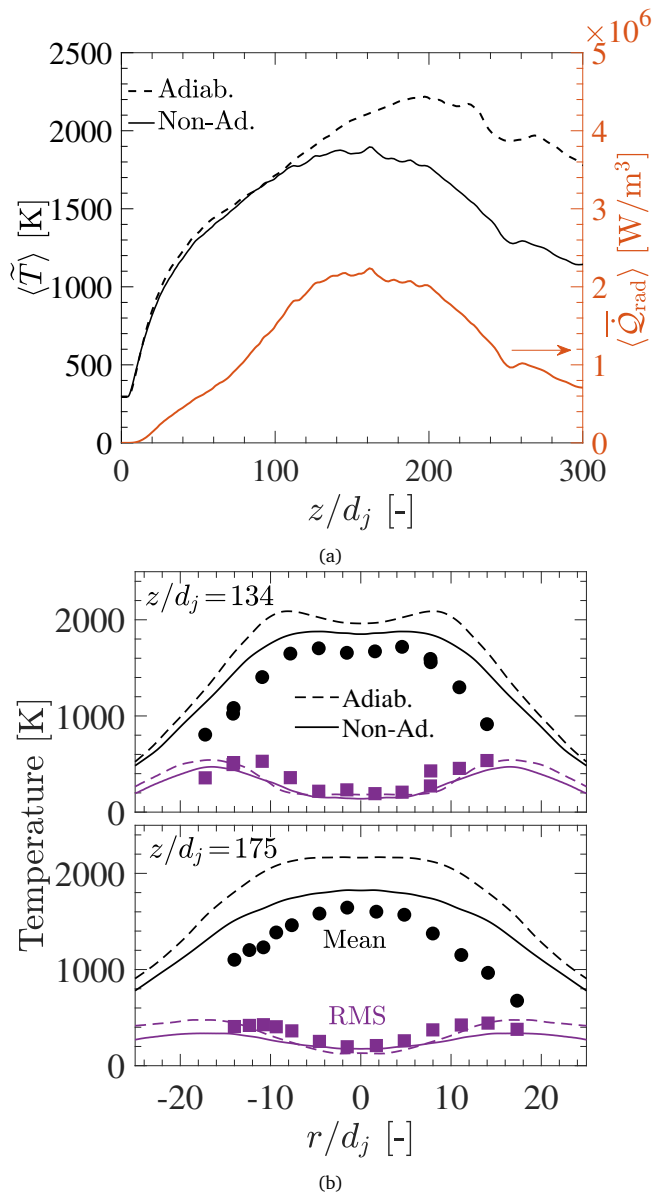
Figure 7.27: Computed centerline profiles for mean temperature and radiative power (a), and comparison between experimental (symbols) and numerical (line) data for radial mean and RMS of temperature (b) for the adiabatic and non-adiabatic conditions.

thermal radiation, the formation of A4 and C_2H_2 is reduced within the soot formation zone, which leads to lowered rates of soot growth through condensation and surface growth processes. Near the lower flame region ($z/d_j \simeq$ 30-70), the concentration
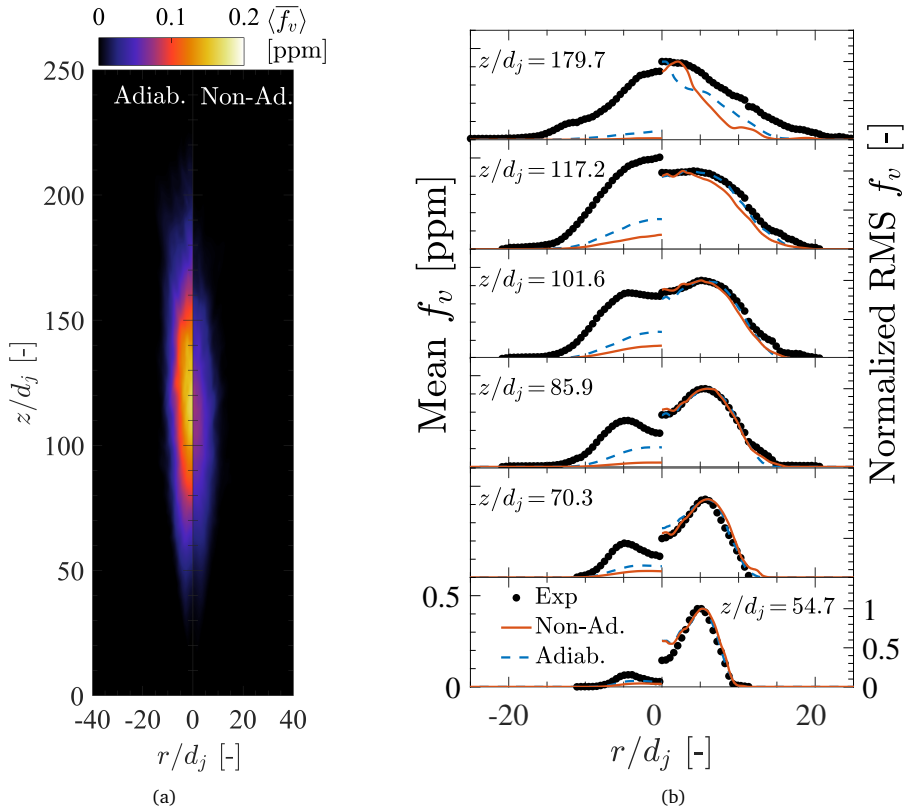
Figure 7.28: Time-averaged fields of soot volume fraction for the non-adiabatic case with FGM-C closure models (a), comparison between experimental (symbols) and numerical (line) data for mean and normalized RMS of soot volume fraction profiles at several axial heights (b).

of A4 is found to be higher in the non-adiabatic case, as compared to the adiabatic case. Consequently, a higher number density of incipient soot particles is noticed (see Fig. 7.26a). In the middle region of the flame ($z/d_j \simeq 100\text{-}150$), where surface growth is predominant, the C_2H_2 mass fraction is lowered for the case with radiation, affecting surface growth rates. Therefore, the reduction in the concentration of soot precursors by thermal radiation leads to lowered soot growth. In addition to lowered precursor concentrations, the reduced temperature cause reduction in rate coefficients for different soot subprocesses.

The LES results demonstrate the strong impact of thermal radiation in the overall prediction of soot in turbulent flames. Therefore, soot models may require further improvement, and validation under non-adiabatic conditions to yield more accurate predictions. Note that the radiation-turbulence interactions are not included in the present formalism, which can further influence the soot formation characteristics. These aspects are left for future investigation.

Figure 7.29: Comparison between experimental (symbols) and numerical (line) data for mean and RMS of soot volume fraction profiles at the centerline for adiabatic and non-adiabatic cases.

Figure 7.30: Computed centerline profiles of mean A4 (a), and C_2H_2 (b) mass fraction for adiabatic and non-adiabatic conditions.
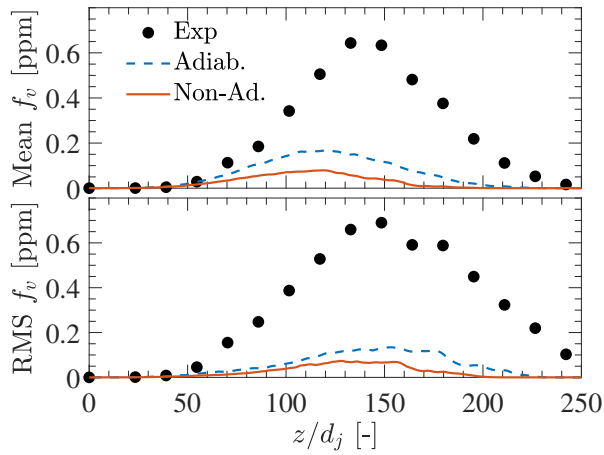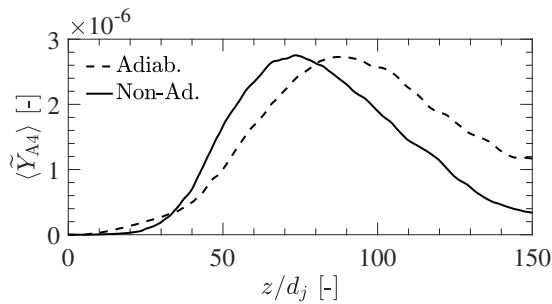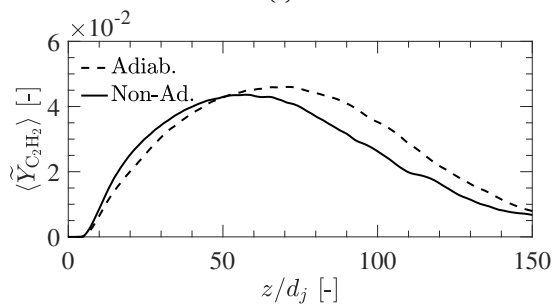
7.8   Concluding summary

This study presents two strategies based on the discrete sectional method coupled with FGM tabulated chemistry in the context of LES for the prediction of soot formation in turbulent non-premixed flames. The performance of two strategies for modeling soot source terms is assessed on a turbulent non-premixed jet flame with a focus on the prediction of soot formation and particle size distributions. The LES results for the gas phase and soot phase are compared against the available experimental data. Despite some discrepancies, the results for the soot phase show reasonable agreement with experimental results.

The LES study suggests that the soot source term closure in FGM-DSM coupling substantially influences the quantitative and qualitative prediction of soot formation in turbulent conditions. The observed differences in soot prediction for the investigated soot source-term models can be attributed to their capabilities in capturing unsteady chemical trajectories of soot formation, which evolve at a slower time scale than flame propagation. The computationally efficient model based on tabulated soot formation rates with a presumed PDF (probability density function) approach tends to yield good quantitative soot prediction, making it a promising tool to study soot production in light of industrial applications with LES. However, it was found that tabulating soot chemistry has limitations in capturing the transient evolution of soot. Therefore, the tabulated soot source term approach requires further improvements to meet limitations regarding capturing soot history effects. On the other end, the model which solves for the complete set of soot formation subprocesses provides a better qualitative description of soot formation and evolution. It is further observed that the separation of soot and gas phase terms only marginally impacts soot formation prediction for the run-time soot source term computation model in turbulent conditions.

The assessment of a computationally efficient approach based on the clustering of the soot sections was conducted for turbulent flames. The results showed that the clustering of soot sections, followed by reconstruction, can efficiently reproduce the soot formation and PSD evolution characteristics in turbulent flames predicted without the clustering of sections, making it a promising tool to study soot production in light of industrial applications. It is also observed that the inclusion of preferential diffusion effects in the flamelet calculation can significantly impact (by a factor of 2 in current LES) soot formation prediction in turbulent conditions and may lead to discrepancies in quantitative soot prediction. The use of non-unity Lewis number transport in flamelet calculations tends to yield better quantitative prediction of soot than the unity-Lewis approximation.

The effects of hydrogen addition to fuel on soot formation in turbulent conditions were studied. Similar to our earlier study on laminar flames, the soot formation is found to be reduced in the presence of hydrogen as a consequence of the reduction in soot precursor concentrations. Finally, the influence of non-adiabatic effects associated with thermal radiation on soot prediction was investigated. The quantitative

prediction of soot formation in turbulent flames is found to be lowered by factor 2 on the inclusion of thermal radiation. Compared to adiabatic conditions, the lowered concentration of soot precursors, and temperature in the non-adiabatic case leads to a reduction in the soot formation.

In summary, the present study demonstrates that the sectional soot model coupled with FGM chemistry is a feasible and efficient approach to predict soot production in turbulent flames. The results obtained using the LES-FGM-DSM framework in this study for turbulent non-premixed flames demonstrate both qualitative and quantitative comparability with the current state-of-the-art in the field. Additionally, the application of the LES-FGM-DSM strategy in combination with clustering has shown excellent accuracy in predicting soot in aero-engine model burner [248] as well as turbulent spray flames [229]. This highlights the attractiveness of the proposed LES framework as a modeling choice for reducing the computational cost of sooting flame calculations in industry-relevant conditions, while still maintaining state-of-the-art predictive capabilities.

Nevertheless, models accounting for subgrid-scale interactions of multi-physical phenomena (e.g. radiative heat transfer) may be useful for the improvement of the LES-FGM-DSM framework. Moreover, developing models to account for the non-linear effects (between soot and gas phase) in tabulated soot formation rates would be an important advancement in the current LES-FGM-DSM framework.

8

Conclusions and outlook

This final chapter offers a summary of the research work reported in the thesis, and the main conclusions are reviewed. In the next paragraphs, the main achievements and limitations of different tasks conducted in the course of fulfillment of this thesis are presented. In the end, future perspectives concerning the present work are discussed to highlight possible research directions which could favorably contribute to the understanding of soot formation and its mitigation from practical combustion systems.

8.1 Conclusions

Due to the harmful impacts of soot on health and the environment, controlling soot formation from practical combustion systems is a major challenge. To facilitate the design and development of efficient and clean combustion devices, a fundamental understanding of soot formation processes is required. In this context, high-fidelity, predictive numerical tools play a crucial role in the systematic investigation of various processes associated with soot production. Therefore, the primary goal of this thesis was to develop high-fidelity, computationally efficient numerical strategies for modeling soot formation in both laminar and turbulent flames and evaluate their predictive capabilities. To accomplish this goal, the present thesis comprised different tasks, which concern:

- The detailed modeling of soot formation in laminar flames with the sectional method

- The development of a computationally efficient framework for modeling soot formation with the sectional method and FGM tabulated chemistry

- The development of an LES framework for modeling soot formation in turbulent flames

These tasks and the most relevant findings obtained from their completion are summarized below:

In Chapter 2, the sectional soot model [98] was introduced and challenged for soot prediction in laminar non-premixed and premixed flames over a wide range of operating conditions. The soot modeling approach integrated with detailed chemistry provides good qualitative, as well as, quantitative agreement between experimental and computed soot quantities for laminar flames. The strain rate sensitivity of soot formation, dilution effects, pressure effects, unsteady effects, and radiation effects are well captured by the employed soot model despite several modeling assumptions (e.g., uni-variate description, no agglomeration, single PAH species, etc.). However, the predictive response of the soot model to premixed and non-premixed flames is found to be particularly sensitive to the treatment of the surface growth sub-process. Therefore, when considering combustion systems where multiple combustion regimes coexist, a consistent model for surface radical treatment would be instrumental.

Concerning future clean combustion systems, hydrogen is often perceived as a promising alternative to hydrocarbon fuels. In this context, the focus of Chapter 3 was to investigate the impact of adding hydrogen (H_2) to the fuel and water vapour (H_2O) to the oxidizer on soot formation in counterflow diffusion flames. Numerical results reveal that the hydrogen enrichment of fuel and addition of H_2O to the oxidizer reduces the soot formation through both chemical effects and dilution effects. The chemical effects of H_2 tend to suppress the H-abstraction reaction in the HACA surface growth mechanism as a consequence of increased molecular hydrogen concentration. For the addition of H_2O, the contribution of the chemical effect in the reduction of soot formation is found to be very small compared to the dilution effect. Simultaneous addition of H_2 and H_2O decreases soot formation compared to their separate addition for an identical dilution level, with very weak synergistic effects. Changes in rates of surface growth and coagulation processes, as a consequence of H_2 and H_2O addition, impact the overall soot particle size distribution (PSD), with the effect of the latter being stronger. The addition of H_2 and H_2O to the fuel and oxidizer, respectively, causes an increase in the number density of small-sized particles, and decreases the growth of larger particles, which leads to a reduction in the average soot particle size.

In practical environments, unsteady hydrodynamics introduces spatio-temporally fluctuating flow strain and curvature to the flames. Therefore, in Chapter 4 the response of soot formation to flame curvature was examined in counterflow flames under both steady and unsteady conditions. Detailed analysis using detailed kinetics and the sectional soot model showed that in the presence of curvature, the velocity of soot particles is significantly altered due to changes in the surface area along the flame. In flames with negative curvature (where the center of curvature is on the fuel-rich side of the flame front), the soot particle velocity is lower compared to that in a flat flame, resulting in an increased residence time in the soot formation zone and higher soot volume fractions. Positive curvature, on the other hand, has the opposite effect causing lowered soot concentration. This study also demonstrated that the response of soot in curved counterflow flames is strongly correlated to the differential transport of soot particles due to their high Schmidt numbers. For negative curvature, soot par-

ticles are differentially transported towards lower mixture fractions, which promotes their growth through surface reactions in the soot formation zone. When the flame is subjected to harmonic curvature fluctuations, the overall response of soot volume fraction is predominantly governed by the evolution of larger particles due to their large chemical time scales. With an increase in the imposed frequency, the soot formation gets attenuated leading to lower amplitudes of the induced oscillations and a phase lag. The response of soot becomes more complex when the flame is subjected to simultaneous strain rate and curvature fluctuations. In this case, the overall unsteady soot response under strain rate-curvature oscillations is determined by the locally adverse/favorable conditions encountered by the soot formation process during transient evolution. Although a direct correlation of these laminar flame findings to turbulent combustion was unexplored in this study, the analysis of unsteady curvature effects on soot formation provides valuable insights into the interaction between soot kinetics and fluid dynamics to guide further modeling efforts.

The sectional soot modeling approach enables the accurate description of the dynamics of soot particles without any complex closure models. However, its high computational cost makes the use of the sectional model restrictive for many practical applications. To facilitate the application of the sectional soot modeling approach to multi-dimensional flame simulations, the sectional soot model was combined with FGM tabulated chemistry. In Chapter 5, different approaches for coupling the FGM chemistry with the sectional soot model were evaluated for their accuracy of soot prediction and the overall CPU cost, using a range of conditions in a laminar flame configuration. The accuracy of soot prediction with FGM chemistry was found to be sensitive to the concentrations of PAH species tabulated in the model. An unaccounted consumption of PAH, originating from PAH-based processes, leads to significant overprediction of soot. The approach of including a contribution from soot nucleation during the flamelet computation stage performed better in terms of accuracy and computational time than the approach that solved an additional transport equation for PAH species to account for its consumption through soot formation. Numerical results reveal that the strategy of including the complete soot model during the flamelet computation reproduces the detailed chemistry solutions most accurately because it correctly incorporated the mass exchange between soot and gas chemistry. The approaches that solved transport equations for soot sections captured the unsteady dynamics of soot formation reasonably well. On the other hand, the approach, in which soot mass fractions are retrieved directly from the manifold is influenced by the mapping of sectional soot mass fractions in mixture fraction and progress variable space and thus fails to capture the unsteady soot formation. Computational time analysis indicates that the FGM-DSM modeling strategies can reduce the computational time by 1 to 2 orders of magnitude compared to detailed chemistry simulations.

In the aforementioned approaches, the CPU speedup was mainly due to the reduction of gas-phase kinetics, as the calculation of the soot source term remains computationally intensive. To address this, in Chapter 6 a novel approach called FGM-CDSM was

proposed for predicting soot formation in combustion simulations within the FGM-DSM framework. This model aims to investigate if fully tabulating and clustering the source terms can yield accurate predictions of global soot quantities and particle size distributions (PSD) within the FGM-DSM framework. Unlike conventional DSM, in FGM-CDSM, governing equations for soot mass fractions are solved for the clusters, by using a pre-computed lookup table with tabulated soot source terms from the flamelet manifold, while the original soot PSDF is re-constructed in a post-processing stage. The nonlinear dependence of different soot subprocesses on sectional soot mass fractions is not explicitly solved in the CFD calculation but is included in the flamelet computations. A comparative assessment of FGM-CDSM is conducted in laminar counterflow and coflow diffusion flames for its accuracy and computational performance. Numerical results reveal that the FGM-CDSM can favorably reproduce the global soot quantities and capture their dynamic response predicted by detailed kinetics with a good qualitative agreement. Compared to run-time soot source term computation, the FGM-CDSM approach based on soot source term tabulation in combination with clustering yields approximately an order of magnitude speed-up in computations. In the FGM-CDSM approach, the soot source terms are calculated for soot mass fractions (and other variables) in a steady state and stored in the manifold. Therefore, the chemical trajectories concerning the formation of soot from the gas phase to the steady state are not explicitly present in the FGM manifold. As a result, using the tabulated soot chemistry of FGM-CDSM for an essentially unsteady soot formation process will not be very accurate.

For the prediction of soot formation in turbulent flames, an LES formalism based on the sectional method and FGM chemistry was developed in Chapter 7. Two elementary modeling strategies were considered for describing soot formation rates, and their impact on soot prediction in turbulent non-premixed sooting flame was analyzed. These strategies concern: (1) *a-priori* tabulation of soot formation rates with presumed-PDF closure for sub-grid scale soot-turbulence interactions, and (2) run-time computation of soot formation rates without sub-grid scale STI model. The results for the soot phase show reasonable agreement with experimental results in terms of the magnitude, localization, and intermittency of soot. The computationally efficient model based on tabulated soot formation rates with a presumed PDF approach tends to predict several features of soot formation in turbulent flames well. However, it was found that tabulating soot chemistry has limitations in capturing the transient evolution of soot. In contrast, the model that solves for the complete set of soot formation subprocesses provides a better qualitative description of soot formation and evolution. The LES study is extended to evaluate the performance of the clustering method in turbulent flames. A good agreement is obtained between clustering and non-clustering-based solutions, indicating the promising capabilities of the FGM-CDSM approach to capture the qualitative and quantitative features of soot formation and PSD distribution under turbulent conditions with a significantly reduced number of transported soot variables. It is also observed that the inclusion of preferential diffusion effects in the flamelet calculation can significantly impact soot prediction in

turbulent conditions and may lead to discrepancies in quantitative soot prediction. The influence of hydrogen addition to fuel on soot formation is studied in turbulent conditions. Similar to laminar flames, the soot formation is reduced by hydrogen addition. The soot-inhibiting effect of hydrogen addition is primarily attributed to the reduction in the formation of soot precursors. The impact of radiative heat transfer on soot prediction is investigated using models based on the optically thin approximation. The thermal radiation significantly affected soot prediction in the investigated turbulent flame. The reduced concentration of soot precursors in non-adiabatic conditions leads to a lowered soot formation compared to adiabatic conditions.

In summary, the current work comprehensively addressed the challenges associated with different variants of the FGM-DSM framework in terms of soot prediction in laminar and turbulent conditions. The present study demonstrates that the sectional soot model coupled with FGM chemistry is a promising tool to predict soot production in industrial combustors for optimizing the development of clean engines and burners. In this context, the future perspective of this thesis can be highlighted as follows.

8.2   Outlook and recommendations

Although the sectional soot modeling approach employed in the present study is state-of-the-art, several improvements could be made. Concerning the soot formation sub-processes, the inclusion of multiple polycyclic aromatic hydrocarbons (PAHs) in the model (e.g. Ref. [27, 249]) for the nucleation process is expected to make the model more consistent with experimental observations. Additionally, improvements to the surface reaction/oxidation models with additional species, and the inclusion of steric factor expressions for surface radical sites, could be useful. The model could also be expanded to include soot agglomeration and fragmentation processes, which would improve the accuracy of the model in capturing soot particle dynamics and fractal structure of particles. Using more advanced models for radiative heat transfer from gas and soot particles would also improve the prediction of soot properties.

In the current work, soot formation in ethylene-fueled flames is primarily considered during different fundamental studies and various stages of soot model development. However, the application of this soot modeling approach can be extended to the combustion of higher-hydrocarbon fuels, including kerosene and other surrogates. A recent LES study by Bao et al. [229] showed promising agreement between FGM-CDSM results and experimental measurements in predicting soot formation in n-dodecane spray flames. Nevertheless, before applying the soot modeling framework to practical fuels, it is necessary to calibrate the model and extensively validate the sectional method in combination with detailed gas-phase kinetics. The computationally efficient strategies discussed in this work are expected to perform as demonstrated regardless of the fuel type. However, a dedicated investigation into the application of the FGM-DSM approach in predicting soot formation in laminar and turbulent flames of complex fuels is an important future step for this research.

This thesis investigated the computationally efficient coupling of the FGM with the sectional soot model. In this method (referred to as FGM-CDSM), the non-linear dependence of soot source terms on the soot variables was considered only for the soot consumption rates by linearization approach. The accuracy of the FGM-CDSM approach could be further improved by developing new models or by extending the linearization model used to account for the non-linear effects of the soot production rate.

The large eddy simulation framework developed in this work for the FGM-DSM coupling does not consider subgrid-scale interactions between soot and turbulence. Including subgrid-scale soot-turbulence interaction models in the LES, the framework would be an important extension to investigate their impact on overall soot prediction. New models discussed in (e.g. Ref. [66, 73, 89]) can be explored for the treatment of soot-turbulence interactions in turbulent flames. Additionally, the inclusion of models accounting for sub-grid scale interactions between thermal radiation and turbulence [250] would be useful for practical applications of the LES framework in the future.

This study investigated the soot-inhibiting effects of hydrogen addition in laminar and turbulent flames. Hydrogen and PAH species exhibit strong non-unity Lewis number effects impacting soot formation prediction in simulations. Therefore, implementing preferential diffusion effects into the FGM method for LES application would also be an essential extension of the present work. Finally, the inclusion of curvature effects in the FGM manifold and an evaluation of their impact on soot formation in turbulent flames would be an interesting progressive step in future work.

The reliable predictive tools for soot formation in practical combustion systems are crucial in the development and optimization of clean combustion technologies. The FGM-DSM modeling framework explored in the current work is a promising approach to achieving this goal. Hence, investigating the application of this framework to industry-relevant burner configurations could provide valuable insights into the behavior of soot formation in practical combustion systems, which is the broad direction in the future outlook.

A

Assessment of chemical kinetic mechanism

The performance of the sectional model in soot prediction is strongly influenced by the description of gas phase precursors. Therefore the choice of kinetic scheme plays a crucial role in the overall soot modeling. In this section, a comparison of kinetic mechanisms for the prediction of key gas phase species is presented. Three chemical mechanisms from the literature describing ethylene (C2) oxidation pathways and PAHs up to 4 rings are considered for this assessment. The details of these mechanisms are summarized in Table A.1.

The target flame considered for this assessment is laminar counterflow flame experimentally investigated by Jiang et al. [252]. The fuel stream is pure ethylene, while the oxidizer streams consisted of a binary mixture of O_2/N_2 with a 0.18/0.82 molar ratio. Both fuel and oxidizer streams are maintained at 298 K temperature and atmospheric pressure with a nozzle separation distance of 8 mm. The fuel stream velocity is 18.98 cm/s and oxidizer stream is maintained at 26.25 cm/s. 1-D steady-state simulations (without soot chemistry) are carried out with the CHEM1D [108] code, using a mixture-averaged transport model for species diffusion. The velocity corrections are included in the boundary conditions of the strain rate equation (Eq. 2.85) to account for the two-dimensional effects of the counterflow burner in the 1-D calculations.

Computed profiles of temperature and axial velocity are presented in Fig. A.1 along with the measured data. The agreements between the measured and computed pro-

Table A.1: Brief description of the evaluated kinetic mechanisms.

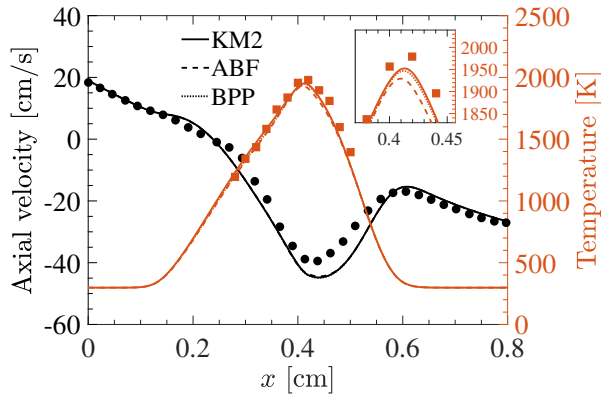| Name	Size (Sp./Reac.)	Comments	Reference
ABF	101/544	C2 hydrocarbons with PAH prediction up to A4	Appel et al. [23]
BPP	148/928	C2-C4 hydrocarbons with PAH prediction up to A4	Blanquart et al. [251]
KM2	202/1351	C1-C4 hydrocarbons with PAH prediction up to A7	Wang et al. [105]

Figure A.1: Measured (symbols) and computed (lines) profiles of temperature and axial velocity for different mechanisms.

files obtained for the different mechanisms are satisfactory. Compared to ABF, the temperatures predicted by BPP and KM2 match closely with the measurements. The thermochemical structures of flame, characterized by mole fractions of major combustion products and aromatic species, are compared in Fig. A.2. Compared to measurements, no substantial differences are observed in the prediction of CO and CO_2 mole fractions for all the kinetic schemes. On the other hand, concentrations of acetylene (C_2H_2) and H_2, species relevant in HACA surface reactions, are well captured by the KM2 mechanism compared to ABF and BPP. In addition to major combustion species, the mole fractions of vinylacetylene (C_4H_4) along with aromatic compounds benzene (A1) and naphthalene (A2) predicted by KM2 show close agreement with
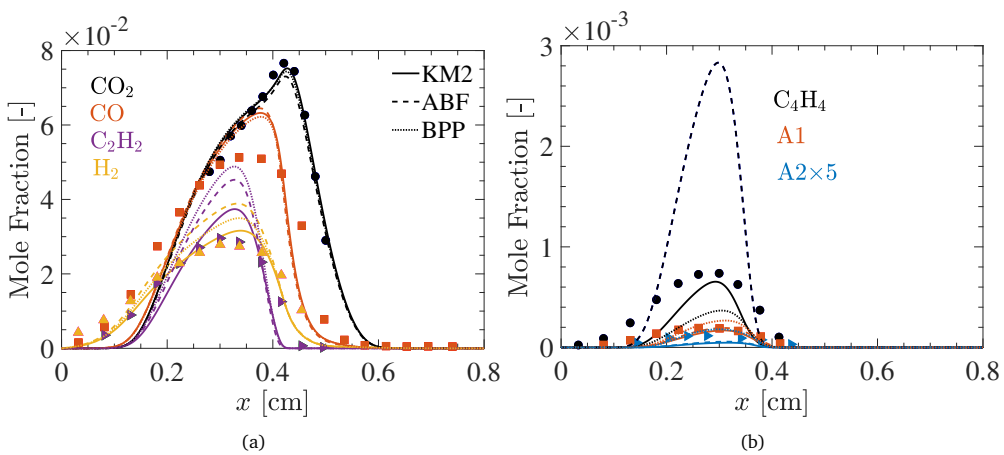
Figure A.2: Measured (symbols) and computed (lines) mole fraction profiles of major species including CO_2, CO, C_2H_2, H_2 (a), and minor species including C_4H_4, A1 and A2 (b).

234

measurements as compared to the other two schemes. Moreover, in the work of Rodrigues [99], a good agreement is obtained in ethylene premixed flames for PAHs evolution prediction compared to several other kinetic schemes. Given the good predictive accuracy, as well as the moderate size computational cost, the KM2 mechanism is selected (unless specifically mentioned) in the present study for simulations of soot formation in ethylene flames. Additional results concerning the assessment of the KM2 scheme can be found elsewhere [98, 105].

B

Sensitivity study of DSM parameters

The sensitivity of the sectional soot model introduced in Chapter 2 to different model parameters is presented here. The baseline laminar counterflow flame studied by Wang et al. [27] is considered for the sensitivity study. The flame consists of a pure C_2H_4 fuel reacting with an oxidizer composed of 25% of O_2 and 75% of N_2 (on a molar basis). The reactant nozzles are separated with a distance of 8 mm. The flow velocities for both the fuel and oxidizer streams are set at 20 cm/s.

B.1   Sensitivity to number of sections

The sensitivity of the sectional soot model to the number of sections in a laminar counterflow flame is presented in Fig. B.1. It can be observed in Fig. B.1 maximum soot volume fraction approximately relaxes to an asymptotic solution with 60 sections. This choice for the number of sections is optimal enough to obtain an estimation of the soot volume fraction and number density with negligible errors when compared with calculations based on more sections. Therefore 1-D flame computations in the present work have been performed with 60 sections.
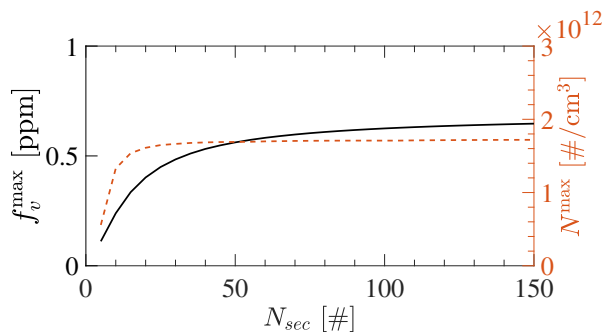

Figure B.1: Impact of the number of sections used in the sectional method for the prediction of peak soot volume fraction and maximum number density.

B.2   Sensitivity to the size of largest particle

The other important parameter that needs to consider in DSM is the volume of the largest particle size. In theory, the largest particle in the PSDF can be infinitely large in size. However, in the numerical simulation, it is essential to define a finite limit for PSD. Hence, assumptions are made to clip the PSD by defining the volume of the largest modeled particle, $V_{\max}$, in the soot model. This large $V_{\max}$ ensures that soot mass will no longer accumulate in the last section. The effect of the $V_{\max}$ on f_v profiles is shown in Fig. B.2. The computed peak soot volume fraction is found to be not very sensitive to the choice of the upper bound $V_{\max}$. In the computations carried out in the present work, the largest $V_{\max}$ is assumed to be 5.23×10^{-10} cm^3, which is equivalent to the volume of 4.88×10^{13} carbon atoms.
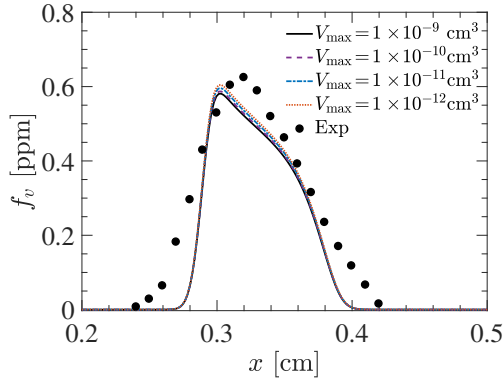
Figure B.2: Sensitivity of computed soot volume fraction to the size of the largest soot particle ($N_{sec}=60$).

B.3   Sensitivity to surface radical treatment

The important soot formation sub-process contributing to soot mass is HACA-based surface growth. Thus, the treatment of surface radicals during the C_2H_2 addition stage of the HACA mechanism is critical for the prediction of surface growth rates. The modeling parameter ξ_{dc} is proposed by Hoerlle & Pereira [94] with an assumption that the radical sites in the HACA surface growth mechanism are neither depleted nor conserved. To analyze the impact of the radical treatment parameter on the soot prediction, the profiles of soot volume fraction obtained are compared for several ξ_{dc} values in Fig. B.3. The results suggest that the prediction of soot volume fraction is highly sensitive to the ξ_{dc} values. It can be observed that the assumption of completely depleted surface sites tends to underpredict the soot content in the current counterflow flame. Although ξ_{dc} does not have a definite physical validity, the calibration study [94] suggested that the ξ_{dc} show significant dispersion ranging from 0.5-0.9 for counterflow ethylene flames.

Figure B.3: Sensitivity of computed soot volume fraction to the surface radicals treatment parameter.
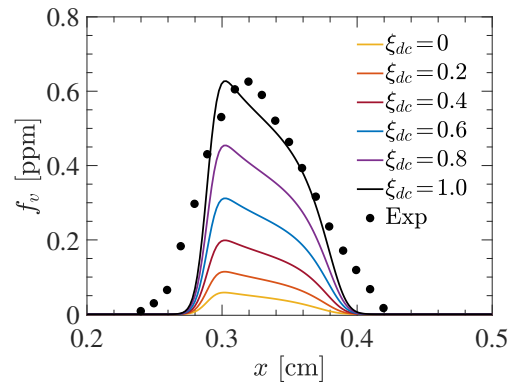
C

Sectional model implementation in Alya

For the numerical prediction of soot formation in the multi-dimensional flames sectional soot model is integrated with the multi-physics CFD code, Alya [219] developed at the Barcelona Supercomputing Centre. Alya is based on the finite element spatial discretization method of reacting flow equations. The verification of the sectional model implementation in Alya is presented here for detailed chemistry-based calculations.

C.1   Numerical method

In the Alya solver, a conservative finite element convective scheme with low-dissipation characteristics [241] is employed for the discretization strategy. The low-Mach number approximation of the Navier-Stokes equations is utilized in the weak form. Pressure stabilization is introduced in the continuity equation using a non-incremental fractional-step method that is modified to accommodate variable density effects. No additional stabilization is applied to the mass and momentum conservation equations. For the time integration of the discretized governing equations, an explicit 3rd-order Runge-Kutta temporal scheme is used. The fractional step method is incorporated within the Runge-Kutta steps for the time-marching of the velocity field. The solution time step is determined as the minimum of the time step for the momentum equations and scalar transport equations. The self-adaptive strategy [253] is used for the momentum equations, while the standard Courant-Friedrichs-Lewy (CFL) condition is applied for the scalar equations. Further details regarding the numerical method and solution algorithm can be found in Both et al. [241].

C.2   Coupling with finite rate chemistry solver

In Alya, the Strang splitting strategy is employed for the transport of chemical species with a finite-rate chemistry model. In this strategy, the non-linear stiff chemical source term is treated separately using an implicit numerical ODE solver, and the non-stiff advection and the diffusion term, are treated explicitly. The transport equation for the mass fraction of chemical species including gas-phase consumption through soot

formation subprocesses ($\dot{\omega}_k^s$) can be written as:

$$\frac{\partial(\rho Y_k)}{\partial t} = \underbrace{-\nabla \cdot (\rho \boldsymbol{u} Y_k)}_{C(\boldsymbol{Y_k})} \underbrace{-\nabla \cdot (\rho \boldsymbol{V}_k Y_k)}_{D(\boldsymbol{Y_k})} + \underbrace{\dot{\omega}_k}_{S(\boldsymbol{Y_k})} + \underbrace{\dot{\omega}_k^s}_{S_s(\boldsymbol{Y_k})} \quad \forall \quad k \in [1, N_s] \tag{C.1}$$

where $C(\boldsymbol{Y_k})$, $D(\boldsymbol{Y_k})$, $S(\boldsymbol{Y_k})$, are, respectively, the symbolic notations for the advection, diffusion, and chemical source terms for a gas-phase specie k. The term $S_s(\boldsymbol{Y_k})$ represents the mass-exchange rate between the soot and gas phase during different subprocesses. Similarly, the transport equation for sectional soot mass fraction can be arranged as:

$$\frac{\partial(\rho Y_{s,i})}{\partial t} = \underbrace{-\nabla \cdot (\rho \boldsymbol{u} Y_{s,i})}_{C(\boldsymbol{Y_s})} + \underbrace{\nabla \cdot (\rho D_{s,i} \nabla Y_{s,i})}_{D(\boldsymbol{Y_s})} + \underbrace{\rho_s \dot{Q}_{s,i}}_{S(\boldsymbol{Y_s})} \underbrace{-\nabla \cdot (\rho \, \boldsymbol{V_T} Y_{s,i})}_{S_T(\boldsymbol{Y_s})} \quad \forall \quad i \in [1, N_{sec}]$$

$$\tag{C.2}$$

where $C(\boldsymbol{Y_s})$, $D(\boldsymbol{Y_s})$, $S(\boldsymbol{Y_s})$, $S_T(\boldsymbol{Y_s})$ denote advection, diffusion, soot source, and thermophoretic diffusion term, respectively. In the present splitting algorithm, $C(\boldsymbol{Y_k})$, $D(\boldsymbol{Y_k})$ (also referred to as transport terms), and $S_s(\boldsymbol{Y_k})$ terms from species transport Eq. C.1 are integrated with explicit Runge-Kutta 3rd order temporal discretization scheme, while reaction term $S(\boldsymbol{Y_k})$ is integrated with stiff implicit solver CVODE solver during the temporal marching. The time-step size for the transport of the chemical species is determined by the CFL number based only on the flow. The reacting flow validation for finite rate chemistry and details of numerical implementation of the splitting strategy can be found in [254]. Contrary to species transport, the sectional soot transport equations are treated without the Strang-splitting strategy. This is because the chemical timescales of soot formation subprocesses are large and are often comparable to the flow time scales. This enables the solver to take large time steps during the solution of soot equations. In the present framework, all the terms on the right-hand side of soot transport Eq. C.2 are temporally integrated with the explicit Runge-Kutta 3rd-order accurate scheme.

For the verification of the sectional model implementation algorithm in Alya, the laminar counterflow diffusion flame studied by Wang et al. [27] is simulated. The baseline flame consists of a pure C_2H_4 fuel reacting with an oxidizer composed of 25% of O_2 and 75% of N_2 (on a molar basis). The reactant nozzles are separated with a distance of 8 mm. The flow velocities for both the fuel and oxidizer streams are set at 20 cm/s and 300 K inlet temperature. Numerical simulations are performed on a 2-D computational domain using the KM2 [105] kinetic scheme. The diffusion transport of chemical species is described using the mixture-averaged transport model. The reference simulation for this flame is conducted with the CHEM1D code considering the same soot model parameters.

A steady-state temperature field and comparison of centerline temperature against its CHEM1D counterpart are presented in Fig. C.1. A very good agreement with the
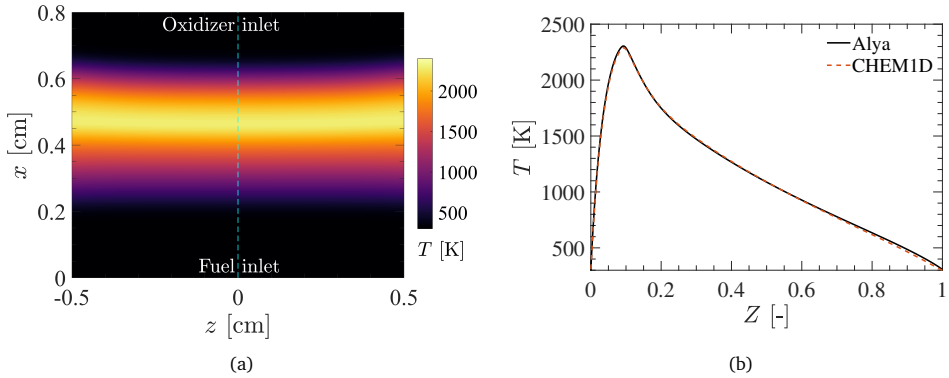
Figure C.1: Representation of the temperature field (a), and comparison of centerline temperature for Alya and CHEM1D solver in composition space (b) in an ethylene counterflow diffusion flame.
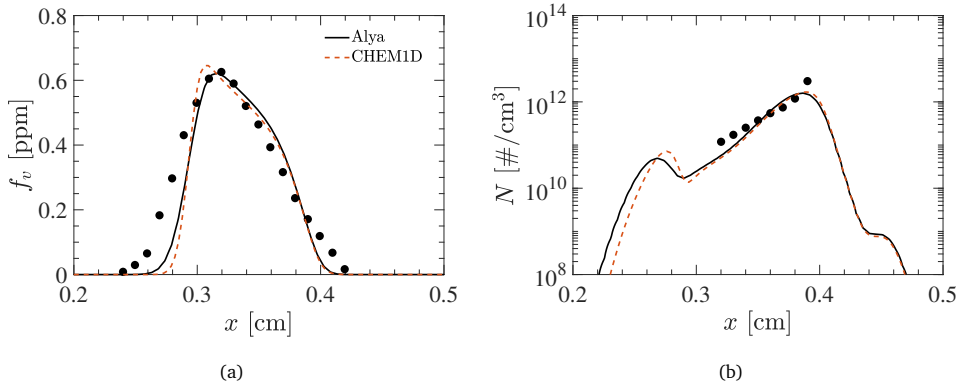
Figure C.2: Comparisons between Alya and CHEM1D solutions for soot volume fraction (a), and soot number density (b). Measurements are shown with symbols.

reference solution can be observed for the temperature, ensuring the accuracy of the flame structure before the comparison of soot profiles. The computed profiles (on centerline) of soot volume fraction and number density are compared in Fig. C.2 for Alya and CHEM1D solver. Besides, experimental measurements are also plotted for reference. In general, Alya solutions show a good agreement with the CHEM1D counterparts for soot quantities, only small differences are found. This verifies the code for its application to soot prediction in reacting flow simulations.

D

Radiative heat transfer

D.1 Radiative heat transfer model

The thermal radiation model employed in the present work is based on grey-gas approximation (neglecting the wave number dependence), and the optically thin limit (neglecting radiation absorption and scattering) for the medium. Accordingly, the radiation source term is included in the enthalpy conservation equation. The radiation source term for gas-phase is given by:

$$\dot{\mathcal{Q}}_{\mathrm{rad}} = -4\sigma \left[\sum_i p_i \alpha_{p,i} \right] \left(T^4 - T_a^4 \right) \tag{D.1}$$

where σ is the Stefan-Boltzmann constant ($5.669 \times 10^{-8}\,\mathrm{Wm^{-2}K^{-4}}$), p_i is the partial pressure (atm) and $\alpha_{p,i}$ is the extinction coefficient for species i; T_a is the ambient temperature (298 K). The extinction coefficients $\alpha_{p,i}$ for species CO_2, H_2O are calculated from:

$$\log \left(\frac{\alpha_{p,i}}{\alpha_{p,i}^{\mathrm{ref}}} \right) = \sum_{n=0}^{6} a_{i,n} \left(\frac{T}{300} \right)^n \tag{D.2}$$

where $\alpha_{p,i}^{\mathrm{ref}} = 1\,\mathrm{atm^{-1}}$ and $a_{i,n}$ coefficients are taken from Ref. [128]. Similarly, extinction coefficients for CO and CH_4 species are calculated from:

$$\alpha_{p,i} = \sum_{n=0}^{4} b_{i,n} T^n \tag{D.3}$$

where $b_{i,n}$ values are taken from Ref. [129].

D.2 Implementation in Alya solver

The radiative heat transfer model is implemented in Alya solver to account for non-adiabatic effects in combustion simulations. In the context of FGM chemistry, two
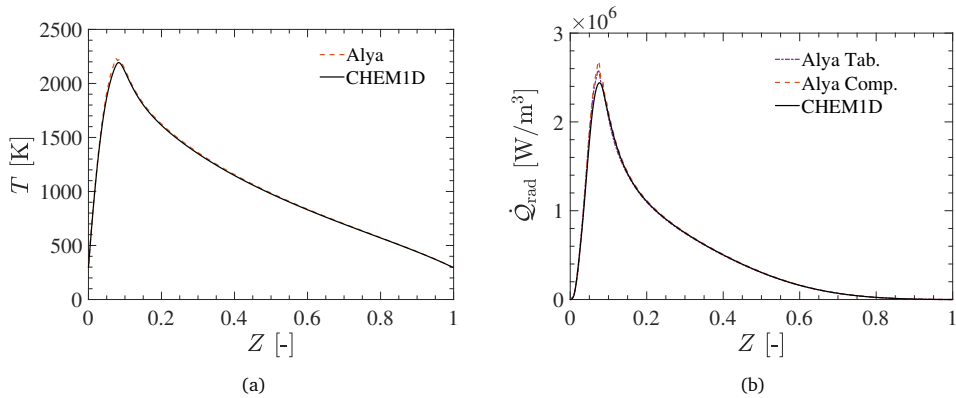
Figure D.1: Comparison of the temperature (a), and radiative source term (b) for Alya and CHEM1D solver in an ethylene counterflow diffusion flame.

strategies are implemented. The First strategy involves tabulation of $\dot{Q}_{rad}$ in the manifold, while the second strategy concern run-time computation of $\dot{Q}_{rad}$ using tabulated species and computed temperature. For the verification of implementation, the ethylene-air laminar counterflow diffusion flame described in Appendix C is considered. The counterflow flame is simulated with FGM chemistry (without the soot model) by including radiative heat transfer. The FGM manifold is generated using flamelets with radiative heat loss. The profiles of temperature and radiative heat source term obtained with Alya code are compared against corresponding CHEM1D flamelet in Fig. D.1. A good agreement can be observed between Alya and CHEM1D results. Furthermore, the tabulated source term and computed source term profiles match closely, which further verifies the implementation.

E

Presumed PDF model

In Chapter 7, the β-PDF model is used to account for the sub-grid scale turbulence-chemistry interactions. In this section, the details of the β-PDF model and the algorithm for the FGM tabulation are presented.

E.1   Beta (β) probability density function

The probability density function (PDF) of the beta distribution, for $0 \le x \le 1$, and shape parameters $\alpha, \beta > 0$, is a power function of the variable x and of its reflection, $(1 - x)$ as follows:

$$\begin{aligned} p(x; \alpha, \beta) &= \frac{\Gamma(\alpha + \beta)}{\Gamma(\alpha)\Gamma(\beta)} \, x^{\alpha-1}(1-x)^{\beta-1} \\ &= \frac{1}{B(\alpha, \beta)} \, x^{\alpha-1}(1-x)^{\beta-1} \end{aligned} \tag{E.1}$$

with $B(\alpha, \beta)$ the Beta function, which acts as a normalization constant to ensure that the total probability is 1.

E.2 β-PDF integration

To compute the mean of a variable $f(x)$ for a given beta distribution of x with parameters α and β, the following integral has to be computed

$$\bar{f} = \int_0^1 f(x) \, p(x; \alpha, \beta) \, dx \tag{E.2}$$

This integral can be approximated numerically for a discrete representation $f_i = f(x_i)$ of the variable f on mesh points x_i. As $p(x)$ is singular at $x = 0$ and $x = 1$ for $\alpha < 1$ and $\beta < 1$ respectively, numerical evaluation and integration of the integrand $f(x)p(x)$ is not straightforward. To avoid this singularity, Eq. (E.2) is approximated with a

weighted sum of the values at the mesh points

$$\bar{f} = \sum_i w_i f_i \tag{E.3}$$

where w_i are the weights. The function $f(x)$ can be approximated by using linear interpolation, resulting in a piecewise linear function. In each interval $x \in [x_i, x_{i+1}]$, this gives

$$f(x) = f_i + (x - x_i)\frac{f_{i+1} - f_i}{x_{i+1} - x_i} = a_i + b_i x \tag{E.4}$$

with

$$a_i = f_i - x_i \frac{f_{i+1} - f_i}{x_{i+1} - x_i} = \frac{x_{i+1}}{x_{i+1} - x_i} f_i - \frac{x_i}{x_{i+1} - x_i} f_{i+1} \tag{E.5}$$

$$b_i = \frac{f_{i+1} - f_i}{x_{i+1} - x_i} = \frac{-1}{x_{i+1} - x_i} f_i + \frac{1}{x_{i+1} - x_i} f_{i+1} \tag{E.6}$$

The integral (E.2) can then be written as the sum of the integrals over each interval

$$\bar{f} = \sum_{i=1}^{n-1} \int_{x_i}^{x_{i+1}} (a_i + b_i x)\, p(x; \alpha, \beta)\, dx \tag{E.7}$$

where n is the number of mesh points. Note that $x_1 = 0$, $x_n = 1$, and $x_{i+1} > x_i$. Each part of the sum can then be written as:

$$\int_{x_i}^{x_{i+1}} (a_i + b_i x)\, p(x; \alpha, \beta)\, dx =$$

$$a_i \int_{x_i}^{x_{i+1}} p(x; \alpha, \beta)\, dx + b_i \int_{x_i}^{x_{i+1}} x\, p(x; \alpha, \beta)\, dx \tag{E.8}$$

The two terms on the right-hand side can be expressed in terms of the cumulative distribution function P, namely

$$a_i \int_{x_i}^{x_{i+1}} p(x; \alpha, \beta) =$$

$$a_i \left[P(x_{i+1}; \alpha, \beta) - P(x_i; \alpha, \beta) \right] = a_i A_i \tag{E.9}$$

and

$$b_i \int_{x_i}^{x_{i+1}} x\, p(x; \alpha, \beta) =$$

$$b_i \frac{\alpha}{\alpha + \beta} \left[P(x_{i+1}; \alpha + 1, \beta) - P(x_i; \alpha + 1, \beta) \right] = b_i B_i \tag{E.10}$$

Using these results, substituting (E.5) and (E.6), and gathering the terms with f_i and f_{i+1}, equation (E.7) becomes

$$\bar{f} = \sum_{i=1}^{n-1} \frac{A_i x_{i+1} - B_i}{x_{i+1} - x_i} f_i + \frac{B_i - A_i x_i}{x_{i+1} - x_i} f_{i+1} \tag{E.11}$$

$$= \sum_{i=1}^{n-1} \frac{A_i x_{i+1} - B_i}{x_{i+1} - x_i} f_i + \sum_{i=2}^{n} \frac{B_{i-1} - A_{i-1} x_{i-1}}{x_i - x_{i-1}} f_i \tag{E.12}$$

$$= \sum_{i=1}^{n} w_i f_i \tag{E.13}$$

with

$$w_i = \begin{cases} \dfrac{A_1 x_2 - B_1}{x_2 - x_1} & \text{if } i = 1 \\[2ex] \dfrac{A_i x_{i+1} - B_i}{x_{i+1} - x_i} + \dfrac{B_{i-1} - A_{i-1} x_{i-1}}{x_i - x_{i-1}} & \text{if } i = 2, \ldots, n-1 \\[2ex] \dfrac{B_{n-1} - A_{n-1} x_{n-1}}{x_n - x_{n-1}} & \text{if } i = n \end{cases} \tag{E.14}$$

These weights can be calculated for given values of α and β, and are independent of the variable f that is integrated. Therefore, they can be stored and reused.

The current derivation was done for a piecewise linear approximation of $f(x)$. Since all other operations are exact, the error is of second order in the mesh spacing. Higher-order methods can be derived by using higher-order polynomial approximations of $f(x)$.

Integration of multivariate functions with beta distributions of the independent variables is performed by subsequently integrating over each variable. For a bi-variate function $f(x,y)$, the mean can be found for instance by evaluating the following integral:

$$\bar{f} = \int_0^1 \int_0^1 f(x,y) \, p(x; \alpha_x, \beta_x) \, dx \, p(y; \alpha_y, \beta_y) \, dy \tag{E.15}$$

Applying the same procedure as discussed above results in the numerical approximation

$$\bar{f} = \int_0^1 \sum_i w_i f(x_i, y) \, p(y; \alpha_y, \beta_y) \, dy \tag{E.16}$$

$$= \sum_j v_j \sum_i w_i f(x_i, y_j) \tag{E.17}$$

where v_j are the weight coefficients for the integration in y-direction.

Bibliography

[1] IEA, "Key world energy statistics 2021", *World Energy Outlook 2021*, https://www.iea.org/reports/key-world-energy-statistics-2021. (*p.* 1)

[2] Oberdörster, G., Sharp, Z., Atudorei, V., Elder, A., Gelein, R., Kreyling, W., Cox, C., "Translocation of inhaled ultrafine particles to the brain", *Inhalation toxicology* 16:437–445 (2004). (*p.* 2)

[3] Baird, W.M., Hooven, L.A., Mahadevan, B., "Carcinogenic polycyclic aromatic hydrocarbon-dna adducts and mechanism of action", *Environmental and Molecular Mutagenesis* 45:106–114 (2005). (*p.* 2)

[4] Haynes, B.S., Wagner, H.G., "Soot formation", *Progress in Energy and Combustion Science* 7:229–273 (1981). (*p.* 2, 3, 56)

[5] ICAO, "The landing and take-off particulate matter standards for aircraft gas turbine engines", *Environmental Report 2019*, https://www.icao.int/environmental-protection/pages/envrep2019.aspx. (*p.* 2, 3)

[6] EEA, "Regulation (EC) no 715/2007 of the european parliament and of the council of 20 june 2007 on type approval of motor vehicles with respect to emissions from light passenger and commercial vehicles (euro 5 and euro 6)", *Report 2020*, https://eur-lex.europa.eu/legal-content/EN/TXT/?uri=CELEX%3A02007R0715-20200901. (*p.* 2)

[7] Frenklach, M., "Reaction mechanism of soot formation in flames", *Physical Chemistry Chemical Physics* 4:2028–2037 (2002). (*p.* 4)

[8] Wang, Y., Chung, S.H., "Soot formation in laminar counterflow flames", *Progress in Energy and Combustion Science* 74:152–238 (2019). (*p.* 4, 37, 55, 56)

[9] Valencia, S., Ruiz, S., Manrique, J., Celis, C., Figueira da Silva, L.F., "Soot modeling in turbulent diffusion flames: review and prospects", *Journal of the Brazilian Society of Mechanical Sciences and Engineering* 43:1–24 (2021). (*p.* 4)

[10] Frenklach, M., Wang, H., "Detailed mechanism and modeling of soot particle formation", *Soot Formation in Combustion, Mechanism and Models*, Springer, pp. 165–192 (1994). (*p.* 4, 5, 6, 8, 27)

[11] Shukla, B., Koshi, M., "A highly efficient growth mechanism of polycyclic aromatic hydrocarbons", *Physical Chemistry Chemical Physics* 12:2427–2437 (2010). (*p.* 4)

[12] Raj, A., Sander, M., Janardhanan, V., Kraft, M., "A study on the coagulation of polycyclic aromatic hydrocarbon clusters to determine their collision efficiency", *Combustion and Flame* 157:523–534 (2010). (*p.* 4)

[13] Richter, H., Howard, J.B., "Formation of polycyclic aromatic hydrocarbons and their growth to soot—a review of chemical reaction pathways", *Progress in Energy and Combustion science* 26:565–608 (2000). (*p.* 4, 9)

[14] Frenklach, M., Wang, H., "Detailed modeling of soot particle nucleation and growth", *Symposium (International) on Combustion* 23:1559–1566 (1991). (*p.* 4, 5, 6, 7, 8, 27, 64, 67, 115)

[15] Mercier, X., Carrivain, O., Irimiea, C., Faccinetto, A., Therssen, E., "Dimers of polycyclic aromatic hydrocarbons: the missing pieces in the soot formation process", *Physical Chemistry Chemical Physics* 21:8282–8294 (2019). (*p.* 4, 6)

[16] Faccinetto, A., Irimiea, C., Minutolo, P., Commodo, M., D'anna, A., Nuns, N., Carpentier, Y., Pirim, C., Desgroux, P., Focsa, C., et al., "Evidence on the formation of dimers of polycyclic aromatic hydrocarbons in a laminar diffusion flame", *Communications Chemistry* 3:1–8 (2020). (*p.* 4, 6)

[17] Wang, H., "Formation of nascent soot and other condensed-phase materials in flames", *Proceedings of the Combustion Institute* 33:41–67 (2011). (*p.* 4)

[18] Chung, S.H., Violi, A., "Nucleation of fullerenes as a model for examining the formation of soot", *The Journal of Chemical Physics* 132:174502 (2010). (*p.* 4)

[19] D'Anna, A., "Combustion-formed nanoparticles", *Proceedings of the Combustion Institute* 32:593–613 (2009). (*p.* 4, 7)

[20] D'Anna, A., Sirignano, M., Kent, J., "A model of particle nucleation in premixed ethylene flames", *Combustion and Flame* 157:2106–2115 (2010). (*p.* 4)

[21] Johansson, K., Head-Gordon, M., Schrader, P., Wilson, K., Michelsen, H., "Resonance-stabilized hydrocarbon-radical chain reactions may explain soot inception and growth", *Science* 361:997–1000 (2018). (*p.* 4, 7)

[22] Frenklach, M., "On surface growth mechanism of soot particles", *Symposium (International) on Combustion* 26:2285–2293 (1996). (*p.* 5)

[23] Appel, J., Bockhorn, H., Frenklach, M., "Kinetic modeling of soot formation with detailed chemistry and physics: laminar premixed flames of C2 hydrocarbons", *Combustion and Flame* 121:122–136 (2000). (*p.* 5, 6, 7, 27, 28, 60, 169, 233)

[24] Mauss, F., Schäfer, T., Bockhorn, H., "Inception and growth of soot particles in dependence on the surrounding gas phase", *Combustion and Flame* 99:697–705 (1994). (*p.* 5)

[25] Hwang, J., Chung, S., "Growth of soot particles in counterflow diffusion flames of ethylene", *Combustion and Flame* 125:752–762 (2001). (*p.* 5, 7, 34, 85)

[26] Blanquart, G., Pitsch, H., "Analyzing the effects of temperature on soot formation with a joint volume-surface-hydrogen model", *Combustion and Flame* 156:1614–1626 (2009). (*p.* 5, 9, 22)

[27] Wang, Y., Raj, A., Chung, S.H., "Soot modeling of counterflow diffusion flames of ethylene-based binary mixture fuels", *Combustion and Flame* 162:586–596 (2015). (*p.* 5, 6, 7, 32, 33, 35, 39, 59, 85, 123, 159, 231, 237, 242)

[28] Eaves, N.A., Dworkin, S.B., Thomson, M.J., "Assessing relative contributions of PAHs to soot mass by reversible heterogeneous nucleation and condensation", *Proceedings of the Combustion Institute* 36:935–945 (2017). (*p.* 5)

[29] Fenimore, C.P., Jones, G.W., "Oxidation of soot by hydroxyl radicals", *The Journal of Physical Chemistry* 71:593–597 (1967). (*p.* 6)

[30] Von Gersum, S., Roth, P., "High temperature oxidation of soot particles by O atoms and OH radicals", *Journal of Aerosol Science* 21:S31–S34 (1990). (*p.* 6)

[31] Stanmore, B.R., Brilhac, J.F., Gilot, P., "The oxidation of soot: a review of experiments, mechanisms and models", *carbon* 39:2247–2268 (2001). (*p.* 6)

[32] Roth, P., Brandt, O., Von Gersum, S., "High temperature oxidation of suspended soot particles verified by CO and CO_2 measurements", *Symposium (International) on Combustion* 23:1485–1491 (1991). (*p.* 6, 7)

[33] Matarrese, R., Castoldi, L., Lietti, L., "Oxidation of model soot by NO_2 and O_2 in the presence of water vapor", *Chemical Engineering Science* 173:560–569 (2017). (*p.* 6, 7)

[34] Sirignano, M., Kent, J., D'Anna, A., "Further experimental and modelling evidences of soot fragmentation in flames", *Proceedings of the Combustion Institute* 35:1779–1786 (2015). (*p.* 6)

[35] Netzell, K., Lehtiniemi, H., Mauss, F., "Calculating the soot particle size distribution function in turbulent diffusion flames using a sectional method", *Proceedings of the Combustion Institute* 31:667–674 (2007). (*p.* 6, 9, 20, 23, 115, 116, 151)

[36] Aubagnac-Karkar, D., Michel, J.B., Colin, O., Vervisch-Kljakic, P.E., Darabiha, N., "Sectional soot model coupled to tabulated chemistry for diesel RANS simulations", *Combustion and Flame* 162:3081–3099 (2015). (*p.* 6, 9, 116, 152, 181, 188)

[37] Salenbauch, S., Cuoci, A., Frassoldati, A., Saggese, C., Faravelli, T., Hasse, C., "Modeling soot formation in premixed flames using an extended conditional quadrature method of moments", *Combustion and Flame* 162:2529–2543 (2015). (*p.* 6, 9, 151)

[38] Charest, M.R., Gülder, Ö.L., Groth, C.P., "Numerical and experimental study of soot formation in laminar diffusion flames burning simulated biogas fuels at elevated pressures", *Combustion and Flame* 161:2678–2691 (2014). (*p.* 6)

[39] Aubagnac Karkar, D., *Sectional soot modeling for Diesel RANS simulations*, Ph.D. thesis, Châtenay-Malabry, Ecole centrale de Paris (2014). (*p.* 6, 7, 20, 115, 180)

[40] Roy, S., *Aerosol-dynamics-based soot modeling of flames*, Ph.D. thesis, Pennsylvania State University (2014). (*p.* 6, 20, 23, 29)

[41] Bisetti, F., Blanquart, G., Mueller, M., Pitsch, H., "On the formation and early evolution of soot in turbulent nonpremixed flames", *Combustion and Flame* 159:317–335 (2012). (*p.* 6, 82, 92, 120, 180)

[42] Yapp, E.K., Chen, D., Akroyd, J., Mosbach, S., Kraft, M., Camacho, J., Wang, H., "Numerical simulation and parametric sensitivity study of particle size distributions in a burner-stabilised stagnation flame", *Combustion and Flame* 162:2569–2581 (2015). (*p.* 7, 74, 76, 77, 78)

[43] Rodrigues, P., Franzelli, B., Vicquelin, R., Gicquel, O., Darabiha, N., "Unsteady dynamics of PAH and soot particles in laminar counterflow diffusion flames", *Proceedings of the Combustion Institute* 36:927–934 (2017). (*p.* 7, 83, 101, 103, 104, 105, 163)

[44] Eaves, N., Dworkin, S., Thomson, M., "The importance of reversibility in modeling soot nucleation and condensation processes", *Proceedings of the Combustion Institute* 35:1787–1794 (2015). (*p.* 7)

[45] D'Anna, A., Sirignano, M., "Detailed kinetic mechanisms of PAH and soot formation", *Computer Aided Chemical Engineering*, Elsevier, vol. 45, pp. 647–672 (2019). (*p.* 7)

[46] Nobili, A., Maffei, L.P., Baggioli, A., Pelucchi, M., Cuoci, A., Cavallotti, C., Faravelli, T., "On the radical behavior of large polycyclic aromatic hydrocarbons in soot formation and oxidation", *Combustion and Flame* 235:111692 (2022). (*p.* 7)

[47] Kholghy, M.R., Kelesidis, G.A., Pratsinis, S.E., "Reactive polycyclic aromatic hydrocarbon dimerization drives soot nucleation", *Physical Chemistry Chemical Physics* 20:10926–10938 (2018). (*p.* 7)

[48] Singh, J., Balthasar, M., Kraft, M., Wagner, W., "Stochastic modeling of soot particle size and age distributions in laminar premixed flames", *Proceedings of the Combustion Institute* 30:1457–1465 (2005). (*p.* 7, 8)

[49] Veshkini, A., Dworkin, S.B., Thomson, M.J., "A soot particle surface reactivity model applied to a wide range of laminar ethylene/air flames", *Combustion and Flame* 161:3191–3200 (2014). (*p.* 7)

[50] Neoh, K., Howard, J., Sarofim, A., "Effect of oxidation on the physical structure of soot", *Symposium (International) on Combustion* 20:951–957 (1985). (*p.* 7)

[51] Haudiquert, M., Cessou, A., Stepowski, D., Coppalle, A., "OH and soot concentration measurements in a high-temperature laminar diffusion flame", *Combustion and Flame* 111:338–349 (1997). (*p.* 7, 42)

[52] D'anna, A., Kent, J., "A model of particulate and species formation applied to laminar, nonpremixed flames for three aliphatic-hydrocarbon fuels", *Combustion and Flame* 152:573–587 (2008). (*p.* 7, 9)

[53] Xu, F., El-Leathy, A., Kim, C., Faeth, G., "Soot surface oxidation in hydrocarbon/air diffusion flames at atmospheric pressure", *Combustion and Flame* 132:43–57 (2003). (*p.* 7)

[54] Khosousi, A., Dworkin, S.B., "Detailed modelling of soot oxidation by O_2 and OH in laminar diffusion flames", *Proceedings of the Combustion Institute* 35:1903–1910 (2015). (*p.* 7)

[55] Moss, J., Stewart, C., Syed, K., "Flowfield modelling of soot formation at elevated pressure", *Symposium (International) on Combustion* 22:413–423 (1989). (*p.* 8)

[56] Kennedy, I.M., Kollmann, W., Chen, J.Y., "A model for soot formation in a laminar diffusion flame", *Combustion and Flame* 81:73–85 (1990). (*p.* 8)

[57] Leung, K.M., Lindstedt, R.P., Jones, W.P., "A simplified reaction mechanism for soot formation in nonpremixed flames", *Combustion and Flame* 87:289–305 (1991). (*p.* 8)

[58] Lindstedt, P.R., "Simplified soot nucleation and surface growth steps for non-premixed flames", *Soot formation in combustion*, Springer, pp. 417–441 (1994). (*p.* 8)

[59] Lindstedt, R.P., Louloudi, S.A., "Joint-scalar transported pdf modeling of soot formation and oxidation", *Proceedings of the Combustion Institute* 30:775–783 (2005). (*p.* 8)

[60] Bolla, M., Wright, Y.M., Boulouchos, K., Borghesi, G., Mastorakos, E., "Soot formation modeling of n-heptane sprays under diesel engine conditions using the conditional moment closure approach", *Combustion Science and Technology* 185:766–793 (2013). (*p.* 8)

[61] Balthasar, M., Kraft, M., "A stochastic approach to calculate the particle size distribution function of soot particles in laminar premixed flames", *Combustion and Flame* 133:289–298 (2003). (*p.* 8, 151)

[62] Celnik, M., Patterson, R., Kraft, M., Wagner, W., "Coupling a stochastic soot population balance to gas-phase chemistry using operator splitting", *Combustion and Flame* 148:158–176 (2007). (*p.* 8)

[63] Frenklach, M., Harris, S.J., "Aerosol dynamics modeling using the method of moments", *Journal of Colloid and Interface Science* 118:252–261 (1987). (*p.* 8, 9)

[64] Frenklach, M., "Method of moments with interpolative closure", *Chemical Engineering Science* 57:2229–2239 (2002). (*p.* 8, 9, 151)

[65] Mueller, M.E., Blanquart, G., Pitsch, H., "Hybrid method of moments for modeling soot formation and growth", *Combustion and Flame* 156:1143–1155 (2009). (*p.* 8, 9, 115, 116, 121, 151)

[66] Mueller, M.E., Pitsch, H., "LES model for sooting turbulent nonpremixed flames", *Combustion and Flame* 159:2166–2180 (2012). (*p.* 8, 10, 116, 151, 152, 180, 181, 206, 207, 232)

[67] McGraw, R., "Description of aerosol dynamics by the quadrature method of moments", *Aerosol Science and Technology* 27:255–265 (1997). (*p.* 9)

[68] Blacha, T., Di Domenico, M., Gerlinger, P., Aigner, M., "Soot predictions in premixed and non-premixed laminar flames using a sectional approach for PAHs and soot", *Combustion and Flame* 159:181–193 (2012). (*p.* 9, 115)

[69] Saggese, C., Ferrario, S., Camacho, J., Cuoci, A., Frassoldati, A., Ranzi, E., Wang, H., Faravelli, T., "Kinetic modeling of particle size distribution of soot in a premixed burner-stabilized stagnation ethylene flame", *Combustion and Flame* 162:3356–3369 (2015). (*p.* 9, 10)

[70] Pejpichestakul, W., Ranzi, E., Pelucchi, M., Frassoldati, A., Cuoci, A., Parente, A., Faravelli, T., "Examination of a soot model in premixed laminar flames at fuel-rich conditions", *Proceedings of the Combustion Institute* 37:1013–1021 (2019). (*p.* 9)

[71] Gelbard, F., Tambour, Y., Seinfeld, J.H., "Sectional representations for simulating aerosol dynamics", *Journal of Colloid and Interface Science* 76:541–556 (1980). (*p.* 9, 19, 20, 115, 151)

[72] Zhang, Q., *Detailed modeling of soot formation/oxidation in laminar coflow diffusion flames*, Ph.D. thesis (2009). (*p.* 9, 23, 115)

[73] Rodrigues, P., Franzelli, B., Vicquelin, R., Gicquel, O., Darabiha, N., "Coupling an LES approach and a soot sectional model for the study of sooting turbulent non-premixed flames", *Combustion and Flame* 190:477–499 (2018). (*p.* 9, 10, 20, 26, 116, 117, 121, 151, 152, 180, 181, 188, 196, 200, 202, 207, 232)

[74] Aksit, I., Moss, J., "A hybrid scalar model for sooting turbulent flames", *Combustion and Flame* 145:231–244 (2006). (*p.* 9)

[75] Yang, S., Lew, J., Mueller, M., "Large eddy simulation of soot evolution in turbulent reacting flows: Presumed subfilter PDF model for soot–turbulence–chemistry interactions", *Combustion and Flame* 209:200–213 (2019). (*p.* 9, 10, 151, 180, 181)

[76] Ong, J.C., Pang, K.M., Walther, J.H., Ho, J.H., Ng, H.K., "Evaluation of a lagrangian soot tracking method for the prediction of primary soot particle size under engine-like conditions", *Journal of Aerosol Science* 115:70–95 (2018). (*p.* 9)

[77] Gallen, L., Felden, A., Riber, E., Cuenot, B., "Lagrangian tracking of soot particles in les of gas turbines", *Proceedings of the Combustion Institute* 37:5429–5436 (2019). (*p.* 9)

[78] Dellinger, N., Bertier, N., Dupoirieux, F., Legros, G., "Hybrid eulerian-lagrangian method for soot modelling applied to ethylene-air premixed flames", *Energy* 194:116858 (2020). (*p.* 9)

[79] Felden, A., Riber, E., Cuenot, B., "Impact of direct integration of analytically reduced chemistry in LES of a sooting swirled non-premixed combustor", *Combustion and Flame* 191:270–286 (2018). (*p.* 10, 180)

[80] van Oijen, J., de Goey, L., "Modelling of premixed laminar flames using flamelet-generated manifolds", *Combustion Science and Technology* 161:113–137 (2000). (*p.* 10, 184)

[81] D Pierce, C., Moin, P., "Progress-variable approach for large-eddy simulation of non-premixed turbulent combustion", *Journal of Fluid Mechanics* 504:73 (2004). (*p.* 10, 117, 181)

[82] Gicquel, O., Darabiha, N., Thévenin, D., "Liminar premixed hydrogen/air counterflow flame simulations using flame prolongation of ildm with differential diffusion", *Proceedings of the Combustion Institute* 28:1901–1908 (2000). (*p.* 10)

[83] Snegirev, A., Markus, E., Kuznetsov, E., Harris, J., Wu, T., "On soot and radiation modeling in buoyant turbulent diffusion flames", *Heat and Mass Transfer* 54:2275–2293 (2018). (*p.* 10)

[84] Xuan, Y., Blanquart, G., "Effects of aromatic chemistry-turbulence interactions on soot formation in a turbulent non-premixed flame", *Proceedings of the Combustion Institute* 35:1911–1919 (2015). (*p.* 10, 152, 181, 202)

[85] Gkantonas, S., Sirignano, M., Giusti, A., D'Anna, A., Mastorakos, E., "Comprehensive soot particle size distribution modelling of a model rich-quench-lean burner", *Fuel* 270:117483 (2020). (*p.* 11, 180, 181)

[86] Sewerin, F., Rigopoulos, S., "An LES-PBE-PDF approach for modeling particle formation in turbulent reacting flows", *Physics of Fluids* 29:105105 (2017). (*p.* 11)

[87] Jadidi, M., Kostic, S., Zimmer, L., Dworkin, S.B., "An artificial neural network for the low-cost prediction of soot emissions", *Energies* 13:4787 (2020). (*p.* 11, 152)

[88] Colmán, H., Cuoci, A., Darabiha, N., Fiorina, B., "A virtual chemistry model for soot prediction in flames including radiative heat transfer", *Combustion and Flame* 238:111879 (2022). (*p.* 11, 152, 182, 201)

[89] Rigopoulos, S., "Modelling of soot aerosol dynamics in turbulent flow", *Flow, Turbulence and Combustion* 103:565–604 (2019). (*p.* 11, 179, 181, 232)

[90] Poinsot, T., Veynante, D., *Theoretical and Numerical Combustion*, RT Edwards, Inc., 2005. (*p.* 15, 18, 179, 183, 184)

[91] Wilke, C., "A viscosity equation for gas mixtures", *Journal of Chemical Physics* 18:517–519 (1950). (*p.* 16)

[92] Hirschfelder, J.O., Curtiss, C.F., Bird, R.B., Mayer, M.G., *Molecular Theory of Gases and Liquids*, vol. 165, Wiley New York, New York, USA, 2 ed., 1964. (*p.* 17, 137, 158, 215)

[93] Mathur, S., Tondon, P., Saxena, S., "Thermal conductivity of binary, ternary and quaternary mixtures of rare gases", *Molecular Physics* 12:569–579 (1967). (*p.* 17)

[94] Hoerlle, C.A., Pereira, F.M., "Effects of CO_2 addition on soot formation of ethylene non-premixed flames under oxygen enriched atmospheres", *Combustion and Flame* 203:407–423 (2019). (*p.* 20, 28, 56, 67, 77, 87, 151, 158, 238)

[95] Friendlander, S., *Smoke, Dust and Haze: Fundamentals of Aerosol Dynamics*, Oxford University Press, New York, USA, 2000. (*p.* 22)

[96] Waldmann, L., Schmitt, K., "Thermophoresis and diffusiophoresis of aerosols", *Aerosol science*, Academic Press New York, vol. 137 (1966). (*p.* 22)

[97] Zimmer, L., *Numerical study of soot formation in laminar ethylene diffusion flames*, Ph.D. thesis, Universidade Federal do Rio Grande do Sul (2016). (*p.* 22, 117, 132, 153)

[98] Hoerlle, C., *Modelling of soot formation based on the Discrete Sectional Method: CO_2 effects and coupling with the FGM technique*, Ph.D. thesis, Universidade Federal do Rio Grande do Sul (2020). (*p.* 23, 24, 29, 30, 31, 32, 82, 83, 97, 228, 235)

[99] Rodrigues, P., *Multiphysics modeling of turbulent flames followed with the consideration of radiative transfers and parérate heat transfers.*, Ph.D. thesis, Université Paris-Saclay (2018). (*p.* 23, 26, 32, 188, 217, 235)

[100] Kumar, S., Ramkrishna, D., "On the solution of population balance equations by discretization—i. a fixed pivot technique", *Chemical Engineering Science* 51:1311–1332 (1996). (*p.* 25)

[101] Cunningham, E., "On the velocity of steady fall of spherical particles through fluid medium", *Proceedings of the Royal Society of London. Series A, Containing Papers of a Mathematical and Physical Character* 83:357–365 (1910). (*p.* 27)

[102] Zimmer, L., Pereira, F.M., van Oijen, J.A., de Goey, L.P.H., "Investigation of mass and energy coupling between soot particles and gas species in modelling ethylene counterflow diffusion flames", *Combustion Theory and Modelling* 21:358–379 (2017). (*p.* 31)

[103] Chase Jr., M., "NIST-JANAF Thermochemical tables", *Journal of Physical and Chemical Reference Data Monographs* 9 (1998). (*p.* 31)

[104] Crowe, C.T., *Multiphase flow handbook*, CRC press, 2005. (*p.* 31)

[105] Wang, Y., Raj, A., Chung, S.H., "A PAH growth mechanism and synergistic effect on PAH formation in counterflow diffusion flames", *Combustion and Flame* 160:1667–1676 (2013). (*p.* 32, 60, 64, 85, 123, 158, 193, 233, 235, 242)

[106] Mahmoud, N., Yan, F., Zhou, M., Xu, L., Wang, Y., "Coupled effects of carbon dioxide and water vapor addition on soot formation in ethylene diffusion flames", *Energy & Fuels* 33:5582–5596 (2019). (*p.* 32, 57, 58, 62)

[107] Hirschfelder, J.O., Curtiss, C.F., Bird, R.B., *Molecular Theory of Gases and Liquids*, John Wiley and Sons, Inc., New York, NY, 2 ed., 1964. (*p.* 32)

[108] Somers, B., *The simulation of flat flames with detailed and reduced chemical models*, Ph.D. thesis, Eindhoven University of Technology (1994). (*p.* 32, 158, 233)

[109] "One-dimensional laminar flame code, Eindhoven University of Technology", (2023). (*p.* 32)

[110] Kee, R.J., Grcar, J.F., Smooke, M.D., Miller, J.A., Meeks, E., "PREMIX: a Fortran program for modeling steady laminar one-dimensional premixed flames", *Sandia National Laboratories Report* (1985). (*p.* 32)

[111] Dixon-Lewis, G., "Structure of laminar flames", *Symposium (International) on Combustion* 23:305–324 (1991). (*p.* 32, 33)

[112] Kee, R.J., Coltrin, M.E., Glarborg, P., *Chemically reacting flow: theory and practice*, John Wiley & Sons, 2005. (*p.* 32)

[113] Wang, Y., Chung, S., "Strain rate effect on sooting characteristics in laminar counterflow diffusion flames", *Combustion and Flame* 165:433–444 (2016). (*p.* 37, 38, 39, 83, 96, 123)

[114] Wang, Y., Chung, S.H., "Formation of soot in counterflow diffusion flames with carbon dioxide dilution", *Combustion Science and Technology* 188:805–817 (2016). (*p.* 39, 123, 159)

[115] Xu, L., Yan, F., Zhou, M., Wang, Y., Chung, S.H., "Experimental and soot modeling studies of ethylene counterflow diffusion flames: Non-monotonic influence of the oxidizer composition on soot formation", *Combustion and Flame* 197:304–318 (2018). (*p.* 39, 56, 123, 159)

[116] Amin, H.M., Roberts, W.L., "Soot measurements by two angle scattering and extinction in an N_2-diluted ethylene/air counterflow diffusion flame from 2 to 5 atm", *Proceedings of the Combustion Institute* 36:861–869 (2017). (*p.* 40, 41)

[117] Frenklach, M., Singh, R.I., Mebel, A.M., "On the low-temperature limit of HACA", *Proceedings of the Combustion Institute* 37:969–976 (2019). (*p.* 40)

[118] Mansouri, A., Zimmer, L., Dworkin, S.B., Eaves, N.A., "Impact of pressure-based HACA rates on soot formation in varying-pressure coflow laminar diffusion flames", *Combustion and Flame* 218:109–120 (2020). (*p.* 40)

[119] Quadarella, E., Li, Z., Guo, J., Roberts, W.L., Im, H.G., "Investigation of soot sensitivity to strain rate in ethylene counterflow soot formation oxidation flames", *Proceedings of the Combustion Institute* (2022). (*p.* 41, 42)

[120] Li, G., Zhou, M., Wang, Y., "Sensitivity of soot formation to strain rate in steady counterflow flames determines its response under unsteady conditions", *Combustion and Flame* 241:112107 (2022). (*p.* 43, 163, 167)

[121] Cuoci, A., Frassoldati, A., Faravelli, T., Ranzi, E., "Soot formation in unsteady counterflow diffusion flames", *Proceedings of the Combustion Institute* 32:1335–1342 (2009). (*p.* 44, 83, 104, 143, 163, 165)

[122] Camacho, J., Liu, C., Gu, C., Lin, H., Huang, Z., Tang, Q., You, X., Saggese, C., Li, Y., Jung, H., et al., "Mobility size and mass of nascent soot particles in a benchmark premixed ethylene flame", *Combustion and Flame* 162:3810–3822 (2015). (*p.* 46, 47, 48)

[123] Abid, A.D., Camacho, J., Sheen, D.A., Wang, H., "Quantitative measurement of soot particle size distribution in premixed flames–the burner-stabilized stagnation flame approach", *Combustion and Flame* 156:1862–1870 (2009). (*p.* 45)

[124] "International Sooting Flame (ISF) workshop", https://www.adelaide.edu.au/cet/isfworkshop/, accessed: 2019-05. (*p.* 46, 191, 221)

[125] Langenkamp, P., van Oijen, J., Levinsky, H., Mokhov, A., "Growth of soot volume fraction and aggregate size in 1D premixed C_2H_4/air flames studied by laser-induced incandescence and angle-dependent light scattering", *Journal of Combustion* 2018 (2018). (*p.* 49, 50)

[126] Xu, F., Sunderland, P., Faeth, G., "Soot formation in laminar premixed ethylene/air flames at atmospheric pressure", *Combustion and Flame* 108:471–493 (1997). (*p.* 50)

[127] Smooke, M., McEnally, C., Pfefferle, L., Hall, R., Colket, M., "Computational and experimental study of soot formation in a coflow, laminar diffusion flame", *Combustion and Flame* 117:117–139 (1999). (*p.* 50)

[128] Chen, J.Y., Liu, Y., Rogg, B., "CO-H_2-N_2/air diffusion flames: Thermal radiation and transient effects", *Reduced kinetic mechanisms for applications in combustion systems*, Springer, pp. 196–223 (1993). (*p.* 50, 245)

[129] TNF, *International Workshop on Measurement and Computation of Turbulent Nonpremixed Flames*, https://tnfworkshop.org/radiation/. (*p.* 50, 245)

[130] Kalbhor, A., van Oijen, J., "Effects of hydrogen enrichment and water vapour dilution on soot formation in laminar ethylene counterflow flames", *International Journal of Hydrogen Energy* 45:23653–23673 (2020). (*p.* 55)

[131] Liu, F., Consalvi, J.L., Fuentes, A., "Effects of water vapor addition to the air stream on soot formation and flame properties in a laminar coflow ethylene/air diffusion flame", *Combustion and Flame* 161:1724–1734 (2014). (*p.* 55, 57, 68)

[132] Schug, K., Manheimer-Timnat, Y., Yaccarino, P., Glassman, I., "Sooting behavior of gaseous hydrocarbon diffusion flames and the influence of additives", *Combustion Science and Technology* 22:235–250 (1980). (*p.* 56)

[133] Axelbaum, R., Law, C.K., "Soot formation and inert addition in diffusion flames", Elsevier, 23, pp. 1517–1523 (1991). (*p.* 56)

[134] Du, D., Axelbaum, R., Law, C.K., "Soot formation in strained diffusion flames with gaseous additives", *Combustion and Flame* 102:11–20 (1995). (*p.* 56)

[135] Gülder, Ö., Snelling, D., Sawchuk, R., "Influence of hydrogen addition to fuel on temperature field and soot formation in diffusion flames", Elsevier, 26, pp. 2351–2358 (1996). (*p.* 56)

[136] Guo, H., Liu, F., Smallwood, G.J., Gülder, Ö.L., "Numerical study on the influence of hydrogen addition on soot formation in a laminar ethylene-air diffusion flame", *Combustion and Flame* 145:324–338 (2006). (*p.* 56, 60, 62, 63, 67, 68)

[137] Yoon, S., Anh, D., Chung, S., "Synergistic effect of mixing dimethyl ether with methane, ethane, propane, and ethylene fuels on polycyclic aromatic hydrocarbon and soot formation", *Combustion and Flame* 154:368–377 (2008). (*p.* 56)

[138] Sirignano, M., Salamanca, M., D'Anna, A., "The role of dimethyl ether as substituent to ethylene on particulate formation in premixed and counter-flow diffusion flames", *Fuel* 126:256–262 (2014). (*p.* 56)

[139] Gu, M., Chu, H., Liu, F., "Effects of simultaneous hydrogen enrichment and carbon dioxide dilution of fuel on soot formation in an axisymmetric coflow laminar ethylene/air diffusion flame", *Combustion and Flame* 166:216–228 (2016). (*p.* 56, 60, 61)

[140] Choi, J.H., Hwang, C.H., Choi, S.K., Lee, S.M., Lee, W.J., Jang, S.H., Park, S.H., "Impacts of hydrogen addition on micro and nanostructure of soot particles formed in C_2H_4/air counter diffusion flames", *International Journal of Hydrogen Energy* 41:15852–15858 (2016). (*p.* 56, 77)

[141] Deng, S., Mueller, M.E., Chan, Q.N., Qamar, N.H., Dally, B.B., Alwahabi, Z.T., Nathan, G.J., "Hydrodynamic and chemical effects of hydrogen addition on

soot evolution in turbulent nonpremixed bluff body ethylene flames", *Proceedings of the Combustion Institute* 36:807–814 (2017). (*p.* 56)

[142] Wang, Y., Liu, X., Gu, M., An, X., "Numerical simulation of the effects of hydrogen addition to fuel on the structure and soot formation of a laminar axisymmetric coflow $C_2H_4/(O_2$-$CO_2)$ diffusion flame", *Combustion Science and Technology* 191:1743–1768 (2019). (*p.* 56, 61, 63, 66, 67, 68)

[143] Yen, M., Magi, V., Abraham, J., "Modeling the effects of hydrogen and nitrogen addition on soot formation in laminar ethylene jet diffusion flames", *Chemical Engineering Science* 196:116–129 (2019). (*p.* 56)

[144] Dai, W., Yan, F., Xu, L., Zhou, M., Wang, Y., "Effects of carbon monoxide addition on the sooting characteristics of ethylene and propane counterflow diffusion flames", *Fuel* 271:117674 (2020). (*p.* 56)

[145] Antunes, J.G., Mikalsen, R., Roskilly, A., "An investigation of hydrogen-fuelled HCCI engine performance and operation", *International Journal of Hydrogen Energy* 33:5823–5828 (2008). (*p.* 56)

[146] Ji, C., Wang, S., "Effect of hydrogen addition on combustion and emissions performance of a spark ignition gasoline engine at lean conditions", *International Journal of Hydrogen Energy* 34:7823–7834 (2009). (*p.* 56)

[147] Roy, M.M., Tomita, E., Kawahara, N., Harada, Y., Sakane, A., "An experimental investigation on engine performance and emissions of a supercharged H_2-diesel dual-fuel engine", *International Journal of Hydrogen Energy* 35:844–853 (2010). (*p.* 56)

[148] Liew, C., Li, H., Nuszkowski, J., Liu, S., Gatts, T., Atkinson, R., Clark, N., "An experimental investigation of the combustion process of a heavy-duty diesel engine enriched with H_2", *International Journal of Hydrogen Energy* 35:11357–11365 (2010). (*p.* 56)

[149] Shin, B., Cho, Y., Han, D., Song, S., Chun, K.M., "Hydrogen effects on NOx emissions and brake thermal efficiency in a diesel engine under low-temperature and heavy-EGR conditions", *International Journal of Hydrogen Energy* 36:6281–6291 (2011). (*p.* 56)

[150] Karagöz, Y., Güler, İ., Sandalcı, T., Yüksek, L., Dalkılıç, A.S., "Effect of hydrogen enrichment on combustion characteristics, emissions and performance of a diesel engine", *International Journal of Hydrogen Energy* 41:656–665 (2016). (*p.* 56)

[151] Sun, Y., Yu, X., Jiang, L., "Effects of direct hydrogen injection on particle number emissions from a lean burn gasoline engine", *International Journal of Hydrogen Energy* 41:18631–18640 (2016). (*p.* 56)

[152] Pandey, P., Pundir, B., Panigrahi, P., "Hydrogen addition to acetylene–air laminar diffusion flames: studies on soot formation under different flow arrangements", *Combustion and Flame* 148:249–262 (2007). (*p.* 56)

[153] Park, S.H., Lee, K.M., Hwang, C.H., "Effects of hydrogen addition on soot formation and oxidation in laminar premixed C_2H_2/air flames", *International Journal of Hydrogen Energy* 36:9304–9311 (2011). (*p.* 56)

[154] De Iuliis, S., Maffi, S., Migliorini, F., Cignoli, F., Zizak, G., "Effect of hydrogen addition on soot formation in an ethylene/air premixed flame", *Applied Physics B* 106:707–715 (2012). (*p.* 56)

[155] Liu, F., Ai, Y., Kong, W., "Effect of hydrogen and helium addition to fuel on soot formation in an axisymmetric coflow laminar methane/air diffusion flame", *International Journal of Hydrogen Energy* 39:3936–3946 (2014). (*p.* 56)

[156] Wei, M., Liu, J., Guo, G., Li, S., "The effects of hydrogen addition on soot particle size distribution functions in laminar premixed flame", *International Journal of Hydrogen Energy* 41:6162–6169 (2016). (*p.* 56)

[157] Ahmed, A.M., Mancarella, S., Desgroux, P., Gasnot, L., Pauwels, J.F., El Bakali, A., "Experimental and numerical study on rich methane/hydrogen/air laminar premixed flames at atmospheric pressure: Effect of hydrogen addition to fuel on soot gaseous precursors", *International Journal of Hydrogen Energy* 41:6929–6942 (2016). (*p.* 56)

[158] Sun, Z., Dally, B., Nathan, G., Alwahabi, Z., "Effects of hydrogen and nitrogen on soot volume fraction, primary particle diameter and temperature in laminar ethylene/air diffusion flames", *Combustion and Flame* 175:270–282 (2017). (*p.* 56)

[159] Wu, Y., Liu, F., Sun, Y., Zhu, B., "Effects of carbon dioxide and water vapor addition on benzene and PAH formation in a laminar premixed C_2H_4/O_2/Ar flame", *Combustion Science and Technology* 191:1866–1897 (2019). (*p.* 56, 57)

[160] Ezenwajiaku, C., Talibi, M., Doan, N.A.K., Swaminathan, N., Balachandran, R., "Study of polycyclic aromatic hydrocarbons (PAHs) in hydrogen-enriched methane diffusion flames", *International Journal of Hydrogen Energy* 44:7642–7655 (2019). (*p.* 56)

[161] Xu, L., Yan, F., Wang, Y., Chung, S.H., "Chemical effects of hydrogen addition on soot formation in counterflow diffusion flames: Dependence on fuel type and oxidizer composition", *Combustion and Flame* 213:14–25 (2020). (*p.* 56, 59, 61, 63, 67, 68)

[162] Qiu, L., Hua, Y., Zhuang, Y., Wei, J., Qian, Y., Cheng, X., "Numerical investigation into the decoupling effects of hydrogen blending on flame structure and soot formation in a laminar ethylene diffusion flame", *International Journal of Hydrogen Energy* (2020). (*p.* 56)

[163] Rao, V., Bardon, M., "The effect of water on gas phase soot formation in laminar diffusion flames", *Combustion and Flame* 55:73–78 (1984). (*p.* 57)

[164] Roberts, C.E., Naegeli, D., Chadwell, C., "The effect of water on soot formation chemistry", *SAE Transactions* pp. 1656–1672 (2005). (*p.* 57)

[165] Arnal, C., Alzueta, M., Millera, A., Bilbao, R., "Influence of water vapor addition on soot oxidation at high temperature", *Energy* 43:55–63 (2012). (*p.* 57)

[166] Zhang, Y., Wang, L., Liu, P., Guan, B., Ni, H., Huang, Z., Lin, H., "Experimental and kinetic study of the effects of CO_2 and H_2O addition on PAH formation in laminar premixed $C_2H_4/O_2/Ar$ flames", *Combustion and Flame* 192:439–451 (2018). (*p.* 57)

[167] Ying, Y., Liu, D., "Effects of water addition on soot properties in ethylene inverse diffusion flames", *Fuel* 247:187–197 (2019). (*p.* 57)

[168] Liu, F., He, X., Ma, X., Zhang, Q., Thomson, M., Guo, H., Smallwood, G., Shuai, S., Wang, J., "An experimental and numerical study of the effects of dimethyl ether addition to fuel on polycyclic aromatic hydrocarbon and soot formation in laminar coflow ethylene/air diffusion flames", *Combustion and Flame* 158:547–563 (2011). (*p.* 63)

[169] Zhao, B., Yang, Z., Li, Z., Johnston, M.V., Wang, H., "Particle size distribution function of incipient soot in laminar premixed ethylene flames: effect of flame temperature", *Proceedings of the Combustion Institute* 30:1441–1448 (2005). (*p.* 74)

[170] Abid, A.D., Heinz, N., Tolmachoff, E.D., Phares, D.J., Campbell, C.S., Wang, H., "On evolution of particle size distribution functions of incipient soot in premixed ethylene–oxygen–argon flames", *Combustion and Flame* 154:775–788 (2008). (*p.* 74)

[171] Singh, J., Patterson, R.I., Kraft, M., Wang, H., "Numerical simulation and sensitivity analysis of detailed soot particle size distribution in laminar premixed ethylene flames", *Combustion and Flame* 145:117–127 (2006). (*p.* 74, 75)

[172] Bhatt, J., Lindstedt, R., "Analysis of the impact of agglomeration and surface chemistry models on soot formation and oxidation", *Proceedings of the Combustion Institute* 32:713–720 (2009). (*p.* 77)

[173] Kalbhor, A., van Oijen, J., "Effects of curvature on soot formation in steady and unsteady counterflow diffusion flames", *Combustion and Flame* 241:112108 (2022). (*p.* 81, 160)

[174] Glassman, I., "Soot formation in combustion processes", Elsevier, 22, pp. 295–311 (1989). (*p.* 81)

[175] Xuan, Y., Blanquart, G., "A flamelet-based a priori analysis on the chemistry tabulation of polycyclic aromatic hydrocarbons in non-premixed flames", *Combustion and Flame* 161:1516–1525 (2014). (*p.* 81, 82, 83, 87, 92, 129, 196)

[176] Lignell, D., Chen, J., Smith, P., Lu, T., Law, C., "The effect of flame structure on soot formation and transport in turbulent nonpremixed flames using direct numerical simulation", *Combustion and Flame* 151:2–28 (2007). (*p.* 82, 92)

[177] Franzelli, B., Cuoci, A., Stagni, A., Ihme, M., Faravelli, T., Candel, S., "Numerical investigation of soot-flame-vortex interaction", *Proceedings of the Combustion Institute* 36:753–761 (2017). (*p.* 82, 87)

[178] Göktolga, M., de Goey, L., van Oijen, J., "Modeling curvature effects in turbulent autoigniting non-premixed flames using tabulated chemistry", *Proceedings of the Combustion Institute* 38:2741–2748 (2021). (*p.* 83)

[179] Decroix, M., Roberts, W., "Transient flow field effects on soot volume fraction in diffusion flames", *Combustion Science and Technology* 160:165–189 (2000). (*p.* 83)

[180] Xiao, J., Austin, E., Roberts, W., "Relative polycyclic aromatic hydrocarbon concentrations in unsteady counterflow diffusion flames", *Combustion Science and Technology* 177:691–713 (2005). (*p.* 83)

[181] Wang, Y., Chung, S., "Effect of strain rate on sooting limits in counterflow diffusion flames of gaseous hydrocarbon fuels: Sooting temperature index and sooting sensitivity index", *Combustion and Flame* 161:1224–1234 (2014). (*p.* 83)

[182] Huijnen, V., Evlampiev, A., Somers, L., Baert, R., de Goey, L., "The effect of the strain rate on PAH/soot formation in laminar counterflow diffusion flames", *Combustion Science and Technology* 182:103–123 (2010). (*p.* 83, 96)

[183] Cuoci, A., Frassoldati, A., Faravelli, T., Ranzi, E., "Formation of soot and nitrogen oxides in unsteady counterflow diffusion flames", *Combustion and Flame* 156:2010–2022 (2009). (*p.* 83, 98, 103, 104, 143)

[184] van Oijen, J., Donini, A., Bastiaans, R., ten Thije Boonkkamp, J., de Goey, L., "State-of-the-art in premixed combustion modeling using flamelet generated manifolds", *Progress in Energy and Combustion Science* 57:30–74 (2016). (*p.* 84, 117, 118, 154, 155, 184)

[185] Ramaekers, W., *Development of flamelet generated manifolds for partially-premixed flame simulations*, Ph.D. thesis, Eindhoven University of Technology (2011). (*p.* 84)

[186] de Goey, L., ten Thije Boonkkamp, J., "A flamelet description of premixed laminar flames and the relation with flame stretch", *Combustion and Flame* 119:253–271 (1999). (*p.* 84)

[187] Peters, N., *Turbulent Combustion*, Cambridge University Press, Cambridge, UK, 2000. (*p.* 85)

[188] Bilger, R., Stårner, S., Kee, R., "On reduced mechanisms for methane-air combustion in nonpremixed flames", *Combustion and Flame* 80:135–149 (1990). (*p.* 85, 118, 158)

[189] Wang, P., Hu, S., Pitz, R., "Numerical investigation of the curvature effects on diffusion flames", *Proceedings of the Combustion Institute* 31:989–996 (2007). (*p.* 87)

[190] Pitsch, H., Peters, N., "A consistent flamelet formulation for non-premixed combustion considering differential diffusion effects", *Combustion and Flame* 114:26–40 (1998). (*p.* 92)

[191] Cuoci, A., Frassoldati, A., Faravelli, T., Ranzi, E., "Frequency response of counter flow diffusion flames to strain rate harmonic oscillations", *Combustion Science and Technology* 180:767–784 (2008). (*p.* 96)

[192] Egolfopoulos, F., Campbell, C., "Unsteady counterflowing strained diffusion flames: diffusion-limited frequency response", *Journal of Fluid Mechanics* 318:1–29 (1996). (*p.* 104, 143)

[193] Kalbhor, A., van Oijen, J., "An assessment of the sectional soot model and FGM tabulated chemistry coupling in laminar flame simulations", *Combustion and Flame* 229:111381 (2021). (*p.* 115, 153, 158, 173)

[194] Kazakov, A., Frenklach, M., "Dynamic modeling of soot particle coagulation and aggregation: Implementation with the method of moments and application to high-pressure laminar premixed flames", *Combustion and Flame* 114:484–501 (1998). (*p.* 115)

[195] Violi, A., "Modeling of soot particle inception in aromatic and aliphatic premixed flames", *Combustion and Flame* 139:279–287 (2004). (*p.* 115)

[196] Balthasar, M., Frenklach, M., "Detailed kinetic modeling of soot aggregate formation in laminar premixed flames", *Combustion and Flame* 140:130–145 (2005). (*p.* 115)

[197] Dorey, L.H., Bertier, N., Tessé, L., Dupoirieux, F., "Soot and radiation modeling in laminar ethylene flames with tabulated detailed chemistry", *Comptes Rendus Mécanique* 339:756–769 (2011). (*p.* 116)

[198] Xuan, Y., Blanquart, G., "Numerical modeling of sooting tendencies in a laminar co-flow diffusion flame", *Combustion and Flame* 160:1657–1666 (2013). (*p.* 116)

[199] Dupoirieux, F., Bertier, N., "Methodology for the numerical prediction of soot formation in turbulent reactive flows and application to aircraft engine combustors", *International Journal of Sustainable Aviation* 2:15–33 (2016). (*p.* 116)

[200] Geigle, K.P., Köhler, M., O'Loughlin, W., Meier, W., "Investigation of soot formation in pressurized swirl flames by laser measurements of temperature, flame structures and soot concentrations", *Proceedings of the Combustion Institute* 35:3373–3380 (2015). (*p.* 116)

[201] Franzelli, B., Riber, E., Cuenot, B., Ihme, M., "Numerical modeling of soot production in aero-engine combustors using large eddy simulations", *ASME Turbo Expo 2015: Turbine Technical Conference and Exposition*, American Society of Mechanical Engineers Digital Collection (2015). (*p.* 116, 180, 182)

[202] Lecocq, G., Poitou, D., Hernández, I., Duchaine, F., Riber, E., Cuenot, B., "A methodology for soot prediction including thermal radiation in complex industrial burners", *Flow, Turbulence and Combustion* 92:947–970 (2014). (*p.* 116)

[203] Kim, T., Kim, Y., "Interactive transient flamelet modeling for soot formation and oxidation processes in laminar non-premixed jet flames", *Combustion and Flame* 162:1660–1678 (2015). (*p.* 116)

[204] Wick, A., Attili, A., Bisetti, F., Pitsch, H., "DNS-driven analysis of the flamelet/progress variable model assumptions on soot inception, growth, and oxidation in turbulent flames", *Combustion and Flame* 214:437–449 (2020). (*p.* 117, 120, 121, 155, 180)

[205] Busupally, M.R., De, A., "Numerical modeling of soot formation in a turbulent C_2H_4/air diffusion flame", *International Journal of Spray and Combustion Dynamics* 8:67–85 (2016). (*p.* 117)

[206] Akargun, H.Y., Akkurt, B., Deen, N.G., "Extending the flamelet generated manifold for soot and NOx modeling in diesel spray combustion", *The Proceedings of the International Symposium on Diagnostics and Modeling of Combustion in Internal Combustion Engines 2017.9*, The Japan Society of Mechanical Engineers, p. A105 (2017). (*p.* 117)

[207] van Oijen, J., de Goey, L., "Modelling of premixed counterflow flames using the flamelet-generated manifold method", *Combustion Theory and Modelling* 6:463–478 (2002). (*p.* 117, 147)

[208] van Oijen, J., de Goey, L., "A numerical study of confined triple flames using a flamelet-generated manifold", *Combustion Theory and Modelling* 8:141–164 (2004). (*p.* 117)

[209] Peters, N., "Laminar diffusion flamelet models in non-premixed turbulent combustion", *Progress in Energy and Combustion Science* 10:319–339 (1984). (*p.* 117)

[210] Vasavan, A., de Goey, P., van Oijen, J., "A novel method to automate FGM progress variable with application to igniting combustion systems", *Combustion Theory and Modelling* 24:221–244 (2020). (*p.* 118)

[211] Ihme, M., Pitsch, H., "Modeling of radiation and nitric oxide formation in turbulent nonpremixed flames using a flamelet/progress variable formulation", *Physics of Fluids* 20:055110 (2008). (*p.* 120, 217)

[212] Attili, A., Bisetti, F., Mueller, M.E., Pitsch, H., "Formation, growth, and transport of soot in a three-dimensional turbulent non-premixed jet flame", *Combustion and Flame* 161:1849–1865 (2014). (*p.* 141, 180)

[213] Kalbhor, A., Mira, D., van Oijen, J., "A computationally efficient approach for soot modeling with the discrete sectional method and FGM chemistry", *Combustion and Flame (in press)* (2023). (*p.* 151, 182)

[214] Mitchell, P., Frenklach, M., "Monte Carlo simulation of soot aggregation with simultaneous surface growth-why primary particles appear spherical", *Proceedings of the Combustion Institute* 27:1507–1514 (1998). (*p.* 151)

[215] Carbonell, D., Oliva, A., Perez-Segarra, C.D., "Implementation of two-equation soot flamelet models for laminar diffusion flames", *Combustion and Flame* 156:621–632 (2009). (*p.* 153, 182)

[216] Cuoci, A., Frassoldati, A., Faravelli, T., Ranzi, E., "Soot formation in unsteady counterflow diffusion flames", *Proceedings of the Combustion Institute* 32:1335–1342 (2009). (*p.* 163)

[217] Delhaye, S., Somers, L., van Oijen, J., de Goey, L., "Incorporating unsteady flow-effects in flamelet-generated manifolds", *Combustion and Flame* 155:133–144 (2008). (*p.* 165)

[218] Pitsch, H., Ihme, M., "An unsteady/flamelet progress variable method for LES of nonpremixed turbulent combustion", *43rd AIAA Aerospace Sciences Meeting and Exhibit*, p. 557 (2005). (*p.* 165)

[219] Vázquez, M., Houzeaux, G., Koric, S., Artigues, A., Aguado-Sierra, J., Arís, R., Mira, D., Calmet, H., Cucchietti, F., Owen, H., et al., "Alya: Multiphysics engineering simulation toward exascale", *Journal of Computational Science* 14:15–27 (2016). (*p.* 169, 194, 241)

[220] Mira, D., Lehmkuhl, O., Both, A., Stathopoulos, P., Tanneberger, T., Reichel, T.G., Paschereit, C.O., Vázquez, M., Houzeaux, G., "Numerical characterization of a premixed hydrogen flame under conditions close to flashback", *Flow, Turbulence and Combustion* 104:479–507 (2020). (*p.* 169, 180, 184, 185, 187)

[221] Both, A., Lehmkuhl, O., Mira, D., Ortega, M., "Low-dissipation finite element strategy for low mach number reacting flows", *Computers and Fluids* 200:104436 (2020). (*p.* 169, 184, 194)

[222] Gövert, S., Mira, D., Kok, J., Vázquez, M., Houzeaux, G., "The effect of partial premixing and heat loss on the reacting flow field prediction of a swirl stabilized gas turbine model combustor", *Flow, Turbulence and Combustion* 100:503–534 (2018). (*p.* 169)

[223] Guo, H., Smallwood, G.J., "The effect of preferential diffusion on soot formation in a laminar ethylene/air diffusion flame", *Combustion Theory and Modelling* 15:125–140 (2010). (*p.* 170)

[224] Malik, N., Løvås, T., Mauss, F., "The effect of preferential diffusion on the soot initiation process in ethylene diffusion flames", *Flow, Turbulence and Combustion* 87:293–312 (2011). (*p.* 170, 215)

[225] Yang, S., Lew, J.K., Mueller, M.E., "Large eddy simulation of soot evolution in turbulent reacting flows: Strain-sensitive transport approach for polycyclic aromatic hydrocarbons", *Combustion and Flame* 220:219–234 (2020). (*p.* 180, 217)

[226] Sun, B., Rigopoulos, S., "Modelling of soot formation and aggregation in turbulent flows with the LES-PBE-PDF approach and a conservative sectional method", *Combustion and Flame* 242:112152 (2022). (*p.* 180, 181, 182, 188, 201, 202)

[227] Franzelli, B., Tardelli, L., Stöhr, M., Geigle, K., Domingo, P., "Assessment of LES of intermittent soot production in an aero-engine model combustor using high-speed measurements", *Proceedings of the Combustion Institute* (2022). (*p.* 180)

[228] Benajes, J., García-Oliver, J.M., Pastor, J.M., Olmeda, I., Both, A., Mira, D., "Analysis of local extinction of a n-heptane spray flame using large-eddy simulation with tabulated chemistry", *Combustion and Flame* 235:111730 (2022). (*p.* 180, 217)

[229] Bao, H., Kalbhor, A., Maes, N., Somers, B., van Oijen, J., "Investigation of soot formation in n-dodecane spray flames using LES and a discrete sectional method", *Proceedings of the Combustion Institute* (2022). (*p.* 180, 226, 231)

[230] Consalvi, J., Nmira, F., "Transported scalar PDF modeling of oxygen-enriched turbulent jet diffusion flames: Soot production and radiative heat transfer", *Fuel* 178:37–48 (2016). (*p.* 180)

[231] Pachano, L., Xu, C., García-Oliver, J.M., Pastor, J.M., Novella, R., Kundu, P., "A two-equation soot-in-flamelet modeling approach applied under spray A conditions", *Combustion and Flame* 231:111488 (2021). (*p.* 180)

[232] Tian, L., Schiener, M., Lindstedt, R., "Fully coupled sectional modelling of soot particle dynamics in a turbulent diffusion flame", *Proceedings of the Combustion Institute* 38:1365–1373 (2021). (*p.* 180, 181, 202)

[233] Ferraro, F., Gierth, S., Salenbauch, S., Han, W., Hasse, C., "Soot particle size distribution reconstruction in a turbulent sooting flame with the split-based extended quadrature method of moments", *Physics of Fluids* 34:075121 (2022). (*p.* 180, 181, 188)

[234] Colmán, H.M., Darabiha, N., Veynante, D., Fiorina, B., "A turbulent combustion model for soot formation at the LES subgrid-scale using virtual chemistry approach", *Combustion and Flame* 247:112496 (2023). (*p.* 180)

[235] El-Asrag, H., Menon, S., "Large eddy simulation of soot formation in a turbulent non-premixed jet flame", *Combustion and Flame* 156:385–395 (2009). (*p.* 181)

[236] Mueller, M.E., Pitsch, H., "Large eddy simulation subfilter modeling of soot-turbulence interactions", *Physics of Fluids* 23:115104 (2011). (*p.* 181)

[237] Grader, M., Eberle, C., Gerlinger, P., "Large-eddy simulation and analysis of a sooting lifted turbulent jet flame", *Combustion and Flame* 215:458–470 (2020). (*p.* 181)

[238] Sewerin, F., Rigopoulos, S., "An LES-PBE-PDF approach for predicting the soot particle size distribution in turbulent flames", *Combustion and Flame* 189:62–76 (2018). (*p.* 182)

[239] Vreman, A., "An eddy-viscosity subgrid-scale model for turbulent shear flow: Algebraic theory and applications", *Physics of Fluids* 16:3670–3681 (2004). (*p.* 184)

[240] Huang, X., Tummers, M.J., van Veen, E.H., Roekaerts, D.J., "Modelling of mild combustion in a lab-scale furnace with an extended FGM model including turbulence–radiation interaction", *Combustion and Flame* 237:111634 (2022). (*p.* 187, 217)

[241] Both, A., Lehmkuhl, O., Mira, D., Ortega, M., "Low-dissipation finite element strategy for low mach number reacting flows", *Computers & Fluids* 200:104436 (2020). (*p.* 187, 241)

[242] Zhang, J., Shaddix, C.R., Schefer, R.W., "Design of "model-friendly" turbulent non-premixed jet burners for C2+ hydrocarbon fuels", *Review of Scientific Instruments* 82:074101 (2011). (*p.* 191, 192)

[243] Pope, S.B., "Ten questions concerning the large-eddy simulation of turbulent flows", *New Journal of Physics* 6:35 (2004). (*p.* 192)

[244] ANSYS, "Fluent user's guide, 2022 R1", *Ansys Fluent Inc* (2022). (*p.* 193)

[245] Abtahizadeh, E., de Goey, P., van Oijen, J., "LES of delft jet-in-hot coflow burner to investigate the effect of preferential diffusion on autoignition of CH_4/H_2 flames", *Fuel* 191:36–45 (2017). (*p.* 217)

[246] Hoerlle, C.A., França, F.H.R., Pagot, P.R., Pereira, F.M., "Effects of radiation modeling on non-premixed sooting flames simulations under oxyfuel conditions", *Combustion and Flame* 217:294–305 (2020). (*p.* 217)

[247] Liu, F., Consalvi, J.L., Nmira, F., "The importance of accurately modelling soot and radiation coupling in laminar and laboratory-scale turbulent diffusion flames", *Combustion and Flame* p. 112573 (2022). (*p.* 217)

[248] Garćıa-Oliver, J., Pastor, J., Olmeda, I., Kalbhor, A., Mira, D., van Oijen, J., "LES of a pressurized sooting RQL-like combustor with a computationally efficient discrete sectional method coupled to tabulated chemistry", *11th European Combustion Meeting (ECM 2023)* (2023). (*p.* 226)

[249] Zhang, C., Chen, L., Ding, S., Xu, H., Li, G., Consalvi, J.L., Liu, F., "Effects of soot inception and condensation PAH species and fuel preheating on soot formation modeling in laminar coflow CH_4/air diffusion flames doped with n-heptane/toluene mixtures", *Fuel* 253:1371–1377 (2019). (*p.* 231)

[250] Coelho, P.J., "Turbulence radiation interaction: from theory to application in numerical simulations", *International Heat Transfer Conference*, 49439, pp. 251–270 (2010). (*p.* 232)

[251] Blanquart, G., Pepiot-Desjardins, P., Pitsch, H., "Chemical mechanism for high temperature combustion of engine relevant fuels with emphasis on soot precursors", *Combustion and Flame* 156:588–607 (2009). (*p.* 233)

[252] Jiang, P., Zhou, M., Wen, D., Wang, Y., "An experimental multiparameter investigation on the thermochemical structures of benchmark ethylene and propane counterflow diffusion flames and implications to their numerical modeling", *Combustion and Flame* 234:111622 (2021). (*p.* 233)

[253] Trias, F., Lehmkuhl, O., "A self-adaptive strategy for the time integration of Navier-Stokes equations", *Numerical Heat Transfer, Part B: Fundamentals* 60:116–134 (2011). (*p.* 241)

[254] Surapaneni, A., *Development of a finite rate chemistry solver with tabulated dynamic adaptive chemistry*, Master's thesis, Delft University of Technology (2019). (*p.* 242)

Acknowledgments

This is perhaps the most important part of this document. I would like to express my deepest gratitude and immense appreciation to all those who have supported me throughout my PhD research at TU/e. This milestone would not have been possible without their guidance, encouragement, and unwavering support.

First and foremost, I would like to sincerely thank my first promotor, Prof. Jeroen van Oijen, for providing me with this life-changing opportunity. I am truly grateful for your invaluable mentorship, constant guidance, and insightful feedback that have shaped my research and helped me grow as a researcher. The freedom of thinking you provided and the trust you showed in me, have given me the motivation and confidence to succeed during this PhD journey. Whenever I needed any professional or personal help, you were always there. It has been an honor to learn from you, and I am thankful for all the moments we have shared. I profoundly admire your passion for research and commitment to excellence. I consider myself fortunate to have been supervised by you.

I want to express special thanks to Dr. Daniel Mira for his guidance throughout my research. Our regular Wednesday morning discussions and interactions at project meetings were always enjoyable. I will never forget the challenging task of doing code development over Zoom calls during the COVID-19 pandemic. Your never-ending enthusiasm for research made all our conversations very pleasant. I am grateful for your constant support.

I would also like to thank Dr. Bart Somers for agreeing to be my second promotor and evaluating my thesis. It has been a pleasure working together, especially in the field of spray combustion. I am immensely grateful to the members of my dissertation committee, Prof. Andreas Kempf, Prof. Benedicte Cuenot, and Prof. Rick de Lange, for their expertise, constructive criticism, and valuable suggestions. I thank all the committee members for their time and effort in reviewing and approving this thesis.

This PhD project was supported by European Union's Horizon 2020 programme, under the project name 'ESTiMatE'. I would like to acknowledge the ESTiMatE consortium members for their contributions and regular academic interaction, particularly Anurag, Ambrus, Ivan, Robert, Eduardo, Federica, Astrid, Leonardo, and Petros. It has been a pleasure working with all of you.

The PhD journey would not have been as enjoyable without my colleagues in the Power and Flow group at TU/e. Over the past four years, I have had the pleasure of meeting many interesting people who have become a part of my life. I would like to start by thanking my office mates Jinlin, Aled, Andrea, Gabriela, Helen, Aravind, Mark, Robbert, Sina, Noud, and others for creating a vibrant and collaborative work environment. I owe a huge thanks to my colleagues Chih-Chia, Xin, Thijs, Conrad,

Scientific Contributions

List of Publications

Journals

1. **Kalbhor A.** and van Oijen J., Effects of hydrogen enrichment and water vapour dilution on soot formation in laminar ethylene counterflow flames, *International Journal of Hydrogen Energy*, 45:23653–23673 (2020)

2. **Kalbhor A.** and van Oijen J., An assessment of the sectional soot model and FGM tabulated chemistry coupling in laminar flame simulations, *Combustion and Flame*, 229:111381 (2021)

3. **Kalbhor A.** and van Oijen J., Effects of curvature on soot formation in steady and unsteady counterflow diffusion flames, *Combustion and Flame*, 241:112108 (2022)

4. Bao H., **Kalbhor A.**, Maes N., Somers, B., and van Oijen, J., Investigation of soot formation in n-dodecane spray flames using LES and a discrete sectional method, *Proceedings of the Combustion Institute*, (2022)*

5. **Kalbhor A.**, Mira D., and van Oijen J., A computationally efficient approach for soot modeling with discrete sectional method and FGM chemistry, *Combustion and Flame* (2023) *In-press*

6. **Kalbhor A.**, Mira D., Both A., and van Oijen J., Modeling of soot formation in turbulent non-premixed flames with LES-FGM-DSM approach, *Submitted*

7. **Kalbhor A.**, Schmitz R., Ramirez A., Vlavakis P., Hagen F., Ferraro F., Braun-Unkhoff M., Kathrotia T., Riedel U., Trimis D., van Oijen J., Hasse C., Mira D., Experimental and numerical investigation on soot formation and evolution of particle size distribution in laminar counterflow ethylene flames, *Submitted**

8. Garćia-Oliver J., Pastor J., Olmeda I., **Kalbhor A.**, Mira D., and van Oijen J., LES of a pressurized sooting aero-engine model burner using a computationally efficient discrete sectional method coupled to tabulated chemistry, *In preparation**

Conference contributions

1. **Kalbhor A.**, and van Oijen J., Assessment of a sectional model for soot formation in laminar flames: sensitivity to model parameters, and application to practical fuels, *Combura Symposium*, Soesterberg, the Netherlands (2019)

---

*contribution not included in the thesis

2. **Kalbhor A.**, and van Oijen J., Effects of preferential diffusion on soot modeling with the sectional method and FGM tabulated chemistry, *10th European Combustion Meeting*, Napoli, Italy (2021)

3. **Kalbhor A.**, and van Oijen J., Modeling soot formation in burner-stabilized stagnation flames, *Combura Symposium*, Soesterberg, the Netherlands (2021)

4. **Kalbhor A.**, and van Oijen J., Effects of flame curvature on soot formation in SF and SFO counterflow diffusion flames, *13th Asia-Pacific Conference on Combustion*, Abu Dhabi, UAE (2021)

5. **Kalbhor A.**, Mira D., and van Oijen J., Computationally efficient integration of a sectional soot model with FGM chemistry *18th International Conference on Numerical Combustion*, San Diego, USA (2022)

6. **Kalbhor A.**, Mira D., and van Oijen J., LES study of soot formation in turbulent non-premixed flame with sectional method, *Combura Symposium*, Soesterberg, the Netherlands (2022)

7. Mira D., Pérez-Sánchez E., Lehmkuhl O., **Kalbhor A.**, van Oijen J., Ramírez A., Braun-Unkhoff M., Riedel U., Schmitz R., Ferraro F., Hasse C., Olmeda I., Moreno-Montagud C., Garćia-Oliver J., Pastor J., Carreres M., Vlavakis P., Bach E., Stathopoulos P., and Eggels R., Recent advances in the prediction of soot formation in aeroengine combustors, *Towards Sustainable Aviation Summit*, Toulouse, France (2022)*

8. **Kalbhor A.**, and van Oijen J., Modeling soot formation in normal and inverse diffusion flames using FGM chemistry and sectional method, *12th Mediterranean Combustion Symposium*, Luxor, Egypt (2023)*

9. Garćia-Oliver J., Pastor J., Olmeda I., **Kalbhor A.**, Mira D., and van Oijen J., LES of a pressurized sooting RQL-like combustor with a computationally efficient discrete sectional method coupled to tabulated chemistry *11th European Combustion Meeting*, Rouen, France (2023)*

Curriculum Vitae

Abhijit Jijaba Kalbhor was born on September 13, 1992, in Pune, India. He received his bachelor's degree in mechanical engineering in 2014 at the National Institute of Technology in Raipur, India with a university gold medal. In 2017, he completed his master's in aerospace engineering at the Indian Institute of Science (IISc) in Bangalore, India with a major in combustion and propulsion. In February 2019 he started a PhD project in Power & Flow group at the Eindhoven University of Technology, the Netherlands. The results of his PhD research are presented in this dissertation. Before PhD, he also worked as a maintenance engineer for the Govt. of India PSU, Bharat Petroleum Corporation Limited, and as a research associate in the 'Reactive Flow Physics Laboratory' at the IISc. Since 2023 he is employed at ASML within the Bright Society Programme.

With increasingly stringent regulations on emissions, there is an urgent need for accurate and reliable soot models to accelerate the combustor design process. In this regard, this research focuses on the development of a computationally efficient modeling strategy for the prediction of soot formation and evolution in conditions relevant to the practical combustion systems.

2023